A Complete Asymptotic Analysis of the Spectral Instabilities of Small-Amplitude Periodic Water Waves

Ryan P. Creedon

A dissertation
submitted in partial fulfillment of the
requirements for the degree of

Doctor of Philosophy

University of Washington

2022

Reading Committee:

Bernard Deconinck, Chair

Anne Greenbaum

Thomas Trogdon

Program Authorized to Offer Degree:
Applied Mathematics

University of Washington

Abstract

A Complete Asymptotic Analysis of the Spectral Instabilities of Small-Amplitude Periodic Water Waves

Ryan P. Creedon

Chair of the Supervisory Committee:
Professor Bernard Deconinck
Department of Applied Mathematics

Euler's equations govern the behavior of gravity waves on the surface of an incompressible, inviscid, and irrotational fluid (water, in this case). We consider the small-amplitude, periodic traveling-wave solutions of Euler's equations known as the Stokes waves. Our focus is on the instabilities of Stokes waves present in the spectrum of the linearized Euler's equations about these solutions. These instabilities encompass the Benjamin-Feir (or modulational) instability as well as the recently discovered high-frequency instabilities. In this dissertation, we develop a perturbation method to describe the unstable spectral elements associated with each of these instabilities, allowing us to obtain desirable asymptotic properties that connect recent numerical and rigorous studies. As a proof of concept, we first develop the method for simpler, heuristic models of water waves. In all cases, we compare our asymptotic results with direct numerical computations of these instabilities and find excellent agreement, giving confidence in the validity of the perturbation method.

TABLE OF CONTENTS

LIST OF FIGURES

Figure Number Page

ACKNOWLEDGMENTS

When I was a kid, I swore I'd be a weatherman[1], but as I got older, I began to realize that maybe, just maybe, I was meant to be a mathematician instead. One of the biggest drivers of this change was my eighth grade algebra teacher, Robert Moyer, whose enthusiasm and passion for his craft inspired me to want to teach and study math as well. Without his class and his encouragement at that young age, I am not so certain that I would be finishing this PhD today. I want to thank Mr. Moyer for his years inspiring students like myself to achieve feats we never expected or thought possible. I hope I can be half as good an educator to my students some day.

I want to acknowledge Dr. Marcelo Chamecki, who introduced me to asymptotic and perturbation methods during my junior year at Penn State. This course helped me to realize exactly what I wanted to study in graduate school. In fact, many of the techniques used in this dissertation I learned first in Marcelo's course, so thank you, Marcelo. Even though you are a meteorologist by training, you are very much an applied mathematician, and your class inspired me to become a researcher with similar interests and skillset.

It would be remiss of me not to mention my PhD advisor, Dr. Bernard Deconinck, on the first page of my acknowledgement section. Working with Bernard has been one of the biggest honors in my life. Not only is he an expert in his field of study, but he also treats his students with the kind of respect and empathy that are hard to come by in academia these days. His dry sense of humor, sharp wit, and colorful backstories no doubt cheered me up during weeks of slow research progress, and of course, his baking skills never failed to dazzle and impress. Throughout the PhD, Bernard and I would joke that the only reason I

---

[1] I suspect the movie *Twister* had something to do with it.

chose him as my advisor was because of his baking prowess. While I concede that this was certainly a positive factor in my decision, it was his commitment to his students and his sound professional and personal advice that really made my decision so easy. Thank you, Bernard, for all of your guidance over the past six years. I'm grateful to know you, to have worked (and joked) with you, and to learn from you. You've certainly made me appreciate the value of tackling hard problems, and I hope to continue this theme in my own research going forward.

I'd like to thank my committee members Dr. Anne Greenbaum, Dr. Jim Riley, and Dr. Tom Trogdon for their feedback over the past few years. This dissertation is above and beyond what I could have ever hoped to achieve in large part due to their input and suggestions. I appreciate their flexibility during the pandemic, and their willingness to attend my defense early on a Monday morning during the last week of classes.

I'd like to thank my fellow labmates in Bernard's group, including Mark Bennett, Matthew Farkas, Ben Segal, Jeremy Upsal, and Xin Yang, for the shared camaraderie over the years and for the many hours spent playing outdated trivia games in the upstairs lounge and on retreats. I would like to thank especially Jorge Cisneros, who started as one of my mentees during my second year of graduate school and quickly became one of my closest friends. Let it be known that the two of us finished our dissertations together over the weekend of his sister's wedding. I would also like to thank Dr. John Carter, Dr. Olga Trichtchenko, and Dr. Katie Oliveras for their feedback and guidance over the past few years.

I also owe a big thank you to the staff of the department, including Karen Beaudry, Laurie Feldman, Tony Garcia, and Sarah Riley. I will never forget organizing the department's fiftieth anniversary conference with all of you and temporarily moving to Gerberding Hall while Lewis underwent earthquake proofing. I want to thank Lauren Lederer especially, who was the graduate senior advisor for most of my time in the PhD program. I regret that we didn't get a chance to co-organize a department yoga event, but perhaps we can arrange something similar in the future.

I would also like to thank the many friends that I've made during my time in the department. For the inspiring teaching-related discourse, I'd like to thank Craig Gin, Kelsey Marcinko, and Kelsey Maass. For the most delicious chocolate dessert I've ever tasted (excluding Bernard's) and for the best rounds of Codenames ever, I'd like to thank Ben Liu and Natalie Wellen. For being a fellow Aries, I'd like to thank Nora Gilbertson. For making my first year in the program extra special, I'd like to thank Bobby Baraldi, Nathan Lee, Megan Morrison, Rose Nguyen, and Katherine Owens. I'd also like to thank Lizeth Cisneros for the many visits to Seattle Pops and late night McDonald's conversations. There are so many others I wish to thank, but for sake of brevity, I'll stop here. Thank you to everyone I've met here in Seattle: I am grateful to know each and every one of you.

Lastly, I need to thank my family. My parents, the Pegs, are not mathematicians, nor do they understand how their son became so enamored with the subject. However, they did teach me that value of hard work and an education, and without their love and support, I could not imagine finishing a PhD. My mother always said, "To those who have been given much, much is required," and with this PhD, I intend to pay it forward. Thank you from the bottom of my heart for everything—your love, your generosity, and your guidance.

I want to thank my brother, Rob, and sister-in-law, Emily, who supported me every step of the way in this program. Watching your family grow since the time I started this PhD has been a joy of a lifetime. I am so lucky to be an uncle not just to one outstanding nephew, but to two. I only wish I lived a little closer to see both Landon and Grant grow up, but I treasure the times that we do get to spend together.

I want to thank my *wonderful* grandparents on my mom's side, Grandma and Pap Kvederis. Our monthly conversations about useless knowledge no doubt sharpened my abilities to finish this thesis. Perhaps, Grandma, you can show me now your secret to computing ratios so quickly, as I've been told you're a local expert. I also want to thank my grandmother on my dad's side, Gran, who taught me how *not* to do long division or multiplication. She did, however, teach me how to get into trouble in the kitchen and in a Walmart, and that's proved to be a useful skill. I also want to thank her sister, Aunt Jo, who was a witness to many of these stunts and who has always been there for me.

Last, but certainly not least, I need to thank my partner, Enoc De Santiago, and his family. If you were to tell me when I started this PhD program that I not only would be out but in a relationship, I would not have believed it. Words cannot express how grateful I am to have met you, Enoc. You are the most patient, considerate, and empathetic person I have ever had the pleasure to meet, and as cliché as it sounds, you challenge me every day to be a person of the same integrity. I am so blessed to have you and yours in my life. Te amo muchisimo, pavo—siempre por siempre.

DEDICATION

To Gran, whose keen sense of humor no doubt solved many of life's hard problems,
and to Pap, who taught me that every problem can be solved in ten days.
You both are dearly missed.

Chapter 1

INTRODUCTION

1.1 Relevant History

1.1.1 Models of Water Waves

In his celebrated Principia, Newton derived a relationship between the speed and wavelength[1] of water waves in infinite depth, becoming one of the first scientists to anticipate a mathematical study of water waves [27, 72]. It was not until several decades later, when Euler published his laws of hydrodynamics [40, 41, 42], that more could be said about the mathematical behavior of water and other fluids. From these laws, Cauchy [20] and Poisson [80, 81] eventually formulated the governing equations of water waves in finite and infinite depth. Their formulation of water waves is the starting point of this work.

For simplicity, we consider waves dependent on one horizontal coordinate x, a vertical coordinate z, and time t. We align the undisturbed surface of the water with the reference level $z = 0$ without loss of generality and assume the bottom boundary of the water has constant bathymetry along $z = -h$, where $h > 0$ is the mean depth of the water. We denote the displacement of the free surface relative to the reference level $z = 0$ by $\eta = \eta(x,t)$ and the velocity field in the bulk of the water by $\mathbf{u} = \mathbf{u}(x,z,t)$. In this work, we are concerned only with periodic water waves, so we assume that η and $\mathbf{u}$ are $2\pi/\kappa$-periodic in the x-direction, where $\kappa > 0$ represents the wavenumber of the periodic disturbance at the surface of the water, see Figure 1.1 for a schematic.

To obtain governing equations for η and $\mathbf{u}$, we assume the flow of water is *ideal*, meaning

(i) The flow is *irrotational*, or free of vorticity. As a result, the velocity field $\mathbf{u} = \mathbf{u}(x,z,t)$

---

[1] What we now would call the linear dispersion relation.

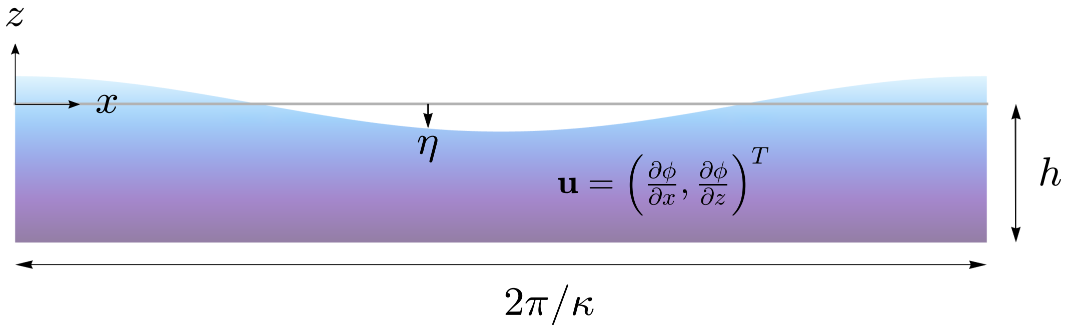

Figure 1.1: A schematic of the water wave problem in two spatial dimensions, x and z. The variable η represents the displacement of the free surface from $z = 0$. The variable ϕ represents the velocity potential in the bulk. The spatial gradient of ϕ gives the velocity in the bulk of the water $\mathbf{u}$. In this work, we consider waves that are $2\pi/\kappa$-periodic in the x-direction with constant bathymetry along $z = -h$.

may be represented by the spatial gradient of a velocity potential $\phi = \phi(x, z, t)$.

(ii) The water has *constant density*. Thus, the flow is incompressible, and the divergence of $\mathbf{u}$ vanishes for all time t.

(iii) The water has *negligible internal viscosity*, implying that the flow of the water is not dissipative and will not exert tangential forces on the bottom boundary of the domain.

If, in addition to these assumptions, we assume that the water is free of surface tension and does not escape the free surface[2] $z = \eta$ nor penetrate the bottom surface $z = -h$, the governing equations for periodic water waves become

$$\phi_{xx} + \phi_{zz} = 0, \qquad (x, z) \in (-\pi/\kappa, \pi/\kappa) \times (-h, \eta)\,, \tag{1.1a}$$

$$\phi_z = 0, \qquad z = -h, \tag{1.1b}$$

$$\eta_t + \eta_x \phi_x = \phi_z, \qquad z = \eta, \tag{1.1c}$$

$$\phi_t + \frac{1}{2}\left(\phi_x^2 + \phi_z^2\right) + g\eta = 0, \qquad z = \eta, \tag{1.1d}$$

---

[2] This implies that the water cannot spray into the atmosphere above.

together with the periodicity conditions

$$\eta(x-\pi/\kappa,t)=\eta(x+\pi/\kappa,t) \quad \text{and} \quad \mathbf{u}(x-\pi/\kappa,z,t)=\mathbf{u}(x+\pi/\kappa,z,t), \tag{1.2}$$

where g represents the magnitude of the vertical acceleration due to Earth's gravity and subscripts denote their corresponding partial derivatives. A full derivation of (1.1a)-(1.1d) is provided in [63, 76, 84], for example. We take these equations as given.

Historically, equations (1.1a)-(1.1d) are attributed to Euler[3], and because of such, we refer to (1.1a)-(1.1d) collectively as *Euler's equations.* At the heart of Euler's equations is the Laplace equation (1.1a). One might naively conclude that equations (1.1a)-(1.1d) are easily solved, since the Laplace equation is linear. This would be the case if the domain over which one solves the Laplace equation was known, but this domain changes in time according to the nonlinear evolution equations (1.1c) and (1.1d). In reality, Euler's equations are far from an "easy" linear problem: not only are they nonlinear because of (1.1c) and (1.1d), but they are nonlocal because the evolution of the free surface depends on knowledge of the evolution of the entire bulk of the fluid according to (1.1a).

To simplify some of these difficulties in Euler's equations, it becomes useful to develop asymptotic models of water waves. These are simplified equations derived from (1.1a)-(1.1d) that replicate the full dynamics of water waves in certain parameter regimes. For example, when the period of the surface waves is large compared to the depth of the water (so that $\kappa h \ll 1$) and the amplitude of the waves ε is small compared to the depth (so that $\varepsilon/h \ll 1$), we have the shallow water equations due to Boussinesq [13]:

$$\eta_t = -hu_x - (\eta u)_x, \tag{1.3a}$$

$$u_t = -uu_x - g\eta_x, \tag{1.3b}$$

where u represents the horizontal velocity along the bottom surface $z=-h$. Restricting further to unidirectional waves that evolve on long time scales, we arrive at

$$\eta_t = -\left(\sqrt{gh}\right)\eta_x - \left(\frac{3}{2}\sqrt{\frac{g}{h}}\right)\eta\eta_x - \left(\frac{1}{6}\sqrt{gh^5}\right)\eta_{xxx}, \tag{1.4}$$

---

[3] Although Lord Kelvin was the first to write them using the notation in (1.1a)-(1.1d), see [27].

which is the celebrated Korteweg-deVries (KdV) equation [14] in a frame traveling at the shallow water velocity $c_{SW} = \sqrt{gh}$. In addition to these equations are countless other asymptotic models of Euler's equations, including the extended KdV equations [68], Kadomtsev-Petviashvili equation [25], nonlinear Schrödinger equation [78], Zakharov equation [95], and Davey-Stewartson system [32], to name a few. Each of these models is valid in a distinct parameter regime of the full governing equations of water waves and, therefore, has its own set of advantages and disadvantages.

Complementary to the asymptotic models are heuristic models designed to match phenomenological observations of water waves. Many of these models are inspired by Euler's equations, but are not consistently derived from them. The Kawahara equation

$$\eta_t = \alpha\eta_{xxx} + \beta\eta_{5x} + 2\sigma\eta\eta_x, \tag{1.5}$$

with free parameters $\alpha, \beta, \sigma \in \mathbb{R} \setminus \{0\}$ is an example of a heuristic model for unidirectional shallow water waves with dispersion and surface tension [58]. Upon closer inspection, we see that (1.5) is a rescaled KdV equation with an additional fifth-order dispersion term that models the effect of surface tension on the waves. For this reason, the Kawahara equation is sometimes called the super-KdV equation.

A second example of a heuristic model is the Boussinesq-Whitham system introduced by Hur and Pandey [51]:

$$\eta_t = -hu_x - (u\eta)_x \tag{1.6a}$$

$$u_t = -g\mathcal{K}(\eta_x) - uu_x, \qquad \mathcal{K}(f) = \left(\frac{\tanh(hD)}{hD}\right) f, \tag{1.6b}$$

where $D = -i\partial_x$. Here, the Fourier multiplier $\mathcal{K}$ is inserted provisionally in the shallow water equations (1.3a)-(1.3b) so that the linearized dispersion relation of (1.6a)-(1.6b) matches that of Euler's equations[4]. As a consequence, (1.6a)-(1.6b) represents a heuristic model of shallow

---

[4] In fact, a Fourier multiplier can be inserted in a number of places in the shallow water equations to achieve the same effect, leading to an entire family of Boussinesq-Whitham systems [19]. Of all these systems, (1.6a)-(1.6b) has desirable local well-posedness properties, see [38].

water waves with full dispersion that captures more intricate phenomena than is observed in the shallow water equations alone, such as wave peaking [52].

As with the asymptotic models, there are several heuristic models that are used to study water waves. It is impossible to summarize all of these models here. Rather, we focus on the two mentioned above: the Kawahara equation and the Hur-Pandey Boussinesq-Whitham (HPBW) system. As will be seen in Chapters 2 and 3, both of these models capture instabilities of small-amplitude periodic water waves that are central to this thesis and to the study of periodic water waves as a whole.

1.1.2 Stokes Wave Solutions

Despite the inherent complexities of Euler's equations, there exists a special class of solutions that can be understood analytically. In particular, Stokes showed in 1847 how to derive an asymptotic expansion for the small-amplitude, periodic traveling-wave solutions of Euler's equations in infinitely deep water. Seventy-five years later, Nekrasov [71] and Levi-Civita [64] proved the convergence of Stokes' series, and Struik [87] extended these considerations to the case of finite depth. More recently, it has been shown that the Kawahara equation and HPBW system exhibit similarly behaved solutions, as proved in [48] and [51], respectively.

Today, these special solutions are known as the *Stokes waves* of Euler's equations[5]. Without loss of generality, their asymptotic expansion takes the form

$$\eta_S(\xi;\varepsilon) = \varepsilon\cos(\kappa\xi) + \sum_{j=2}^{\infty}\eta_j(\xi)\varepsilon^j, \tag{1.7}$$

where η_S represents the surface displacement of the Stokes wave, ε is a small parameter that is related to the amplitude of the wave, η_j are $2\pi/\kappa$-periodic functions of ξ (that have auxiliary dependence on g, κ, and h), and ξ is the traveling coordinate

$$\xi = x - ct, \tag{1.8}$$

---

[5] Or of the Kawahara equation or HPBW system, depending on the choice of governing equations.

where c is the velocity of the Stokes wave. It can be shown (see Chapter 4) that the higher-order corrections η_j take the form

$$\eta_j(\xi) = \sum_{\substack{\ell=2 \\ \ell \text{ even}}}^{j} \hat{N}_{j,\ell} \cos(\ell\kappa\xi) \quad \text{for} \quad j \text{ even}, \tag{1.9a}$$

$$\eta_j(\xi) = \sum_{\substack{\ell=3 \\ \ell \text{ odd}}}^{j} \hat{N}_{j,\ell} \cos(\ell\kappa\xi) \quad \text{for} \quad j \text{ odd}, \tag{1.9b}$$

without loss of generality, where the coefficients $\hat{N}_{j,\ell}$ are explicit functions of κ, h, and g.

Because Euler's equations are nonlinear, the velocity of the Stokes wave is coupled to its amplitude so that

$$c(\varepsilon) = c_0 + \sum_{j=1}^{\infty} c_{2j}\varepsilon^{2j}, \tag{1.10}$$

where the leading-order term

$$c_0 = \pm\sqrt{\frac{g}{\kappa}\tanh(\kappa h)}, \tag{1.11}$$

is consistent with the linear dispersion relation of the Euler equations. The higher-order coefficients c_{2j} are explicit functions of g, κ, and h, to be obtained in Chapter 4. That c is even in ε also follows from work in this chapter. Figure 1.2 compares numerical computations of the Stokes waves using the numerical continuation method presented in Appendix A against the asymptotic expansions (1.7) and (1.10) to $\mathcal{O}\left(\varepsilon^4\right)$. Excellent agreement between the two is found in all depths, giving confidence that the expansions above are correct.

To date, Stokes waves remain one of the few nontrivial solutions of Euler's equations that are supported by rigorous results and that can be constructed analytically with the help of perturbation methods. These waves also well-approximate small-amplitude periodic water waves observed in wave tank experiments, *e.g.*, [9, 43], and in nature [70], which makes them a useful benchmark to compare predictions of Euler's equations with real data. The Stokes waves can also be used to assess the accuracy of new numerical methods for water waves.

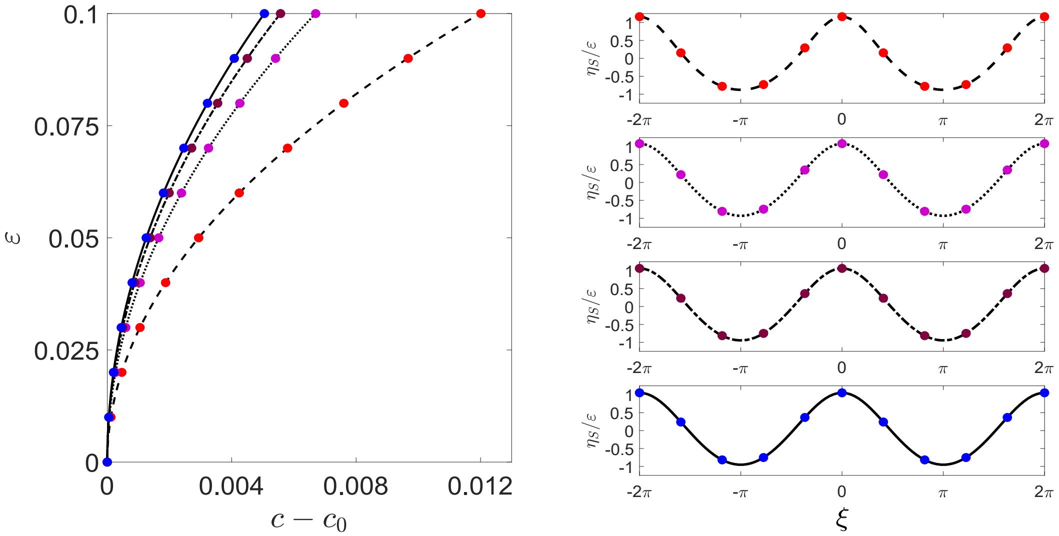

Figure 1.2: (Left) An amplitude *vs.* velocity bifurcation diagram of a 2π-periodic Stokes waves (*i.e.*, $\kappa = 1$) in depth $h = 1$ (dashed line), $h = 1.5$ (dotted line), $h = 2$ (dot-dashed line), and $h = \infty$ (solid line), according to our $\mathcal{O}\left(\varepsilon^4\right)$ asymptotic calculations. The zeroth-order contribution c_0 is removed for better visibility. The numerical results are given by the colored dots. Red dots correspond to $h = 1$, magenta dots correspond to $h = 1.5$, purple dots correspond to $h = 2$, and blue dots correspond to $h = \infty$. (Right) Plots of η_S/ε as a function of ξ when $\varepsilon = 0.1$, $\kappa = 1$, and $h = 1, 1.5, 2$, and ∞ (arranged from top to bottom using the same line styles as in the left figure). A sampling of numerical results is given by the colored dots using the same color scheme as in the left figure.

1.1.3 Spectral Instabilities of Stokes Waves

After a lull in research activity following Nekrasov, Levi-Civita, and Struik, Stokes waves regained scientific interest in the early 1960s as a result of wave tank experiments by Benjamin and Feir at the University of Cambridge. Initial experiments by Benjamin and Feir suggested that Stokes waves become unstable in the direction transverse to their velocity[6], challenging preconceived notions of the day that Stokes waves are stable [50]. Upon recreating these instabilities at the National Physics Lab in London a few years later, Benjamin and Feir

---

[6] In our case, the waves propagate in the x-direction so that the transverse direction is the y-direction.

published their results [9], and Benjamin, in particular, sought to investigate the stability of the Stokes waves analytically.

By brute-force formal calculations, Benjamin showed in 1967 that Stokes waves lose the permanence of their shapes due to longitudinal[7] sideband[8] perturbations provided $\kappa h > \alpha_{BW} = 1.36278...$ [8]. This same threshold of instability was derived concurrently and independently by Whitham using variational techniques [91, 92]. By the end of the 1960s, it became clear that Stokes waves are indeed unstable in sufficiently deep water and that the resulting instability modulates the original periodic wavetrain into wave packets. Today, we refer to this instability as the modulational instability, sideband instability, or, in the context of water waves, the Benjamin-Feir instability.

In the years since the pioneering work of Benjamin, Feir, and Whitham, several papers have explored the Benjamin-Feir instability experimentally, numerically, and analytically. We highlight a few works below that are most relevant to this thesis, but by no means do we give a complete account of all related works. For a more comprehensive history of the Benjamin-Feir instability, see [27, 45, 94] and, in different contexts, [35, 61, 96].

In the 1970s, Bryant [17, 18] studied the stability of Stokes waves in shallow water ($\kappa h < \alpha_{BW}$) with respect to co-periodic longitudinal and transverse perturbations, respectively. Around the same time, Longuet-Higgins [65, 66] considered the stability of Stokes waves with respect to sub- and super-harmonic longitudinal perturbations in infinitely deep water. These are perturbations that are an integer multiple or integer quotient of the fundamental period of the Stokes wave, respectively. In 1982, McLean [69] generalized the results of Bryant and Longuet-Higgins by investigating the stability of Stokes waves in finite depth with respect to sub- and super-harmonic transverse perturbations. McLean is often credited as the first to address the transverse modulational instabilities originally observed in the experiments of Benjamin and Feir.

The results of Bryant and Longuet-Higgins are obtained by perturbing a Stokes wave

---

[7] In the direction of propagation of the Stokes waves.

[8] Meaning the perturbations had nearly the same period as the Stokes waves themselves.

with a quasi-periodic function in the ξ-direction:

$$\eta(\xi, t; \varepsilon, \rho) = \eta_S(\xi; \varepsilon) + \rho e^{i\mu\kappa\xi + \lambda t} w(\xi; \varepsilon) + c.c. + \mathcal{O}(\rho^2). \tag{1.12}$$

Here, $\mu \in [-1/2, 1/2)$ is a free parameter called the Floquet exponent that specifies the degree of quasi-periodicity of the perturbation, $w(\xi; \varepsilon)$ is a sufficiently smooth, $2\pi/\kappa$-periodic function, $\lambda \in \mathbb{C}$ is the exponential growth rate of the perturbation, and *c.c.* denotes the complex conjugate of what immediately preceeds. Linearizing Euler's equations with respect to the small parameter ρ in a frame traveling with the Stokes waves, one arrives at a spectral problem whose eigenfunctions are $w(\xi; \varepsilon)$ and corresponding eigenvalues are λ. Upon choosing a mesh for μ, this problem is solved numerically using methods such as the Floquet-Fourier-Hill (FFH) method [34], yielding estimates for the exponential growth rates of the perturbations. The results of McLean follow in a similar way if a transverse variable y is introduced appropriately in (1.12) [69]. In this thesis, we only consider the stability of Stokes waves with respect to the quasi-periodic longitudinal perturbations given by (1.12).

The union of λ over $\mu \in [-1/2, 1/2)$ is referred to as the *stability spectrum* of the Stokes wave. For fixed wave amplitude ε, this spectrum decomposes into a countable set of finite-multiplicity eigenvalues for each Floquet exponent μ, resulting in a purely continuous spectrum when the union of $\mu \in [-1/2, 1/2)$ is taken. This spectrum is analytic with respective to ε for almost all values of μ, as Akers and Nicholls show in [5, 6, 74]. Because Euler's equations are Hamiltonian [95], the stability spectrum is also symmetric about the real and imaginary axes [47], see Figure 1.3 for a visualization. Hence, for a Stokes wave with amplitude ε to be spectrally stable, its stability spectrum must be a subset of the imaginary axis. Otherwise, there exists a perturbation of the Stokes wave that grows exponentially in time, leading to spectral instability.

When $\varepsilon = 0$, the stability spectrum is purely imaginary, implying that a Stokes wave of zero amplitude (*i.e.*, flat water) is spectrally stable. When $0 < \varepsilon \ll 1$, MacKay and Saffman [67] derived two necessary conditions for eigenvalues to leave the imaginary axis via a Hamiltonian-Hopf bifurcation:

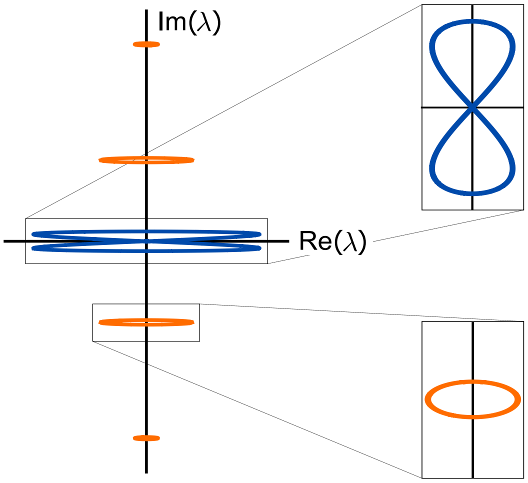

Figure 1.3: A schematic of the stability spectrum for a small-amplitude Stokes wave in sufficiently deep water. The Benjamin-Feir figure-eight curve is colored blue, while the high-frequency instabilities are colored orange. The spectrum is purely continuous and parameterized by the Floquet exponent $\mu \in [-1/2, 1/2)$ for fixed ε. Because of the Hamiltonian structure of Euler's equations, the stability spectrum has quadrafold symmetry about the real and imaginary axes.

(i) Eigenvalues leave the imaginary axis in pairs because of the quadrafold symmetry of the stability spectrum.

(ii) If a pair of eigenvalues leaves the imaginary axis, these eigenvalues must have opposite *Krein signatures.*

The Krein signature of an eigenvalue is defined as the sign of the curvature of the Hamiltonian of the linearized Euler equations evaluated at the corresponding eigenfunctions [62]. Often, though not always, condition (i) implies condition (ii), allowing one to skip the Krein signature calculation, see [36] for examples.

The Benjamin-Feir instability is a consequence of eigenvalues colliding at the origin of the complex spectral plane for $0 < \varepsilon \ll 1$. The seminal work of Bridges and Mielke [15] uses spatial dynamics and center manifold theory to prove the existence of unstable eigenvalues generated by this collision when $kh > \alpha_{BW}$ and $0 < \varepsilon \ll 1$, effectively proving the existence of the Benjamin-Feir instability. The proof is valid for any finite depth but fails in water of infinite depth for reasons that we address in Chapter 5 of this thesis. Only in the past two years have Nguyen and Strauss [73] developed a proof based on Lyapunov-Schmidt reduction that works in both finite and infinite depth. Another proof based on periodic Evans functions appeared in the literature more recently [53].

In 2011, Deconinck and Oliveras [35] revisited the numerical computations of McLean and others. Their numerical results showed for the first time a fully resolved plot (to within machine precision) of the stability spectrum for sufficiently small-amplitude Stokes waves. The Benjamin-Feir instability appears in this spectrum as a figure-eight centered at the origin of the complex spectral plane, as depicted in Figure 1.3. Extensive work by Berti, Maspero, and Ventura [10, 11] has recently proven this result using Kato's theory of similarity transformations [57] and KAM theory.

In addition to the Benjamin-Feir figure-eight, Deconinck and Oliveras found evidence of instabilities away from the origin, now called the *high-frequency instabilities*, that were ignored in McLean's original work. These additional "isolas" (or bubbles) of instability are parameterized by narrow intervals of the Floquet exponent that drift with ε, making them difficult for numerical methods to detect without additional information, see Figure 1.4. Unlike the Benjamin-Feir instability, the high-frequency instabilities persist in numerical computations for all kh, suggesting that Stokes waves are not only unstable in sufficiently deep water, but unstable in all depths. In addition, the high-frequency instabilities can even dominate the Benjamin-Feir instability in certain depths, see Figure 1.5, for instance.

High-frequency instabilities are not unique to Euler's equations. They exist for an entire class of dispersive, Hamiltonian equations with Stokes-like solutions [36]. This includes the Kawahara equation [29, 89] and the HPBW system [28], as will be seen. Unlike the Benjamin-Feir instability, high-frequency instabilities have yet to be observed in experiments or in nature, and it appears unlikely that results in either setting will be found any time soon, at least on this planet. Using the growth rates of high-frequency instabilities computed in [35, 90], a Stokes waves of period 0.1m in a tank of depth 1m would require the length of

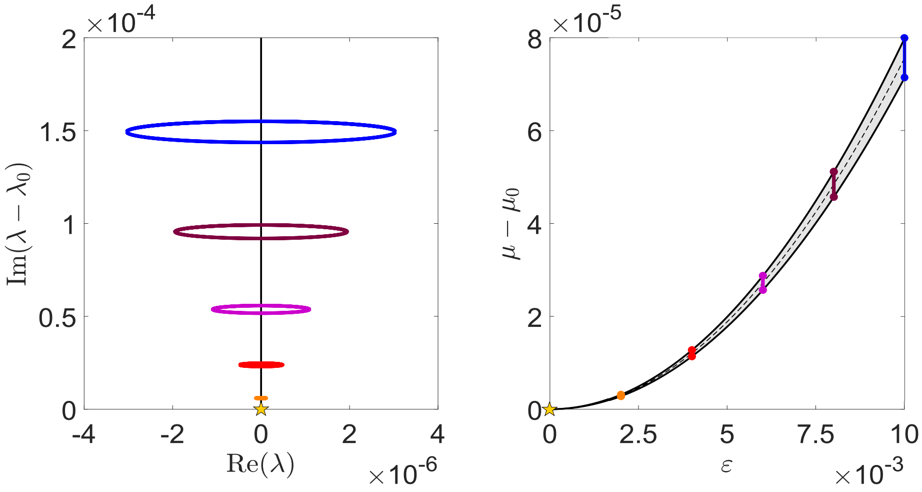

Figure 1.4: (Left) The high-frequency isola closest to the origin for a 2π-periodic Stokes wave in depth $h = 1.5$ with amplitude $\varepsilon = 2 \times 10^{-3}$ (orange), $\varepsilon = 4 \times 10^{-3}$ (red), $\varepsilon = 6 \times 10^{-3}$ (magenta), $\varepsilon = 8 \times 10^{-3}$ (purple), and $\varepsilon = 10^{-2}$ (blue). The imaginary axis is recentered to show the drift of the isola from the collided eigenvalues at λ_0. (Right) The interval of Floquet exponents that parameterizes the isola closest to the origin in depth $h = 1.5$ as a function of the amplitude. The solid black lines indicate the boundaries of this interval, while the dashed black line gives the Floquet exponent corresponding to the most unstable eigenvalue on the isola. The colored lines give the Floquet exponents corresponding to the similarly colored isolas in the left figure. The Floquet axis is recentered to show the drift of the parameterizing interval from the Floquet exponent μ_0 that corresponds to the collided eigenvalues.

the tank to be $\sim$ 1000km before a high-frequency instability would become visible. By that point, other physics, such as internal viscosity, may have already arrested the growth of these instabilities. Presumably, high-frequency instabilities can appear in contexts outside of water waves as well, for example, in crystalline structures or nonlinear optics, provided a Hamiltonian-Hopf bifurcation takes place in the associated spectral stability problem. At present, these applications have yet to be explored in full detail.

Both the Benjamin-Feir and high-frequency instabilities play an important role not only in the hydrodynamic stability of periodic water waves, but also in problems where these waves are slightly perturbed due to nonconstant bottom bathymetry, vorticity, density strat-

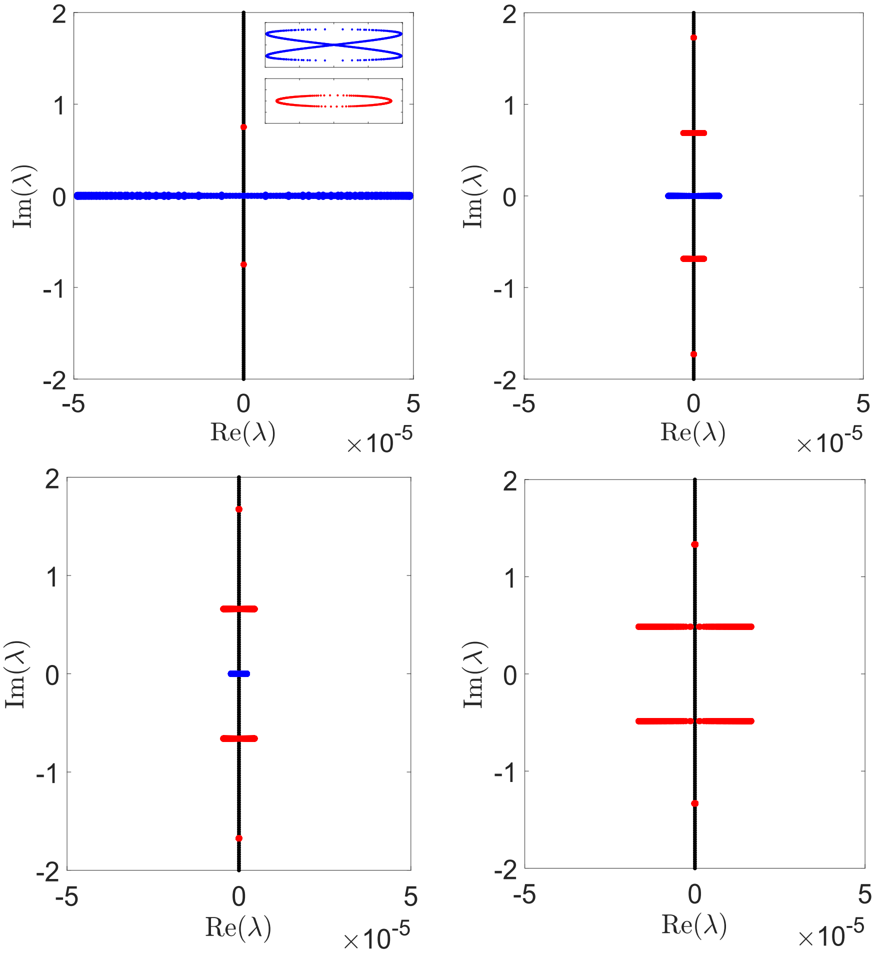

Figure 1.5: The stability spectrum of a 2π-periodic Stokes wave with amplitude $\varepsilon = 0.01$ and (Top, Left) $h = \infty$, (Top, Right) $h = 1.5$, (Bottom, Left) $h = 1.4$, and (Bottom, Right) $h = 1$. The Benjamin-Feir figure-eight is in blue, the high-frequency isolas are in red, and purely imaginary eigenvalues are in black. A zoom-in of the Benjamin-Feir and high-frequency instabilities is inlaid in the top, left plot.

ification, shear layers, or surface tension, for instance. Irrespective of the source of these perturbations, one's first inclination when faced with these problems is always to linearize Euler's equations about the Stokes waves, which leads to a spectral problem whose elements are precisely the stability spectrum. The unstable elements of this spectrum correspond to modes of the unperturbed problem that resonate with the perturbations themselves, giving the unstable spectra immense significance from a phenomenological perspective. Moreover, if the approximate whereabouts of the unstable eigenvalues are known ahead of time (at least in Floquet space), this allows for more efficient numerical resolution of this resonance between the unperturbed problem and the perturbations themselves.

1.2 Overview of the Dissertation

Almost all investigations of high-frequency instabilities, apart from the author's recent contributions in [28, 29, 30], have been numerical in nature [22, 35, 36, 89, 90] and limited to the first few isolas. It is conjectured, however, that the stability spectrum of Stokes waves has an infinite number of high-frequency isolas. One of the primary challenges in finding the remaining isolas is to obtain their Floquet parameterizations, as the intervals corresponding to these parameterizations become increasingly more narrow as one considers high-frequency isolas further from the origin. A second challenge concerns the size of the isolas themselves. Outside of the first few, most have maximum real component smaller than what standard double precision affords, making them undetectable in typical computational settings.

In 2015, Akers [3] introduced a perturbation method to predict Floquet exponents μ for which the stability spectrum in infinite depth loses analyticity with respect to sufficiently small ε. This method can be modified to predict the interval of Floquet exponents that parameterizes the high-frequency isolas, as the boundaries of this interval correspond precisely to those Floquet exponents for which the spectrum is not analytic in ε. A major goal of this thesis is to develop this perturbation method for high-frequency isolas in both finite and infinite depth and push the method to produce high-order asymptotic approximations of these isolas and their Floquet parameterizations. From these expansions, we hope to provide new insights into the following questions:

(i) How many high-frequency isolas exist in the stability spectrum of Stokes waves?

(ii) What are asymptotic estimates for the growth rates of each isola? How do these growth rates change with ε?

(iii) What are the asymptotically correct intervals of the Floquet exponent μ that parameterize each isola? How do these intervals change with ε?

(iv) In what depths can we expect high-frequency isolas to appear in the stability spectrum?

Ideally, we want to address these questions for the Stokes waves of Euler's equations, but for simplicity and as a proof of concept, we first develop our perturbation method in the context of heuristic models. In particular, in Chapter 2, we apply the perturbation method to high-frequency instabilities of the Kawahara equation. This allows for a nice introduction to the essential ingredients of the perturbation method, as the Kawahara equation is a scalar partial differential equation with nonlinearities that are less severe than those in Euler's equations. In Chapter 3, we increase the difficulty by studying the high-frequency instabilities of the HPBW system, which can be viewed as a vector equation that introduces a nonlocal integro-differential operator. Finally, in Chapter 4, we consider the full extension of the perturbation method to Euler's equations in finite and infinite depth, using a powerful reformulation of the governing equations. In all three chapters, we obtain asymptotic approximations of the high-frequency isolas that match the numerical computations of [22, 35, 36, 89, 90] and, in the case of Chapter 4, have even inspired recent rigorous results [53].

In addition to the high-frequency isolas, we can modify the perturbation method to obtain high-order asymptotic approximations of the Benjamin-Feir figure-eight curve in finite and infinite depth. We consider this modification in Chapter 5. Our expansions of the figure-eight are compared directly with numerical computations and recent rigorous results by [10, 11], to excellent agreement. Using results in Chapters 4 and 5, we compare the growth rates of the Benjamin-Feir and high-frequency instabilities analytically for the first time. This comparison suggests three regimes for Stokes waves: (i) shallow water ($\kappa h < \alpha_{BW} = 1.36278...$), in which only high-frequency instabilities exist, (ii) intermediate water ($\alpha_{BW} < \kappa h < \alpha_{DO}(\varepsilon) = 1.43080... + \mathcal{O}(\varepsilon^2)$), in which both instabilities exist but high-frequency instabilities dominate, and (iii) deep water ($\kappa h > \alpha_{DO}(\varepsilon)$), in which both instabilities are present, but the Benjamin-Feir instability dominates.

To summarize, this thesis completely characterizes the asymptotic behavior of the unstable spectrum for small-amplitude Stokes waves in finite and infinite depth. The asymptotic behavior of the high-frequency instabilities is presented in the first three chapters, first for heuristic models of water waves and then for Euler's equations. Excellent agreement between asymptotic and numerical computations of these instabilities is found in all cases. In the final chapter, we derive the asymptotic behavior of the Benjamin-Feir instability, which is also in agreement with numerical computations and the recent rigorous results of [10, 11].

Chapter 2

HIGH-FREQUENCY INSTABILITIES OF THE KAWAHARA EQUATION

2.1 About the Kawahara Equation

In this chapter, we study the Kawahara equation

$$\eta_t = \alpha\eta_{xxx} + \beta\eta_{5x} + 2\sigma\eta\eta_x, \tag{2.1}$$

where α, β, $\sigma \in \mathbb{R} \setminus \{0\}$ are free parameters. This equation was first proposed in [58] as a shallow water model for unidirectional waves with surface tension. The Kawahara equation is dispersive, with linear dispersion relation

$$\omega(k) = \alpha k^3 - \beta k^5. \tag{2.2}$$

The equation is also canonically Hamiltonian

$$\eta_t = \partial_x \frac{\delta\mathcal{H}}{\delta\eta}, \tag{2.3}$$

with

$$\mathcal{H} = \int_{-\pi/\kappa}^{\pi/\kappa} \left(-\frac{\alpha}{2}\eta_x^2 + \frac{\beta}{2}\eta_{xx}^2 + \frac{\sigma}{3}\eta^3 \right) dx, \tag{2.4}$$

assuming η is $2\pi/\kappa$-periodic.

The relevant solutions of (2.1) are the small-amplitude, $2\pi/\kappa$-periodic traveling waves, which can be expressed as a power series in a small parameter related to the amplitude of the solutions, see [48] and Section 2.2 below for more details. Because of their similarities to the Stokes waves of Euler's equations, we refer to these solutions as the Stokes waves of the Kawahara equation throughout this chapter.

Perturbing the Stokes waves by functions bounded in space and exponential in time yields a spectral problem whose elements characterize the temporal growth rates of the perturbations, as discussed in the Introduction and, in more detail, Section 2.3 below. The collection of these spectral elements yields the stability spectrum of the Stokes waves.

In contrast with the completely integrable KdV equation ($\beta = 0$) [33, 75, 77], considerably less is known about the stability spectrum of Stokes waves to (2.1). Haragus, Lombardi, and Scheel [48] prove the spectrum is imaginary for small-amplitude Stokes waves in a particular scaling regime. Such solutions are, therefore, spectrally stable. More recently, Trichtchenko, Deconinck, and Kollár [89] determine regimes for which the Stokes waves are unstable to high-frequency instabilities. An example of a spectrum in this regime is given in Figure 2.1. Notice the presence of a high-frequency isola. This isola, as well as the rest of the stability spectrum in Figure 2.1, is obtained numerically using the Floquet-Fourier-Hill (FFH) method, see Appendix B or [31, 34] for details.

We focus on the regime of the Kawahara equation for which high-frequency instabilities are present and develop a spectral perturbation method that obtains the following properties of these high-frequency instabilities:

(i) the asymptotic range of Floquet exponents that parameterize the high-frequency isolas observed in numerical computations of the stability spectrum,

(ii) asymptotic estimates of the most unstable spectral elements of the high-frequency isolas, and

(iii) expressions for curves asymptotic to these isolas, as seen in Figure 2.1.

These asymptotic results are then compared directly with numerical results from the FFH method to give confidence in the perturbation method.

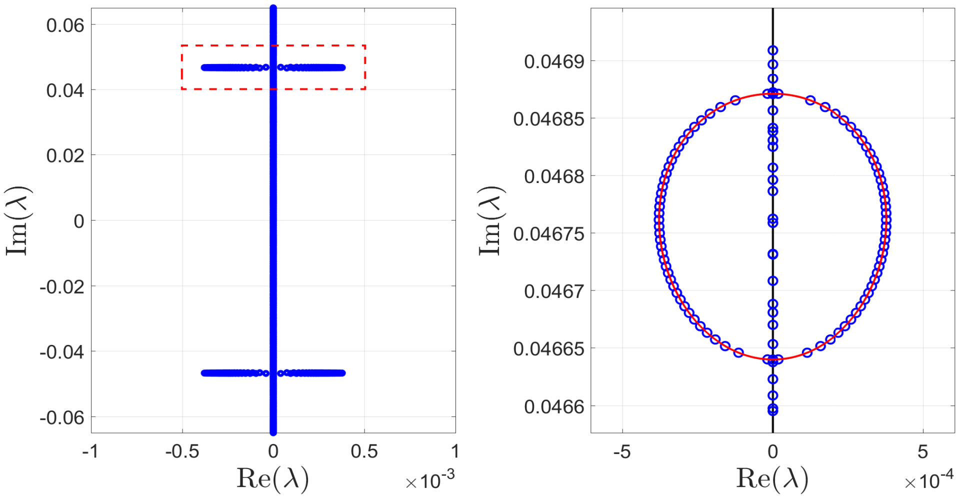

Figure 2.1: (Left) The stability spectrum of Stokes wave solutions of (2.1) with $\alpha = 1$, $\beta = 0.7$, $\sigma = 1$, and small-amplitude parameter $\varepsilon = 10^{-3}$, computed using the FFH method. A uniform grid of 10^3 Floquet exponents between $[-1/2, 1/2)$ approximates the imaginary point spectra but misses the high-frequency isolas. A uniform grid of 4×10^3 Floquet exponents in the interval described by (2.54) captures these isolas, as will be shown. (Right) A zoom-in of the high-frequency isola boxed in the left plot (with fewer point spectra shown for ease of visibility). The red curve is obtained in this chapter and approximates the isola.

2.2 *Stokes Wave Solutions*

To obtain the Stokes waves of the Kawahara equation, we first move to a traveling frame so that $x \to x - ct$, where c is the velocity of the waves. Then, equation (2.1) becomes

$$\eta_t = c\eta_x + \alpha\eta_{xxx} + \beta\eta_{5x} + 2\sigma\eta\eta_x. \tag{2.5}$$

Because the Stokes waves are time-independent in the traveling frame, we equate the time derivative in (2.5) to zero and integrate in x, arriving at

$$c\eta + \alpha\eta_{xx} + \beta\eta_{4x} + \sigma\eta^2 = \mathcal{C}, \tag{2.6}$$

where $\mathcal{C}$ is a constant of integration. Using the Galilean symmetry of (2.1), there exists a boost ψ such that, with $c \to c + \psi$ and $\eta \to \eta + \psi$, $\mathcal{C}$ can be omitted from (2.6), yielding

$$c\eta + \alpha\eta_{xx} + \beta\eta_{4x} + \sigma\eta^2 = 0. \tag{2.7}$$

Remark 2.2.1. *As a consequence of removing the constant $\mathcal{C}$ from* (2.6)*, the average value of η over one period will be nonzero. Often in applications, it is useful to require the Stokes waves to have zero average. In that case, $\mathcal{C}$ is retained in* (2.6) *and later expanded as a power series in ε to enforce the zero-average constraint on the Stokes wave expansion. For the purpose of studying the high-frequency instabilities, there are no differences in the outcomes of these calculations, so we choose to remove $\mathcal{C}$ for simplicity.*

Given $\alpha \neq 0$, we divide (2.7) by α and redefine the constants c, β, and σ appropriately. Rescaling x and η according to $x \to x/\kappa$ and $\eta \to \eta/(\sigma\kappa^2)$, respectively, and redefining c and β one final time allows us to consider 2π-periodic solutions of

$$c\eta + \eta_{xx} + \beta\eta_{4x} + \eta^2 = 0, \tag{2.8}$$

without loss of generality.

A standard Lyapunov-Schmidt argument [48] proves the existence of an ε-parameter family of 2π-periodic solutions to (2.8) provided $c = c(\varepsilon)$ and ε is sufficiently small. We denote these solutions by $\eta_S = \eta_S(x;\varepsilon)$, similar to the Stokes waves of Euler's equations in the Introduction. The parameter ε is defined to be twice the first Fourier coefficient of $\eta_S(x;\varepsilon)$. More explicitly, we have

$$\varepsilon = 2\mathcal{F}_1[\eta_S(x;\varepsilon)] = \frac{1}{\pi}\int_{-\pi}^{\pi} \eta_S(x;\varepsilon)e^{-ix}dx, \tag{2.9}$$

where

$$\mathcal{F}_k[f(x)] = \frac{1}{2\pi}\int_{-\pi}^{\pi} f(x)e^{-ikx}dx, \tag{2.10}$$

denotes the Fourier transform of $f(x)$ on the interval $(-\pi,\pi)$. Because the $\mathrm{L}^2(-\pi,\pi)$ norm of $\eta_S(x;\varepsilon)$ scales with ε when $|\varepsilon| \ll 1$, we call ε the small-amplitude parameter.

From [48], expansions for $\eta_S(x;\varepsilon)$ and $c(\varepsilon)$ take the form

$$\eta_S(x;\varepsilon) = \sum_{j=1}^{\infty} \eta_j(x)\varepsilon^j, \tag{2.11a}$$

$$c(\varepsilon) = \sum_{j=0}^{\infty} c_{2j}\varepsilon^{2j}, \tag{2.11b}$$

where $\eta_j(x)$ is analytic and 2π-periodic for each j. Exploiting the invariance of (2.8) under $x \to -x$ and $x \to x + \phi$ for any $\phi \in \mathbb{R}$, we can always arrange for $\eta_j(x) = \eta_j(-x)$, implying that $\eta_S(x;\varepsilon)$ is even in x without loss of generality. Substituting these expansions into (2.8) and following a Poincaré-Lindstedt perturbation method [79], one finds corrections to $\eta_S(x;\varepsilon)$ and $c(\varepsilon)$ order by order in ε.

One difficulty occurs at leading order of this perturbation method. Substituting expansions (2.11) into (2.8) and collecting terms of $\mathcal{O}(\varepsilon)$, we find

$$\left(c_0 + \partial_x^2 + \beta\partial_x^4\right)\eta_1(x) = 0. \tag{2.12}$$

Applying the Fourier transform to (2.12) and evaluating at the first mode yields

$$(c_0 - 1 + \beta)\mathcal{F}_1[\eta_1(x)] = 0, \tag{2.13}$$

which implies that

$$c_0 = 1 - \beta, \tag{2.14}$$

since $\mathcal{F}_1[\eta_1(x)] = 1/2$ from our definition of ε above. By inspection,

$$\eta_1(x) = \cos(x) \tag{2.15}$$

is a solution to (2.12) that is analytic, 2π-periodic, even in x, and satisfies the normalization $\mathcal{F}_1[\eta_1(x)] = 1/2$. However, if $\beta = 1/(1+N^2)$ for any integer $N > 1$, then

$$u_1(x) = \cos(x) + C_N\cos(Nx), \tag{2.16}$$

where C_N is an arbitrary real constant, is an equally valid solution. In this case, the Stokes waves exhibit resonance, resulting in Wilton ripples [93]. Expansions (2.11) must be modified as a result, see [4, 7, 49], for instance.

In this chapter, we restrict to nonresonant Stokes waves:

$$\beta \neq \frac{1}{1+N^2}, \tag{2.17}$$

so that (2.14) and (2.15) are the unique leading-order behaviors of $c(\varepsilon)$ and $\eta_S(x;\varepsilon)$, respectively. From this point on, the Poincaré-Lindstedt method follows as usual. Terminating this method after third-order in ε, we obtain the following expansions:

$$\begin{aligned} \eta_S(x;\varepsilon) &= \varepsilon\eta_1(x) + \varepsilon^2\eta_2(x) + \varepsilon^3\eta_3(x) + \mathcal{O}(\varepsilon^4) \\ &= \varepsilon\cos(x) + \varepsilon^2\frac{1}{2}\left(-\frac{1}{c_0} + \frac{2}{\Omega(2)}\cos(2x)\right) + \varepsilon^3\frac{3}{\Omega(2)\Omega(3)}\cos(3x) + \mathcal{O}(\varepsilon^4), \qquad (2.18a) \\ c(\varepsilon) &= c_0 + c_2\varepsilon^2 + \mathcal{O}(\varepsilon^4) \\ &= 1 - \beta + \left(\frac{1}{c_0} - \frac{1}{\Omega(2)}\right)\varepsilon^2 + \mathcal{O}(\varepsilon^4), \qquad (2.18b) \end{aligned}$$

where Ω is the linear dispersion relation of the Kawahara equation (2.1) (with $\alpha = 1 = \sigma$) in a frame traveling at velocity c_0. Explicitly,

$$\Omega(k) = -c_0k + k^3 - \beta k^5. \tag{2.19}$$

2.3 The Spectral Stability Problem

We perturb the Stokes waves $\eta_S(x;\varepsilon)$ according to

$$\eta(x,t) = \eta_S(x;\varepsilon) + \rho v(x,t) + \mathcal{O}(\rho^2), \tag{2.20}$$

where $|\rho| \ll 1$ is a small parameter independent of ε and $v(x,t)$ is a sufficiently smooth, bounded function of x on the whole real line for each $t \geq 0$. Substituting (2.20) into (2.1) (with $\alpha = 1$ and $\sigma = 1$) and linearizing in ρ, we find by formally separating variables

$$v(x,t) = e^{\lambda t}W(x) + c.c., \tag{2.21}$$

where *c.c.* denotes the complex conjugate of what precedes and $W(x)$ satisfies the spectral problem

$$\mathcal{L}_{\varepsilon}W(x) = \lambda W(x), \tag{2.22}$$

for the linear operator

$$\mathcal{L}_{\varepsilon} = c(\varepsilon)\partial_x + \partial_x^3 + \beta\partial_x^5 + 2\eta_S(x;\varepsilon)\partial_x + 2\eta_{S,x}(x;\varepsilon). \tag{2.23}$$

According to Floquet theory [47], all solutions of (2.22) that are bounded over $\mathbb{R}$ take the form

$$W(x) = e^{i\mu x}w(x), \tag{2.24}$$

where $\mu \in [-1/2, 1/2)$ is the Floquet exponent and $w(x)$ is 2π-periodic in an appropriately chosen function space.

Remark 2.3.1. *The conjugate of* $W(x)$ *is a solution of* (2.22) *with corresponding spectral parameter conjugate to* λ*. Since the spectrum of* $\mathcal{L}_{\varepsilon}$ *is invariant under conjugation according to [47], one can restrict* μ *to the interval* $[0, 1/2]$ *without loss of generality.*

Upon substituting (2.24) into (2.22), our spectral problem for fixed ε becomes the family of spectral problems

$$\mathcal{L}_{\mu,\varepsilon}w(x) = \lambda w(x), \tag{2.25}$$

where $\mathcal{L}_{\mu,\varepsilon}$ is $\mathcal{L}_{\varepsilon}$ with $\partial_x \to i\mu + \partial_x$. In light of (2.25), we require $w(x) \in \mathrm{H}^5_{\mathrm{per}}(0, 2\pi)$ so that $\mathcal{L}_{\mu,\varepsilon}$ is a closed operator densely defined on the separable Hilbert space $\mathrm{L}^2_{\mathrm{per}}(0, 2\pi)$ for a given μ. Then, $\mathcal{L}_{\mu,\varepsilon}$ has a discrete spectrum of eigenvalues λ for each μ and the union of these eigenvalues over all $\mu \in [-1/2, 1/2)$ yields the purely continuous stability spectrum of the Stokes waves. Since (2.1) is Hamiltonian, the stability spectrum exhibits quadrafold symmetry, meaning Stokes waves are only spectrally stable if their stability spectrum is a subset of the imaginary axis.

2.4 Necessary Conditions for High-Frequency Instabilities

If $\varepsilon = 0$, the operator $\mathcal{L}_{\mu,\varepsilon}$ reduces to

$$\mathcal{L}_{\mu,0} = c_0(i\mu + \partial_x) + (i\mu + \partial_x)^3 + \beta(i\mu + \partial_x)^5, \tag{2.26}$$

which is constant-coefficient. As a result, the eigenvalues and eigenfunctions of this operator are known exactly:

$$\lambda_{\mu,0,n} = -i\Omega(\mu + n), \tag{2.27}$$

and

$$w_{0,n}(x) = \gamma_n e^{inx}, \tag{2.28}$$

respectively, where $n \in \mathbb{Z}$, Ω is the linearized dispersion relation given in the previous section, and γ_n is an arbitrary complex constant. Since Ω is real-valued for all μ and n, we see that the eigenvalues are imaginary, implying that the zero-amplitude solution of the Kawahara equation is spectrally stable, as one would hope.

However, though the eigenvalues (2.27) are imaginary, not all of them have algebraic multiplicity equal to one. In fact, using the theory developed in [60] and [89], one can show that there exists collided eigenvalues away from the origin in the $\varepsilon = 0$ spectrum that could lead to instability when $0 < \varepsilon \ll 1$. The precise statement and its proof are as follows:

Theorem 2.4.1. *For each $p \in \mathbb{N}$, there exists a unique Floquet exponent $\mu_0 \in [0, 1/2]$ and unique integers m and n such that*

$$\lambda_{\mu_0,0,m} = \lambda_{\mu_0,0,n} \neq 0, \tag{2.29}$$

for m - n = p, provided the parameter β is nonresonant (2.17) *and satisfies the inequality*

$$\begin{aligned} max\left(\frac{3}{5p^2}, \frac{1}{1+p^2}\right) < \beta < min\left(\frac{6}{5p^2}, \frac{1}{\left(\frac{p}{2}\right)^2 + 1}\right) \quad &for \quad p < 3, \\ \frac{1}{1+p^2} < \beta < \frac{1}{1 + \left(\frac{p}{2}\right)^2} \quad &for \quad p \geq 3. \end{aligned} \tag{2.30}$$

Proof. Define

$$F(k;p) = \frac{\Omega(k+p) - \Omega(k)}{p}. \tag{2.31}$$

Using the definition of the dispersion relation Ω,

$$\begin{aligned} F(k;p) = 5\beta k^4 + 10\beta p k^3 + (10\beta p^2 - 3)k^2 + (5\beta p^3 - 3p)k \\ + \beta p^4 - (p)^2 + 1 - \beta. \end{aligned} \tag{2.32}$$

A direct calculation shows that

$$F(k,p) = F(-(k+p),p). \tag{2.33}$$

Hence, the graph of F is symmetric about $k = -p/2$, a fact we make extensive use of in the arguments below. We will show by cases that F has a negative root k_* for each $p \in \mathbb{N}$ such that $\Omega(k_*) \neq 0$, which will imply the desired result.

Case 1. Suppose $p = 1$. Then, $k_1 = 0$ and $k_2 = -1$ are roots of F by inspection. The remaining roots are

$$k_{3,4} = \frac{-1 \pm \sqrt{\frac{12}{5\beta} - 3}}{2}. \tag{2.34}$$

Because β satisfies (2.30), one can show that

$$0 < \frac{12}{5\beta} - 3 < 1, \tag{2.35}$$

so that $k_{3,4} \in (k_2, k_1)$. Because F is symmetric about $k = -p/2$, we have $k_3 \in (-1/2, 0)$ and $k_4 \in (-1, -1/2)$.

Each of these wavenumbers k_j is mapped to a Floquet exponent $\mu \in (-1/2, 1/2]$ according to

$$\mu(k) = k - [k], \tag{2.36}$$

where $[\cdot]$ denotes the nearest integer function[1]. Both k_1 and k_2 map to $\mu = 0$. One checks that $\mu(k_3) = -\mu(k_4) \neq 0$ and $|\mu(k_3)| = |\mu(k_4)| < 1/2$, since $k_4 = -(k_3 + 1)$ and $-1/2 < k_3 < 0$.

---

[1] In borderline cases, the convention here is $[p/2] = (p-1)/2$ for p odd.

Thus, the requisite $\mu_0 \in (0, 1/2)$ is $\mu(k_j)$, where j is either 3 or 4 depending on which has the correct sign. Then, $n = [k_j]$ and $m = n + p$. These are unique by the uniqueness of k_j.

Case 2. Suppose $p = 2$. A calculation of $F(-1; 2)$ and $F_k(-1; 2)$ shows that $k_{1,2} = -1$ is a double root. The remaining roots are

$$k_{3,4} = -1 \pm \sqrt{\frac{3}{5\beta} - 2}. \tag{2.37}$$

Clearly, $\mu(k_{1,2}) = 0$. Since $k_4 = -(k_3 + 2)$, we again have $\mu(k_3) = -\mu(k_4)$. Also, from the formula for k_3 above, we have that $-1 < k_3 < 0$ by (2.30), so $\mu(k_3)$ is nonzero. Thus, $\mu(k_j)$ is the requisite $\mu_0 \in (0, 1/2]$, where j is either 3 or 4 depending on which has the correct sign. Again, $n = [k_j]$ and $m = n + p$ are uniquely defined. Unlike in the first case, note that we cannot guarantee $\mu_0 \neq 1/2$. Indeed, this value can be achieved when $\beta = 4/15$.

Case 3. Suppose $p \geq 3$. The discriminant of $F(k; p)$ with respect to k is

$$\Delta_k[F] = 5\beta \left[p^2 - 4\right] \left[\beta(p^2 + 4) - 4\right] \left[5\beta \left(\beta \left(p^4 + 4\right) - 2\left(p^2 + 2\right)\right) + 9\right]^2. \tag{2.38}$$

For β satisfying inequality (2.30), we have $\Delta_k[F] < 0$, implying there are two distinct real roots of F. These roots must be nonpositive by an application of Descartes' Rule of Signs on F. Without loss of generality, suppose $k_2 < k_1$. Then, by the symmetry of F about $k = -p/2$, $k_2 = -(k_1 + p)$. It follows that $\mu(k_1) = -\mu(k_2)$. Thus, $\mu(k_j)$ is the requisite value of $\mu_0 \in [0, \frac{1}{2}]$, where $j = 1$ or 2 depending on which has the correct sign. The integers n and m are uniquely defined as before. In each of these cases, we have found $k_j < 0$ such that $F(k_j; p) = 0$. We now check that $\Omega(k_j) \neq 0$ for such k_j. Suppose instead $\Omega(k_j) = 0$. A direct calculation shows that $k_j = \pm 1$, 0, or $k_j^2 = (1 - \beta)/\beta$. The cases $k_j = 0$ or 1 give immediate contradictions. If $k_j = -1$, then $F(-1; p) = 0$ implies $\beta = 1/[(p-1)^2 + 1]$, which contradicts (2.17) when $p \neq 2$. If $p = 2$, $\beta = 1/2$, which contradicts (2.30).

It remains to be seen if $k_j^2 = (1 - \beta)/\beta$ leads to contradiction. Indeed, a straightforward (although tedious) calculation shows that, if $k_j^2 = (1-\beta)/\beta$ and $F(k_j; p) = 0$, then $\beta = 0$, $\beta = 1/[1 + (p/2)^2]$, $\beta = 1/[1 + (p-1)^2]$, or $\beta = 1/[1 + (p+1)^2]$. All of these lead to contradictions of (2.17) or (2.30). Therefore, we must have $\Omega(k_j) = \Omega(\mu_0 + n) = \Omega(\mu_0 + m) \neq 0$ in all cases, as desired. $\square$

Remark 2.4.1. *A similar statement holds for* $p < 0$*. The collided eigenvalues in this case are conjugate to those in the theorem above.*

Remark 2.4.2. *The eigenfunctions corresponding to the collided eigenvalues take the form*

$$w_{0,m,n}(x) = \gamma_m e^{imx} + \gamma_n e^{inx}, \tag{2.39}$$

where γ_m, γ_n *are arbitrary complex constants and* m *and* n *are given by the theorem above. Notice this eigenspace is two-dimensional, reflecting the higher-multiplicity of the collided eigenvalues.*

At first glance, it appears there exists a countable number of collided eigenvalues away from the origin in the $\varepsilon = 0$ spectrum: one for each value of p. However, as $p \to \infty$, β eventually falls outside the requisite interval (2.30). Thus, there can only be a finite number of collisions away from the origin when $\varepsilon = 0$. This is in contrast to the HPBW system and Euler's equations, for which there are an infinite number of eigenvalue collisions when $\varepsilon = 0$.

For high-frequency instabilities to appear when $0 < \varepsilon \ll 1$, not only must collided eigenvalues exist when $\varepsilon = 0$, but these collided eigenvalues must have opposite Krein signature per MacKay and Saffman [67]. It is shown in [36, 60, 89] that this condition is equivalent to

$$(\mu_0 + m)(\mu_0 + n) < 0, \tag{2.40}$$

where μ_0, m, and n are obtained from (2.29). A direct calculation shows that (2.40) automatically holds for any β satisfying (2.17) and (2.30) and any μ_0, m, and n satisfying (2.29). Thus, all nonzero collided eigenvalues of the $\varepsilon = 0$ spectrum have opposite Krein signature. This sets the stage for a finite number of high-frequency instabilities to develop when $0 < \varepsilon \ll 1$. These instabilities are enumerated by $p \in \mathbb{N}$.

2.5 Asymptotic Description of the $p = 1$ *High-Frequency Instability*

2.5.1 The $\mathcal{O}(\varepsilon^0)$ *Problem*

For simplicity, we investigate the $p = 1$ high-frequency instability first. Let m and n be the unique integers that satisfy condition (2.29) with $m - n = p = 1$, and let μ_0 be the corresponding unique Floquet exponent in $[0, 1/2]$. Then, the spectral data of $\mathcal{L}_{\mu_0,0}$ giving rise to the $p = 1$ high-frequency instability are

$$\lambda_{\mu_0,0,m} = -i\Omega(\mu_0+m) = \lambda_{\mu_0,0,n} = -i\Omega(\mu_0 + n) \neq 0, \tag{2.41a}$$

$$w_{0,m,n}(x) = \gamma_m e^{imx} + \gamma_n e^{inx}. \tag{2.41b}$$

For ease of notation, we denote the collided eigenvalue $\lambda_{\mu_0,0,m}$ and its corresponding eigenfunction $w_{0,m,n}$ by λ_0 and w_0, respectively, for the remainder of this section.

As ε increases from zero, we assume the spectral data (2.41) depend analytically on ε for $0 < \varepsilon \ll 1$ so that

$$\lambda(\varepsilon) = \lambda_0 + \varepsilon\lambda_1 + \mathcal{O}(\varepsilon^2), \tag{2.42a}$$

$$w(x; \varepsilon) = w_0(x) + \varepsilon w_1(x) + \mathcal{O}(\varepsilon^2), \tag{2.42b}$$

where $\lambda(\varepsilon)$ and $w(x; \varepsilon)$ are eigenpairs of the spectral problem (2.25). Since λ_0 is a semi-simple and isolated eigenvalue of $\mathcal{L}_{\mu_0,0}$ and $\mathcal{L}_{\mu,\varepsilon}$, in general, inherits Hamiltonian structure from the Kawahara equation, expansions (2.42a) and (2.42b) may be justified using results of analytic perturbation theory, provided μ_0 is fixed [57]. If the Floquet exponent is fixed in this way, however, one obtains at most two eigenvalues on the high-frequency isola for sufficiently small ε. Typically, these eigenvalues do not have the largest real part on the isola, making it impossible to derive the maximum growth rates of the high-frequency instability. For this reason, we expand the Floquet exponent about its resonant value

$$\mu = \mu(\varepsilon) = \mu_0 + \varepsilon\mu_1 + \mathcal{O}(\varepsilon^2). \tag{2.43}$$

This is a purely formal assumption but is absolutely crucial to the analysis. We will see aposteriori that μ_1 assumes an interval of values parameterizing a curve asymptotic to the entire $p = 1$ high-frequency isola. Corrections beyond $\mathcal{O}(\varepsilon)$ deform this interval.

Like Akers [3], we impose the following normalization condition on the eigenfunction w for convenience:

$$\mathcal{F}_n[w(x; \varepsilon)] = 1, \tag{2.44}$$

where $\mathcal{F}_n$ is the Fourier transform evaluated at the nth mode. Substituting (2.42b) into this normalization condition, we find $\mathcal{F}_n[w_0(x)] = 1$ and $\mathcal{F}_n[w_j(x)] = 0$ for $j \in \mathbb{N}$, meaning that the leading-order behavior w_0 entirely supports the nth Fourier mode of the full eigenfunction w. As a consequence, (2.41) becomes

$$w_0(x) = e^{inx} + \gamma_0 e^{imx}, \tag{2.45}$$

where we have also made the replacement $\gamma_m \to \gamma_0$ for reasons that will become clear as our calculation proceeds. Although w_0 does not appear to be unique at this order, we will find an expression for γ_0 at the next order.

2.5.2 The $\mathcal{O}(\varepsilon)$ Problem

Substituting expansions (2.42a), (2.42b), and (2.43) into the spectral problem (2.25) and equating terms of $\mathcal{O}(\varepsilon)$ yields

$$(\mathcal{L}_{\mu_0,0} - \lambda_0) w_1(x) = \lambda_1 w_0(x) - \mathcal{L}_1 w_0(x), \tag{2.46}$$

where

$$\mathcal{L}_1 = ic_0\mu_1 + 3i\mu_1(i\mu_0 + \partial_x)^2 + 5i\beta\mu_1(i\mu_0 + \partial_x)^4 + 2\eta_1(x)(i\mu_0 + \partial_x) + 2\eta_{1,x}(x). \tag{2.47}$$

Using (2.18) to replace η_1, (2.45) to replace w_0, and $m - n = 1$ to simplify, (2.46) becomes

$$\begin{aligned}(\mathcal{L}_{\mu_0,0} - \lambda_0) w_1(x) = &\left[\lambda_1 + i\mu_1 c_g(\mu_0 + n) - i\gamma_0(\mu_0 + n)\right] e^{inx} \\ &+ \left[\gamma_0\left(\lambda_1 + i\mu_1 c_g(\mu_0 + m)\right) - i(\mu_0 + m)\right] e^{imx} \\ &- i(\mu_0 + n - 1)e^{i(n-1)x} - i\gamma_0(\mu_0 + m + 1)e^{i(m+1)x},\end{aligned} \tag{2.48}$$

where $c_g(k) = d\Omega/dk$ is the group velocity of Ω.

If (2.48) can be solved for $w_1(x) \in \mathrm{H}^5_{\text{per}}(-\pi, \pi)$, the Fredholm alternative requires that the inhomogeneous terms of (2.48) are orthogonal (in the $\mathrm{L}^2_{\text{per}}(-\pi, \pi)$ sense) to the nullspace of the hermitian adjoint of $\mathcal{L}_{\mu_0,0} - \lambda_0$, denoted $(\mathcal{L}_{\mu_0,0} - \lambda_0)^\dagger$. A quick computation shows that $\mathcal{L}_{\mu_0,0} - \lambda_0$ is skew-Hermitian. Thus, the nullspace of $(\mathcal{L}_{\mu_0,0} - \lambda_0)^\dagger$ coincides with the eigenspace of the zeroth-order problem:

$$\text{Null}\left((\mathcal{L}_{\mu_0,0} - \lambda_0)^\dagger\right) = \text{Span}\left(e^{inx}, e^{imx}\right). \tag{2.49}$$

As a result, the solvability conditions of (2.48) are

$$\begin{aligned}\left\langle e^{inx}, \left[\lambda_1 + i\mu_1 c_g(\mu_0+n) - i\gamma_0(\mu_0+n)\right] e^{inx}\right\rangle &= 0, \\ \implies \lambda_1 + i\mu_1 c_g(\mu_0+n) - i\gamma_0(\mu_0+n) &= 0, \qquad (2.50\text{a}) \\ \left\langle e^{imx}, \left[\gamma_0\left(\lambda_1 + i\mu_1 c_g(\mu_0+m)\right) - i(\mu_0+m)\right] e^{imx}\right\rangle &= 0, \\ \implies \gamma_0\left(\lambda_1 + i\mu_1 c_g(\mu_0+m)\right) - i(\mu_0+m) &= 0, \qquad (2.50\text{b})\end{aligned}$$

where $\langle \cdot, \cdot \rangle$ is the standard complex inner product on $\mathrm{L}^2(-\pi,\pi)$.

Remark 2.5.1. *Both solvability conditions act to remove secular inhomogeneous terms in* (2.48)*. The first solvability condition* (2.50a) *also coincides with the normalization condition* $\mathcal{F}_n[w_1(x)] = 0$ *for the first-order eigenfunction correction.*

The solvability conditions (2.50a) and (2.50b) yield a nonlinear system for λ_1 and γ_0. The solutions of this system are

$$\begin{aligned}\lambda_1 &= \lambda_{1,r} + i\lambda_{1,i}, \qquad (2.51\text{a}) \\ \gamma_0 &= \frac{i(\mu_0+m)}{\lambda_1 + i\mu_1 c_g(\mu_0+m)}, \qquad (2.51\text{b})\end{aligned}$$

where

$$\begin{aligned}\lambda_{1,r} &= \pm\sqrt{-\mu_1^2\left[\frac{c_g(\mu_0+m) - c_g(\mu_0+n)}{2}\right]^2 - (\mu_0+m)(\mu_0+n)}, \qquad (2.52\text{a}) \\ \lambda_{1,i} &= -\mu_1\left(\frac{c_g(\mu_0+m) + c_g(\mu_0+n)}{2}\right). \qquad (2.52\text{b})\end{aligned}$$

If $\mu_1 \in (-M_1, M_1)$ for

$$M_1 = \frac{2\sqrt{-(\mu_0+m)(\mu_0+n)}}{|c_g(\mu_0+m) - c_g(\mu_0+n)|}, \tag{2.53}$$

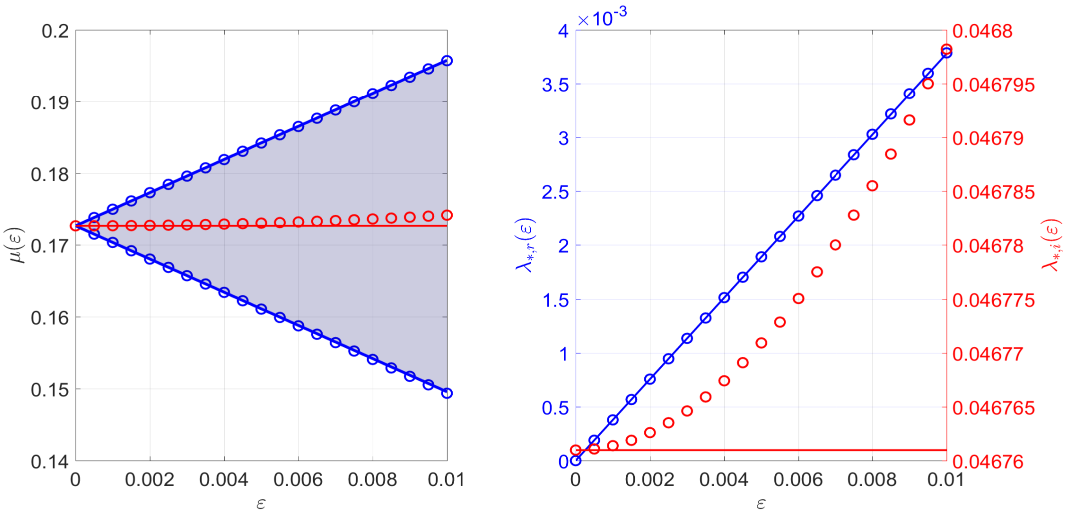

Figure 2.2: (Left) The interval of Floquet exponents parameterizing the $p = 1$ high-frequency isola for $\beta = 0.7$ as a function of ε. The solid blue curves indicate the asymptotic boundaries of this interval according to (2.54). The blue circles indicate the numerical boundaries computed using the FFH method. The solid red curve gives the Floquet exponent corresponding to the most unstable spectral element of the isola according to (2.55). The red circles indicate the numerical result according to FFH. (Right) The real (blue) and imaginary (red) parts of the most unstable spectral element of the isola as a function of ε. The solid curves illustrate asymptotic result (2.56). The circles illustrate numerical results according to the FFH method.

it follows that λ_1 has nonzero real part, since $(\mu_0 + m)(\mu_0 + n) < 0$ by the Krein condition and choice of β. Therefore, the $p = 1$ high-frequency instability is parameterized by

$$\mu \in (\mu_0 - \varepsilon M_1, \mu_0 + \varepsilon M_1) + \mathcal{O}\left(\varepsilon^2\right). \tag{2.54}$$

This interval agrees with numerical results using the FFH method for $|\varepsilon| \ll 1$, see Figure 2.2. The interval is also well-defined for all β since $c_g(\mu_0 + m) \neq c_g(\mu_0 + n)$ by the following theorem:

Theorem 2.5.1. *Fix $p \in \mathbb{N}$ and choose β so that (2.17) and (2.30) are satisfied. Let $\mu_0 \in [0, 1/2]$ correspond to the unique solution of $\Omega(\mu_0 + m) = \Omega(\mu_0 + n)$ for the unique* *integers m, n such that $m-n = p$. Suppose, in addition, that μ_0 solves $c_g(\mu_0+m) = c_g(\mu_0+n)$, where $c_g(k) = d\Omega/dk$. Then, $p = 2$ and $\mu_0 = 0$ necessarily.*

Proof. If $\Omega(\mu_0 + m) = \Omega(\mu_0 + n)$ and $c_g(\mu_0 + m) = c_g(\mu_0 + n)$, then $k_0 = \mu_0 + m$ is a double root of $F(k;p) = \left(\Omega(k+p) - \Omega(k)\right)/p$. Working through the cases from our theorem in Section 2.4, we see that F only has a double root when $p = 2$. This double root occurs at $k_0 = -1$, which implies $\mu_0 = 0$, as desired. □

For $p = 2$ and $\mu_0 = 0$, the eigenvalues collide at the origin of the complex spectral plane, which does not correspond to a high-frequency instability and, therefore, is not of interest to us in this chapter. It follows that $c_g(\mu_0 + m) \neq c_g(\mu_0 + n)$ for all relevant β, so M_1 is well-defined and, consequently, so is the parameterizing interval of Floquet exponents (2.54).

Remark 2.5.2. *The zeroth-order eigenfunction coefficient γ_0 is also well-defined, as $\lambda_1 + i\mu_1 c_g(\mu_0 + m)$ is necessarily a complex number with nonzero real part.*

Equating $\mu_1 = 0$ maximizes the real part of λ_1 in (2.50a). Thus, the Floquet exponent corresponding to the most unstable eigenvalue of the $p = 1$ high-frequency isola has asymptotic expansion

$$\mu_* = \mu_0 + \mathcal{O}(\varepsilon^2). \tag{2.55}$$

The corresponding real and imaginary parts of this eigenvalue have asymptotic expansions

$$\lambda_{*,r} = \varepsilon\sqrt{-(\mu_0 + m)(\mu_0 + n)} + \mathcal{O}(\varepsilon^2), \tag{2.56a}$$

$$\lambda_{*,i} = -\Omega(\mu_0 + n) + \mathcal{O}(\varepsilon^2), \tag{2.56b}$$

respectively. The first of these expansions provides an estimate for the growth rates of the $p = 1$ high-frequency instabilities. Figure 2.2 compares these expansions with numerical results according to the FFH method. From this comparison, we see that the expansion for the real part of the most unstable eigenvaule is in excellent agreement with numerical results, while the expansion for the imaginary part requires a higher-order calculation.

Decomposing the expansion of λ into its real λ_r and imaginary λ_i parts, dropping terms of $\mathcal{O}\left(\varepsilon^2\right)$ and smaller, and eliminating the μ_1 dependence gives

$$\frac{\lambda_r^2}{\varepsilon^2}+\frac{\left(\lambda_i+\Omega(\mu_0+n)\right)^2}{\varepsilon^2\left(\frac{c_g(\mu_0+m)+c_g(\mu_0+n)}{c_g(\mu_0+m)-c_g(\mu_0+n)}\right)^2}=-(\mu_0+m)(\mu_0+n)+\mathcal{O}(\varepsilon). \tag{2.57}$$

Thus, to $\mathcal{O}\left(\varepsilon\right)$, the $p=1$ high-frequency isola is an ellipse with center at the zeroth-order collided eigenvalue λ_0 and with semi-major and -minor axes

$$a_1=\varepsilon\sqrt{-(\mu_0+m)(\mu_0+n)}, \tag{2.58a}$$

$$b_1=a_1\left|\frac{c_g(\mu_0+m)+c_g(\mu_0+n)}{c_g(\mu_0+m)-c_g(\mu_0+n)}\right|, \tag{2.58b}$$

respectively. This ellipse agrees well with the numerically computed high-frequency isola, particularly with respect to the maximum real part of both curves. There is noteable discrepancy in the imaginary part of the isola and in the Floquet parameterization of the imaginary part of the isola, even for $\varepsilon=10^{-3}$ (Figure 2.3). This discrepancy will be resolved by a higher-order calculation in the next subsection.

2.5.3 The $\mathcal{O}\left(\varepsilon^2\right)$ Problem

To complete our work at the previous order, we obtain a particular solution for the first-order correction of the eigenfunction w_1 in (2.48) using, for example, the method of undetermined coefficients. Uniting this particular solution with the nullspace of $\mathcal{L}_{\mu_0,0}-\lambda_0$ (*i.e.*, the eigenspace of λ_0) and enforcing our normalization of w_1, we find

$$w_1(x)=Q_{n,n-1}e^{i(n-1)x}+\gamma_0Q_{n,m+1}e^{i(m+1)x}+\gamma_1e^{imx}, \tag{2.59}$$

where

$$Q_{J,K}=\frac{(\mu_0+K)}{\Omega(\mu_0+K)-\Omega(\mu_0+J)}, \tag{2.60}$$

and γ_1 is an undetermined constant (at this order).

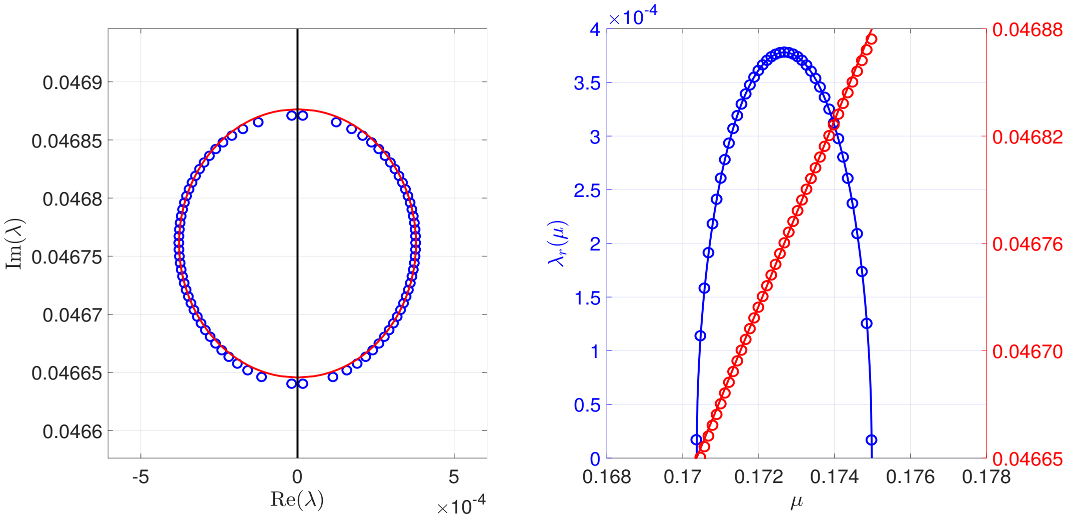

Figure 2.3: (Left) The $p = 1$ high-frequency isola for $\beta = 0.7$ and $\varepsilon = 10^{-3}$. The solid red curve is the ellipse (2.57). The blue circles are a subset of spectral elements from the numerically computed isola using FFH. (Right) The Floquet parameterization of the real (blue) and imaginary (red) parts of the isola. The solid curves illustrate the asymptotic result (2.51a). The circles indicate numerical results according to FFH.

At $\mathcal{O}(\varepsilon^2)$, we have

$$\begin{aligned}(\mathcal{L}_{\mu_0,0} - \lambda_0)w_2(x) = {} & \lambda_2 w_0(x) + \lambda_1 w_1(x) - ic_0(\mu_1 w_1(x) + \mu_2 w_0(x)) - c_2(i\mu_0 + \partial_x)w_0(x) \\ & - 3i(i\mu_0 + \partial_x)^2(\mu_1 w_1(x) + \mu_2 w_0(x)) + 3\mu_1^2(i\mu_0 + \partial_x)w_0(x) \\ & - 5\beta i(i\mu_0 + \partial_x)^4(\mu_1 w_1(x) + \mu_2 w_0(x)) + 10\beta\mu_1^2(i\mu_0 + \partial_x)^3 w_0(x) \\ & - 2(i\mu_0 + \partial_x)(\eta_1(x)w_1(x) + \eta_2(x)w_0(x)) - 2i\mu_1\eta_1(x)w_0(x). \qquad (2.61)\end{aligned}$$

Upon substituting expressions for w_0, w_1, η_1, and η_2 into (2.61), the solvability conditions of the second-order problem simplify to a 2×2 linear system

$$\begin{pmatrix} 1 & -i(\mu_0 + n) \\ \gamma_0 & \lambda_1 + i\mu_1 c_g(\mu_0 + m) \end{pmatrix} \begin{pmatrix} \lambda_2 \\ \gamma_1 \end{pmatrix} = i \begin{pmatrix} \gamma_0\mu_1 - \tilde{\mathcal{C}}^{n,-1}_{\mu_2,\mu_1,\mu_0} \\ \mu_1 - \gamma_0\tilde{\mathcal{C}}^{m,1}_{\mu_2,\mu_1,\mu_0} \end{pmatrix}, \qquad (2.62)$$

where

$$\tilde{C}^{N,k}_{\mu_2,\mu_1,\mu_0} = \mu_2 c_g(\mu_0 + N) - \tilde{\mathcal{P}}^{N,k}_{\mu_0} + \mu_1^2 \mathcal{D}^N_{\mu_0}, \tag{2.63a}$$

$$\tilde{P}^{N,k}_{\mu_0} = (\mu_0 + N)\left[(Q_{n,N+k} + 2\upsilon_{2,0}) + c_2\right], \tag{2.63b}$$

$$D^N_{\mu_0} = 3(\mu_0 + N) - 10\beta(\mu_0 + N)^3. \tag{2.63c}$$

For $\mu_1 \in (-M_1, M_1)$ (2.53), one can show that

$$\det \begin{pmatrix} 1 & -i(\mu_0 + n) \\ \gamma_0 & \lambda_1 + i\mu_1 c_g(\mu_0 + m) \end{pmatrix} = 2\lambda_{1,r}, \tag{2.64}$$

with $\lambda_{1,r}$ given in (2.52a). Since $\lambda_{1,r} \neq 0$ for $|\mu_1| < M_1$, it follows that (2.62) is invertible. Using Cramer's rule to solve for λ_2 and the solvability conditions at the previous order (2.50a)-(2.50b) to simplify, we arrive at

$$\lambda_2 = -\frac{i}{2\lambda_{1,r}}\left(\mathcal{A}\lambda_1 + i\mu_1\mathcal{B}\right), \tag{2.65}$$

where

$$\mathcal{A} = \tilde{\mathcal{C}}^{m,1}_{\mu_2,\mu_1,\mu_0} + \tilde{\mathcal{C}}^{n,-1}_{\mu_2,\mu_1,\mu_0}, \tag{2.66a}$$

$$\mathcal{B} = c_g(\mu_0 + m)\tilde{\mathcal{C}}^{n,-1}_{\mu_2,\mu_1,\mu_0} + c_g(\mu_0 + n)\tilde{\mathcal{C}}^{m,1}_{\mu_2,\mu_1,\mu_0} - (2\mu_0 + m + n). \tag{2.66b}$$

A quick calculation shows that (i) λ_2 inherits two branches, $\lambda_{2,+}$ and $\lambda_{2,-}$, from $\lambda_{1,r}$ and (ii), for any $\mu_2 \in \mathbb{R}$, $\lambda_{2,+} = -\overline{\lambda_{2,-}}$, where the overbar denotes complex conjugation. Consequently, (2.65) (together with lower-order results) predicts a spectrum that is symmetric about the imaginary axis regardless of μ_2. We want this spectrum to be a continuous, closed curve about the imaginary axis. As we show momentarily, this additional constraint is enough to determine μ_2 uniquely. We call this constraint the *regular curve condition.*

To motivate the regular curve condition, consider the real and imaginary parts of (2.65):

$$\lambda_{2,r} = \frac{1}{2\lambda_{1,r}}\left(\mathcal{A}\lambda_{1,i} + \mu_1\mathcal{B}\right), \tag{2.67a}$$

$$\lambda_{2,i} = -\frac{\mathcal{A}}{2}. \tag{2.67b}$$

As $|\mu_1| \to M_1$, $\lambda_{1,r} \to 0$. To avoid unbounded behavior in $\lambda_{2,r}$, we must impose

$$\lim_{|\mu_1| \to M_1} \left(\mathcal{A}\lambda_{1,i} + \mu_1 \mathcal{B} \right) = 0. \tag{2.68}$$

Since μ_1 appears in $\mathcal{A}$ only as μ_1^2, we can rewrite (2.68) with the help of (2.51a) as

$$\lim_{\mu_1^2 \to M_1^2} \left(-\frac{\mathcal{A}}{2}\left(c_g(\mu_0+m) + c_g(\mu_0+n)\right) + \mathcal{B} \right) = 0. \tag{2.69}$$

Equation (2.69) is the regular curve condition for second-order corrections to the $p = 1$ isola. Unpacking the definitions of $\mathcal{A}$ and $\mathcal{B}$ above, the regular curve condition implies that

$$\mu_2 = \frac{\mathrm{P}_{\mu_0}^{m,1} - \mathrm{P}_{\mu_0}^{n,-1}}{c_g(\mu_0+m) - c_g(\mu_0+n)} - \frac{2(2\mu_0+m+n)}{\left(c_g(\mu_0+m) - c_g(\mu_0+n)\right)^2}, \tag{2.70}$$

where

$$\mathrm{P}_{\mu_0}^{N,k} = \tilde{\mathcal{P}}_{\mu_0}^{N,k} + \frac{4(\mu_0+m)(\mu_0+n)}{\left(c_g(\mu_0+m) - c_g(\mu_0+n)\right)^2}\mathcal{D}_{\mu_0}^{N}. \tag{2.71}$$

Therefore, the asymptotic interval of Floquet exponents parameterizing the $p = 1$ high-frequency isola is

$$\mu \in \left(\mu_0 - \varepsilon M_1 + \varepsilon^2 \mu_2, \mu_0 + \varepsilon M_1 + \varepsilon^2 \mu_2\right) + \mathcal{O}\left(\varepsilon^3\right). \tag{2.72}$$

Remark 2.5.3. *Corrections to the Floquet exponent are introduced at each order beyond* $\mathcal{O}\left(\varepsilon^2\right)$*. The solvability conditions at these orders will not be enough to determine the Floquet corrections. Instead, the regular curve condition will determine these corrections.*

The real part of our isola has expansion

$$\lambda_r = \varepsilon \lambda_{1,r} + \varepsilon^2 \lambda_{2,r} + \mathcal{O}\left(\varepsilon^3\right), \tag{2.73}$$

where $\lambda_{1,r}$ and $\lambda_{2,r}$ are given in (2.52a) and (2.67a), respectively. Without loss of generality, suppose the positive branch of $\lambda_{1,r}$ is chosen. To obtain the Floquet exponent of the most unstable eigenvalue on the isola, we consider the critical points of (2.73) with respect to μ_1:

$$\left.\frac{\partial \lambda_r}{\partial \mu_1}\right|_{\mu_{*,1}} = 0, \tag{2.74}$$

where $\mu_{*,1}$ denotes the critical points. After a series of straightforward (but tedious) calculations, (2.74) yields the following equation for $\mu_{*,1}$:

$$
\begin{aligned}
&-\mu_{*,1}\lambda_{*,1,r}^2\left(\frac{c_g(\mu_0+m)-c_g(\mu_0+n)}{2}\right)^2+\frac{\varepsilon}{2}\left[\lambda_{*,1,r}^2\left(\lambda_{*,1,i}\frac{\partial\mathcal{A}}{\partial\mu_1}\bigg|_{\mu_{*,1}}+\mathcal{A}_*\frac{\partial\lambda_{1,i}}{\partial\mu_1}\bigg|_{\mu_{*,1}}\right.\right.\\
&\left.\left.+\,\mu_{*,1}\frac{\partial\mathcal{B}}{\partial\mu_1}\bigg|_{\mu_{*,1}}+\mathcal{B}_*\right)+\mu_{*,1}\left(\mathcal{A}_*\lambda_{*,1,i}+\mu_{*,1}\mathcal{B}_*\right)\left(\frac{c_g(\mu_0+m)-c_g(\mu_0+n)}{2}\right)^2\right]=0, \quad (2.75)
\end{aligned}
$$

where starred variables are evaluated at $\mu_1=\mu_{*,1}$. Unpacking the definitions of $\mathcal{A}$, $\mathcal{B}$, $\lambda_{1,r}$, and $\lambda_{1,i}$ reveals that (2.75) is a quartic equation for $\mu_{*,1}$ with the highest degree coefficient multiplied by the small parameter ε. Therefore, rather than solving for $\mu_{*,1}$ directly, we obtain the roots perturbatively.

An application of the method of dominant balance to (2.75) shows that all of its roots exhibit singular behavior as $\varepsilon \to 0$, except for one. Because we anticipate that $\lim_{\varepsilon\to 0}\mu_{*,1}=0$ to match results for the most unstable eigenvalue at the previous order, it is this non-singular root that we expect to yield the correct expression for $\mu_{*,1}$. Therefore, we need not concern ourselves with singular perturbation methods and, instead, make the following ansatz:

$$\mu_{*,1}=\mu_{*,1,0}+\varepsilon\mu_{*,1,1}+O(\varepsilon^2). \tag{2.76}$$

Substituting our ansatz into (2.75), we find by equating the lowest powers in ε that $\mu_{*,1,0}=0$, consistent with results from the previous order. At the next order, we arrive at the following linear equation for $\mu_{*,1,1}$:

$$-\mu_{*,1,1}\left(\frac{c_g(\mu_0+m)-c_g(\mu_0+n)}{2}\right)^2+\frac{1}{2}\left(\mathcal{B}_0-\mathcal{A}_0\right)=0, \tag{2.77}$$

where $\mathcal{A}_0$ and $\mathcal{B}_0$ denote $\mathcal{A}$ and $\mathcal{B}$ evaluated at $\mu_1=0$, respectively. Using the definition of $\mathcal{A}$ and $\mathcal{B}$ together with the expression for μ_2 in (2.70) above, one finds

$$\mu_{*,1,1}=-4(\mu_0+m)(\mu_0+n)\left(\frac{\mathcal{D}_{\mu_0}^m-\mathcal{D}_{\mu_0}^n}{(c_g(\mu_0+m)-c_g(\mu_0+n))^3}\right). \tag{2.78}$$

It follows that the Floquet exponent corresponding to the most unstable eigenvalue of the $p=1$ high-frequency isola has asymptotic expansion

$$\mu_*=\mu_0+\varepsilon^2(\mu_2+\mu_{*,1,1})+O(\varepsilon^3). \tag{2.79}$$

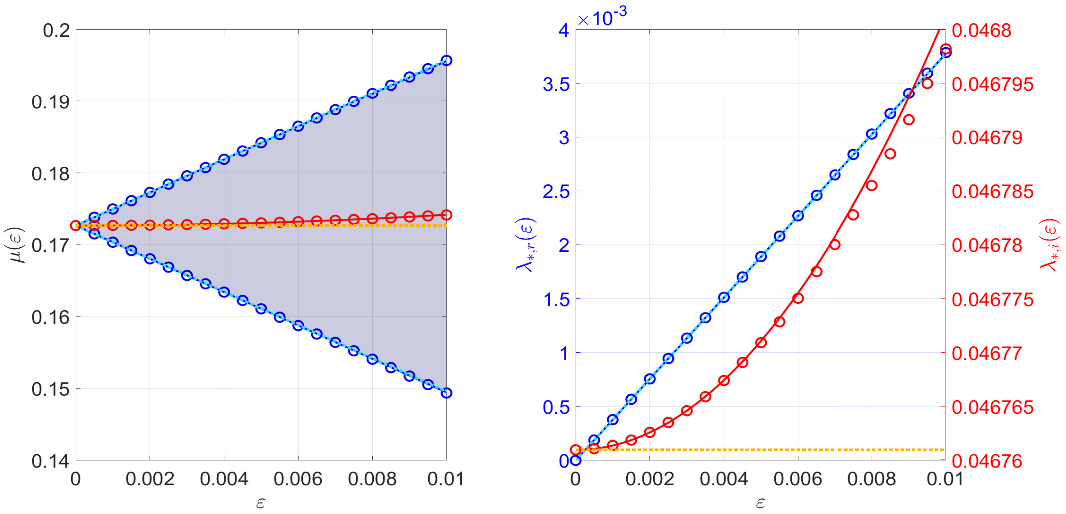

Figure 2.4: (Left) The interval of Floquet exponents that parameterizes the $p = 1$ high-frequency isola for $\beta = 0.7$ as a function of ε. The solid blue curves indicate the asymptotic boundaries of this interval according to (2.72), while the dotted cyan curves give the $\mathcal{O}(\varepsilon)$ result. The blue circles indicate the numerical boundaries computed by the FFH method. The solid red curve gives the Floquet exponent corresponding to the most unstable spectral element of the isola according to (2.79), while the dotted orange curve gives the $\mathcal{O}(\varepsilon)$ result. The red circles indicate numerical results by the FFH method. (Right) The real (blue) and imaginary (red) parts of the most unstable spectral element of the isola as a function of ε. The solid curves illustrate asymptotic result (2.80). The dotted (cyan and orange) curves illustrate the (real and imaginary) asymptotic results only to $\mathcal{O}(\varepsilon)$. The circles illustrate numerical results according to the FFH method.

The most unstable eigenvalue is then

$$\lambda_* = \lambda_0 + \varepsilon\lambda_1\big|_{\mu_1=\mu_{1,*,0}} + \varepsilon^2\lambda_2\big|_{\mu_1=\mu_{1,*,0}} + O(\varepsilon^3). \tag{2.80}$$

Figures 2.4 and 2.5 show considerable improvements to the results at the previous order. In addition, Figure 2.5 demonstrates that our higher-order asymptotic calculations predict deformations of the high-frequency isola from its original elliptic shape consistent with numerical results, giving confidence that these expansions are correct.

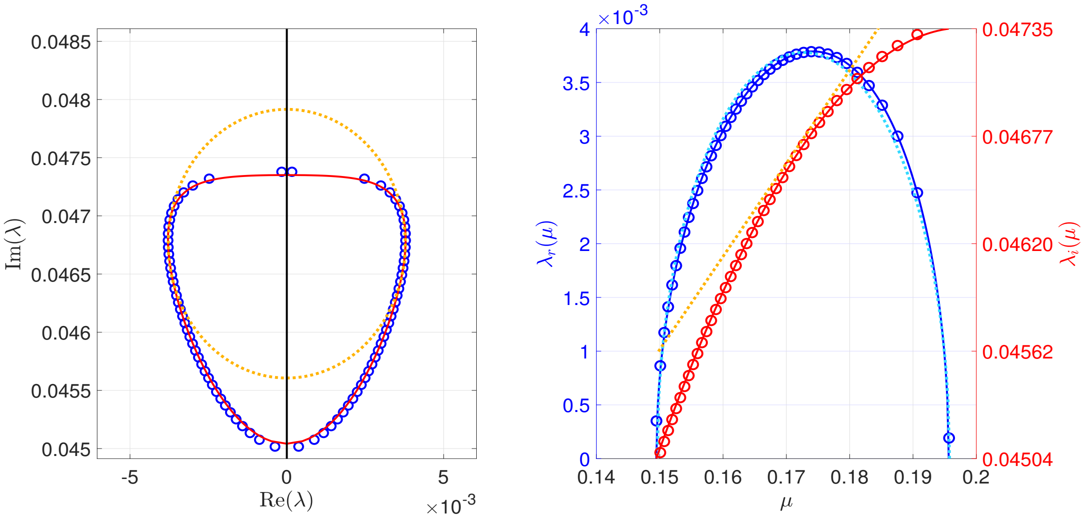

Figure 2.5: (Left) The $p = 1$ high-frequency isola for $\beta = 0.7$ and $\varepsilon = 10^{-2}$. (The parameter ε has been increased to constrast the second- and first-order asymptotic predictions and exaggerate the deformations of the isola from its original elliptic shape.) The solid red curve is parameterized by (2.65). The dotted orange curve is the ellipse found at $\mathcal{O}(\varepsilon)$. The blue circles are a subset of spectral elements from the numerically computed isola by the FFH method. (Right) The Floquet parameterization of the real (blue) and imaginary (red) parts of the isola. The solid curves illustrate the asymptotic result (2.65). The dotted (cyan and orange) curves illustrate the (real and imaginary) asymptotic results only to $\mathcal{O}(\varepsilon)$. The circles indicate numerical results according to the FFH method.

2.6 Asymptotic Description of the $p = 2$ *High-Frequency Instability*

Let m, n, and μ_0 satisfy the condition (2.29) for $p = 2$ and appropriately chosen β parameter. Then, (2.41) gives a collided eigenpair of $\mathcal{L}_{\mu_0,0}$. We assume (2.42a), (2.42b), and (2.43) remain valid expansions for this eigenvalue, eigenfunction, and Floquet exponent when $0 < \varepsilon \ll 1$. We obtain the coefficients of these expansions order by order in much the same way as the $p = 1$ high-frequency instabilities.

2.6.1 The $\mathcal{O}(\varepsilon)$ Problem

Substituting expansions (2.42a), (2.42b), and (2.43) into the spectral problem (2.25) and collecting terms of $\mathcal{O}(\varepsilon)$ yields

$$\begin{aligned}(\mathcal{L}_{\mu_0,0}-\lambda_0)w_1(x) = &-i(\mu_0+n-1)e^{i(n-1)x}+\left[\lambda_1+i\mu_1c_g(\mu_0+n)\right]e^{inx}\\ &-i(\mu_0+n+1)(1+\gamma_0)e^{i(n+1)x}+\gamma_0\left[\lambda_1+i\mu_1c_g(\mu_0+m)\right]e^{imx}\\ &-i(\mu_0+m+1)e^{i(m+1)x},\end{aligned} \tag{2.81}$$

where we have replaced η_1 by (2.18). Equation (2.81) shares similar features with (2.48), but since $m-n\neq 1$ in this case, (2.81) cannot be simplified further.

The solvability conditions of (2.81) are

$$\lambda_1+i\mu_1c_g(\mu_0+n)=0, \tag{2.82a}$$

$$\gamma_0\left[\lambda_1+i\mu_1c_g(\mu_0+m)\right]=0. \tag{2.82b}$$

From our theorem in the previous subsection, $c_g(\mu_0+m)\neq c_g(\mu_0+n)$. Moreover, $\gamma_0\neq 0$, otherwise the $\varepsilon=0$ eigenspace would cease to be two-dimensional. Thus, the solvability conditions above imply

$$\lambda_1=\mu_1=0. \tag{2.83}$$

Solving (2.81) for w_1 and imposing our normalization (2.44), one finds

$$w_1(x)=\tau_{1,n-1}e^{i(n-1)x}+\tau_{1,n+1}e^{i(n+1)x}+\tau_{1,m+1}e^{i(m+1)x}+\gamma_1e^{imx}, \tag{2.84}$$

where γ_1 is a constant to be determined at higher order,

$$\tau_{1,n-1}=Q_{n,n-1}, \tag{2.85a}$$

$$\tau_{1,n+1}=(1+\gamma_0)Q_{n,n+1}, \tag{2.85b}$$

$$\tau_{1,m+1}=\gamma_0Q_{n,m+1}, \tag{2.85c}$$

and $Q_{J,K}$ is given in (2.60).

2.6.2 The $\mathcal{O}\left(\varepsilon^2\right)$ Problem

Substituting (2.42a), (2.42b), and (2.43) into (2.25) and collecting terms of $\mathcal{O}(\varepsilon^2)$ yields

$$(\mathcal{L}_{\mu_0,0} - \lambda_0)w_1(x) = \lambda_2 w_0(x) - \mathcal{L}_2|_{\mu_1=0} w_0(x) - \mathcal{L}_1|_{\mu_1=0} w_1(x), \tag{2.86}$$

where $\mathcal{L}_1|_{\mu_1=0}$ is as before (but evaluated at $\mu_1 = 0$) and

$$\begin{aligned}\mathcal{L}_2|_{\mu_1=0} = {}& ic_0\mu_2 + c_2(i\mu_0 + \partial_x) + 3\mu_2 i(i\mu_0 + \partial_x)^2 + 5\mu_2 i(i\mu_0 + \partial_x)^4 \\ & + 2\eta_2(x)(i\mu_0 + \partial_x) + 2\eta_{2,x}(x).\end{aligned} \tag{2.87}$$

As in the previous order, we evaluate the inhomogeneous terms of (2.86) using (2.18) to replace η_2, (2.45) to replace w_0, and (2.84) to replace w_1. If, in addition to these replacements, one exploits the evenness of η_2 so that $\mathcal{F}_{-2}[\eta_2(x)] = \mathcal{F}_2[\eta_2(x)]$ and uses $m - n = p = 2$ to simplify, one arrives at the solvability conditions:

$$\lambda_2 + i\mathcal{C}^n_{\mu_2,\mu_0} = i\gamma_0\mathcal{S}_2(\mu_0 + n), \tag{2.88a}$$

$$\gamma_0\left[\lambda_2 + i\mathcal{C}^m_{\mu_2,\mu_0}\right] = i\mathcal{S}_2(\mu_0 + m), \tag{2.88b}$$

where

$$\mathcal{C}^N_{\mu_2,\mu_0} = \mu_2 c_g(\mu_0 + N) - \mathcal{P}^N_{\mu_0}, \tag{2.89a}$$

$$\mathcal{P}^N_{\mu_0} = (\mu_0 + N)\left[(Q_{n,N-1} + Q_{n,N+1} + 2\widehat{u_2(x)}_0) + c_2\right], \tag{2.89b}$$

$$\mathcal{S}_2 = (Q_{n,n+1} + 2\widehat{u_2(x)}_2). \tag{2.89c}$$

Similar to the $p = 1$ case, (2.88a) and (2.88b) form a nonlinear system for λ_2 and γ_0. The solutions of this system are

$$\lambda_2 = \lambda_{2,r} + i\lambda_{2,i}, \tag{2.90a}$$

$$\gamma_0 = \frac{i(\mu_0 + m)(Q_{n,n+1} + 2\upsilon_{2,-2})}{\lambda_2 + i\mathcal{C}^m_{\mu_2,\mu_0}}, \tag{2.90b}$$

where

$$\lambda_{2,i} = -\left(\frac{\mathcal{C}^m_{\mu_2,\mu_0} + \mathcal{C}^n_{\mu_2,\mu_0}}{2}\right), \tag{2.91a}$$

$$\lambda_{2,r} = \pm\sqrt{-\left[\frac{\mathcal{C}^m_{\mu_2,\mu_0} - \mathcal{C}^n_{\mu_2,\mu_0}}{2}\right]^2 - \mathcal{S}_2^2(\mu_0+m)(\mu_0+n)}. \tag{2.91b}$$

Provided $\mathcal{S}_2 \neq 0$, there exists an interval of $\mu_2 \in (M_{2,-}, M_{2,+})$, where

$$M_{2,\pm} = \frac{\mathcal{P}^m_{\mu_0} - \mathcal{P}^n_{\mu_0}}{c_g(\mu_0+m) - c_g(\mu_0+n)} \pm 2\left|\frac{\mathcal{S}_2}{c_g(\mu_0+m) - c_g(\mu_0+n)}\right|\sqrt{-(\mu_0+m)(\mu_0+n)}, \tag{2.92}$$

such that λ_2 has a nonzero real part. This is guaranteed by the following theorem:

Theorem 2.6.1. *For $\mathcal{S}_2$ defined in* (2.89c) *and β satisfying inequality* (2.30) *with $p = 2$, $\mathcal{S}_2 \neq 0$.*

Proof. Since $p = 2$, we have from (2.30) that $1/5 < \beta < 3/10$. Using results from the previous theorems, $k_{1,2} = 1$ is a double root of $F(k;p) = (\Omega(k+p) - \Omega(k))/p$ for all $1/5 < \beta < 3/10$. The remaining roots of F are

$$k_{3,4} = -1 \pm \sqrt{\frac{3}{5\beta} - 2}, \tag{2.93}$$

which correspond to the nonzero eigenvalue collisions that give rise to the $p = 2$ high-frequency instability.

The quantity $\mathcal{S}_2$ can be written in terms of $k_{3,4}$ as

$$\mathcal{S}_2 = \left[\frac{k_{3,4}+1}{\Omega(k_{3,4}+1) - \Omega(k_{3,4})} + \frac{1}{\Omega(2)}\right], \tag{2.94}$$

Because $k_{3,4}$ are symmetric about $k = 1$ (from the symmetry of F), the value of $\mathcal{S}_2$ is independent of the choice of $k_{3,4}$. Using the definition of the dispersion relation Ω (2.19), (2.94) simplifies to

$$\mathcal{S}_2 = \frac{1}{2(1-5\beta)}, \tag{2.95}$$

which is nonzero for $1/5 < \beta < 3/10$. $\square$

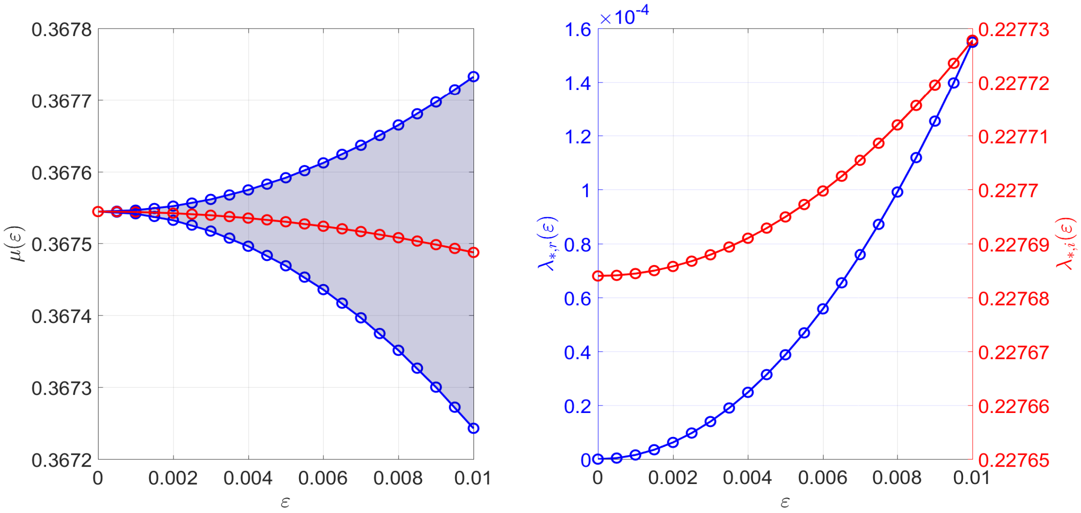

Figure 2.6: (Left) The interval of Floquet exponents that parameterizes the $p = 2$ high-frequency isola for $\beta = 0.25$ as a function of ε. (The parameter β must be changed to satisfy (2.30) for a $p = 2$ isola to arise.) The solid blue curves indicate the asymptotic boundaries of this interval according to (2.96). The blue circles indicate the numerical boundaries computed using the FFH method. The solid red curve gives the Floquet exponent corresponding to the most unstable spectral element of the isola according to (2.97). The red circles indicate the numerical results according to the FFH method. (Right) The real (blue) and imaginary (red) parts of the most unstable spectral element of the isola as a function of ε. The solid curves illustrate the asymptotic result (2.98). The circles illustrate numerical results according to the FFH method.

Thus, the interval of Floquet exponents parameterizing the $p = 2$ high-frequency isola has asymptotic expansion

$$\mu \in \left(\mu_0 + \varepsilon^2 M_{2,-}, \mu_0 + \varepsilon^2 M_{2,+}\right) + \mathcal{O}\left(\varepsilon^3\right). \tag{2.96}$$

Unlike in (2.54) for the $p = 1$ instabilities, the center of (2.96) changes at the same rate as its width. Moreover, this width is an order of magnitude smaller than that of the $p = 1$ instabilities. This explains in part why numerical calculations involving the $p = 2$ instability are more challenging than those for the $p = 1$ instabilities. With the help of our asymptotic expansion (2.96), this difficulty is overcome, see Figure 2.6.

Using our results above, we can obtain an asymptotic expansion for the Floquet exponent of the most unstable spectral element of the $p = 2$ high-frequency isola:

$$\mu_* = \mu_0 + \frac{\mathcal{P}^m_{\mu_0} - \mathcal{P}^n_{\mu_0}}{c_g(\mu_0 + m) - c_g(\mu_0 + n)}\varepsilon^2 + \mathcal{O}(\varepsilon^3). \tag{2.97}$$

Asymptotic expansions for the real and imaginary part of this spectral element are

$$\lambda_{*,r} = \varepsilon^2|\mathcal{S}_2|\sqrt{-(\mu_0 + m)(\mu_0 + n)} + \mathcal{O}(\varepsilon^3), \tag{2.98a}$$

$$\lambda_{*,i} = -\Omega(\mu_0 + n) - \left[\frac{\mathcal{P}^m_{\mu_0}c_g(\mu_0 + n) - \mathcal{P}^n_{\mu_0}c_g(\mu_0 + m)}{c_g(\mu_0 + m) - c_g(\mu_0 + n)}\right]\varepsilon^2 + \mathcal{O}(\varepsilon^3), \tag{2.98b}$$

respectively. These expansions are in excellent agreement with numerical computations using the FFH method, as is seen in Figure 2.6. This is a consequence of resolving quadratic corrections to the real and imaginary parts of the $p = 2$ high-frequency isolas simultaneously, unlike in the $p = 1$ case.

Analogous to the derivation of (2.57), the ellipse given by

$$\frac{\lambda_r^2}{\varepsilon^4} + \frac{\left[\lambda_i + \Omega(\mu_0 + n) + \varepsilon^2\left(\frac{\mathcal{P}^m_{\mu_0}c_g(\mu_0+n) - \mathcal{P}^n_{\mu_0}c_g(\mu_0+m)}{c_g(\mu_0+m) - c_g(\mu_0+n)}\right)\right]^2}{\varepsilon^4\left(\frac{c_g(\mu_0+m) + c_g(\mu_0+n)}{c_g(\mu_0+m) - c_g(\mu_0+n)}\right)^2} = -\mathcal{S}_2^2(\mu_0 + m)(\mu_0 + n) + O(\varepsilon). \tag{2.99}$$

is asymptotic to the $p = 2$ high-frequency isola. This ellipse has center that drifts from the collision site at a rate comparable to its semi-major and -minor axes,

$$a_2 = \varepsilon^2|\mathcal{S}_2|\sqrt{-(\mu_0 + m)(\mu_0 + n)} \tag{2.100a}$$

$$b_2 = a_2\left|\frac{c_g(\mu_0 + m) + c_g(\mu_0 + n)}{c_g(\mu_0 + m) - c_g(\mu_0 + n)}\right|, \tag{2.100b}$$

respectively. This behavior is distinct from that in the $p = 1$ case, where the center drifts slower than the axes grow. Comparison with numerical computations using the FFH method show that (2.99) is an excellent approximation for $p = 2$ high-frequency isolas, giving confidence in our asymptotic calculations, see Figure 2.7.

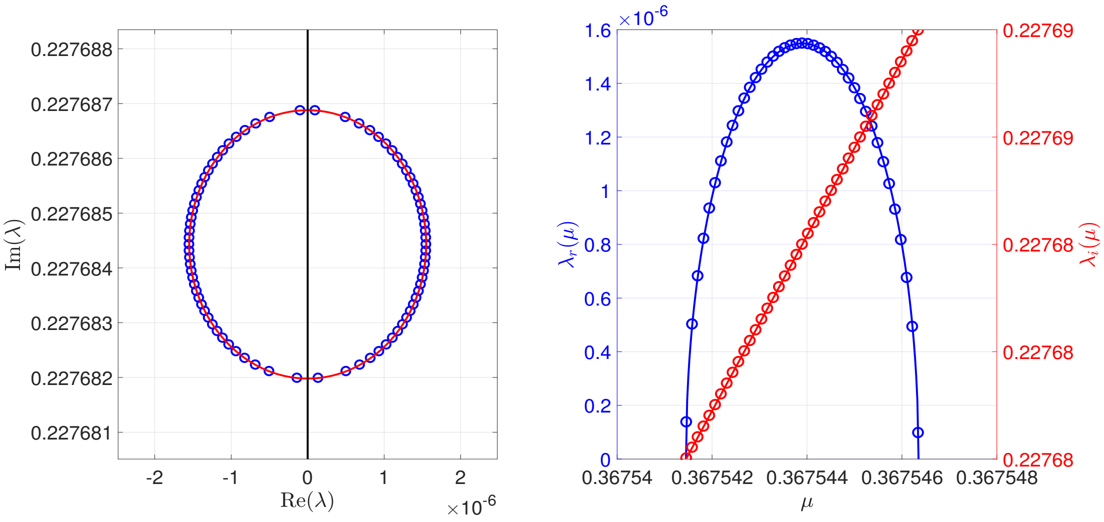

Figure 2.7: (Left) The $p = 2$ high-frequency isola for $\beta = 0.25$ and $\varepsilon = 10^{-3}$. The solid red curve is the ellipse (2.99). The blue circles are a subset of spectral elements from the numerically computed isola using the FFH method. The blue circles are a subset of spectral elements from the numerically computed isola using the FFH method. (Right) The Floquet parameterization of the real (blue) and imaginary (red) parts of the isola. The solid curves illustrate the asymptotic result (2.90a). The circles indicate numerical results according to the FFH method.

2.7 Asymptotic Description of Higher-Order Isolas

The spectral method used to obtain the leading-order behavior of the $p = 1, 2$ high-frequency instabilities generalizes to higher-order isolas. The method consists of the following steps, each of which is readily implemented in a symbolic programming language of the reader's choice:

(i) Given $p \in \mathbb{N}$, determine the unique μ_0, m, and n to satisfy condition (2.29), assuming β satisfies (2.30).

(ii) Expand about the collided eigenvalues in a formal power series of ε and similarly expand their corresponding eigenfunctions and Floquet exponents. To maintain uniqueness of the eigenfunctions, choose the normalization (2.44).

(iii) Substitute these expansions into the spectral problem (2.25). Equate powers of ε to construct a hierarchy of inhomogeneous linear problems to solve.

(iv) Proceed order by order. At each order, impose solvability and normalization conditions. Invert the linear operator against its range using the method of undetermined coefficients, for instance. Use previous normalization and solvability conditions as well as condition (2.30) to simplify problems if necessary.

We conjecture that this method yields the first nonzero real part correction to the pth high-frequency isola at $\mathcal{O}(\varepsilon^p)$. We have shown that this conjecture holds for $p = 1, 2$. For $p = 3$, one can show that the high-frequency isola is asymptotic to the ellipse

$$\frac{\lambda_r^2}{\varepsilon^6} + \frac{\left(\lambda_i + \Omega(\mu_0 + n) + \varepsilon^2 \left[\frac{\mathcal{P}_{\mu_0}^m c_g(\mu_0+n) - \mathcal{P}_{\mu_0}^n c_g(\mu_0+m)}{c_g(\mu_0+m) - c_g(\mu_0+n)}\right]\right)^2}{\varepsilon^6 \left(\frac{c_g(\mu_0+m)+c_g(\mu_0+n)}{c_g(\mu_0+m)-c_g(\mu_0+n)}\right)^2} = -\mathcal{S}_3^2(\mu_0 + m)(\mu_0 + n) + O(\varepsilon), \tag{2.101}$$

where

$$\mathcal{S}_3 = \left[Q_{n,n+1}Q_{n,n+2} + 2\mathcal{F}_2[\eta_2(x)](Q_{n,n+1} + Q_{n,n+2}) + 2\mathcal{F}_3[\eta_3(x)]\right], \tag{2.102}$$

and $\mathcal{P}_{\mu_0}^N$ are the same as for the $p = 2$ isola. The semi-major and -minor axes of (2.101) scale as $\mathcal{O}(\varepsilon^3)$, as the conjecture predicts. If true for all p, this conjecture explains why the higher-order isolas are so challenging to detect both in numerical and perturbation calculations of the stability spectrum.

The center of (2.101) drifts similarly to that of the $p = 2$ high-frequency isola (2.99). In fact, centers of isolas beyond $p = 1$ all drift at a similar rate, as these isolas all satisfy the same $\mathcal{O}(\varepsilon^2)$ problem. As a consequence, one should expect corrections to the imaginary part of the high-frequency isola before reaching $\mathcal{O}(\varepsilon^p)$, making it more difficult to prove the conjecture about the first occurrence of a nonzero real part.

Remark 2.7.1. *Once the leading-order behavior of the high-frequency isola is determined at $\mathcal{O}(\varepsilon^p)$, an additional step to the method is required to determine the higher-order Floquet corrections. This is where the regular curve condition is used.*

2.8 Conclusions

In this chapter, we have investigated the asymptotic behavior of high-frequency instabilities of small-amplitude Stokes waves of the Kawahara equation. For the largest of these instabilities ($p = 1, 2$), we introduced a spectral perturbation method to compute explicitly

(i) the asymptotic interval of Floquet exponents that parameterizes the high-frequency isola,

(ii) the leading-order behavior of its most unstable spectral elements, and

(iii) the leading-order curve asymptotic to the isola.

We then compared these asymptotic expansions with numerical results of the FFH method and found excellent agreement between the two, giving confidence in our perturbation method. We also obtained a higher-order asymptotic result for the $p = 1$ high-frequency isola by introducing the regular curve condition. A similar technique may be used to describe the higher-order asymptotic behavior of $p \geq 3$ isolas.

The perturbation method used throughout this chapter holds only for nonresonant Stokes waves (2.17). Resonant waves require a modified Stokes expansion, and as a result of this modification, the leading-order behaviors of the high-frequency isolas change. Some numerical work has been done to investigate this effect, see [89], but no perturbation methods have yet to be proposed.

Chapter 3

HIGH-FREQUENCY INSTABILITIES OF A BOUSSINESQ-WHITHAM SYSTEM

3.1 About the Hur-Pandey Boussinesq-Whitham System

In this chapter, we investigate the small-amplitude, $2\pi/\kappa$-periodic traveling waves modeled by a Boussinesq-Whitham system proposed in Hur and Pandey [51] and developed further in Hur and Tao [52]:

$$\begin{aligned} \eta_t &= -hu_x - (\eta u)_x, \\ u_t &= -g\mathcal{K}[\eta_x] - uu_x. \end{aligned} \tag{3.1}$$

In this model, $\eta(x,t)$ represents the displacement of a wave profile from its equilibrium depth h, $u(x,t)$ is the horizontal velocity along $z=-h$, and $\mathcal{K}$ is a Fourier multiplier operator defined so that the linearized dispersion relation of (3.1) matches that of Euler's equations. For functions $f \in \mathrm{L}^1_{\text{per}}(-\pi/\kappa, \pi/\kappa)$, $\mathcal{K}$ is defined as

$$\mathcal{F}_n\left(\mathcal{K}[f]\right) = \frac{\tanh(n\kappa h)}{n\kappa h}\mathcal{F}_n(f), \quad n \in \mathbb{Z}, \tag{3.2}$$

where $\mathcal{F}_j$ denotes the Fourier transform of f. Explicitly,

$$\mathcal{F}_j(f) = \frac{\kappa}{2\pi}\int_{-\pi/\kappa}^{\pi/\kappa} f(x)e^{-ij\kappa x}dx. \tag{3.3}$$

Alternatively, $\mathcal{K}$ can be defined in physical variables as the pseudo-differential operator

$$\mathcal{K}[f] = \left(\frac{\tanh(hD)}{hD}\right)f, \tag{3.4}$$

where $D = -i\partial_x$. For the remainder of this manuscript, we refer to (3.1) as the Hur-Pandey Boussinesq-Whitham system, or HPBW for short.

The HPBW system can be expressed as a non-canonical Hamiltonian system of the form

$$\frac{\partial}{\partial t}\begin{pmatrix}\eta\\ u\end{pmatrix} = J\frac{\delta\mathcal{H}}{\delta(\eta,u)}, \tag{3.5}$$

where

$$\mathcal{H} = \frac{1}{2}\int_{-\pi/\kappa}^{\pi/\kappa}\left(hu^2 + g\eta\mathcal{K}[\eta] + \eta u^2\right)dx, \tag{3.6}$$

and

$$J = -\begin{pmatrix}0 & \partial_x\\ \partial_x & 0\end{pmatrix}. \tag{3.7}$$

The system has an ε-parameter family of small-amplitude, $2\pi/\kappa$-periodic traveling-wave solutions for each $\kappa > 0$. We call these solutions the Stokes waves of HPBW by analogy with solutions of Euler's equations of the same name. In Section 3.2, we derive a power series expansion for HPBW Stokes waves in a small parameter ε that scales with the amplitude of the waves.

Perturbing Stokes waves with functions bounded in space and exponential in time yields a spectral problem after linearizing the governing equations of the perturbations, as discussed in the Introduction. The spectral elements of this problem define the stability spectrum of Stokes waves. This spectrum exhibits quadrafold symmetry from the Hamiltonian structure of (3.1). Because of quadrafold symmetry, all elements of the stability spectrum have non-positive real component only if the stability spectrum is a subset of the imaginary axis. Therefore, HPBW Stokes waves are only spectrally stable if all spectral elements reside on the imaginary axis. Otherwise, the Stokes waves are spectrally unstable.

If the aspect ratio κh is sufficiently large, Stokes waves of HPBW and Stokes waves of Euler's equations both have stability spectra near the origin that leave the imaginary axis for $0 < |\varepsilon| \ll 1$, resulting in modulational instability. The proof for HPBW is given in [51]. Recent numerical work by [22] shows that HPBW Stokes waves also have stability spectra away from the origin that leave the imaginary axis, regardless of κh. These spectra correspond to the high-frequency instabilities.

As discussed in the Introduction and in Chapter 2, high-frequency instabilities arise from the collision of nonzero stability spectra of zero-amplitude Stokes waves. At these collided spectral elements, a Hamiltonian-Hopf bifurcation occurs, resuting in a locus of spectral elements bounded away from the origin that peel off the imaginary axis as ε increases. We refer to this locus of spectral elements as a high-frequency isola.

The HPBW system is among the simplest nonlinear models to exhibit high-frequency instabilities and retain the full dispersion relation of the more complicated Euler equations. In contrast with other Boussinesq-Whitham systems [19, 22], HPBW also has desirable well-posedness results for Cauchy problems on the whole real line: most relevant to our work is the robustness of HPBW to changes in the average value of the initial condition [38]. For these reasons, HPBW is an ideal candidate to obtain asymptotic information about high-frequency instabilities for $0 < \varepsilon \ll 1$. Similar to the isolas of the Kawahara equation, we obtain the following for isolas of HPBW:

(i) an asymptotic range of Floquet exponents that parameterize the isola,

(ii) an asymptotic estimate for the most unstable spectral element of the isola,

(iii) expressions of curves that are asymptotic to the isola, and

(iv) wavenumbers that do not have an isola.

Our approach is inspired by the perturbation method outlined in the previous chapter for the Kawahara equation, but modified appropriately for a vector equation with a nonlocal operator. As in the previous chapter, we compare all of our asymptotic results with numerical computations using the Floquet-Fourier Hill (FFH) method, as described in Appendix B.

3.2 Stokes Wave Solutions

In a traveling frame moving with velocity c, $x \to x - ct$ and (3.1) becomes

$$\begin{aligned} \eta_t &= c\eta_x - hu_x - (\eta u)_x, \\ u_t &= cu_x - g\mathcal{K}(\eta_x) - uu_x. \end{aligned} \tag{3.8}$$

Non-dimensionalizing (3.8) according to $\eta \to h\eta$, $u \to u\sqrt{gh}$, $x \to \alpha^{-1}hx$, $t \to t\sqrt{h/g}$, and $c \to c\sqrt{gh}$ yields the following system:

$$\begin{aligned} \alpha^{-1}\eta_t &= c\eta_x - u_x - (\eta u)_x, \\ \alpha^{-1}u_t &= cu_x - \mathcal{K}_\alpha(\eta_x) - uu_x. \end{aligned} \tag{3.9}$$

The parameter α is chosen to map $2\pi/\kappa$-periodic solutions of (3.8) to 2π-periodic solutions of (3.9). Consequently, $\alpha = \kappa h > 0$, the aspect ratio of the solutions, and

$$\mathcal{F}_n[\mathcal{K}_\alpha[f]] = \frac{\tanh(\alpha n)}{\alpha n}\mathcal{F}_n[f], \quad n \in \mathbb{Z}, \tag{3.10}$$

or, alternatively,

$$\mathcal{K}_\alpha[f] = \left(\frac{\tanh(\alpha D)}{\alpha D}\right) f, \tag{3.11}$$

for $f \in \mathrm{L}^1_{\text{per}}(-\pi, \pi)$. Here, the Fourier transform (3.3) is redefined over $(-\pi, \pi)$ (so $\kappa = 1$).

Stokes wave solutions of (3.9) are independent of time. Equating time derivatives in (3.9) to zero and integrating in x, we find

$$\begin{aligned} c\eta &= u + \eta u + \mathcal{I}_1 \\ cu &= \mathcal{K}_\alpha(\eta) + \frac{1}{2}u^2 + \mathcal{I}_2, \end{aligned} \tag{3.12}$$

where $\mathcal{I}_j$ are integration constants. For each $\alpha > 0$, there exists an ε-parameter family of infinitely differentiable, even, small-amplitude, 2π-periodic solutions of (3.12), provided $\mathcal{I}_j$ are sufficiently small [51]. We call these solutions the HPBW Stokes waves, denoted $(\eta_S(x;\varepsilon,\mathcal{I}_j), u_S(x;\varepsilon,\mathcal{I}_j))^T$, where ε is a small-amplitude parameter defined implicitly in terms of the first Fourier mode of $\eta_S(x;\varepsilon,\mathcal{I}_j)$:

$$\varepsilon = 2\mathcal{F}_1[\eta_S](1) = \frac{1}{\pi}\int_{-\pi}^{\pi} \eta_S(x;\varepsilon,\mathcal{I}_j)e^{-ix}dx. \tag{3.13}$$

This definition ensures $\eta_S(x;\varepsilon,\mathcal{I}_j) \sim \varepsilon\cos(x)$ as $\varepsilon \to 0$.

Remark 3.2.1. *Redefining $c \to c - \mathcal{I}_1$ and $u \to u - \mathcal{I}_1$ in (3.12) implies $\mathcal{I}_1 = 0$ without loss of generality. If one requires η_S to have zero average over one period, then $\mathcal{I}_2 = \mathcal{I}_2(\varepsilon)$ must be expanded a power series in ε. To streamline the perturbation calculation, we instead equate $\mathcal{I}_2 = 0$. This leads to an expansion for η_S with nonzero average, but the calculations of the high-frequency instabilities that follow are not significantly affected by a nonzero $\mathcal{I}_2$.*

The Stokes waves and their velocity may be expanded as power series in ε:

$$\eta_S = \eta_S(x;\varepsilon) = \varepsilon\cos(x) + \sum_{j=2}^{\infty} \eta_j(x)\varepsilon^j, \tag{3.14a}$$

$$u_S = u_S(x;\varepsilon) = c_0\varepsilon\cos(x) + \sum_{j=2}^{\infty} u_j(x)\varepsilon^j, \tag{3.14b}$$

$$c = c(\varepsilon) = c_0 + \sum_{j=1}^{\infty} c_{2j}\varepsilon^{2j}, \quad c_0^2 = \frac{\tanh(\alpha)}{\alpha}, \tag{3.14c}$$

where η_j and u_j are analytic, even[1], and 2π-periodic for each j. Substituting these expansions into (3.12) (with $\mathcal{I}_j = 0$) and following a Poincaré-Lindstedt perturbation method as in the case of the Kawahara equation, one can determine η_j, u_j, and c_{2j} order by order in ε. Introducing the intermediate variables

$$C_k^2 = \frac{\tanh(\alpha k)}{\alpha k} \quad \text{and} \quad D_z = \frac{1}{c_0^2 - z^2}, \quad \text{where} \quad c_0^2 = C_1^2. \tag{3.15}$$

the surface displacement of the Stokes wave $\eta_S(x;\varepsilon)$ has explicit expansion

$$\begin{aligned}\eta_S(x;\varepsilon) &= \varepsilon\eta_1(x) + \varepsilon^2\eta_2(x) + \varepsilon^3\eta_3(x) + \varepsilon^4\eta_4(x) + \mathcal{O}\left(\varepsilon^5\right) \\ &= \varepsilon\cos(x) + \Big(N_{2,0} + 2N_{2,2}\cos(2x)\Big)\varepsilon^2 + 2N_{3,3}\varepsilon^3\cos(3x) \\ &\quad + \Big(N_{4,0} + 2N_{4,2}\cos(2x) + 2N_{4,4}\cos(4x)\Big)\varepsilon^4 + \mathcal{O}\left(\varepsilon^5\right),\end{aligned} \tag{3.16}$$

where

$$N_{2,0} = \frac{3c_0^2 D_1}{4}, \tag{3.17a}$$

---

[1] These functions are even without loss of generality since the pre-integrated version of equation (3.12) respects the symmetries $x \to x + \phi$ for any $\phi \in \mathbb{R}$ and $x \to -x$.

$$N_{2,2} = \frac{3c_0^2 D_{C_2}}{8}, \tag{3.17b}$$

$$N_{3,3} = \frac{c_0^2 D_{C_2} D_{C_3}}{16}\Big(5c_0^2 + 4C_2^2\Big), \tag{3.17c}$$

$$\begin{aligned} N_{4,0} = &-\frac{3c_0^2 D_1^3 D_{C_2}^2}{64}\Big(25c_0^8 + 4C_2^4 + 2c_0^2 C_2^2(-7 + 2C_2^2) - 4c_0^6(2 + 11C_2^2) \\ &\qquad + c_0^4(1 + 22C_2^2 + 10C_2^4)\Big), \end{aligned} \tag{3.17d}$$

$$\begin{aligned} N_{4,2} = &\frac{c_0^2 D_1 D_{C_2}^3 D_{C_3}}{64}\Big(- 20c_0^8 + 4C_2^4 C_3^2 + c_0^6(2 + 31C_2^2 + 50C_3^2) \\ &\qquad + c_0^2 C_2^2(C_3^2 + 2C_2^2(10 + 7C_3^2)) - c_0^4(38C_2^4 + 32C_3^2 + C_2^2(-5 + 37C_3^2))\Big), \end{aligned} \tag{3.17e}$$

$$N_{4,4} = \frac{c_0^2 D_{C_2}^2 D_{C_3} D_{C_4}}{128}\Big(35c_0^6 - 20C_2^4 C_3^2 + 5c_0^4(4C_2^2 + 5C_3^2) - 4c_0^2(7C_2^4 + 8C_2^2 C_3^2)\Big). \tag{3.17f}$$

Similarly, for the corresponding velocity $u_S(x;\varepsilon)$ along the bottom boundary of the domain,

$$\begin{aligned} u_S(x;\varepsilon) &= \varepsilon u_1(x) + \varepsilon^2 u_2(x) + \varepsilon^3 u_3(x) + \varepsilon^4 u_4(x) + \mathcal{O}\left(\varepsilon^5\right) \\ &= c_0\varepsilon\cos(x) + \Big(U_{2,0} + 2U_{2,2}\cos(2x)\Big)\varepsilon^2 + \Big(2U_{3,1}\cos(x) + 2U_{3,3}\cos(3x)\Big)\varepsilon^3 \\ &\qquad + \Big(U_{4,0} + 2U_{4,2}\cos(2x) + 2U_{4,4}\cos(4x)\Big)\varepsilon^4 + \mathcal{O}\left(\varepsilon^5\right), \end{aligned} \tag{3.18}$$

where

$$U_{2,0} = \frac{c_0 D_1}{4}\Big(2 + c_0^2\Big), \tag{3.19a}$$

$$U_{2,2} = \frac{c_0 D_{C_2}}{8}\Big(2C_2^2 + c_0^2\Big), \tag{3.19b}$$

$$U_{3,1} = \frac{3c_0^3 D_1 D_{C_2}}{32}\Big(1 - 3c_0^2 + 2C_2^2\Big), \tag{3.19c}$$

$$U_{3,3} = \frac{c_0 D_{C_2} D_{C_3}}{16}\Big(c_0^4 + 2C_2^2 C_3^2 + 2c_0^2(C_2^2 + 2C_3^2)\Big), \tag{3.19d}$$

$$U_{4,0} = \frac{-3c_0^3 D_1^3 D_{C_2}^2(2 + c_0^2)}{64}\Big(2c_0^4(-2 + 5c_0^2) + C_2^2(-3 + 8c_0^2 - 17c_0^4) + 2C_2^4(1 + 2c_0^2)\Big), \tag{3.19e}$$

$$\begin{aligned} U_{4,2} = &\frac{c_0 D_1 D_{C_2}^3 D_{C_3}}{128}\Big(- 25c_0^{10} + 8C_2^6 C_3^2 + c_0^8(7 - C_2^2 + 45C_3^2) + c_0^6\big(C_2^2 + 32C_2^4 \\ &\qquad + C_3^2(-27 + 37C_2^2)\big) - c_0^4(60C_2^6 + 37C_2^2 C_3^2 + C_2^4(-22 + 56C_3^2))\Big), \end{aligned} \tag{3.19f}$$

$$U_{4,4} = \frac{c_0 D_{C_2}^2 D_{C_3} D_{C_4}}{128}\Big(5c_0^8 - 8C_2^4 C_3^2 C_4^2 + 2c_0^4(-2C_2^4 + 5C_3^2 C_4^2 + 6C_2^2(-C_3^2 + C_4^2))$$

$$+ c_0^6(8C_2^2 + 15(C_3^2 + 2C_4^2)) - 4c_0^2(5C_2^2C_3^2C_4^2 + 3C_2^4(C_3^2 + 2C_4^2))\Big). \tag{3.19g}$$

Finally, for the velocity of the Stokes waves $c(\varepsilon)$,

$$c(\varepsilon) = c_0 + c_2\varepsilon^2 + c_4\varepsilon^4 + \mathcal{O}\left(\varepsilon^6\right), \tag{3.20}$$

where

$$c_2 = \frac{3c_0D_1D_{C_2}}{16}\Big(c_0^2 + 5c_0^4 - 2C_2^2(2 + c_0^2)\Big), \tag{3.21a}$$

$$\begin{aligned} c_4 = \frac{3c_0D_1^3D_{C_2}^3D_{C_3}}{512}\Big(&3c_0^2\big(c_0^6 - 3c_0^8 + 15c_0^{10} - 85c_0^{12} + c_0^4C_2^2(11 + 3c_0^2 - 3c_0^4 + 205c_0^6) \\ &- 4c_0^2C_2^4(-2 + 15c_0^2 + 3c_0^4 + 38c_0^6) - 4C_2^6(-4 + 12c_0^2 - 27c_0^4 + c_0^6)\big) \\ &+ C_3^2\big(c_0^6(-103 + 309c_0^2 - 345c_0^4 + 355c_0^6) - 3c_0^4C_2^2(31 - 57c_0^2 + 57c_0^4 + 185c_0^6) \\ &+ 36c_0^2C_2^4(2 - 3c_0^2 + 9c_0^4 + 10c_0^6) - 4C_2^6(2 + c_0^2)(-2 + 7c_0^2 + 13c_0^4)\big)\Big). \end{aligned} \tag{3.21b}$$

3.3 The Spectral Stability Problem

We consider perturbations of $(\eta_S, u_S)^T$ of the form

$$\begin{pmatrix} \eta(x,t;\varepsilon,\rho) \\ u(x,t;\varepsilon,\rho) \end{pmatrix} = \begin{pmatrix} \eta_S \\ u_S \end{pmatrix} + \rho \begin{pmatrix} H(x,t) \\ U(x,t) \end{pmatrix} + \mathcal{O}\left(\rho^2\right), \tag{3.22}$$

where $|\rho| \ll 1$ is a parameter independent of ε and H and U are sufficiently smooth, bounded functions of $x \in \mathbb{R}$ for all $t \geq 0$. When (3.22) is substituted into (3.9), terms of $\mathcal{O}\left(\rho^0\right)$ cancel by (3.12) (with $\mathcal{I}_j = 0$). Equating terms of $\mathcal{O}(\rho)$, the perturbation $(H, U)^T$ solves the linear system

$$\frac{\partial}{\partial t}\begin{pmatrix} H \\ U \end{pmatrix} = \alpha \begin{pmatrix} -u_{S,x} + (c - u_S)\partial_x & -\eta_{S,x} - (1 + \eta_S)\partial_x \\ -\frac{i\tanh(\alpha D)}{\alpha} & -u_{S,x} + (c - u_S)\partial_x \end{pmatrix} \begin{pmatrix} H \\ U \end{pmatrix}. \tag{3.23}$$

Formally separating variables,

$$\begin{pmatrix} H(x,t) \\ U(x,t) \end{pmatrix} = e^{\lambda t} \begin{pmatrix} \mathcal{H}(x) \\ \mathcal{U}(x) \end{pmatrix} + c.c., \tag{3.24}$$

where $(\mathcal{H},\mathcal{U})^T$ solves the spectral problem

$$\lambda \begin{pmatrix} \mathcal{H} \\ \mathcal{U} \end{pmatrix} = \alpha \begin{pmatrix} -u_{S,x} + (c-u_S)\partial_x & -\eta_{S,x} - (1+\eta_S)\partial_x \\ -\frac{i\tanh(\alpha D)}{\alpha} & -u_{S,x} + (c-u_S)\partial_x \end{pmatrix} \begin{pmatrix} \mathcal{H} \\ \mathcal{U} \end{pmatrix}. \tag{3.25}$$

Since the entries of the matrix operator above are 2π-periodic, one can use Floquet theory[2] to solve (3.25) for $(\mathcal{H},\mathcal{U})^T$. These solutions take the form

$$\begin{pmatrix} \mathcal{H}(x) \\ \mathcal{U}(x) \end{pmatrix} = e^{i\mu x} \begin{pmatrix} \mathfrak{h}(x) \\ \mathfrak{u}(x) \end{pmatrix}, \tag{3.26}$$

where $\mu \in [-1/2, 1/2)$ is called the Floquet exponent and $\mathfrak{h}, \mathfrak{u} \in \mathrm{H}^1_{\text{per}}(-\pi,\pi)$. Substituting (3.26) into (3.25) results in a spectral problem for $\mathbf{w} = (\mathfrak{h}, \mathfrak{u})^{\mathbf{T}}$:

$$\lambda \mathbf{w} = \mathcal{L}_{\mu,\varepsilon}\mathbf{w}, \tag{3.27}$$

with

$$\mathcal{L}_{\mu,\varepsilon} = \alpha \begin{pmatrix} -u_{S,x} + (c-u_S)(i\mu+\partial_x) & -\eta_{S,x} - (1+\eta_S)(i\mu+\partial_x) \\ -\frac{i\tanh(\alpha(\mu+D))}{\alpha} & -u_{S,x} + (c-u_S)\partial_x \end{pmatrix}. \tag{3.28}$$

For sufficiently small ε, (3.27) has a countable collection of eigenvalues λ for each Floquet exponent μ [55]. The union of these eigenvalues over $\mu \in [-1/2, 1/2)$ recovers the purely continuous stability spectrum of (3.25) for fixed ε. Because HPBW is Hamiltonian, the stability spectrum has quadrafold symmetry, similar to Euler's equations and the Kawahara equation. Thus, Stokes waves are spectrally stable only if their stability spectrum is a subset of the imaginary axis.

3.4 Necessary Conditions for High-Frequency Instabilities

When $\varepsilon = 0$, $\mathcal{L}_{\mu,0}$ has constant coefficients, and its spectral elements are given exactly by

$$\lambda^{(\sigma)}_{0,\mu,n} = -i\Omega_\sigma(n+\mu), \quad n \in \mathbb{Z}, \quad \sigma = \pm 1, \tag{3.29}$$

---

[2] Strictly speaking, Floquet theory applies only to linear, local operators. Work by [16] extends this theory to nonlocal operators.

where Ω_σ are the two branches of the linear dispersion relation of (3.9) with $c \to c_0$, where c_0 is given in (3.14). Explicitly,

$$\Omega_\sigma(k) = -\alpha c_0 k + \sigma\omega_\alpha(k), \tag{3.30}$$

where

$$\omega_\alpha(k) = \operatorname{sgn}(k)\sqrt{\alpha k \tanh(\alpha k)}. \tag{3.31}$$

As expected, $\lambda^{(\sigma)}_{0,\mu,n}$ is a countable collection of eigenvalues for each μ, and the resulting stability spectrum has quadrafold symmetry. In addition, the stability spectrum coincides with the imaginary axis, implying that zero-amplitude Stokes waves are spectrally stable.

For a particular Floquet exponent μ, $\mathcal{L}_{\mu,0}$ may have nonzero collided eigenvalues that give rise to high-frequency instabilities when $0 < |\varepsilon| \ll 1$. These eigenvalues exist provided there exists Floquet exponent μ_0 and integers m and n such that

$$\lambda^{(\sigma_1)}_{0,\mu_0,n} = \lambda^{(\sigma_2)}_{0,\mu_0,m} \neq 0. \tag{3.32}$$

It can be shown that such a collision occurs only if $\sigma_1 \neq \sigma_2$ [5, 36, 51]. Moreover, we have the following result:

Theorem 3.4.1. *If* $c_0 > 0$, *then, for each* $p \in \mathbb{Z} \setminus \{0, \pm 1\}$, *there exists a unique Floquet exponent* $\mu_0 \in [-1/2, 1/2]$ *and integers* m *and* n *giving rise to a collided eigenvalue*

$$\lambda^{(1)}_{0,\mu_0,n} = \lambda^{(-1)}_{0,\mu_0,m} \neq 0, \tag{3.33}$$

where $p = m - n$. *Moreover, for fixed* $\alpha > 0$, *the imaginary part of the collided eigenvalues is strictly monotonically decreasing with* p.

Hence, there are a countably infinite number of nonzero eigenvalue collisions in the zero-amplitude stability spectrum of the HPBW system. Each collision has potential to develop a high-frequency instability in the small-amplitude stability spectrum. This is in contrast with the Kawahara equation, where only a finite number of such collisions occur. Also notice that there are no $p = 1$ high-frequency instabilities for HPBW. This is because the $p = 1$ instability appears at the origin of the complex spectral plane.

To prove the result above, we simplify (3.32) to

$$\Omega_1(\mu_0 + n) = \Omega_{-1}(\mu_0 + m) \neq 0. \tag{3.34}$$

Defining $k = \mu_0 + n$ and $p = m - n$, (3.34) becomes

$$\Omega_1(k) = \Omega_{-1}(k + p) \neq 0. \tag{3.35}$$

We call (3.35) the collision condition. For each $p \in \mathbb{Z} \setminus \{0, \pm 1\}$, we prove that there exists a unique $k = k(p; \alpha)$ that satisfies the collision condition. These solutions $k(p; \alpha)$ are distinct from each other for each $\alpha > 0$ and result in an infinite number of distinct collision points on the imaginary axis, according to (3.32). To show this, we must establish important monotonicity properties of the dispersion relation $\Omega_\sigma(k)$, as defined in (3.30).

Lemma 3.4.1. *The function $\omega_\alpha(k) = sgn(k)\sqrt{\alpha k \tanh(\alpha k)}$ is strictly increasing for $k \in \mathbb{R}$. If $|k| > 1$, then $d\omega_\alpha/dk < \alpha|c_0|$, where $c_0^2 = \tanh(\alpha)/\alpha$.*

Proof. A direct calculation shows

$$\frac{d\omega_\alpha}{dk} = \frac{1}{2}\left(\sqrt{\frac{\alpha \tanh(\alpha k)}{k}} + \alpha\sqrt{\frac{\alpha k}{\sinh(\alpha k)}}\operatorname{sech}^{3/2}(\alpha k)\right), \tag{3.36}$$

from which $d\omega_\alpha/dk > 0$. This proves the first claim. Since $\tanh(\alpha k)/(\alpha k) \leq 1$, $\alpha k/\sinh(\alpha k) \leq 1$, and $\operatorname{sech}(\alpha k) \leq 1$, (3.36) gives

$$\frac{d\omega_\alpha}{dk} \leq \frac{1}{2}\left(\sqrt{\frac{\alpha \tanh(\alpha k)}{k}} + \alpha \operatorname{sech}(\alpha k)\right). \tag{3.37}$$

Since $\alpha > 0$, $\sinh(\alpha)/\alpha > 1 > \operatorname{sech}(\alpha)$, so that $\operatorname{sech}(\alpha) < |c_0|$. Because $\operatorname{sech}(z)$ is even and strictly decreasing for $z > 0$, we have

$$\operatorname{sech}(\alpha k) < |c_0|, \quad \text{for} \quad |k| > 1. \tag{3.38}$$

Similarly, since $\tanh(z)/z$ is even and strictly decreasing for $z > 0$,

$$\sqrt{\frac{\alpha\tanh(\alpha k)}{k}} < \alpha\sqrt{\frac{\tanh(\alpha)}{\alpha}} = \alpha|c_0|, \quad \text{for} \quad |k| > 1. \tag{3.39}$$

Together with (3.37), inequalities (3.38) and (3.39) imply $d\omega_\alpha/dk < \alpha|c_0|$ for $|k| > 1$. □

Lemma 3.4.2. *If* $c_0 > 0$, $\Omega_{-1}(k)$ *is strictly decreasing for* $k \in \mathbb{R}$, *and* $\Omega_1(k)$ *is strictly decreasing for* $|k| > 1$. *If* $c_0 < 0$, $\Omega_1(k)$ *is strictly increasing for* $k \in \mathbb{R}$, *and* $\Omega_{-1}(k)$ *is strictly increasing for* $|k| > 1$.

Proof. Suppose $c_0 > 0$. By definition, $d\Omega_\sigma/dk = -\alpha c_0 + \sigma d\omega_\alpha/dk$. If $\sigma = -1$, we use $d\omega_\alpha/dk > 0$ from Lemma 3.3.1 to conclude $d\Omega_{-1}/dk < 0$. If $\sigma = 1$ and $|k| > 1$, we use $d\omega_\alpha/dk < \alpha|c_0|$ from Lemma 3.3.1 to conclude $d\Omega_1/dk = -\alpha c_0 + d\omega_\alpha/dk < 0$, since $c_0 > 0$. An analogous proof holds when $c_0 < 0$. □

For the remainder of this work, we consider $c_0 > 0$, which corresponds to right-traveling Stokes waves. Similar statements hold when $c_0 < 0$ if one rewrites the collision condition (3.35) as $\Omega_{-1}(k) = \Omega_1(k+p) \neq 0$, where k and p are redefined appropriately.

Lemma 3.4.3. *For each* $p \in \mathbb{R}$ *and* $\alpha > 0$, *there exists a unique* $k(p;\alpha) \in \mathbb{R}$ *such that* $\Omega_1(k(p;\alpha)) = \Omega_{-1}(k(p;\alpha) + p)$. *If* $p \in \mathbb{Z}$ *and* $c_0 > 0$, *we have* $\cdots < k(1;\alpha) < k(0;\alpha) < k(-1;\alpha) < \cdots$. *Moreover,* $|k(p;\alpha)| > |p|$ *for* $p \in \mathbb{Z} \setminus \{0, \pm 1\}$ *and* $c_0 > 0$.

Proof. Fix $p \in \mathbb{R}$ and $\alpha > 0$. Define $F(k,p) = \Omega_1(k) - \Omega_{-1}(k+p)$. Then,

$$F(k,p) \sim 2k\sqrt{\frac{\alpha}{|k|}} + \mathcal{O}\left(\frac{1}{\sqrt{|k|}}\right) \quad \text{as} \quad |k| \to \infty. \tag{3.40}$$

Since F has opposite signs as $k \to \pm\infty$, there exists at least one root, denoted $k(p;\alpha)$. Since $\partial_k F(k,p) = d\omega/dk + d\omega(k+p)/dk > 0$ by Lemma 3.3.1, $k(p;\alpha)$ is the only root of F in $\mathbb{R}$, proving the first claim of the theorem.

To prove the second claim, differentiate $F(k(p;\alpha),p)$ with respect to p. Using the definition of Ω_σ,

$$\frac{dk}{dp} = \frac{\left.\frac{d\Omega_{-1}}{dk}\right|_{k(p;\alpha)+p}}{\left.\frac{d\omega}{dk}\right|_{k(p;\alpha)} + \left.\frac{d\omega}{dk}\right|_{k(p;\alpha)+p}}, \tag{3.41}$$

which is well-defined since $F_k(k,p) > 0$. If $c_0 > 0$, then Lemma 3.3.2 implies $dk/dp < 0$. If p is restricted to $\mathbb{Z}$, we have $\cdots < k(1;\alpha) < k(0;\alpha) < k(-1;\alpha) < \cdots$, as desired.

To prove the third claim, first consider $p > 1$. Suppose $k(p;\alpha) \geq -p$. Since $\omega_\alpha(k)$ is odd and strictly increasing by Lemma 3.3.1,

$$\omega_\alpha(k(p;\alpha)) \geq -\,\omega_\alpha(p), \tag{3.42a}$$

$$\omega_\alpha(k(p;\alpha)+p) \geq \omega_\alpha(0) = 0. \tag{3.42b}$$

Using the definition of Ω_σ, $F(k(p;\alpha),p) = 0$ can be rewritten as

$$\omega_\alpha(k(p;\alpha)) + \omega_\alpha(k(p;\alpha)+p) = -\alpha c_0 p. \tag{3.43}$$

Together with (3.43), inequalities (3.42a) and (3.42b) imply

$$-\omega_\alpha(p) \leq -\alpha c_0 p \quad \Rightarrow \quad \frac{\omega_\alpha(p)}{p} \geq \alpha c_0 = \frac{\omega_\alpha(1)}{1}, \tag{3.44}$$

a contradiction since $\omega_\alpha(z)/z$ is strictly decreasing for $z > 0$. Therefore, $k(p;\alpha) < -p$ for $p > 1$. Since $\Omega_\sigma(k)$ is odd, $k(p;\alpha) = -k(-p;\alpha)$. Therefore, when $p < -1$, $k(p;\alpha) > -p$. Combining the two cases yields $|k(p;\alpha)| > |p|$ whenever $p \in \mathbb{Z} \setminus \{0, \pm 1\}$ and $c_0 > 0$, as desired. □

Lemma 3.3.3 has several consequences:

(i) When $c_0 > 0$, $k(p;\alpha) < 0$ for $p > 0$, and $k(p;\alpha) > 0$ for $p < 0$.

(ii) When $c_0 > 0$, $k(p;\alpha) \to \pm\infty$ as $p \to \mp\infty$. In fact, the sequence $\{k(p;\alpha)\}$ must grow at least linearly as $|p| \to \infty$. Formal arguments suggest quadratic growth in this limit.

(iii) Since $F_k(k,p) > 0$, we must have $c_{g_1}(k) \neq c_{g_{-1}}(k+p)$ for $p \in \mathbb{R}$, where $c_{g_\sigma}(k) = d\Omega_\sigma/dk$.

(iv) When $c_0 > 0$, we have $k(p;\alpha)(k(p;\alpha)+p) > 0$ and $\omega_\alpha(k(p;\alpha))\omega_\alpha(k(p;\alpha)+p) > 0$ for all $\alpha > 0$ and $p \in \mathbb{R}\setminus\{0\}$. The latter of these products is related to the Krein signature condition proposed in [67]. In effect, Lemma 3 provides an alternate proof that collided eigenvalues (3.32) have opposite Krein signatures, consistent with the results of [36].

Finally, we prove our main result:

Theorem 3.4.2. *Let* $c_0 > 0$*. If* $p \in \{0, \pm 1\}$*, then the collision condition* (3.35) *is not satisfied. If* $p \in \mathbb{Z} \setminus \{0, \pm 1\}$*, then* $k(p;\alpha)$ *solves the collision condition. Moreover,* $\cdots < \lambda_{i,3} < \lambda_{i,2} < 0 < \lambda_{i,-2} < \lambda_{i,-3} < \cdots$*, where* $\lambda_{i,p}$ *is the imaginary part of the collision point corresponding to* $k(p;\alpha)$*.*

Proof. When $p = 0$ or ± 1, we have $k(p;\alpha) = 0$ or ∓ 1, respectively, by inspection. It follows that $\Omega_1(k(p;\alpha)) = 0$ in all three cases, and so (3.35) is not satisfied. This proves the first claim.

To prove the second claim, consider the sequence $\{\Omega_1(k(p;\alpha))\}$, $p \in \mathbb{Z} \setminus \{0, \pm 1\}$. From Lemma 3.3.3, $\{k(p;\alpha)\}$ is a strictly decreasing sequence, and each element of this sequence satisfies $|k(p;\alpha)| > |p| > 1$. Thus, Lemma 3.3.2 holds, and the sequence $\{\Omega_1(k(p;\alpha))\}$ is strictly increasing. Since $\Omega_1(\pm 1) = 0$, we have $\Omega_1(k(p;\alpha)) \neq 0$. This proves that $k(p;\alpha)$ satisfies the collision condition (3.35) for the relevant values of p.

The proof of the third claim is immediate since $\{\Omega_1(k(p;\alpha))\}$ is strictly increasing. $\square$

The statement of Theorem 3.3.1 follows from the above if $\mu_0 = k(p;\alpha) - [k(p;\alpha)]$, $n = [k(p;\alpha)]$, and $m = p + n$, where $[\cdot]$ denotes the nearest integer function.

3.5 Asymptotic Description of the $p = 2$ *High-Frequency Instability*

We use perturbation methods to investigate the high-frequency instability that develops from the collision of $\lambda^{(1)}_{0,\mu_0,n}$ and $\lambda^{(-1)}_{0,\mu_0,m}$, where $\mu_0 \in [-1/2, 1/2]$ is the unique Floquet exponent for which (3.32) is satisfied and[3] $m - n = 2$. This instability corresponds to the high-frequency isola closest to the origin, per the statement of Theorem 3.3.1. For sufficiently small ε, this is also the isola with largest real component.

---

[3] Because the spectrum (3.30) has the symmetry $\overline{\lambda}^{(\sigma)}_{0,-\mu_0,-n} = \lambda^{(\sigma)}_{0,\mu_0,n}$, where the overbar denotes complex conjugation, choosing $p = -2$ gives the isola conjugate to that for $p = 2$. Thus, we may choose $p = 2$ without loss of generality.

3.5.1 The $\mathcal{O}\left(\varepsilon^0\right)$ Problem

The $p=2$ isola develops from the spectral data

$$\lambda_0 = \lambda^{(1)}_{0,\mu_0,n} = -i\Omega_1(\mu_0+n) = -i\Omega_{-1}(\mu_0+m) = \lambda^{(-1)}_{0,\mu_0,m} \neq 0, \tag{3.45a}$$

$$\mathbf{w_0}(x) = \begin{pmatrix} \mathfrak{h}_0(x) \\ \mathfrak{u}_0(x) \end{pmatrix} = \gamma_0 \begin{pmatrix} 1 \\ -\frac{\omega_\alpha(m+\mu_0)}{\alpha(m+\mu_0)} \end{pmatrix} e^{imx} + \gamma_1 \begin{pmatrix} 1 \\ \frac{\omega_\alpha(n+\mu_0)}{\alpha(n+\mu_0)} \end{pmatrix} e^{inx}, \tag{3.45b}$$

where γ_j are arbitrary, nonzero constants. As $|\varepsilon|$ increases, we assume the spectral data vary analytically with ε about (3.45):

$$\lambda = \lambda_0 + \varepsilon\lambda_1 + \varepsilon^2\lambda_2 + \mathcal{O}\left(\varepsilon^3\right), \tag{3.46a}$$

$$\mathbf{w} = \mathbf{w_0} + \varepsilon\mathbf{w_1} + \varepsilon^2\mathbf{w_2} + \mathcal{O}\left(\varepsilon^3\right) \tag{3.46b}$$

$$= \begin{pmatrix} \mathfrak{h}_0 \\ \mathfrak{u}_0 \end{pmatrix} + \varepsilon \begin{pmatrix} \mathfrak{h}_1 \\ \mathfrak{u}_1 \end{pmatrix} + \varepsilon^2 \begin{pmatrix} \mathfrak{h}_2 \\ \mathfrak{u}_2 \end{pmatrix} + \mathcal{O}\left(\varepsilon^3\right), \tag{3.46c}$$

where we suppress functional dependencies for ease of notation. We normalize $\mathbf{w}$ so that

$$\mathcal{F}_n[\mathfrak{h}] = \frac{1}{2\pi}\int_{-\pi}^{\pi} \mathfrak{h}e^{-inx}dx = 1, \tag{3.47}$$

or, alternatively, so that

$$\begin{aligned} &\mathcal{F}_n[\mathfrak{h}_0] = 1, \\ &\mathcal{F}_n[\mathfrak{h}_j] = 0, \quad \forall j \in \mathbb{N}. \end{aligned} \tag{3.48}$$

This normalization ensures that $\mathfrak{h}_0$ completely resolves the nth Fourier mode of $\mathfrak{h}$, a convenient choice for the perturbation calculations that follow. With this normalization,

$$\mathbf{w_0}(x) = \begin{pmatrix} \mathfrak{h}_0(x) \\ \mathfrak{u}_0(x) \end{pmatrix} = \gamma_0 \begin{pmatrix} 1 \\ -\frac{\omega_\alpha(m+\mu_0)}{\alpha(m+\mu_0)} \end{pmatrix} e^{imx} + \begin{pmatrix} 1 \\ \frac{\omega_\alpha(n+\mu_0)}{\alpha(n+\mu_0)} \end{pmatrix} e^{inx}. \tag{3.49}$$

The arbitrary constant γ_0 will be determined at higher order, leading to a unique expression for $\mathbf{w_0}$.

Similar to the Kawahara equation, we formally expand the Floquet exponent as a power series in ε:

$$\mu = \mu_0 + \varepsilon\mu_1 + \varepsilon^2\mu_2 + \mathcal{O}\left(\varepsilon^3\right). \tag{3.50}$$

As will be seen, $\mu_1 = 0$, and μ_2 is confined to an interval that parameterizes an ellipse asymptotic to the $p = 2$ isola.

Remark 3.5.1. *For ease of readability, select quantities in the subsections that follow are suppressed. If interested, consult the Mathematica file* hptbw_isolap2.nb *for these expressions.*

3.5.2 The $\mathcal{O}(\varepsilon)$ Problem

Substituting the expansions of the Stokes wave (3.14), spectral data (3.46), and Floquet exponent (3.50) into the spectral problem (3.27) and collecting terms of $\mathcal{O}(\varepsilon)$, we find

$$\left(\mathcal{L}_{\mu_0,0} - \lambda_0\right)\mathbf{w_1} = \lambda_1 \mathbf{w_0} - \mathcal{L}_1 \mathbf{w_0}, \tag{3.51}$$

where

$$\mathcal{L}_1 = \alpha \begin{pmatrix} -u_{1,x} + ic_0\mu_1 - u_1(i\mu_0 + \partial_x) & -\eta_{1,x} - i\mu_1 - \eta_1(i\mu_0 + \partial_x) \\ -i\mu_1 \operatorname{sech}^2(\alpha(\mu_0 + D)) & -u_{1,x} + ic_0\mu_1 - u_1(i\mu_0 + \partial_x) \end{pmatrix}. \tag{3.52}$$

The inhomogeneous terms on the RHS of (3.51) can be evaluated using expressions for η_1, u_1, and $\mathbf{w_0}$. Each of these quantities are finite linear combinations of 2π-periodic sinusoids. As a result, the inhomogeneous terms can be rewritten as a finite Fourier series, and (3.51) becomes

$$\left(\mathcal{L}_{\mu_0,0} - \lambda_0\right)\mathbf{w_1} = \sum_{j=n-1}^{m+1} \mathbf{T_{1,j}} e^{ijx}, \tag{3.53}$$

where $\mathbf{T_{1,j}}$ depend on μ_0, α, and γ_0, see the Mathematica file for details.

Remark 3.5.2. *Since $m - n = 2$, the index $j \in \{n-1, n, 1+n, m, m+1\}$. When evaluating the inhomogeneous terms, one finds vector multiples of exp$(i(1+n)x)$ and exp$(i(m-1)x)$. These vectors are combined to give $\mathbf{T_{1,1+n}}$.*

For (3.53) to have a solution $\mathbf{w_1}$, the inhomogeneous terms must be orthogonal (in the $\mathrm{L}^2_{\mathrm{per}}(-\pi,\pi) \times \mathrm{L}^2_{\mathrm{per}}(-\pi,\pi)$ sense) to the nullspace of the hermitian adjoint of $\mathcal{L}_{\mu_0,0} - \lambda_0$ by the Fredholm alternative. The hermitian adjoint of $\mathcal{L}_{\mu_0,0} - \lambda_0$ is

$$\left(\mathcal{L}_{\mu_0,0} - \lambda_0\right)^\dagger = \begin{pmatrix} -\alpha c_0(i\mu_0 + \partial_x) - \overline{\lambda_0} & \tan(\alpha(i\mu_0 + \partial_x)) \\ \alpha(i\mu_0 + \partial_x) & -\alpha c_0(i\mu_0 + \partial_x) - \overline{\lambda_0} \end{pmatrix}, \tag{3.54}$$

where overbars denote complex conjugation. Its nullspace is

$$\text{Null}\left[\left(\mathcal{L}_{\mu_0,0} - \lambda_0\right)^\dagger\right] = \text{Span}\left[\begin{pmatrix} 1 \\ \frac{\alpha(\mu_0+n)}{\omega_\alpha(\mu_0+n)} \end{pmatrix} e^{inx}, \begin{pmatrix} 1 \\ -\frac{\alpha(\mu_0+m)}{\omega_\alpha(\mu_0+m)} \end{pmatrix} e^{imx}\right]. \tag{3.55}$$

Thus, according to the Fredholm alternative, there exists a solution $\mathbf{w_1}$ to (3.53) if

$$\left\langle \begin{pmatrix} 1 \\ \frac{\alpha(\mu_0+n)}{\omega_\alpha(\mu_0+n)} \end{pmatrix} e^{inx}, \mathbf{T_{1,n}} e^{inx} \right\rangle = 0, \quad \left\langle \begin{pmatrix} 1 \\ -\frac{\alpha(\mu_0+m)}{\omega_\alpha(\mu_0+m)} \end{pmatrix} e^{imx}, \mathbf{T_{1,m}} e^{imx} \right\rangle = 0, \tag{3.56}$$

where $\langle \cdot, \cdot \rangle$ is the standard inner product on $\mathrm{L}^2_{\text{per}}(-\pi,\pi) \times \mathrm{L}^2_{\text{per}}(-\pi,\pi)$. Substituting expressions for $\mathbf{T_{1,n}}$ and $\mathbf{T_{1,m}}$ in the above gives solvability conditions

$$\lambda_1 + i\mu_1 c_{g_1}(\mu_0 + n) = 0, \tag{3.57a}$$

$$\gamma_0\left(\lambda_1 + i\mu_1 c_{g_{-1}}(\mu_0 + m)\right) = 0, \tag{3.57b}$$

where $c_{g_\sigma}(k) = d\Omega_\sigma/dk$ is the group velocity of Ω_σ. A consequence of Lemma 3.3.3 shows that $c_{g_1}(\mu_0 + n) \neq c_{g_{-1}}(\mu_0 + m)$. Since γ_0 is nonzero,

$$\lambda_1 = 0 = \mu_1. \tag{3.58}$$

Consequently, $\mathbf{T_{1,n}} = \mathbf{0} = \mathbf{T_{1,m}}$, simplifying the inhomogeneous terms in (3.53).

With the solvability conditions satisfied, we solve for the particular solution of $\mathbf{w_1}$ in (3.53). Combining with the nullspace of $\mathcal{L}_{\mu_0,0} - \lambda_0$,

$$\mathbf{w_1} = \sum_{\substack{j=n-1 \\ j\neq n,m}}^{m+1} \mathcal{W}_{\mathbf{1,j}} e^{ijx} + \beta_{1,m} \begin{pmatrix} 1 \\ -\dfrac{\omega_\alpha(m+\mu_0)}{\alpha(m+\mu_0)} \end{pmatrix} e^{imx} + \beta_{1,n} \begin{pmatrix} 1 \\ \dfrac{\omega_\alpha(n+\mu_0)}{\alpha(n+\mu_0)} \end{pmatrix} e^{inx}, \tag{3.59}$$

where $\beta_{1,j}$ are arbitrary constants and $\mathcal{W}_{\mathbf{1,j}}$ are found in the Mathematica file. Enforcing the normalization condition (3.48), one finds $\beta_{1,n} = 0$. For ease of notation, let $\beta_{1,m} \to \gamma_1$ so that

$$\mathbf{w_1} = \sum_{\substack{j=n-1\\ j\neq n,m}}^{m+1} \mathcal{W}_{\mathbf{1,j}} e^{ijx} + \gamma_1 \begin{pmatrix} 1 \\ -\dfrac{\omega_\alpha(m+\mu_0)}{\alpha(m+\mu_0)} \end{pmatrix} e^{imx}. \tag{3.60}$$

3.5.3 The $\mathcal{O}\left(\varepsilon^2\right)$ Problem

Using (3.58), the spectral problem (3.27) at $\mathcal{O}\left(\varepsilon^2\right)$ is

$$\left(\mathcal{L}_{\mu_0,0} - \lambda_0\right)\mathbf{w_2} = \lambda_2 \mathbf{w_0} - \mathcal{L}_2|_{\mu_1=0}\mathbf{w_0} - \mathcal{L}_1|_{\mu_1=0}\mathbf{w_1}, \tag{3.61}$$

where $\mathcal{L}_1|_{\mu_1=0}$ is the same as above, but evaluated at $\mu_1 = 0$, and

$$\mathcal{L}_2|_{\mu_1=0} = \alpha \begin{pmatrix} -u_{2,x} + (c_2 - u_2)(i\mu_0 + \partial_x) + i\mu_2 c_0 & -\eta_{2,x} - i\mu_2 - \eta_2(i\mu_0 + \partial_x) \\ -i\mu_2 \operatorname{sech}^2(\alpha(\mu_0 + D)) & -u_{2,x} + (c_2 - u_2)(i\mu_0 + \partial_x) + i\mu_2 c_0 \end{pmatrix}. \tag{3.62}$$

One can evaluate the inhomogeneous terms of (3.62) using η_j, u_j, and $\mathbf{w_{j-1}}$ for $j \in \{1, 2\}$. These inhomogeneous terms can be expressed as a finite Fourier series, giving

$$\left(\mathcal{L}_{\mu_0,0} - \lambda_0\right)\mathbf{w_2} = \sum_{\substack{j=n-2\\ j\neq n-1}}^{m+2} \mathbf{T_{2,j}} e^{ijx}. \tag{3.63}$$

It can be shown that $\mathbf{T_{2,n-1}} = \mathbf{0}$.

Proceeding similarly to the previous order, solvability conditions for (3.63) become

$$2\left(\lambda_2 + i\mathcal{C}_{1,n}\right) + i\gamma_0 \mathcal{S}_{2,n} = 0, \tag{3.64a}$$

$$2\gamma_0\left(\lambda_2 + i\mathcal{C}_{-1,m}\right) + i\mathcal{S}_{2,m} = 0, \tag{3.64b}$$

where

$$\mathcal{C}_{1,n} = \mu_2 c_{g_1}(\mu_0 + n) - \mathcal{P}_{2,n}, \tag{3.65a}$$

$$\mathcal{C}_{-1,m} = \mu_2 c_{g_{-1}}(\mu_0 + m) - \mathcal{P}_{2,m}. \tag{3.65b}$$

Expressions for $\mathcal{S}_{2,j}$ and $\mathcal{P}_{2,j}$ have no dependence on γ_0, γ_1, μ_2, or λ_2, see the Mathematica file for details.

Conditions (3.64a) and (3.64b) are a nonlinear system for γ_0 and λ_2. Solving for λ_2 yields

$$\lambda_2 = -i\left(\frac{\mathcal{C}_{-1,m}+\mathcal{C}_{1,n}}{2}\right) \pm \sqrt{-\left(\frac{\mathcal{C}_{-1,m}-\mathcal{C}_{1,n}}{2}\right)^2 - \frac{\mathcal{S}_{2,n}\mathcal{S}_{2,m}}{4}}. \tag{3.66}$$

A direct calculation shows that

$$\mathcal{S}_{2,n}\mathcal{S}_{2,m} = -\frac{\mathcal{S}_2^2}{\omega_\alpha(\mu_0+m)\omega_\alpha(\mu_0+n)}, \tag{3.67}$$

where $\mathcal{S}_2$ is given in the Mathematica file. Then,

$$\lambda_2 = -i\left(\frac{\mathcal{C}_{-1,m}+\mathcal{C}_{1,n}}{2}\right) \pm \sqrt{-\left(\frac{\mathcal{C}_{-1,m}-\mathcal{C}_{1,n}}{2}\right)^2 + \frac{\mathcal{S}_2^2}{4\omega_\alpha(\mu_0+m)\omega_\alpha(\mu_0+n)}}. \tag{3.68}$$

A consequence of Lemma 3.3.3 ensures that $\omega_\alpha(\mu_0+m)\omega_\alpha(\mu_0+n) > 0$, consistent with the Krein condition of MacKay and Saffman [67]. Provided $\mathcal{S}_2 \neq 0$ and, λ_2 has nonzero real part for $\mu_2 \in (M_{2,-}, M_{2,+})$, where

$$\begin{aligned} M_{2,\pm} = {} & \frac{\mathcal{P}_{2,m}-\mathcal{P}_{2,n}}{c_{g_{-1}}(\mu_0+m)-c_{g_1}(\mu_0+n)} \\ & \pm \frac{|\mathcal{S}_2|}{|c_{g_{-1}}(\mu_0+m)-c_{g_1}(\mu_0+n)|\sqrt{\omega_\alpha(\mu_0+m)\omega_\alpha(\mu_0+n)}}. \end{aligned} \tag{3.69}$$

That $c_{g_{-1}}(\mu_0+m) \neq c_{g_1}(\mu_0+n)$ follows from Lemma 3.3.3, as mentioned previously. A plot of $\mathcal{S}_2$ as a function of α suggests that $\mathcal{S}_2 > 0$ for all values of $\alpha > 0$ (Figure 3.1). We conjecture that HPBW Stokes waves of any wavenumber are susceptible to a $p = 2$ high-frequency instability at $\mathcal{O}(\varepsilon^2)$.

For $\mu_2 \in (M_{2,-}, M_{2,+})$, a quick calculation shows that (3.68) parameterizes an ellipse asymptotic to the numerically observed $p = 2$ high-frequency isola (Figure 3.2). The ellipse has semi-major and -minor axes that scale with ε^2, and the center of the ellipse drifts along the imaginary axis like ε^2 from λ_0, the collision point at $\varepsilon = 0$. The midpoint of $(M_{2,-}, M_{2,+})$ maximizes the real part of λ_2. Thus, the most unstable spectral element of the isola has Floquet exponent

$$\mu_* = \mu_0 + \left(\frac{\mathcal{P}_{2,m}-\mathcal{P}_{2,n}}{c_{g_{-1}}(\mu_0+m)-c_{g_1}(\mu_0+n)}\right)\varepsilon^2 + \mathcal{O}\left(\varepsilon^3\right), \tag{3.70}$$

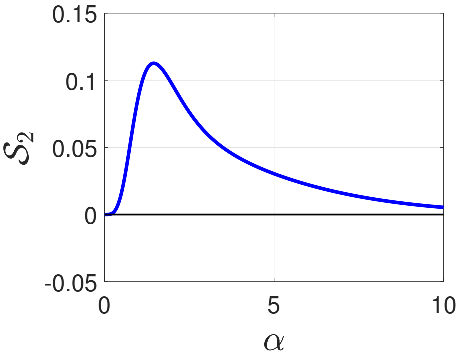

Figure 3.1: A plot of $\mathcal{S}_2$ vs. α. No roots of $\mathcal{S}_2$ are found for $\alpha > 0$. It is likely that HPBW Stokes waves of all wavenumbers experience a $p = 2$ instability.

and its real and imaginary components are

$$\lambda_{r,*} = \left(\frac{|\mathcal{S}_2|}{2\sqrt{\omega_\alpha(\mu_0 + m)\omega_\alpha(\mu_0 + n)}} \right) \varepsilon^2 + \mathcal{O}\left(\varepsilon^3\right), \tag{3.71a}$$

$$\lambda_{i,*} = -\Omega_1(\mu_0 + n) - \mathcal{C}_{1,n}\varepsilon^2 + \mathcal{O}\left(\varepsilon^3\right), \tag{3.71b}$$

respectively. These expansions agree well with results of the FFH method, see Figure 3.3 for more details.

3.6 Asymptotic Description of the $p = 3$ *High-Frequency Instability*

According to Theorem 3.3.1, the $p = 3$ high-frequency instability is the second-closest to the origin. As will be seen, this instability arises at $\mathcal{O}\left(\varepsilon^3\right)$. Let μ_0 correspond to the unique Floquet exponent in $[-1/2, 1/2]$ that satisfies the collision condition (3.32) with $m - n = 3$. Then, the spectral data (3.45) give rise to the $p = 3$ high-frequency instability. We assume these data and the Floquet exponent vary analytically with ε. For uniqueness, we normalize the eigenfunction $\mathbf{w}$ according to (3.48) so that $\mathbf{w_0}$ is given by (3.49). We proceed as in the $p = 2$ case.

Remark 3.6.1. *In the calculations that follow, explicit expressions of select quantities are*

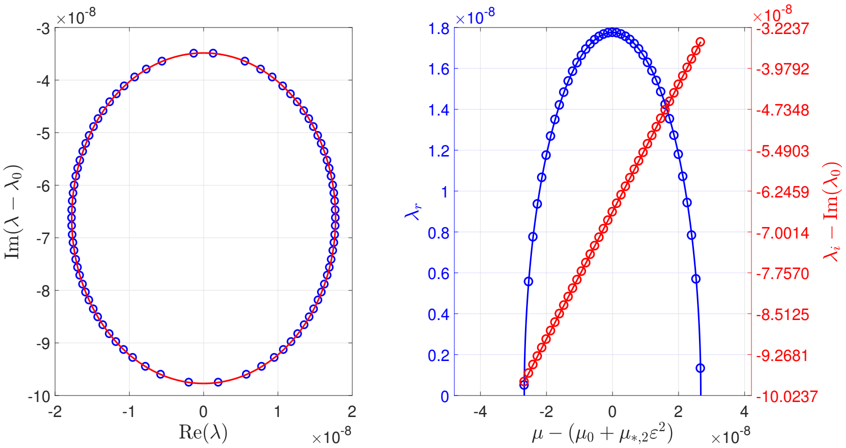

Figure 3.2: (Left) The $p = 2$ isola with $\alpha = 1$ and $\varepsilon = 5 \times 10^{-4}$ (zero-order imaginary correction removed for better visibility). The solid red curve is the ellipse obtained by our perturbation calculations. Blue circles are a subset of spectral elements from the numerically computed isola using the FFH method. (Right) The Floquet parameterization of the real (blue) and imaginary (red) components of the isola (zero- and second-order Floquet corrections and zero-order imaginary correction removed for better visibility). Solid curves illustrate perturbation results. Circles indicate the FFH method results.

suppressed for ease of readability. If interested, consult the Mathematica file hptbw_isolap3.nb *for these expressions.*

3.6.1 The $\mathcal{O}(\varepsilon)$ Problem

Substituting expansions (3.14), (3.46), and (3.50) into the spectral problem (3.27), equating terms of $\mathcal{O}(\varepsilon)$, and using expression for η_1, u_1, and $\mathbf{w_0}$ to simplify, we find

$$\left(\mathcal{L}_{\mu_0,0} - \lambda_0\right)\mathbf{w_1} = \sum_{j=n-1}^{m+1} \mathbf{T_{1,j}} e^{ijx}. \tag{3.72}$$

Expressions for $\mathbf{T_{1,j}}$ depend on μ_0, α, and γ_0, see the Mathematica file. Since $m - n = 3$, $j \in \{n-1, n, 1+n, m-1, m, m+1\}$. The expressions for $\mathbf{T_{1,n-1}}$ and $\mathbf{T_{1,m+1}}$ are identical to those in the $p = 2$ case, but they do not evaluate to the same vectors, as μ_0 is different for $p = 2$ and $p = 3$ in general.

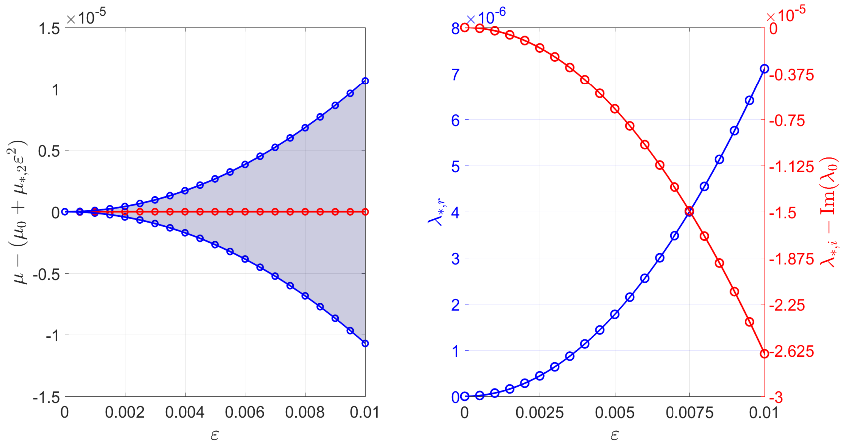

Figure 3.3: (Left) The interval of Floquet exponents that parameterize the $p = 2$ isola as a function of ε with $\alpha = 1$ (zero- and second-order Floquet corrections removed for better visibility). Solid blue curves indicate the boundaries of this interval according to our perturbation calculations. Blue circles indicate the boundaries computed numerically by the FFH method. The solid red curve gives the Floquet exponent corresponding to the most unstable spectral element of the isola according to our perturbation calculations. Red circles indicate the same but computed numerically using the FFH method. (Right) The real (blue) and imaginary (red) components of the most unstable spectral element of the isola as a function of ε (zero-order imaginary correction removed for better visibility). Solid curves illustrate perturbation calculations. Circles illustrate the FFH method results.

Solvability conditions for (3.72) simplify to $\mu_1 = 0 = \lambda_1$. Together with the normalization (3.48), these conditions guarantee a solution to (3.72) of the form

$$\mathbf{w_1} = \sum_{\substack{j=n-1 \\ j\neq n,m}}^{m+1} \mathcal{W}_{\mathbf{1,j}} e^{ijx} + \gamma_1 \begin{pmatrix} 1 \\ -\dfrac{\omega_\alpha(m+\mu_0)}{\alpha(m+\mu_0)} \end{pmatrix} e^{imx}, \tag{3.73}$$

where γ_1 is arbitrary and expressions for $\mathcal{W}_{\mathbf{1,j}}$ are found in the Mathematica file. Because $\mathbf{T_{1,n-1}}$ and $\mathbf{T_{1,m+1}}$ are identical to their $p = 2$ counterparts, $\mathcal{W}_{\mathbf{1,n-1}}$ and $\mathcal{W}_{\mathbf{1,m+1}}$ are as well.

3.6.2 The $\mathcal{O}\left(\varepsilon^2\right)$ Problem

The $\mathcal{O}\left(\varepsilon^2\right)$ problem takes the same form as (3.61). Evaluating at η_j, u_j, and $\mathbf{w_{j-1}}$ for $j \in \{1,2\}$, we find

$$\left(\mathcal{L}_{\mu_0,0} - \lambda_0\right)\mathbf{w_2} = \sum_{\substack{j=n-2 \\ j\neq n-1}}^{m+2} \mathbf{T_{2,j}} e^{ijx}, \tag{3.74}$$

For the same reasons as in the $p=2$ case, $\mathbf{T_{2,n-1}} = \mathbf{0}$, and expressions for $\mathbf{T_{2,n-2}}$ and $\mathbf{T_{2,m+2}}$ are identical to their $p=2$ counterparts.

Since $\gamma_0 \neq 0$, the solvability conditions for (3.74) simplify to

$$\lambda_2 + i\mu_2 c_{g_1}(\mu_0+n) - i\mathcal{P}_{2,n} = 0, \tag{3.75a}$$

$$\lambda_2 + i\mu_2 c_{g_{-1}}(\mu_0+m) - i\mathcal{P}_{2,m} = 0, \tag{3.75b}$$

where $\mathcal{P}_{2,j}$ are independent of λ_2, μ_2, γ_0, and γ_1, see the Mathematica file. Note that these terms are distinct from those introduced in (3.65).

Solving (3.75a) and (3.75b) for λ_2 and μ_2 yields

$$\lambda_2 = -i\left(\frac{\mathcal{P}_{2,m}c_{g_1}(\mu_0+n) - \mathcal{P}_{2,n}c_{g_{-1}}(\mu_0+m)}{c_{g_{-1}}(\mu_0+m) - c_{g_1}(\mu_0+n)}\right), \tag{3.76a}$$

$$\mu_2 = \frac{\mathcal{P}_{2,m} - \mathcal{P}_{2,n}}{c_{g_{-1}}(\mu_0+m) - c_{g_1}(\mu_0+n)}. \tag{3.76b}$$

Therefore, the spectral elements and Floquet parameterization of the $p=3$ isola have nontrivial corrections at $\mathcal{O}\left(\varepsilon^2\right)$. However, since $\mathrm{Re}\left(\lambda_2\right) = 0$, we have not yet determined the leading-order behavior of the isola. We find this at the next order.

Imposing solvability conditions (3.75a) and (3.75b) as well as the normalization condition on $\mathbf{w_2}$, the solution of (3.74) is

$$\mathbf{w_2} = \sum_{\substack{j=n-2 \\ j\neq n-1}}^{m+1} \mathcal{W}_{\mathbf{2,j}} e^{ijx} + \gamma_2 \begin{pmatrix} 1 \\ -\dfrac{\omega_\alpha(m+\mu_0)}{\alpha(m+\mu_0)} \end{pmatrix} e^{imx}, \tag{3.77}$$

where γ_2 is an arbitrary constant. Since $\mathbf{T_{2,n-1}} = \mathbf{0}$, $\mathcal{W}_{\mathbf{2,n-1}} = \mathbf{0}$.

3.6.3 The $\mathcal{O}\left(\varepsilon^3\right)$ Problem

At $\mathcal{O}\left(\varepsilon^3\right)$, the spectral problem (3.27) takes the form

$$\left(\mathcal{L}_{\mu_0,0}-\lambda_0\right)\mathbf{w_3}=\sum_{j=2}^{3}\lambda_j\mathbf{w_{3-j}}-\sum_{j=1}^{3}\mathcal{L}_j|_{\mu_1=0}\mathbf{w_{3-j}}, \tag{3.78}$$

where $\mathcal{L}_j|_{\mu_1=0}$ for $j\in\{1,2\}$ are as before and

$$\mathcal{L}_3|_{\mu_1=0}=\alpha\begin{pmatrix}-u_{3,x}-i\mu_2u_1-u_3(i\mu_0+\partial_x)+i\mu_3c_0 & -\eta_{3,x}-i\mu_3-i\eta_1\mu_2-\eta_3(i\mu_0+\partial_x)\\ -\mu_3\operatorname{sech}^2(\alpha(\mu_0+D)) & u_{3,x}-i\mu_2u_1-u_3(i\mu_0+\partial_x)+i\mu_3c_0\end{pmatrix}. \tag{3.79}$$

Evaluating (3.78) at η_j, u_j, and $\mathbf{w_{j-1}}$ for $j\in\{1,2,3\}$, one finds

$$\left(\mathcal{L}_{\mu_0,0}-\lambda_0\right)\mathbf{w_3}=\sum_{\substack{j=n-3\\ j\neq n-2}}^{m+3}\mathbf{T_{3,j}}e^{ijx}, \tag{3.80}$$

where $\mathbf{T_{3,n-2}}=\mathbf{0}$.

The solvability conditions for (3.80) are

$$2(\lambda_3+i\mu_3c_{g_1}(\mu_0+n))+i\gamma_0\mathcal{S}_{3,n}=0, \tag{3.81a}$$

$$2\gamma_0(\lambda_3+i\mu_3c_{g_{-1}}(\mu_0+m))+i\mathcal{S}_{3,m}+i\gamma_1\mathcal{T}_{3,m}=0, \tag{3.81b}$$

where $\mathcal{S}_{3,j}$ and $\mathcal{T}_{3,m}$ have no dependence on γ_0, γ_1, μ_3, or λ_3; see Mathematica file. Using (3.75a) and (3.75b) from the previous order as well as (3.32), one can show that $\mathcal{T}_{3,m}\equiv 0$. In addition, similar to (3.67) for the $p=2$ isola, we have

$$\mathcal{S}_{3,n}\mathcal{S}_{3,m}=-\frac{\mathcal{S}_3^2}{\omega_\alpha(\mu_0+m)\omega_\alpha(\mu_0+n)}, \tag{3.82}$$

where $\mathcal{S}_3$ is given in the Mathematica file. As a result, (3.81a) and (3.81b) form a nonlinear system for λ_3 and γ_0. Solving for λ_3, one finds

$$\begin{aligned}\lambda_3=&-i\mu_3\left(\frac{c_{g_{-1}}(\mu_0+m)+c_{g_1}(\mu_0+n)}{2}\right)\\ &\pm\sqrt{-\mu_3^2\left(\frac{c_{g_{-1}}(\mu_0+m)-c_{g_1}(\mu_0+n)}{2}\right)^2+\frac{\mathcal{S}_3^2}{4\omega_\alpha(\mu_0+m)\omega_\alpha(\mu_0+n)}}.\end{aligned} \tag{3.83}$$

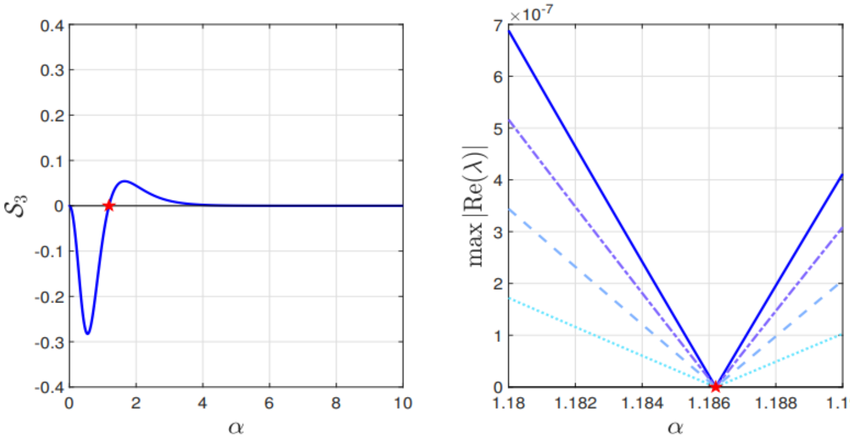

Figure 3.4: (Left) A plot of $\mathcal{S}_3$ vs. α. The quantity $\mathcal{S}_3$ has a root $\alpha = 1.1862...$ (red star), implying HPBT–BW Stokes waves of this aspect ratio do not have a $p = 3$ instability at $\mathcal{O}(\varepsilon^3)$. (Right) A plot of the maximum real component of the numerical $p = 3$ isola (computed by the FFH method) as a function of α for $\varepsilon = 10^{-3}$ (solid blue), $\varepsilon = 7.5 \times 10^{-4}$ (dot-dashed purple), $\varepsilon = 5 \times 10^{-4}$ (dashed light blue), and $\varepsilon = 2.5 \times 10^{-4}$ (dotted cyan). The $p = 3$ isola vanishes when $\alpha = 1.1862...$ (red star).

As in the $p = 2$ case, $\omega_\alpha(\mu_0 + m)\omega_\alpha(\mu_0 + n) > 0$ and $c_{g_{-1}}(\mu_0 + m) \neq c_{g_1}(\mu_0 + n)$. Provided $\mathcal{S}_3 \neq 0$, λ_3 has nonzero real part if $\mu_3 \in (-M_3, M_3)$, where

$$M_3 = \frac{|\mathcal{S}_3|}{|c_{g_{-1}}(\mu_0 + m) - c_{g_1}(\mu_0 + n)|\sqrt{\omega_\alpha(\mu_0 + m)\omega_\alpha(\mu_0 + n)}}. \tag{3.84}$$

A plot of $\mathcal{S}_3$ vs. α reveals that $\mathcal{S}_3 \neq 0$ for almost all $\alpha > 0$, except $\alpha = 1.1862...$ (Figure 3.4). For this aspect ratio, the $p = 3$ instability does not occur at $\mathcal{O}(\varepsilon^3)$. In fact, Figure 3.4 shows that, if α approaches 1.1862.... for fixed ε, the numerical $p = 3$ isola shrinks to a point on the imaginary axis. We conjecture that HPBW Stokes waves with aspect ratio $\alpha = 1.1862...$ do not have a $p = 3$ instability, even beyond $\mathcal{O}(\varepsilon^3)$. Indeed, in the next subsection, we find that λ_4 is purely imaginary, so Stokes waves with aspect ratio $\alpha = 1.1862...$ do not exhibit $p = 3$ instabilities to at least $\mathcal{O}(\varepsilon^4)$.

Assuming $\alpha \neq 1.1862...$, $\mu_3 \in (-M_3, M_3)$ parameterizes an ellipse asymptotic to the $p = 3$ high-frequeny isola; see Figure 3.5. The ellipse has semi-major and -minor axes that scale with ε^3. The center of this ellipse drifts along the imaginary axis like ε^2 due to the

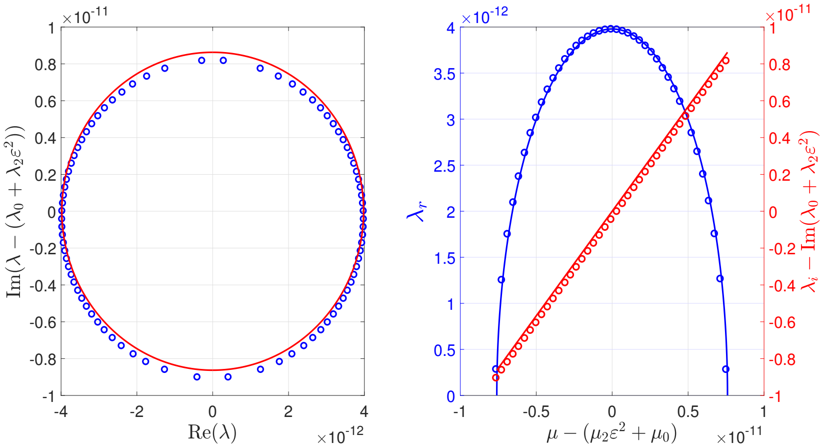

Figure 3.5: (Left) The $p = 3$ isola with $\alpha = 1$ and $\varepsilon = 5 \times 10^{-4}$ (zero- and second-order imaginary corrections removed for better visibility). The solid red curve is the ellipse obtained by our perturbation calculations. The blue circles are a subset of spectral elements from the numerically computed isola using the FFH method. (Right) Floquet parameterization of the real (blue) and imaginary (red) components of the isola (zero- and second-order imaginary and Floquet corrections removed for better visibility). Solid curves illustrate perturbation results. Circles indicate the FFH method results.

purely imaginary correction found at $\mathcal{O}\left(\varepsilon^2\right)$.

The interval of Floquet exponents that parameterizes the $p = 3$ isola is

$$\mu \in \left(\mu_0 + \mu_2\varepsilon^2 - M_3\varepsilon^3, \mu_0 + \mu_2\varepsilon^2 + M_3\varepsilon^3\right) + \mathcal{O}\left(\varepsilon^4\right). \tag{3.85}$$

The width of this interval is an order of magnitude smaller than that of the $p = 2$ isola. Consequently, the $p = 3$ isola is more challenging to find numerically than the $p = 2$ isola for methods like FFH (Table 3.1).

For $\alpha = 1$ and $|\varepsilon| < 5 \times 10^{-4}$, equation (3.85) provides an excellent approximation to the numerically computed interval of Floquet exponents (Figure 3.6). Fourth-order corrections are necessary to improve agreement between (3.85) and numerical computations for larger ε; see Subsection 5.4 below.

Choosing $\mu_2 = 0$ maximizes the real part of λ_3. Thus, the most unstable spectral element

Table 3.1: Intervals of Floquet exponents that parameterize the $p = 2$ and $p = 3$ high-frequency isolas with $\varepsilon = 10^{-3}$ and $\alpha = 1/2, 1$, and 2. The first digit for which the boundary values disagree is underlined and colored red. If a uniform mesh of Floquet exponents in $[-1/2, 1/2]$ is used for numerical methods like the FFH method, the spacing of the mesh must be finer than ε^2 to capture the $p = 2$ instability and ε^3 to capture the $p = 3$ instability. The intervals vary with α as well, making it difficult to adapt and refine a uniform mesh to find high-frequency isolas.

	$p = 2$
$\alpha = \frac{1}{2}$	(-0.106478**8**13547533, -0.106478**6**33575956)
$\alpha = 1$	(-0.260909**9**131823605, -0.26090**8**917941151)
$\alpha = 2$	(-0.330352**1**96060556, -0.330352**2**75321770)

	$p = 3$
$\alpha = \frac{1}{2}$	(-0.37544887**7**009085, -0.37544887**5**412116)
$\alpha = 1$	(0.257196721**1**00572, 0.257196721**3**43587)
$\alpha = 2$	(0.0440583313**4**6416, 0.0440583313**8**4758)

of the $p = 3$ isola has Floquet exponent

$$\mu_* = \mu_0 + \left(\frac{\mathcal{P}_{2,m} - \mathcal{P}_{2,n}}{c_{g_{-1}}(\mu_0 + m) - c_{g_1}(\mu_0 + n)} \right) \varepsilon^2 + \mathcal{O}\left(\varepsilon^4\right), \tag{3.86}$$

and its real and imaginary components are

$$\lambda_{r,*} = \left(\frac{|\mathcal{S}_3|}{2\sqrt{\omega_\alpha(\mu_0 + m)\omega_\alpha(\mu_0 + n)}} \right) \varepsilon^3 + \mathcal{O}\left(\varepsilon^4\right), \tag{3.87a}$$

$$\lambda_{i,*} = -\Omega_1(\mu_0 + n) - \left(\frac{\mathcal{P}_{2,m} c_{g_1}(\mu_0 + n) - \mathcal{P}_{2,n} c_{g_{-1}}(\mu_0 + m)}{c_{g_{-1}}(\mu_0 + m) - c_{g_1}(\mu_0 + n)} \right) \varepsilon^2 + \mathcal{O}\left(\varepsilon^4\right), \tag{3.87b}$$

respectively. The expansion for $\lambda_{r,*}$ is in excellent agreement with numerical results using the FFH method (Figure 3.6). As with (3.85), corrections to μ_* and $\lambda_{i,*}$ at $\mathcal{O}(\varepsilon^4)$ improve the agreement between numerical and asymptotic results for these quantities.

Before proceeding to $\mathcal{O}(\varepsilon^4)$, we solve (3.80) for $\mathbf{w_3}$, assuming solvability conditions

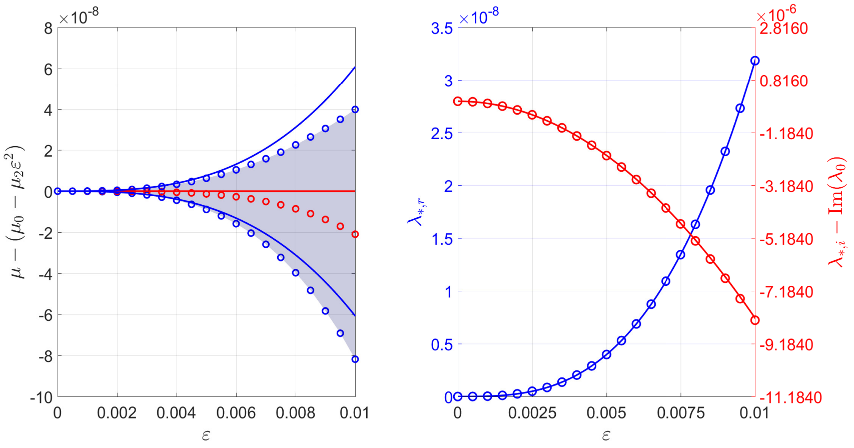

Figure 3.6: (Left) The interval of Floquet exponents that parameterize the $p = 3$ isola as a function of ε with $\alpha = 1$ (zero- and second-order Floquet corrections removed for better visibility). Solid blue curves indicate the boundaries of this interval according to our perturbation calculations. Blue circles indicate the boundaries computed numerically by the FFH method. The solid red curve gives the Floquet exponent corresponding to the most unstable spectral element of the isola according to our perturbation calculations. Red circles indicate the same but computed numerically using the FFH method. (Right) The real (blue) and imaginary (red) components of the most unstable spectral element of the isola as a function of ε (zero- and second-order imaginary and Floquet corrections removed for better visibility). Solid curves illustrate perturbation calculations. Circles illustrate the FFH method results.

(3.75a) and (3.75b) and normalization condition (3.48) are satisfied. We find

$$\mathbf{w_3} = \sum_{\substack{j=n-3 \\ j\neq n-2}}^{m+3} \mathcal{W}_{\mathbf{3,j}} e^{ijx} + \gamma_3 \begin{pmatrix} 1 \\ -\frac{\omega_\alpha(m+\mu_0)}{\alpha(m+\mu_0)} e^{imx} \end{pmatrix}, \tag{3.88}$$

where γ_3 is arbitrary and $\mathcal{W}_{\mathbf{3,n-2}} = \mathbf{0}$ (since $\mathbf{T_{3,n-2}} = \mathbf{0}$).

3.6.4 The $\mathcal{O}(\varepsilon^4)$ Problem

At $\mathcal{O}(\varepsilon^4)$, the spectral problem (3.27) is

$$(\mathcal{L}_{\mu_0,0} - \lambda_0)\,\mathbf{w_4} = \sum_{j=2}^{4} \lambda_j \mathbf{w_{3-j}} - \sum_{j=1}^{4} \mathcal{L}_j|_{\mu_1=0}\mathbf{w_{3-j}}, \tag{3.89}$$

where $\mathcal{L}_j|_{\mu_1=0}$ are as before and

$$\mathcal{L}_4|_{\mu_1=0} = \alpha \begin{pmatrix} \mathcal{L}_4^{(1,1)} & \mathcal{L}_4^{(1,2)} \\ \mathcal{L}_4^{(2,1)} & \mathcal{L}_4^{(1,1)} \end{pmatrix}, \tag{3.90}$$

where

$$\mathcal{L}_4^{(1,1)} = ic_0\mu_4 - i\mu_3 u_1 + i\mu_2(c_2 - u_2) + (c_4 - u_4)(i\mu_0 + \partial_x) - u_{4,x}, \tag{3.91a}$$

$$\mathcal{L}_4^{(1,2)} = -i\mu_4 - i\mu_3\eta_1 - i\mu_2\eta_2 - \eta_4(i\mu_0 + \partial_x) - \eta_{4,x}, \tag{3.91b}$$

$$\mathcal{L}_4^{(2,1)} = -i\mu_4 \operatorname{sech}^2(\alpha(\mu_0 + D)) + i\alpha\mu_2^2 \operatorname{sech}(\alpha(\mu_0 + D)) \tanh(\alpha(\mu_0 + D)). \tag{3.91c}$$

Substituting η_j, u_j, and $\mathbf{w_{j-1}}$ for $j \in \{1, 2, 3\}$ into (3.89), we find

$$(\mathcal{L}_{\mu_0,0} - \lambda_0)\, \mathbf{w_4} = \sum_{\substack{j=n-4 \\ j\neq n-3}}^{m+4} \mathbf{T_{4,j}} e^{ijx}, \tag{3.92}$$

where $\mathbf{T_{4,n-3}} = \mathbf{0}$ (since $\mathcal{W}_{\mathbf{3,n-2}} = \mathbf{0}$).

The solvability conditions for (3.92) can be expressed as

$$\begin{pmatrix} 2 & i\mathcal{S}_{3,n} \\ 2\gamma_0 & 2(\lambda_3 + i\mu_3 c_{g_{-1}}(\mu_0 + m)) \end{pmatrix} \begin{pmatrix} \lambda_4 \\ \gamma_1 \end{pmatrix} + i\gamma_2 \begin{pmatrix} 0 \\ \mathcal{T}_{4,m} \end{pmatrix} = -2i \begin{pmatrix} \mu_4 c_{g_1}(\mu_0 + n) - \mathcal{P}_{4,n} \\ \gamma_0 \left(\mu_4 c_{g_{-1}}(\mu_0 + m) - \mathcal{P}_{4,m}\right) \end{pmatrix}. \tag{3.93}$$

Expressions for $\mathcal{P}_{4,j}$ are in the Mathematica file. Using the solvability condition (3.75b) together with the collision condition (3.32) shows that $\mathcal{T}_{4,m} \equiv 0$. What remains is a linear system for λ_4 and γ_1.

If $\alpha \neq 1.1862...$, then an application of the third-order solvability condition (3.81a) shows that, for $\mu_3 \in (-M_3, M_3)$,

$$\det \begin{pmatrix} 2 & i\mathcal{S}_{3,n} \\ 2\gamma_0 & 2(\lambda_3 + i\mu_3 c_{g_{-1}}(\mu_0 + m)) \end{pmatrix} = 8\lambda_{3,r}, \tag{3.94}$$

where $\lambda_{3,r} = \operatorname{Re}(\lambda_3)$. For μ_3 in this interval, $\lambda_{3,r} \neq 0$ by construction; thus, (3.93) is an invertible linear system.

We solve (3.93) for λ_4 by Cramer's rule, using (3.81a) to eliminate the dependence on γ_0. Then,

$$\begin{aligned}\lambda_4 = i\Bigg[&\frac{(\lambda_3 + i\mu_3 c_{g_{-1}}(\mu_0+m))(c_{g_1}(\mu_0+n) - \mathcal{P}_{4,n})}{2\lambda_{3,r}} \\ &+ \frac{(\lambda_3 + i\mu_3 c_{g_1}(\mu_0+n))(c_{g_{-1}}(\mu_0+m) - \mathcal{P}_{4,m})}{2\lambda_{3,r}}\Bigg].\end{aligned} \tag{3.95}$$

To simplify further, we separate the real and imaginary components of (3.95). Since λ_2 (3.76a) is purely imaginary, $\mathcal{P}_{4,j}$ are real-valued, and $\mu_3 \in (-M_3, M_3)$, we have

$$\lambda_{3,i} = \mathrm{Im}(\lambda_3) = -i\mu_3\left(\frac{c_{g_{-1}}(\mu_0+m) + c_{g_1}(\mu_0+n)}{2}\right), \tag{3.96}$$

according to (3.83). Equation (3.95) decomposes into $\lambda_4 = \lambda_{4,r} + i\lambda_{4,i}$, where

$$\lambda_{4,r} = \frac{\mu_3}{4}\left[(c_{g_{-1}}(\mu_0+m) - c_{g_1}(\mu_0+n))\left(\mu_4(c_{g_{-1}}(\mu_0+m) - c_{g_1}(\mu_0+n)) + \mathcal{P}_{4,n} - \mathcal{P}_{4,m}\right)\right], \tag{3.97a}$$

$$\lambda_{4,i} = -\frac{1}{2}\left[\mu_4(c_{g_{-1}}(\mu_0+m) + c_{g_1}(\mu_0+n)) - (\mathcal{P}_{4,m} - \mathcal{P}_{4,n})\right]. \tag{3.97b}$$

As $|\mu_3| \to M_3$, $\lambda_{3,r} \to 0$. If $\lambda_{4,r}$ is to remain bounded, the numerator of (3.97a) must vanish in this limit. Since $c_{g_{-1}}(\mu_0+m) \neq c_{g_1}(\mu_0+n)$, we must have

$$\mu_4 = \frac{\mathcal{P}_{4,m} - \mathcal{P}_{4,n}}{c_{g_{-1}}(\mu_0+m) - c_{g_1}(\mu_0+n)}. \tag{3.98}$$

We refer to this equality as the *regular curve condition*: it ensures that the curve asymptotic to the $p = 3$ isola is continuous near its intersections with the imaginary axis. From the regular curve condition, we get

$$\lambda_4 = -i\left(\frac{\mathcal{P}_{4,m}c_{g_1}(\mu_0+n) - \mathcal{P}_{4,n}c_{g_{-1}}(\mu_0+m)}{c_{g_{-1}}(\mu_0+m) - c_{g_1}(\mu_0+n)}\right). \tag{3.99}$$

As expected, the Floquet parameterization and imaginary component of the $p = 3$ isola have a nonzero correction at $\mathcal{O}(\varepsilon^4)$. These corrections improve the agreement between numerical and asymptotic results observed at the previous order, see Figure 3.7 and Figure 3.8. No corrections to the real component of the isola are found at fourth order.

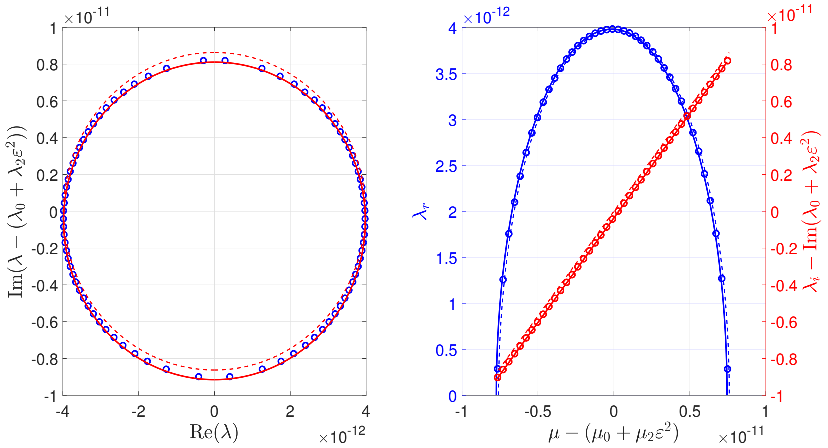

Figure 3.7: (Left) The $p = 3$ isola with $\alpha = 1$ and $\varepsilon = 5 \times 10^{-4}$ (zero- and second-order imaginary corrections removed for better visibility). Solid and dashed red curves are given by perturbation calculations to $\mathcal{O}\left(\varepsilon^4\right)$ and $\mathcal{O}\left(\varepsilon^3\right)$, respectively. Blue circles are a subset of spectral elements from the numerically computed isola using the FFH method. (Right) The Floquet parameterization of the real (blue) and imaginary (red) components of the isola (zero- and second-order imaginary and Floquet corrections removed for better visibility). Solid and dashed curves illustrate perturbation calculations to $\mathcal{O}\left(\varepsilon^4\right)$ and $\mathcal{O}\left(\varepsilon^3\right)$, respectively. Circles indicate the FFH method results.

Remark 3.6.2. *If* $\alpha = 1.1862...$, *one can show that* $\lambda_3 = 0 = \mu_3$ *and* $\mathcal{S}_{3,n} = 0$*. Applying the Fredholm alternative to* (3.93) *gives* (3.98)*. Then,* λ_4 *is given by* (3.99)*, and* $\gamma_0 = 1$*. The constant* γ_1 *remains arbitrary at this order (only for this* α*).*

3.7 Conclusions

We have extended the formal perturbation method for the Kawahara equation to a nonlinear vector equation with a nonlocal operator. Using this method, we have obtained asymptotic behaviors of the largest ($p = 2, 3$) high-frequency instabilities of the HPBW system, including

(i) the interval of Floquet exponents that asymptotically parameterize the pth isola,

(ii) the leading-order behavior of the most unstable eigenvalues,

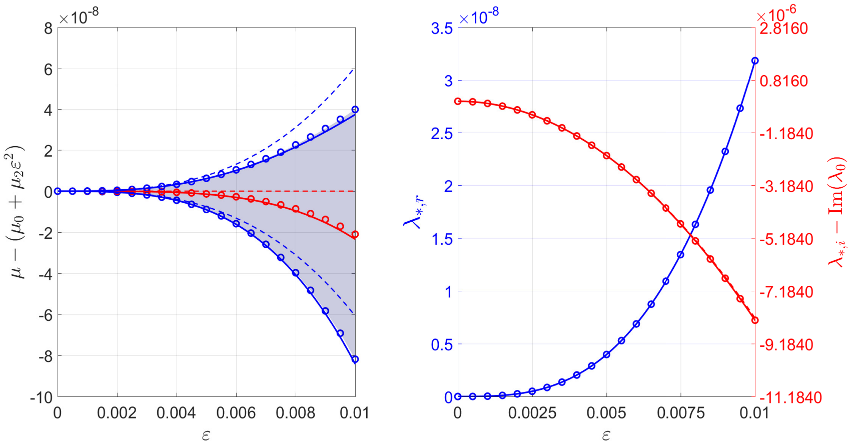

Figure 3.8: (Left) The interval of Floquet exponents that parameterize the $p = 3$ isola as a function of ε with $\alpha = 1$ (zero- and second-order Floquet corrections removed for better visibility). Solid and dashed blue curves indicate the boundaries of this interval according to perturbation calculations to $\mathcal{O}\left(\varepsilon^4\right)$ and $\mathcal{O}\left(\varepsilon^3\right)$, respectively. Blue circles indicate the boundaries computed numerically by the FFH method. The solid red curve gives the Floquet exponent corresponding to the most unstable spectral element of the isola according to our perturbation calculations. Red circles indicate the same but computed numerically using the FFH method. (Right) The real (blue) and imaginary (red) components of the most unstable spectral element of the isola as a function of ε (zero-order imaginary correction removed for better visibility). Solid and dashed curves illustrate perturbation calculations to $\mathcal{O}\left(\varepsilon^4\right)$ and $\mathcal{O}\left(\varepsilon^3\right)$, respectively. Circles illustrate the FFH method results.

(iii) the leading-order curve asymptotic to the isola.

From these expansions, we are able to conclude that Stokes waves of HPBW are unstable to high-frequency instabilities in all depths, similar to those of Euler's equations. This conclusion is also well-supported with numerical results using the FFH method, giving confidence that our expansions are correct.

Although we restrict to the $p = 2$ and $p = 3$ high-frequency instabilities in this chapter, our method works for $p > 3$ isolas as well. We conjecture that this method yields the first real-component correction of the isola at $\mathcal{O}\left(\varepsilon^p\right)$. Proving this claim is challenging, however, as one incurs imaginary corrections to the isolas before the first real correction is obtained.

Chapter 4

HIGH-FREQUENCY INSTABILITIES OF EULER'S EQUATIONS

4.1 Introductory Remarks

Having successfully developed a perturbation method for high-frequency isolas of the Kawahara equation and HPBW system, we return to Euler's equations on a $2\pi/\kappa$-periodic domain:

$$\phi_{xx} + \phi_{zz} = 0 \quad \text{in} \quad \{(x,z) : |x| < \pi/\kappa \text{ and} -h < z < \eta\}, \tag{4.1a}$$

$$\eta_t + \eta_x\phi_x = \phi_z \quad \text{on} \quad z = \eta, \tag{4.1b}$$

$$\phi_t + \tfrac{1}{2}\left(\phi_x^2 + \phi_z^2\right) + g\eta = 0 \quad \text{on} \quad z = \eta, \tag{4.1c}$$

$$\phi_z = 0, \quad \text{on} \quad z = -h, \tag{4.1d}$$

with

$$\eta(-\pi/\kappa, t) = \eta(\pi/\kappa, t), \tag{4.2a}$$

$$\phi_x(-\pi/\kappa, z, t) = \phi_x(\pi/\kappa, z, t), \quad \phi_z(-\pi/\kappa, z, t) = \phi_z(\pi/\kappa, z, t). \tag{4.2b}$$

In this chapter, we derive formal asymptotic expressions for the Stokes waves of (4.1a)-(4.1d) as well as their high-frequency isolas in both finite and infinite depth. For each isola, we obtain

(i) an interval of Floquet exponents that is asymptotic to the interval parameterizing the isola,

(ii) an asymptotic expansion for the most unstable eigenvalue on the isola, and

(iii) a closed-form expression for the curve asymptotic to the isola, similar to the previous chapters. Crucial to our approach is again the expansion for the Floquet parameterization of the isola as power series in the Stokes wave amplitude ε.

Our asymptotic expressions are compared directly with numerical results of the Floquet-Fourier-Hill (FFH) method, to excellent agreement. For almost all aspect ratios κh (except a few isolated values), our asymptotic expressions predict that Stokes waves of sufficiently small (but finite) amplitude are unstable with respect to high-frequency instabilities, extending recent work by Hur and Yang [53] that rigorously establishes the high-frequency instability closest to the origin for $\kappa h \in (0.86430..., 1.00804...)$. Thus, the results in this chapter show formally that Stokes waves in all depths are unstable to high-frequency instabilities.

4.2 The AFM Formulation of Euler's Equations

Euler's equations (4.1a)-(4.1d) together with the auxiliary conditions (4.2a)-(4.2b) constitute a boundary value problem for Laplace's equation in a domain evolving nonlinearly in time. Depending on the application, other formulations of gravity waves may be preferred over (4.1a)-(4.1d). For example, in the study of 1D waves, conformal transformations [39] are used to map the bulk of the fluid to a time-independent domain, at the cost of losing the original physical variables. For 1D and 3D waves, Zakharov [95] writes (4.1a)-(4.1d) as a Hamiltonian system with canonical Poisson structure in physical variables. Going one step further, Craig and Sulem [26] express (4.1a)-(4.1d) as a system of nonlinear evolution equations for the surface variables η and $q = \phi(x, \eta, t)$. This formulation introduces the nonlocal Dirichlet-to-Neumann operator (DNO):

$$G(\eta)q = \phi_z\big|_{z=\eta} - \eta_x\phi_x\big|_{z=\eta}, \tag{4.3}$$

which maps the velocity potential at the surface to its normal derivative.

We consider the Ablowitz-Fokas-Musslimani (AFM) formulation, first proposed in [1]. This formulation has dependence only on surface variables, as in the Zakharov or Craig and Sulem formulations, but avoids direct numerical computations of the Dirichlet-to-Neumann operator.

As shown in [2, 76], Euler's equations (4.1a)-(4.1d) together with the lateral periodic boundary conditions (4.2a)-(4.2b) are equivalent to the following system for the surface variables η and q:

$$\int_{-\pi/\kappa}^{\pi/\kappa} e^{-i\kappa m x}\Big[\eta_t \cosh\left(\kappa m\left(\eta+h\right)\right) + i q_x \sinh\left(\kappa m\left(\eta+h\right)\right)\Big] dx = 0, \quad m \in \mathbb{Z}\setminus\{0\}, \tag{4.4a}$$

$$q_t + \frac{1}{2}q_x^2 + g\eta - \frac{1}{2}\frac{\left(\eta_t + \eta_x q_x\right)^2}{1+\eta_x^2} = 0. \tag{4.4b}$$

We call (4.4a) and (4.4b) the nonlocal and local equations of the AFM formulation, respectively.

Anticipating a Stokes wave calculation in the next section, we transform (4.4a)-(4.4b) to a traveling frame $x \to x - ct$:

$$\int_{-\pi/\kappa}^{\pi/\kappa} e^{-i\kappa m x}\Big[\left(\eta_t - c\eta_x\right) \cosh\left(\kappa m\left(\eta+h\right)\right) + i q_x \sinh\left(\kappa m\left(\eta+h\right)\right)\Big] dx = 0, \quad m \in \mathbb{Z}\setminus\{0\}, \tag{4.5a}$$

$$q_t - cq_x + \frac{1}{2}q_x^2 + g\eta - \frac{1}{2}\frac{\left(\eta_t - c\eta_x + \eta_x q_x\right)^2}{1+\eta_x^2} = 0. \tag{4.5b}$$

Unless otherwise stated, x represents the horizontal coordinate in the traveling frame for the remainder of this work.

Non-dimensionalizing (4.5a)-(4.5b) according to $x \to x/\kappa$, $t \to t/\sqrt{g\kappa}$, $\eta \to \eta/\kappa$, $q \to q\sqrt{g/\kappa^3}$, $c \to c\sqrt{g/\kappa}$, and $h \to \alpha/\kappa$, we arrive at

$$\int_{-\pi}^{\pi} e^{-imx}\Big[\left(\eta_t - c\eta_x\right) \cosh\left(m\left(\eta+\alpha\right)\right) + i q_x \sinh\left(m\left(\eta+\alpha\right)\right)\Big] dx = 0, \quad m \in \mathbb{Z}\setminus\{0\}, \tag{4.6a}$$

$$q_t - cq_x + \frac{1}{2}q_x^2 + \eta - \frac{1}{2}\frac{\left(\eta_t - c\eta_x + \eta_x q_x\right)^2}{1+\eta_x^2} = 0, \tag{4.6b}$$

where $\alpha = \kappa h > 0$ is the aspect ratio of the surface profile η (in dimensional variables). Without loss of generality, we study solutions of the nondimensional equations (4.6a)-(4.6b).

Remark 4.2.1. *The rescaling performed on Euler's equations is inspired by the linearized dispersion relation of water waves in infinite depth and, hence, is well-behaved in this limit. This is to be contrasted with the rescaling used on the HPBW system, which does not hold as* $h \to \infty$*.*

Remark 4.2.2. *Dividing* (4.6a) *by* $\cosh(m\alpha)$ *and taking the limit* $\alpha \to \infty$ *yields (after some manipulation) the nonlocal equation in infinite depth:*

$$\int_{-\pi}^{\pi} e^{-imx+|m|\eta}\Big[\eta_t - c\eta_x + i sgn\,(m)\, q_x\Big]dx = 0, \quad m \in \mathbb{Z}\setminus\{0\}. \tag{4.7}$$

The local equation remains unchanged in infinite depth.

4.3 Stokes Wave Solutions

Using the nondimensional AFM formulation (4.6a)-(4.6b), Stokes waves are defined as surface displacements η_S together with velocity potentials (at the surface) q_S that satisfy the following properties:

(i) η_S and q_S are time-independent, infinitely smooth solutions of (4.6a)-(4.6b).

(ii) η_S and $q_{S,x}$ are 2π-periodic with respect to x (but not so of q_S).

(iii) η_S, $q_{S,x}$, and c (the velocity of the Stokes wave) depend analytically on a small parameter ε such that

$$\eta_S\Big|_{\varepsilon=0} = 0 = q_{S,x}\Big|_{\varepsilon=0} \quad \text{and} \quad ||\eta_S||_{\mathrm{L}^2} = \varepsilon + \mathcal{O}\left(\varepsilon^2\right) \quad \text{as} \quad \varepsilon \to 0.$$

(iv) η_S and $q_{S,x}$ are even in x without loss of generality[1], and $c(\varepsilon)$ is even in ε.

(v) η_S has zero average over one period.

As mentioned in the Introduction, the existence of these waves is proven in [64, 71, 87]. In this section, we derive power series expansions of η_S, $q_{S,x}$, and c in the small parameter ε using the nondimensional AFM formulation. These expansions are required for the stability calculations considered in later sections.

---

[1] These properties follow from the time-independent versions of (4.6a)-(4.6b), which respect the symmetry $x \to x + \phi$ for any $\phi \in \mathbb{R}$ as well as the symmetry $x \to -x$ and $c \to -c$.

Equating time derivatives to zero in (4.6a)-(4.6b) by property (i), integrating the cosh term in (4.6a) by parts using property (ii), and solving for q_x in (4.6b), we arrive at the following equations determining the Stokes waves:

$$\int_{-\pi}^{\pi} e^{-imx}\sqrt{\left(1+\eta_{S,x}^2\right)\left(c^2-2\eta_S\right)}\sinh(m(\eta_S+\alpha))dx=0, \quad m\in\mathbb{Z}\setminus\{0\}, \tag{4.8a}$$

$$q_{S,x}=c\pm\sqrt{\left(1+\eta_{S,x}^2\right)\left(c^2-2\eta_S\right)}. \tag{4.8b}$$

By property (iii), the positive branch of (4.8b) is defined for left-traveling waves ($c<0$), while the negative branch is defined for right-traveling waves ($c>0$) [23]. In what follows, we consider right-traveling waves. Similar results hold for the other case.

Remark 4.3.1. *In infinite depth,* (4.8a) *becomes*

$$\int_{-\pi}^{\pi} e^{-imx+|m|\eta_S}\sqrt{\left(1+\eta_{S,x}^2\right)\left(c^2-2\eta_S\right)}dx=0, \quad m\in\mathbb{Z}\setminus\{0\}. \tag{4.9}$$

By properties (ii) and (iv), η_S has a Fourier cosine series. We define the small-amplitude parameter ε as the first Fourier cosine mode of η_S:

$$\varepsilon=\frac{1}{\pi}\int_{-\pi}^{\pi}\eta_S\cos(x)dx. \tag{4.10}$$

Then, by property (iii),

$$\eta_S(x;\varepsilon)=\varepsilon\cos(x)+\mathcal{O}\left(\varepsilon^2\right), \tag{4.11}$$

for $|\varepsilon|\ll 1$. The leading-order term of η_S completely resolves the first Fourier cosine mode: higher-order corrections do not include terms proportional to $\cos(x)$ as a result.

Using properties (iii) and (iv), we write η_S and c as power series in ε:

$$\eta_S(x;\varepsilon)=\sum_{j=1}^{\infty}\eta_j(x)\varepsilon^j, \tag{4.12}$$

$$c(\varepsilon)=\sum_{j=0}^{\infty}c_{2j}\varepsilon^{2j}. \tag{4.13}$$

Both of these series are substituted into (4.8a) and, after equating powers of ε, a triangular sequence of linear integral equations for η_j and c_{2j} is found. Each of these integral equations depends on m, which can be any nonzero integer.

Remark 4.3.2. *Since η_S is even in x, the integrand of* (4.8a) *modulo the complex exponential is even in x. Therefore, $m \in \mathbb{Z}^+$ without loss of generality.*

The first nontrivial integral equation in this sequence is

$$\int_{-\pi}^{\pi} e^{-imx}\Big[mc_0^2\cosh(m\alpha) - \sinh(m\alpha)\Big]\eta_1(x)dx = 0. \tag{4.14}$$

From above, $\eta_1(x) = \cos(x)$. If (4.14) holds for all $m \in \mathbb{Z}^+$,

$$c_0^2 = \tanh(\alpha), \tag{4.15}$$

otherwise (4.14) is not satisfied when $m = 1$. Since we study right-traveling waves, we choose $c_0 > 0$.

For the jth integral equation in the sequence ($j \geq 2$), one finds

$$\eta_j(x) = \sum_{\substack{\ell=2\\ \ell\ \text{even}}}^{j} \hat{N}_{j,\ell}\cos(\ell x) \quad \text{for} \quad j \text{ even}, \tag{4.16a}$$

$$\eta_j(x) = \sum_{\substack{\ell=3\\ \ell\ \text{odd}}}^{j} \hat{N}_{j,\ell}\cos(\ell x) \quad \text{for} \quad j \text{ odd}, \tag{4.16b}$$

where the coefficients $\hat{N}_{j,\ell}$ are determined by the j^{th} equation with $m = \ell$. No corrections to the velocity c are found when j is even. When j is odd, c_{j-1} is determined by the j^{th} equation with $m = 1$, similar to the $j = 1$ case considered above. This correction is chosen so that $\eta_j(x)$ has no terms proportional to $\cos(x)$.

Expansions of η_S and c are substituted into (4.8b). After equating powers of ε, an expansion for $q_{S,x}$ follows immediately. In general,

$$q_{S,x}(x;\varepsilon) = \sum_{j=1}^{\infty} q_{j,x}(x)\varepsilon^j. \tag{4.17}$$

The corrections $q_{j,x}(x)$ have the same structure as (4.16a)-(4.16b), but also include constant modes (when j is even) and modes proportional to $\cos(x)$ (when j is odd). Thus, $q_{S,x}$ has nonzero average, and the first Fourier cosine mode of $q_{S,x}$ has corrections beyond $\mathcal{O}(\varepsilon)$, unlike η_S.

Remark 4.3.3. *Integrating* (4.17) *term-by-term gives* q_S*. The constant of integration can be eliminated by a Galilean transformation of* (4.8b)*. Because* $q_{S,x}$ *has nonzero average,* q_S *exhibits linear growth in* x*. This behavior captures the mean flow induced by the traveling frame.*

Explicit representations for the expansions of η_S, $q_{S,x}$, and c up to $\mathcal{O}\left(\varepsilon^4\right)$ are as follows. For η_S and q_S,

$$\eta_S(x;\varepsilon) = \varepsilon\cos(x) + \varepsilon^2\hat{N}_{2,2}\cos(2x) + \varepsilon^3\hat{N}_{3,3}\cos(3x) + \varepsilon^4\Big(\hat{N}_{4,2}\cos(2x) + \hat{N}_{4,4}\cos(4x)\Big) + \mathcal{O}\left(\varepsilon^5\right), \tag{4.18a}$$

$$q_{S,x}(x;\varepsilon) = \frac{\varepsilon}{c_0}\cos(x) + \varepsilon^2\Big(\hat{Q}_{2,0} + \hat{Q}_{2,2}\cos(2x)\Big) + \varepsilon^3\Big(\hat{Q}_{3,1}\cos(x) + \hat{Q}_{3,3}\cos(3x)\Big) + \varepsilon^4\Big(\hat{Q}_{4,0} + \hat{Q}_{4,2}\cos(2x) + \hat{Q}_{4,4}\cos(4x)\Big) + \mathcal{O}\left(\varepsilon^5\right), \tag{4.18b}$$

where

$$\hat{N}_{2,2} = \frac{5\cosh(\alpha) + \cosh(3\alpha)}{8\sinh^3(\alpha)}, \tag{4.19a}$$

$$\hat{N}_{3,3} = \frac{3(14 + 15\cosh(2\alpha) + 6\cosh(4\alpha) + \cosh(6\alpha))}{256\sinh^6(\alpha)}, \tag{4.19b}$$

$$\hat{N}_{4,2} = \frac{215 - 418\cosh(2\alpha) - 472\cosh(4\alpha) + 10\cosh(6\alpha) + 17\cosh(8\alpha)}{3072c_0^2\sinh^8(\alpha)}, \tag{4.19c}$$

$$\hat{N}_{4,4} = \frac{203 + 347\cosh(2\alpha) + 158\cosh(4\alpha) + 76\cosh(6\alpha) + 23\cosh(8\alpha) + 3\cosh(10\alpha)}{768c_0^2(2 + 3\cosh(2\alpha))\sinh^8(\alpha)}, \tag{4.19d}$$

$$\hat{Q}_{2,0} = \frac{1}{4c_0^3\cosh^2(\alpha)}, \tag{4.19e}$$

$$\hat{Q}_{2,2} = \frac{3 + 2\cosh(2\alpha) + \cosh(4\alpha)}{8c_0\sinh^3(\alpha)\cosh(\alpha)}, \tag{4.19f}$$

$$\hat{Q}_{3,1} = -\left(\frac{\cosh(2\alpha)\,(2 + \cosh(2\alpha))}{16c_0\sinh^4(\alpha)}\right), \tag{4.19g}$$

$$\hat{Q}_{3,3} = \frac{3\,(26 - 3\cosh(2\alpha) + 10\cosh(4\alpha) + 3\cosh(6\alpha))}{256c_0\sinh^6(\alpha)}, \tag{4.19h}$$

$$\hat{Q}_{4,0} = \frac{48 + 47\cosh(2\alpha) - 20\cosh(4\alpha) - 3\cosh(6\alpha)}{512c_0\sinh^7(\alpha)\cosh(\alpha)}, \tag{4.19i}$$

$$\hat{Q}_{4,2} = -\left(\frac{240 + 82\cosh(2\alpha) + 688\cosh(4\alpha) + 309\cosh(6\alpha) - 16\cosh(8\alpha) - 7\cosh(10\alpha)}{6144c_0\sinh^9(\alpha)\cosh(\alpha)}\right), \tag{4.19j}$$

$$\hat{Q}_{4,4} = \frac{1}{1536c_0(2+3\cosh(2\alpha))\sinh^9(\alpha)\cosh(\alpha)}\Big(408 + 638\cosh(2\alpha) + 230\cosh(4\alpha) + 171\cosh(6\alpha) + 124\cosh(8\alpha) + 43\cosh(10\alpha) + 6\cosh(12\alpha)\Big). \tag{4.19k}$$

For the velocity of the Stokes wave c,

$$c(\varepsilon) = c_0 + c_2\varepsilon^2 + c_4\varepsilon^4 + \mathcal{O}\left(\varepsilon^6\right), \tag{4.20}$$

where

$$c_0^2 = \tanh(\alpha), \tag{4.21a}$$

$$c_2 = \frac{6 + 2\cosh(2\alpha) + \cosh(4\alpha)}{16c_0\sinh^3(\alpha)\cosh(\alpha)}, \tag{4.21b}$$

$$c_4 = \frac{212 + 55\cosh(2\alpha) - 98\cosh(4\alpha) - 23\cosh(6\alpha) + 14\cosh(8\alpha) + 2\cosh(10\alpha)}{2048c_0\sinh^9(\alpha)\cosh(\alpha)}. \tag{4.21c}$$

The Stokes expansions in infinite depth are obtained from the above with $\alpha \to \infty$.

4.4 The Spectral Stability Problem

We consider perturbations to the Stokes waves of the form

$$\begin{pmatrix}\eta(x,t;\varepsilon,\rho)\\ q(x,t;\varepsilon,\rho)\end{pmatrix} = \begin{pmatrix}\eta_S(x;\varepsilon)\\ q_S(x;\varepsilon)\end{pmatrix} + \rho\begin{pmatrix}\eta_\rho(x,t)\\ q_\rho(x,t)\end{pmatrix} + \mathcal{O}\left(\rho^2\right), \tag{4.22}$$

where $|\rho| \ll 1$ is a parameter independent of ε. The perturbations η_ρ and q_ρ are sufficiently smooth functions of x and t that are bounded over the real line for each $t \geq 0$.

The nonlocal equation (4.6a) assumes η, η_t, and q_x are 2π-periodic in x, which is not required of our perturbations. We modify (4.6a) to allow η, η_t, and $q_x \in C^0(\mathbb{R}) \cap L^\infty(\mathbb{R})$ for each $t \geq 0$. The appropriate modification [35] is

$$\left\langle e^{-ikx}\Big[(\eta_t - c\eta_x)\cosh\left(k\left(\eta+\alpha\right)\right) + iq_x\sinh\left(k\left(\eta+\alpha\right)\right)\Big]\right\rangle = 0, \quad k \in \mathbb{R}\setminus\{0\}, \tag{4.23}$$

where

$$\langle f(x)\rangle = \lim_{L\to\infty}\frac{1}{L}\int_{-L/2}^{L/2} f(x)dx, \tag{4.24}$$

for any $f(x)\in C^0(\mathbb{R})\cap L^\infty(\mathbb{R})$ [12, 35]. If η, η_t, and q_x are 2π-periodic in x for each $t\geq 0$, then (4.23) reduces to (4.6a).

Substituting (4.22) into (4.6b) and (4.23) and equating powers of ρ, terms of $\mathcal{O}(\rho^0)$ necessarily cancel, since η_S and q_S solve (4.6b) and (4.23). At $\mathcal{O}(\rho)$, one finds the governing equations for η_ρ and q_ρ:

$$\left\langle e^{-ikx}\left[c\mathcal{C}_k\eta_{\rho,x} + k\left(c\mathcal{S}_k\eta_{S,x} - i\mathcal{C}_k q_{S,x}\right)\eta_\rho - i\mathcal{S}_k q_{\rho,x}\right]\right\rangle = \left\langle e^{-ikx}\mathcal{C}_k\eta_{\rho,t}\right\rangle, \tag{4.25a}$$

$$\eta_{S,x}\zeta^2\eta_{\rho,x} - \eta_\rho - \zeta q_{\rho,x} = q_{\rho,t} - \eta_{S,x}\zeta\eta_{\rho,t}, \tag{4.25b}$$

where

$$\mathcal{C}_k = \cosh(k(\eta_S+\alpha)), \qquad \mathcal{S}_k = \sinh(k(\eta_S+\alpha)), \qquad \zeta = \frac{q_{S,x}-c}{1+\eta_{S,x}^2}. \tag{4.26}$$

Equations (4.25a)-(4.25b) are autonomous in t. We separate variables to find

$$\begin{pmatrix}\eta_\rho(x,t)\\ q_\rho(x,t)\end{pmatrix} = e^{\lambda t}\begin{pmatrix}N(x)\\ Q(x)\end{pmatrix}, \tag{4.27}$$

where $\lambda\in\mathbb{C}$ controls the growth rates of the perturbations. The functions $N(x)$ and $Q(x)$ satisfy

$$\left\langle e^{-ikx}\left[c\mathcal{C}_k N_x + k\left(c\mathcal{S}_k\eta_{S,x} - i\mathcal{C}_k q_{S,x}\right)N - i\mathcal{S}_k Q_x\right]\right\rangle = \lambda\left\langle e^{-ikx}\mathcal{C}_k N\right\rangle, \tag{4.28a}$$

$$\eta_{S,x}\zeta^2 N_x - N - \zeta Q_x = \lambda\left(Q - \eta_{S,x}\zeta N\right). \tag{4.28b}$$

Equations (4.28a)-(4.28b) are invariant under the shift $x\to x+2\pi$ by the periodicity of η_S and $q_{S,x}$. Therefore, we expect the solutions N and Q to have Bloch form [35]

$$\begin{pmatrix}N(x)\\ Q(x)\end{pmatrix} = e^{i\mu x}\begin{pmatrix}\mathcal{N}(x)\\ \mathcal{Q}(x)\end{pmatrix}, \tag{4.29}$$

where $\mu \in \mathbb{R}$ is the Floquet exponent and $\mathcal{N}$ and $\mathcal{Q}$ are sufficiently smooth and 2π-periodic. Note that by redefining $\mathcal{N}$ and $\mathcal{Q}$, $\mu \in [-1/2, 1/2)$, without loss of generality.

Substituting (4.29) into (4.28a)-(4.28b), we arrive at

$$\left\langle e^{-i(k-\mu)x}\left[c\mathcal{C}_k\mathcal{D}_x\mathcal{N} + k\left(c\mathcal{S}_k\eta_{S,x} - i\mathcal{C}_k q_{S,x}\right)\mathcal{N} - i\mathcal{S}_k\mathcal{D}_x\mathcal{Q}\right]\right\rangle = \lambda\left\langle e^{-i(k-\mu)x}\mathcal{C}_k\mathcal{N}\right\rangle, \tag{4.30a}$$

$$\eta_{S,x}\zeta^2\mathcal{D}_x\mathcal{N} - \mathcal{N} - \zeta\mathcal{D}_x\mathcal{Q} = \lambda\left(\mathcal{Q} - \eta_{S,x}\zeta\mathcal{N}\right), \tag{4.30b}$$

where $\mathcal{D}_x = i\mu + \partial_x$.

The integrands of the averaging operators in (4.30a) are 2π-periodic except for the complex exponentials. These operators evaluate to zero unless $k - \mu = n \in \mathbb{Z}$ [35]. For such k, (4.30a) becomes

$$\begin{aligned}\left\langle e^{-inx}\left[c\mathcal{C}_{n+\mu}\mathcal{D}_x\mathcal{N} + (n+\mu)\left(c\mathcal{S}_{n+\mu}\eta_{S,x} - i\mathcal{C}_{n+\mu}q_{S,x}\right)\mathcal{N} - i\mathcal{S}_{n+\mu}\mathcal{D}_x\mathcal{Q}\right]\right\rangle& \\ = \lambda\left\langle e^{-inx}\mathcal{C}_{n+\mu}\mathcal{N}\right\rangle, \quad n \in \mathbb{Z}.&\end{aligned} \tag{4.31}$$

The averaging operators of (4.31) reduce to Fourier transforms:

$$\left\langle e^{-inx}f(x)\right\rangle = \frac{1}{2\pi}\int_{-\pi}^{\pi} e^{-inx}f(x)dx = \mathcal{F}_n[f(x)], \tag{4.32}$$

for any $f(x) \in L^2_{\text{per}}(-\pi,\pi)$. The inverse transform is

$$\mathcal{F}^{-1}[\{f_n\}] = \sum_{n=-\infty}^{\infty} f_n e^{inx}, \tag{4.33}$$

provided $\{f_n\} \in \ell^2(\mathbb{Z})$. Using the inverse transform on (4.31), we find

$$\begin{aligned}&\sum_{n=-\infty}^{\infty} e^{inx}\mathcal{F}_n\left[c\mathcal{C}_{n+\mu}\mathcal{D}_x\mathcal{N} + (n+\mu)\left(c\mathcal{S}_{n+\mu}\eta_{S,x} - i\mathcal{C}_{n+\mu}q_{S,x}\right)\mathcal{N}\right] \\ &\qquad + \sum_{n=-\infty}^{\infty} e^{inx}\mathcal{F}_n\left[-i\mathcal{S}_{n+\mu}\mathcal{D}_x\mathcal{Q}\right] = \lambda\sum_{n=-\infty}^{\infty} e^{inx}\mathcal{F}_n\left[\mathcal{C}_{n+\mu}\mathcal{N}\right].\end{aligned} \tag{4.34}$$

Equations (4.30b) and (4.34) are written compactly as

$$\mathcal{L}_{\mu,\varepsilon}\mathbf{w}_{\mu,\varepsilon} = \lambda_{\mu,\varepsilon}\mathcal{R}_{\mu,\varepsilon}\mathbf{w}_{\mu,\varepsilon}, \tag{4.35}$$

where $\lambda = \lambda_{\mu,\varepsilon}$, $\mathbf{w}_{\mu,\varepsilon} = (\mathcal{N}, \mathcal{Q})^T$, and

$$\mathcal{L}_{\mu,\varepsilon} = \begin{pmatrix} \mathcal{L}^{(1,1)}_{\mu,\varepsilon} & \mathcal{L}^{(1,2)}_{\mu,\varepsilon} \\ \mathcal{L}^{(2,1)}_{\mu,\varepsilon} & \mathcal{L}^{(2,2)}_{\mu,\varepsilon} \end{pmatrix}, \quad \mathcal{R}_{\mu,\varepsilon} = \begin{pmatrix} \mathcal{R}^{(1,1)}_{\mu,\varepsilon} & 0 \\ \mathcal{R}^{(2,1)}_{\mu,\varepsilon} & 1 \end{pmatrix}, \tag{4.36}$$

$$\mathcal{L}^{(1,1)}_{\mu,\varepsilon}[\mathcal{N}] = \sum_{n=-\infty}^{\infty} e^{inx} \mathcal{F}_n\big[c\mathcal{C}_{n+\mu}\mathcal{D}_x\mathcal{N} + (n+\mu)\left(c\mathcal{S}_{n+\mu}\eta_{S,x} - i\mathcal{C}_{n+\mu}q_{S,x}\right)\mathcal{N}\big], \tag{4.37a}$$

$$\mathcal{L}^{(1,2)}_{\mu,\varepsilon}[\mathcal{Q}] = \sum_{n=-\infty}^{\infty} e^{inx} \mathcal{F}_n\big[-i\mathcal{S}_{n+\mu}\mathcal{D}_x\mathcal{Q}\big], \tag{4.37b}$$

$$\mathcal{L}^{(2,1)}_{\mu,\varepsilon}[\mathcal{N}] = \eta_{S,x}\zeta^2\mathcal{D}_x\mathcal{N} - \mathcal{N}, \tag{4.37c}$$

$$\mathcal{L}^{(2,2)}_{\mu,\varepsilon}[\mathcal{Q}] = -\zeta\mathcal{D}_x\mathcal{Q}, \tag{4.37d}$$

$$\mathcal{R}^{(1,1)}_{\mu,\varepsilon}[\mathcal{N}] = \sum_{n=-\infty}^{\infty} e^{inx} \mathcal{F}_n\left[\mathcal{C}_{n+\mu}\mathcal{N}\right], \tag{4.37e}$$

$$\mathcal{R}^{(2,1)}_{\mu,\varepsilon}[\mathcal{N}] = -\eta_{S,x}\zeta\mathcal{N}. \tag{4.37f}$$

For fixed ε, (4.35) represents a one-parameter family of generalized eigenvalue problems for the linear operators $\mathcal{L}_{\mu,\varepsilon}$ and $\mathcal{R}_{\mu,\varepsilon}$.

To be well-defined, these operators require $\mathbf{w}_{\mu,\varepsilon}$ to be at least once weakly differentiable with respect to x in both components. Moreover, because $\mathcal{L}_{\mu,\varepsilon}$ and $\mathcal{R}_{\mu,\varepsilon}$ depend on $\mathcal{C}_{n+\mu}$ and $\mathcal{S}_{n+\mu}$, which satisfy the bounds

$$|\mathcal{C}_{n+\mu}| \le e^{|n+\mu|(\alpha+||\eta_S||_\infty)}, \qquad |\mathcal{S}_{n+\mu}| \le e^{|n+\mu|(\alpha+||\eta_S||_\infty)}, \tag{4.38}$$

Both $\mathcal{F}_n[\mathbf{w}_{\mu,\varepsilon}]$ and $\mathcal{F}_n[\mathbf{w}_{\mu,\varepsilon,x}]$ must decay exponentially fast in both components as $|n| \to \infty$. For real-valued Stokes waves, $||\eta_S||_\infty \le c^2/2$, see (4.8a). Therefore, we require $\mathbf{w}_{\mu,\varepsilon} \in \mathrm{EH}^1_{\mathrm{per}}(-\pi,\pi) \times \mathrm{EH}^1_{\mathrm{per}}(-\pi,\pi)$, where

$$\mathrm{EH}^1_{\mathrm{per}}(-\pi,\pi) = \left\{ f : \sum_{n=-\infty}^{\infty} \left(1+|n|^2\right) e^{|n+\mu|\left(2\alpha+c^2\right)} |\mathcal{F}_n[f]|^2 < \infty \right\}. \tag{4.39}$$

Remark 4.4.1. *Alternatively, the exponential growth of $\mathcal{C}_{n+\mu}$ and $\mathcal{S}_{n+\mu}$ can be removed from the operators $\mathcal{L}_{\mu,\varepsilon}$ and $\mathcal{R}_{\mu,\varepsilon}$ by left multiplication with the following Fourier multiplier:*

$$\mathcal{M}_{\mu,\varepsilon} = \begin{pmatrix} e^{-|D+\mu|\left(\alpha+c^2/2\right)} & 0 \\ 0 & 1 \end{pmatrix}, \tag{4.40}$$

where $D=-i\partial_x$. If $\mathcal{L}_{\mu,\varepsilon}$ and $\mathcal{R}_{\mu,\varepsilon}$ are redefined in this way, $\mathbf{w}_{\mu,\varepsilon}$ can be relaxed to $H^1_{per}(-\pi,\pi)\times H^1_{per}(-\pi,\pi)$, and (4.35) becomes a generalized eigenvalue problem densely defined over $L^2_{per}(-\pi,\pi)\times L^2_{per}(-\pi,\pi)$ for each $\mu\in[-1/2,1/2)$ and ε sufficiently small.

Remark 4.4.2. *In infinite depth,*

$$\mathcal{L}^{(1,1)}_{\mu,\varepsilon}[\mathcal{N}] = \sum_{n=-\infty}^{\infty} e^{inx}\mathcal{F}_n\big[e^{|n+\mu|\eta_S}\big(c\mathcal{D}_x\mathcal{N} + \big(c\eta_{S,x}|n+\mu| - i(n+\mu)q_{S,x}\big)\mathcal{N}\big)\big], \tag{4.41a}$$

$$\mathcal{L}^{(1,2)}_{\mu,\varepsilon}[\mathcal{Q}] = \sum_{n=-\infty}^{\infty} e^{inx}\mathcal{F}_n\big[e^{|n+\mu|\eta_S}\big(-isgn(n+\mu)\mathcal{D}_x\mathcal{Q}\big)\big], \tag{4.41b}$$

$$\mathcal{R}^{(1,1)}_{\mu,\varepsilon}[\mathcal{N}] = \sum_{n=-\infty}^{\infty} e^{inx}\mathcal{F}_n\big[e^{|n+\mu|\eta_S}\mathcal{N}\big]. \tag{4.41c}$$

All other entries are the same as above.

The spectrum of (4.35) has a countable collection of finite-multiplicity eigenvalues $\lambda_{\mu,\varepsilon}$ for each μ. The union of these eigenvalues over $\mu\in[-1/2,1/2)$ is defined as the stability spectrum of Stokes waves with amplitude ε. By quadrafold symmetry, the Stokes waves are stable only if their stability spectrum is a subset of the imaginary axis, as mentioned in the Introduction.

4.5 Necessary Conditions for High-Frequency Instabilities

When $\varepsilon=0$, (4.35) reduces to a generalized eigenvalue problem with constant coefficients:

$$\begin{pmatrix} ic_0(\mu+D)\cosh(\alpha(\mu+D)) & (\mu+D)\sinh(\alpha(\mu+D)) \\ -1 & ic_0(\mu+D)\end{pmatrix}\mathbf{w}_{\mu,0} = \lambda_{\mu,0}\begin{pmatrix}\cosh(\alpha(\mu+D)) & 0 \\ 0 & 1\end{pmatrix}\mathbf{w}_{\mu,0}, \tag{4.42}$$

where $D=-i\partial_x$. The eigenvalues of (4.42) are

$$\lambda^{(\sigma)}_{\mu,0,n} = -i\Omega_\sigma(n+\mu), \qquad \sigma=\pm1, \qquad n\in\mathbb{Z}, \tag{4.43}$$

with

$$\Omega_\sigma(z) = -c_0 z + \sigma\omega(z), \tag{4.44a}$$

$$\omega(z) = \operatorname{sgn}(z)\sqrt{z\tanh(\alpha z)}. \tag{4.44b}$$

Equation (4.44a) is the linear dispersion relation of the nondimensional Euler equations in a frame traveling with velocity c_0. The parameter σ specifies the branch of the dispersion relation. As expected, (4.43) gives a countable collection of eigenvalues for each $\mu \in [-1/2, 1/2)$. These eigenvalues are purely imaginary, and therefore, the zero-amplitude Stokes waves are spectrally stable.

High-frequency instabilities develop from nonzero eigenvalues of (4.42) that have collided for a Floquet exponent μ_0 that satisfies:

$$\lambda^{(\sigma_1)}_{\mu_0,0,n} = \lambda^{(\sigma_2)}_{\mu_0,0,n+p} \neq 0, \tag{4.45}$$

for $p \in \mathbb{Z} \setminus \{0\}$.These eigenvalues occur only if $\sigma_1 \neq \sigma_2$ and $|p| > 1$ [36]. More specifically, we have the following theorem:

Theorem 4.5.1. *Let $c_0 > 0$, $\sigma_1 = 1$, and $\sigma_2 = -1$. For each $p \in \mathbb{Z} \setminus \{0, \pm 1\}$, there exists a unique Floquet exponent $\mu_{0,p} \in [-1/2, 1/2)$ and unique integer n_p such that*

$$\lambda_{0,p} = \lambda^{(1)}_{\mu_{0,p},0,n_p} = \lambda^{(-1)}_{\mu_{0,p},0,n_p+p} \neq 0. \tag{4.46}$$

The eigenvalues have the symmetry $\lambda_{0,-p} = -\lambda_{0,p}$, and the magnitudes of the eigenvalues are strictly monotonically increasing as $|p| \to \infty$. The corresponding eigenfunctions are

$$\mathbf{w}_{0,p} = \beta_0 \begin{pmatrix} 1 \\ \frac{-i}{\omega(n_p+\mu_{0,p})} \end{pmatrix} e^{in_p x} + \gamma_0 \begin{pmatrix} 1 \\ \frac{i}{\omega(n_p+p+\mu_{0,p})} \end{pmatrix} e^{i(n_p+p)x}, \tag{4.47}$$

where ω is given by (4.44b) *and $\beta_0, \gamma_0 \in \mathbb{C} \setminus \{0\}$.*

An important corollary is the following:

Corollary 4.5.1. *Let* $c_0 > 0$*. Let* $\lambda_{0,p}$ *be given by* (4.46) *for some* $p \in \mathbb{Z} \setminus \{0, \pm 1\}$*. Then,*

$$\omega(n_p + \mu_{0,p})\omega(n_p + p + \mu_{0,p}) > 0, \tag{4.48}$$

and

$$c_{g,1}(n_p + \mu_{0,p}) \neq c_{g,-1}(n_p + p + \mu_{0,p}), \tag{4.49}$$

where $c_{g,\sigma}(z)$ *is the group velocity of* $\Omega_\sigma(z)$*,* i.e., $c_{g,\sigma}(z) = \Omega_{\sigma,z}(z)$*.*

Similar results hold if $c_0 < 0$ provided $\sigma_1 = -1$ and $\sigma_2 = 1$. To prove Theorem 4.4.1 and Corollary 4.4.1, note that Ω_σ in (4.44b) is the same as that for the HPBW system up to a factor of $\sqrt{\alpha}$. Then, Theorem 3.3.1 and Lemma 3.3.3 imply Theorem 4.4.1 and Corollary 4.4.1, respectively.

As with the HPBW system, the product (4.48) is equivalent to the Krein condition developed by MacKay and Saffman [67] and, in more generality, Deconinck and Trichtchenko [36]. Corollary 4.4.1 guarantees this condition is satisfied for all nonzero collided eigenvalues of (4.42). As we will see, both (4.48) and (4.49) are crucial to the formal asymptotic expansions of the high-frequency instabilities.

Remark 4.5.1. *In infinite depth,* $\mu_{0,p}$ *and* $\lambda_{0,p}$ *are known explicitly. For* $c_0 > 0$*,*

$$\mu_{0,p} = -\frac{sgn(p)}{8}\big((-1)^p + 1\big), \tag{4.50a}$$

$$\lambda_{0,p} = i\frac{sgn(p)}{4}\big(1 - p^2\big). \tag{4.50b}$$

These eigenvalues have the conjugate symmetry $\lambda_{0,-p} = -\lambda_{0,p}$*, and* $\{|\lambda_{0,p}|\}$ *is strictly monotonically increasing as* $|p| \to \infty$*, similar to the finite-depth case.*

4.6 Asymptotic Description of the $p = 2$ *High-Frequency Instability*

We develop a perturbation method to obtain the leading-order behavior of the high-frequency isola that arises from $\lambda_{0,p}$ with $p = 2$. According to Theorem 4.4.1, this isola is the closest to the origin. We assume the spectral data of (4.35) corresponding to the isola vary analytically with ε, including the Floquet exponent:

$$\lambda_{\mu(\varepsilon),\varepsilon} = \lambda_{0,p} + \lambda_1\varepsilon + \lambda_2\varepsilon^2 + \mathcal{O}\left(\varepsilon^3\right), \tag{4.51a}$$

$$\mathbf{w}_{\mu(\varepsilon),\varepsilon} = \mathbf{w}_{0,p} + \mathbf{w}_1\varepsilon + \mathbf{w}_2\varepsilon^2 + \mathcal{O}\left(\varepsilon^3\right), \tag{4.51b}$$

$$\mu(\varepsilon) = \mu_{0,p} + \mu_1\varepsilon + \mu_2\varepsilon^2 + \mathcal{O}\left(\varepsilon^3\right). \tag{4.51c}$$

If the Floquet exponent is fixed, at most two eigenvalues are found on the isola by standard eigenvalue perturbation theory [57]. If instead the Floquet exponent is formally expanded in ε, all of the eigenvalues on the isola can be approximated at once. We see below that the leading-order behavior of these eigenvalues is obtained at $\mathcal{O}\left(\varepsilon^2\right)$, similar to the HPBW system.

Remark 4.6.1. *Choosing $p = -2$ gives the isola conjugate to the $p = 2$ isola. Thus, we choose $p = 2$ without loss of generality.*

Similar to previous chapters, we impose the following normalization on $\mathbf{w}_{\mu(\varepsilon),\varepsilon}$:

$$\mathcal{F}_{n_p}[\mathbf{w}_{\mu(\varepsilon),\varepsilon} \cdot \mathbf{e}_1] = 1, \tag{4.52}$$

where $n_p \in \mathbb{Z}$ is given by Theorem 4.4.1 and $\mathbf{e}_1 = (1,0)^T$. Then, $\beta_0 = 1$ in (4.47), and all subsequent corrections of $\mathbf{w}_{\mu(\varepsilon),\varepsilon}$ do not include the Fourier mode $\exp(in_px)$ in the first component. The eigenvalue and Floquet expansions, (4.51a) and (4.51c) above, are unaffected by this normalization. For ease of notation, let $\lambda_{0,p} \to \lambda_0$, $\mathbf{w}_{0,p} \to \mathbf{w}_0$, $\mu_{0,p} \to \mu_0$, and $n_p \to n$.

Remark 4.6.2. *Several of the asymptotic expressions that follow are suppressed for ease of readability. See the Mathematica file* wwp_isola_p2.nb *for access to these expressions.*

4.6.1 The $\mathcal{O}(\varepsilon)$ Problem

Substituting expansions (4.51a)-(4.51c) into the generalized eigenvalue problem (4.35) and equating powers of ε, terms of $\mathcal{O}\left(\varepsilon^0\right)$ cancel by the choice of λ_0, $\mathbf{w}_0$, and μ_0. Terms of $\mathcal{O}(\varepsilon)$

yield

$$(L_0 - \lambda_0 R_0)\,\mathbf{w}_1 = (\lambda_1 R_0 - (L_1 - \lambda_0 R_1))\,\mathbf{w}_0, \tag{4.53}$$

where

$$L_j = \frac{1}{j!}\frac{\partial^j \mathcal{L}_{\mu(\varepsilon),\varepsilon}}{\partial \varepsilon^j}\bigg|_{\varepsilon=0}, \qquad R_j = \frac{1}{j!}\frac{\partial^j \mathcal{R}_{\mu(\varepsilon),\varepsilon}}{\partial \varepsilon^j}\bigg|_{\varepsilon=0}, \qquad j \in \mathbb{W}. \tag{4.54}$$

If (4.53) can be solved for $\mathbf{w}_1$, the inhomogeneous terms of (4.53) must be orthogonal to the nullspace of the adjoint of $L_0 - \lambda_0 R_0$ by the Fredholm alternative. A direct calculation shows

$$\mathrm{Null}\left((L_0 - \lambda_0 R_0)^\dagger\right) = \mathrm{Span}\left\{\begin{pmatrix} 1 \\ -i\omega\,(n+\mu_0)\end{pmatrix} e^{inx}, \begin{pmatrix} 1 \\ i\omega\,(n+p+\mu_0)\end{pmatrix} e^{i(n+p)x}\right\}. \tag{4.55}$$

Hence, we impose the following solvability conditions on (4.53):

$$\left\langle \begin{pmatrix} 1 \\ -i\omega\,(n+\mu_0)\end{pmatrix} e^{inx}, (\lambda_1 R_0 - (L_1 - \lambda_0 R_1))\,\mathbf{w}_0 \right\rangle = 0, \tag{4.56a}$$

$$\left\langle \begin{pmatrix} 1 \\ i\omega\,(n+p+\mu_0)\end{pmatrix} e^{i(n+p)x}, (\lambda_1 R_0 - (L_1 - \lambda_0 R_1))\,\mathbf{w}_0 \right\rangle = 0, \tag{4.56b}$$

where $\langle \cdot, \cdot \rangle$ is the standard complex inner-product on $\mathrm{L}^2_{\mathrm{per}}(-\pi,\pi) \times \mathrm{L}^2_{\mathrm{per}}(-\pi,\pi)$. Simplifying both conditions, we arrive at

$$\lambda_1 + i\mu_1 c_{g,1}\,(n+\mu_0) = 0, \tag{4.57a}$$

$$\gamma_0\,(\lambda_1 + i\mu_1 c_{g,-1}\,(n+p+\mu_0)) = 0. \tag{4.57b}$$

Since $\gamma_0 \neq 0$ and $c_{g,1}\,(n+\mu_0) \neq c_{g,-1}\,(n+p+\mu_0)$, we must have

$$\lambda_1 = 0 = \mu_1. \tag{4.58}$$

Thus no instabilities are found at $\mathcal{O}\,(\varepsilon)$.

Before proceeding to $\mathcal{O}(\varepsilon^2)$, we invert $L_0 - \lambda_0 R_0$ against its range to find the particular solution of $\mathbf{w}_1$. Uniting the particular solution with the nullspace of $L_0 - \lambda_0 R_0$,

$$\mathbf{w}_1 = \sum_{\substack{j=n-1 \\ j\neq n,n+p}}^{n+p+1} \hat{\mathcal{W}}_{1,j} e^{ijx} + \beta_1 \begin{pmatrix} 1 \\ \frac{-i}{\omega(n+\mu_0)} \end{pmatrix} e^{inx} + \gamma_1 \begin{pmatrix} 1 \\ \frac{i}{\omega(n+p+\mu_0)} \end{pmatrix} e^{i(n+p)x}, \tag{4.59}$$

where the coefficients $\hat{\mathcal{W}}_{1,j}$ depend on α (possibly through intermediate dependencies on known zeroth-order results) and at most linearly on γ_0. The parameter $\gamma_1 \in \mathbb{C}$ is free at this order. By our choice of normalization (4.52), $\beta_1 = 0$. Thus,

$$\mathbf{w}_1 = \sum_{\substack{j=n-1 \\ j\neq n,n+p}}^{n+p+1} \hat{\mathcal{W}}_{1,j} e^{ijx} + \gamma_1 \begin{pmatrix} 1 \\ \frac{i}{\omega(n+p+\mu_0)} \end{pmatrix} e^{i(n+p)x}. \tag{4.60}$$

4.6.2 The $\mathcal{O}(\varepsilon^2)$ Problem

At $\mathcal{O}(\varepsilon^2)$, the spectral problem (4.35) is

$$(L_0 - \lambda_0 R_0)\,\mathbf{w}_2 = \lambda_2 R_0 \mathbf{w}_0 - (L_1 - \lambda_0 R_1)\,\mathbf{w}_1 - (L_2 - \lambda_0 R_2)\,\mathbf{w}_0, \tag{4.61}$$

using (4.58). Proceeding as above, we obtain the solvability conditions for (4.61):

$$2\left(\lambda_2 + i\mathfrak{c}_{2,1,n}\right) + i\gamma_0 \mathfrak{s}_{2,n} = 0, \tag{4.62a}$$

$$2\gamma_0\left(\lambda_2 + i\mathfrak{c}_{2,-1,n+p}\right) + i\mathfrak{s}_{2,n+p} = 0, \tag{4.62b}$$

where

$$\mathfrak{c}_{2,\sigma,j} = \mu_2 c_{g,\sigma}\left(j+\mu_0\right) - \mathfrak{p}_{2,j}. \tag{4.63}$$

The quantities $\mathfrak{s}_{2,j}$ and $\mathfrak{p}_{2,j}$ depend only on α (possibly through known zeroth- and first-order quantities). Using the collision condition (4.45), it can be shown that the product of $\mathfrak{s}_{2,n}$ and $\mathfrak{s}_{2,n+p}$ is related to a perfect square:

$$\mathfrak{s}_{2,n}\mathfrak{s}_{2,n+p} = -\frac{\mathcal{S}_2^2}{\omega(n+\mu_0)\omega(n+p+\mu_0)}, \tag{4.64}$$

where

$$\mathcal{S}_2 = \mathcal{T}_{2,1} + \mathcal{T}_{2,2}\hat{N}_{2,2} + \mathcal{T}_{2,3}\hat{Q}_{2,2}. \tag{4.65}$$

The expressions $\mathcal{T}_{2,j}$ are functions only of α, as are the Stokes wave corrections $\hat{N}_{2,2}$ and $\hat{Q}_{2,2}$. When fully expanded, $\mathcal{S}_2$ consists of roughly 100 terms (depending on how it is written), but each term depends only on α. The full expression of $\mathcal{S}_2$ is found in the companion Mathematica file.

Solving for λ_2 in (4.62a)-(4.62b),

$$\lambda_2 = -i\left(\frac{\mathfrak{c}_{2,-1,n+p} + \mathfrak{c}_{2,1,n}}{2}\right) \pm \sqrt{-\left(\frac{\mathfrak{c}_{2,-1,n+p} - \mathfrak{c}_{2,1,n}}{2}\right)^2 + \frac{\mathcal{S}_2^2}{4\omega(n+\mu_0)\omega(n+p+\mu_0)}}. \tag{4.66}$$

From Corollary 4.4.1, $\omega(n+\mu_0)\omega(n+p+\mu_0) > 0$. Thus, λ_2 has nonzero real part for $\mu_2 \in (M_{2,-}, M_{2,+})$, where

$$M_{2,\pm} = \mu_{2,*} \pm \frac{|\mathcal{S}_2|}{|c_{g,-1}(n+p+\mu_0) - c_{g,1}(n+\mu_0)|\sqrt{\omega(n+\mu_0)\omega(n+p+\mu_0)}}, \tag{4.67}$$

and

$$\mu_{2,*} = \frac{\mathfrak{p}_{2,n+p} - \mathfrak{p}_{2,n}}{c_{g,-1}(n+p+\mu_0) - c_{g,1}(n+\mu_0)}, \tag{4.68}$$

provided $\mathcal{S}_2 \not\equiv 0$. Note that Corollary 4.4.1 guarantees (4.67) and (4.68) are well-defined, since $c_{g,-1}(n+p+\mu_0)$ and $c_{g,1}(n+\mu_0)$ are never equal.

A plot of $\mathcal{S}_2$ *vs.* α reveals that $\mathcal{S}_2 \neq 0$ except at $\alpha_1 = 1.8494040837...$ (Figure 4.1). For this isolated value of α, λ_2 has no real part at $\mathcal{O}(\varepsilon^2)$. We conjecture that small-amplitude Stokes waves of all wavenumbers and in all depths are unstable to the high-frequency instability closest to the origin, with the possible exception of Stokes waves with $\alpha = \alpha_1$.

To $\mathcal{O}(\varepsilon^2)$, the $p = 2$ isola is an ellipse in the complex spectral plane. The ellipse is constructed explicitly from the real and imaginary parts of

$$\lambda(\mu_2; \varepsilon) = \lambda_0 + \lambda_2(\mu_2)\varepsilon^2, \tag{4.69}$$

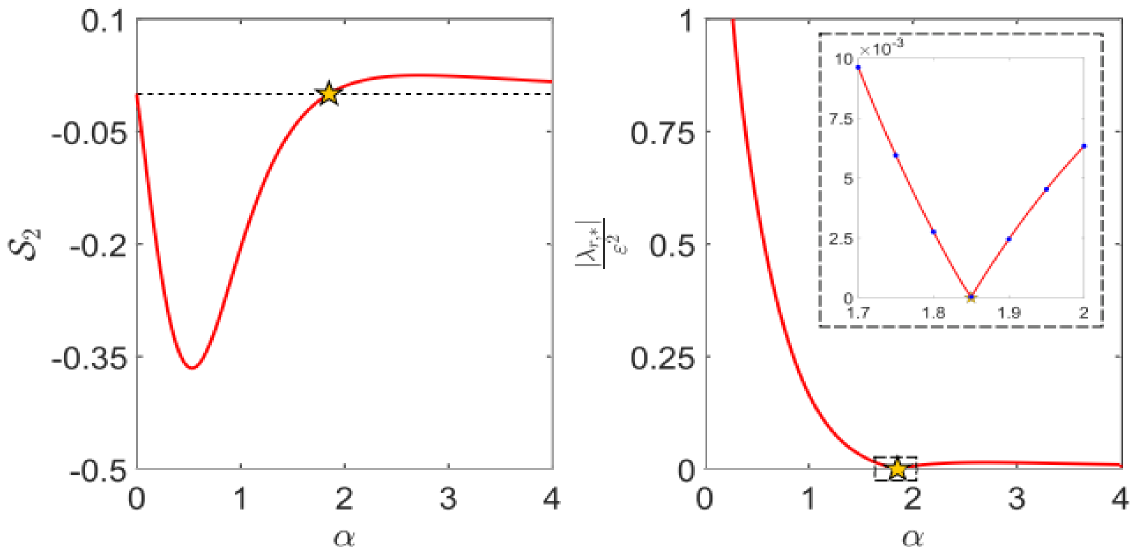

Figure 4.1: (Left) A plot of $\mathcal{S}_2$ *vs.* α (solid red). The zero of $\mathcal{S}_2$ for $\alpha > 0$ is $\alpha_1 = 1.8494040837\ldots$ (gold star). (Right) The real part $\lambda_{r,*}$ of the most unstable eigenvalue on the $p = 2$ isola as a function of α according to our asymptotic calculations (solid red). The real part of the eigenvalue is normalized by ε^2 for better visibility. We zoom-in around $\alpha = \alpha_1$ (gold star) in the inlay. The real part of the most unstable eigenvalue on the isola vanishes as $\alpha \to \alpha_1$ according to our asymptotic calculations, which agrees with our numerical results using the FFH method with $\varepsilon = 0.01$ (blue dots).

for $\mu_2 \in (M_{2,-}, M_{2,+})$. This ellipse has semi-major and -minor axes that are $\mathcal{O}(\varepsilon^2)$, and its center drifts from λ_0 along the imaginary axis like $\mathcal{O}(\varepsilon^2)$. Similarly, the interval of Floquet exponents parameterizing this ellipse has width $\mathcal{O}(\varepsilon^2)$ and drifts from μ_0 like $\mathcal{O}(\varepsilon^2)$. In Figure 4.2, we compare the ellipse with a subset of numerically computed eigenvalues on the $p = 2$ isola for $\varepsilon = 0.01$ and find excellent agreement. We find similar agreement between the Floquet parameterization of the ellipse and of the numerically computed isola. The eigenvalue of largest real part on the ellipse occurs when $\mu_2 = \mu_{2,*}$. Thus, the leading-order behavior of the most unstable eigenvalue on the $p = 2$ isola has real and imaginary parts

$$\lambda_{r,*} = \frac{|\mathcal{S}_2|}{2\sqrt{\omega(n+\mu_0)\omega(n+p+\mu_0)}}\varepsilon^2 + \mathcal{O}\left(\varepsilon^3\right), \tag{4.70a}$$

$$\lambda_{i,*} = -\Omega_1\left(n+\mu_0\right) - \left(\frac{\mathfrak{p}_{2,n+p}c_{g,1}\left(n+\mu_0\right) - \mathfrak{p}_{2,n}c_{g,-1}\left(n+p+\mu_0\right)}{c_{g,-1}\left(n+p+\mu_0\right) - c_{g,1}\left(n+\mu_0\right)}\right)\varepsilon^2 + \mathcal{O}\left(\varepsilon^3\right), \tag{4.70b}$$

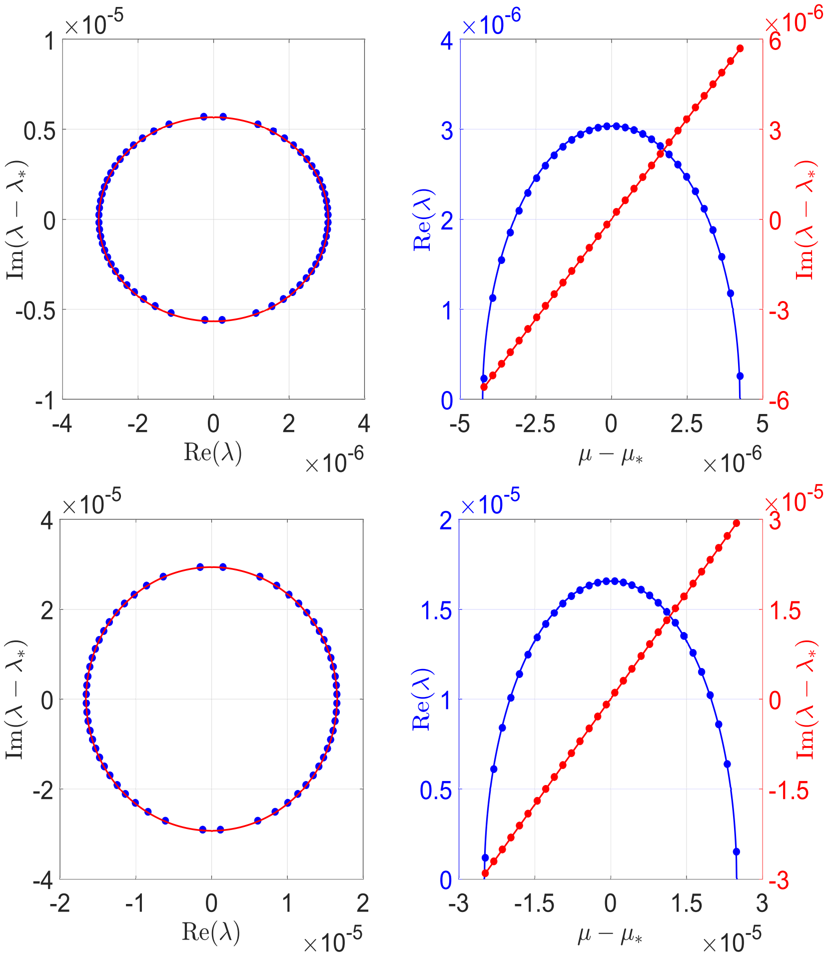

Figure 4.2: (Top, Left) The $p = 2$ isola with $\alpha = 1.5$ and $\varepsilon = 0.01$. The most unstable eigenvalue λ_* is removed from the imaginary axis for better visibility. The solid red curve is the ellipse obtained by our asymptotic calculations. The blue dots are a subset of eigenvalues from the numerically computed isola using the FFH method. (Top, Right) The Floquet parameterization of the real (blue) and imaginary (red) parts of the isola on the left. The most unstable eigenvalue λ_* and its corresponding Floquet exponent μ_* are removed from the imaginary and Floquet axes, respectively, for better visibility. The solid curves are asymptotic results. The colored dots are FFH results. (Bottom, Left & Right) Same with $\alpha = 1$.

respectively. The corresponding Floquet exponent is

$$\mu_* = \mu_0 + \mu_{2,*}\varepsilon^2 + \mathcal{O}\left(\varepsilon^3\right). \tag{4.71}$$

These expansions agree well with numerical results (Figure 4.3).

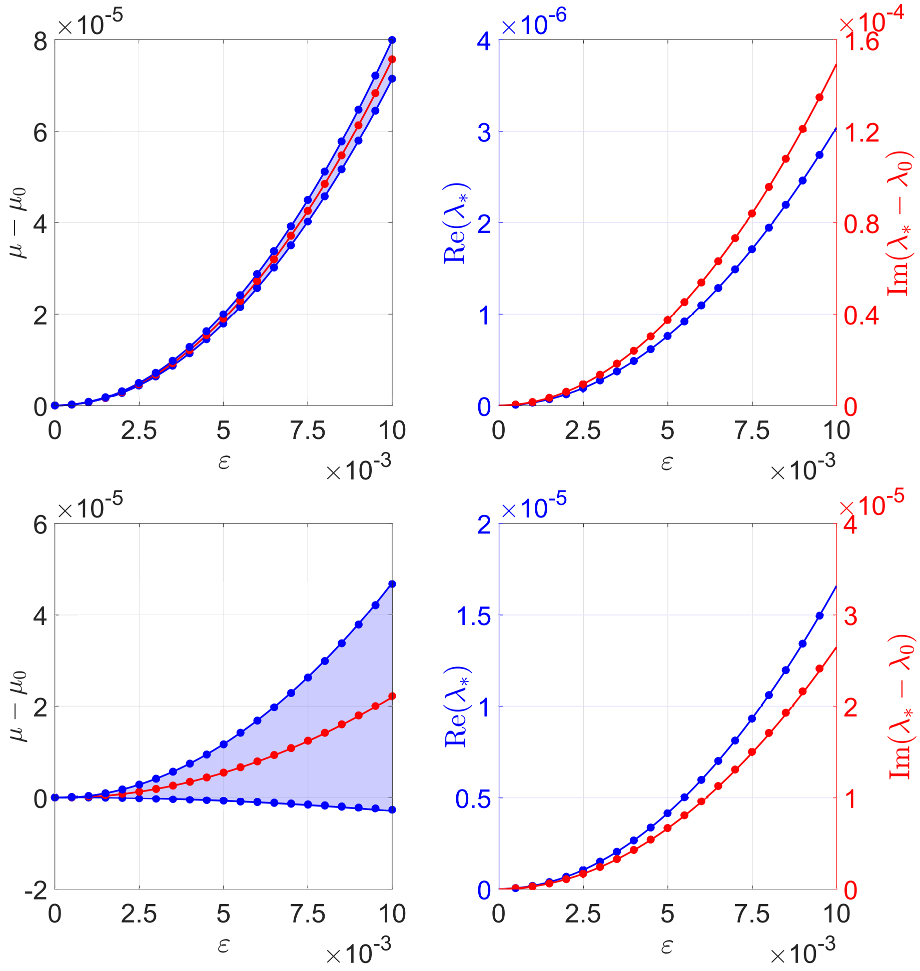

Figure 4.3: (Top, Left) The interval of Floquet exponents parameterizing the $p = 2$ isola as a function of ε for $\alpha = 1.5$. The zeroth-order correction of the Floquet exponent is removed from the Floquet axis for better visibility. The solid blue curves are the boundaries of this interval according to our asymptotic calculations. The blue dots are the boundaries computed numerically by the FFH method. The solid red curve gives the Floquet exponent of the most unstable eigenvalue on the isola according to our asymptotic calculations. The red dots are the Floquet exponent of the most unstable eigenvalue as computed by the FFH method. (Top, Right) The real (blue) and imaginary (red) parts of the most unstable eigenvalue of the $p = 2$ isola with $\alpha = 1.5$ as a function of ε. The zeroth-order correction of the eigenvalue is removed from the imaginary axis for better visibility. The solid curves are our asymptotic calculations. The colored dots are our numerical results using the FFH method. (Bottom, Left & Right) Same with $\alpha = 1$.

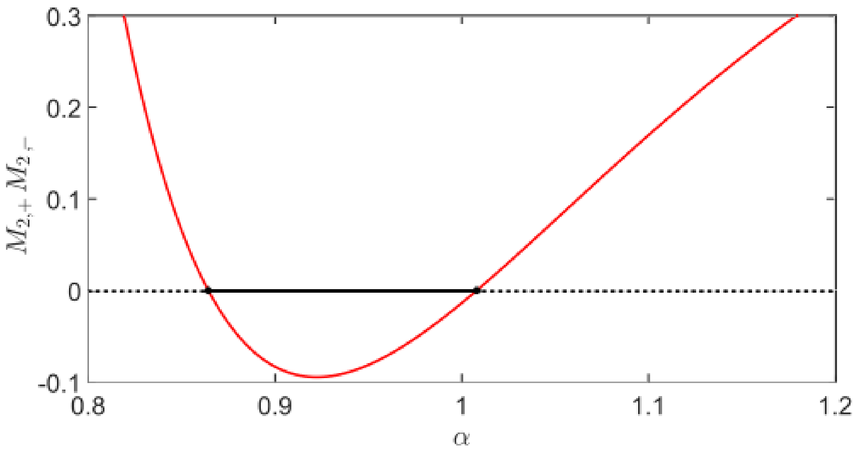

Figure 4.4: A plot of $M_{2,+}M_{2,-}$ *vs.* α (solid red). We find $M_{2,+}M_{2,-} < 0$ only when $\alpha \in (0.8643029367..., 1.0080416077...)$ (solid black). If $M_{2,+}M_{2,-} < 0$, the boundaries of the Floquet exponents parameterizing the $p = 2$ isola have opposite concavities at $\varepsilon = 0$. Only then does μ_0 remain in the interval of Floquet exponents parameterizing the isola for positive ε. can one find an eigenvalue with corresponding Floquet exponent μ_0 on this isola.

Remark 4.6.3. *According to Figure 4.3, μ_0 is contained within the interval parameterizing the $p = 2$ isola if the boundaries of this interval have opposite concavity at $\varepsilon = 0$. This occurs if and only if $M_{2,+}M_{2,-} < 0$. In Figure 4.4, we plot $M_{2,+}M_{2,-}$ as a function of α. We find $M_{2,+}M_{2,-} < 0$ only if $\alpha \in (0.8643029367..., 1.0080416077...)$. As we have demonstrated, to account for $p = 2$ high-frequency instabilities that occur outside this interval, it is necessary to expand the Floquet exponent as a power series in ε about μ_0.*

4.6.3 The Case of Infinite Depth

In infinite depth, the $p = 2$ isola originates from the eigenvalue

$$\lambda_0 = -\frac{3}{4}i, \tag{4.72}$$

with corresponding Floquet exponent $\mu_0 = -1/4$ and $n = -2$, see Remark 6. The corresponding eigenfunction, after normalizing, is

$$\mathbf{w}_0 = \begin{pmatrix} 1 \\ \frac{2}{3}i \end{pmatrix} e^{inx} + \gamma_0 \begin{pmatrix} 1 \\ -2i \end{pmatrix} e^{i(n+p)x}, \tag{4.73}$$

where $\gamma_0 \in \mathbb{C} \setminus \{0\}$. We modify the generalized eigenvalue problem (4.35) according to Remark 5 and expand the spectral data as a power series in ε about the values above.

Terms of $\mathcal{O}(\varepsilon^0)$ cancel by construction. At $\mathcal{O}(\varepsilon)$, the solvability conditions simplify to

$$\lambda_1 = 0 = \mu_1, \tag{4.74}$$

as in finite depth, and the normalized solution of the $\mathcal{O}(\varepsilon)$ problem is

$$\mathbf{w}_1 = \sum_{\substack{j=n-1 \\ j\neq n,n+p}}^{n+p+1} \hat{\mathcal{W}}_{1,j,\infty} e^{ijx} + \gamma_1 \begin{pmatrix} 1 \\ -2i \end{pmatrix} e^{i(n+p)x}, \tag{4.75}$$

where the coefficients $\hat{\mathcal{W}}_{1,j,\infty}$ depend at most linearly on γ_0.

At $\mathcal{O}(\varepsilon^2)$, the solvability conditions are

$$\lambda_2 + i\mathfrak{c}_{2,1,n,\infty} = 0, \tag{4.76a}$$

$$\gamma_0 \left(\lambda_2 + i\mathfrak{c}_{2,-1,n+p,\infty}\right) = 0, \tag{4.76b}$$

where

$$\mathfrak{c}_{2,\sigma,j,\infty} = \mu_2 c_{g,\sigma,\infty}(j+\mu_0) - \mathfrak{p}_{2,j,\infty}, \tag{4.77}$$

with $c_{g,\sigma,\infty}(z) = \lim_{\alpha\to\infty} \Omega_{\sigma,z}(z)$, $\mathfrak{p}_{2,n,\infty} = 9/8$, and $\mathfrak{p}_{2,n+p,\infty} = -1/16$.

Because $\gamma_0 \neq 0$, equations (4.76a)-(4.76b) reduce to a linear system for λ_2 and μ_2. The solution of this system is

$$\lambda_2 = \frac{55}{32}i, \qquad \mu_2 = \frac{57}{64}. \tag{4.78}$$

Since λ_2 is purely imaginary, the leading-order behavior of the $p = 2$ isola does not occur at $\mathcal{O}(\varepsilon^2)$, as expected from (4.70a), since $\lim_{\alpha\to\infty} \mathcal{S}_2 = 0$. Thus, while the asymptotic expressions involved in infinite depth are simpler than those in finite depth, the leading-order behavior of the $p = 2$ isola requires a higher-order calculation in infinite depth. We obtain the normalized solution of the $\mathcal{O}\left(\varepsilon^2\right)$ problem:

$$\mathbf{w}_2 = \sum_{j=n-2}^{n+p+2} \hat{\mathcal{W}}_{2,j,\infty} e^{ijx} + \gamma_2 \begin{pmatrix} 1 \\ -2i \end{pmatrix} e^{i(n+p)x}, \tag{4.79}$$

where the coefficients $\hat{\mathcal{W}}_{2,j,\infty}$ depend at most linearly on γ_0 and γ_1 while $\gamma_2 \in \mathbb{C}$ is a free parameter at this order.

At $\mathcal{O}\left(\varepsilon^3\right)$, the solvability conditions reduce to

$$\lambda_3 + i\mu_3 c_{g,1,\infty}\left(n + \mu_0\right) = 0, \tag{4.80a}$$

$$\gamma_0\left(\lambda_3 + i\mu_3 c_{g,-1,\infty}\left(n + p + \mu_0\right)\right) = 0. \tag{4.80b}$$

As in finite depth, $c_{g,1,\infty}\left(n + \mu_0\right) \neq c_{g,-1,\infty}\left(n + p + \mu_0\right)$, and since $\gamma_0 \neq 0$, we must have

$$\lambda_3 = 0 = \mu_3. \tag{4.81}$$

No instability is observed at this order. The normalized solution of the $\mathcal{O}\left(\varepsilon^3\right)$ problem is

$$\mathbf{w}_3 = \sum_{j=n-3}^{n+p+3} \hat{\mathcal{W}}_{3,j,\infty} e^{ijx} + \gamma_3 \begin{pmatrix} 1 \\ -2i \end{pmatrix} e^{i(n+p)x}, \tag{4.82}$$

where the coefficients $\hat{\mathcal{W}}_{3,j,\infty}$ depend at most linearly on γ_0, γ_1, and γ_2 while the parameter $\gamma_3 \in \mathbb{C}$ is free at this order.

At $\mathcal{O}\left(\varepsilon^4\right)$, the solvability conditions are

$$2\left(\lambda_4 + i\mathfrak{c}_{4,1,n,\infty}\right) + i\gamma_0 \mathfrak{s}_{4,n,\infty} = 0, \tag{4.83a}$$

$$2\gamma_0\left(\lambda_4 + i\mathfrak{c}_{4,-1,n+p,\infty}\right) + i\mathfrak{s}_{4,n+p,\infty} = 0, \tag{4.83b}$$

where

$$\mathfrak{c}_{4,\sigma,j,\infty} = \mu_4 c_{g,\sigma,\infty}\left(j + \mu_0\right) - \mathfrak{p}_{4,j,\infty}, \tag{4.84}$$

with $\mathfrak{s}_{4,n,\infty} = -111/256$, $\mathfrak{s}_{4,n+p,\infty} = 37/256$, $\mathfrak{p}_{4,n,\infty} = 24119/12288$, and $\mathfrak{p}_{4,n+p,\infty} = 24985/36864$. Solving (4.83a)-(4.83b) for λ_4, we find the explicit formula

$$\lambda_4 = \frac{(48671 + 49152\mu_4)}{36864}i \pm \frac{\sqrt{-134933977 + 291053568\mu_4 - 150994944\mu_4^2}}{18432}. \tag{4.85}$$

Equation (4.85) has nonzero real part provided

$$\mu_4 \in \left(\frac{11843}{12288} - \frac{111\sqrt{3}}{1024}, \frac{11843}{12288} + \frac{111\sqrt{3}}{1024}\right). \tag{4.86}$$

Thus, the $p = 2$ isola is an ellipse to $\mathcal{O}\left(\varepsilon^4\right)$ given by the real and imaginary parts of

$$\lambda(\mu_4; \varepsilon) = -\frac{3}{4}i + \frac{55}{32}i\varepsilon^2 + \lambda_4(\mu_4)\varepsilon^4, \tag{4.87}$$

for μ_4 in (4.86). Unlike in finite depth, this ellipse has semi-major and -minor axes that are $\mathcal{O}\left(\varepsilon^4\right)$, while the center drifts from λ_0 like $\mathcal{O}\left(\varepsilon^2\right)$. Similarly, the Floquet parameterization of the isola has width $\mathcal{O}\left(\varepsilon^4\right)$ and drifts from μ_0 like $\mathcal{O}\left(\varepsilon^2\right)$.

In Figure 4.5, we compare the asymptotically computed ellipse with a subset of numerically computed eigenvalues on the $p = 2$ isola for $\varepsilon = 0.01$. Notice this ellipse is considerably smaller than that in finite depth for comparable wave amplitude (Figure 4.2). Excellent agreement is found between the asymptotic and numerical predictions. Similar agreement is found between the Floquet parameterization of the ellipse and of the numerically computed isola.

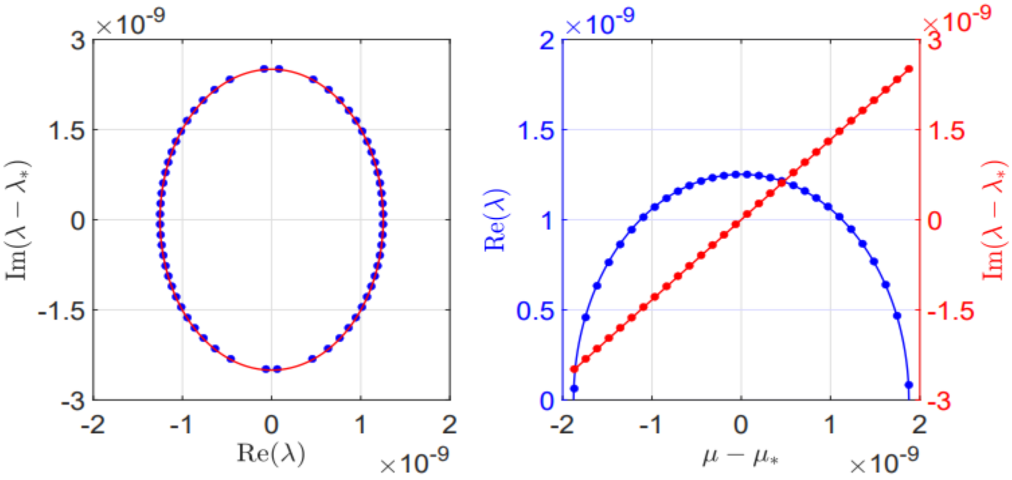

Figure 4.5: (Left) The $p = 2$ isola with $\alpha = \infty$ and $\varepsilon = 0.01$. The most unstable eigenvalue λ_* is removed from the imaginary axis for better visibility. The solid red curve is the ellipse obtained by our asymptotic calculations. The blue dots are a subset of eigenvalues from the numerically computed isola using the FFH method. (Right) The Floquet parameterization of the real (blue) and imaginary (red) parts of the isola. The most unstable eigenvalue λ_* and its corresponding Floquet exponent μ_* are removed from the imaginary and Floquet axes, respectively, for better visibility. The solid curves are our asymptotic results. The colored dots are our numerical results using the FFH method.

The eigenvalue of largest real part on the ellipse occurs when $\mu_4 = 11843/36864$. Thus, the real and imaginary parts of the most unstable eigenvalue on the isola have asymptotic expansions

$$\lambda_{r,*} = \frac{37\sqrt{3}}{512}\varepsilon^4 + \mathcal{O}\left(\varepsilon^5\right), \tag{4.88}$$

$$\lambda_{i,*} = -\frac{3}{4} + \frac{55}{32}\varepsilon^2 + \frac{96043}{36864}\varepsilon^4 + \mathcal{O}\left(\varepsilon^5\right), \tag{4.89}$$

respectively. The corresponding Floquet exponent has expansion

$$\mu_* = -\frac{1}{4} + \frac{57}{64}\varepsilon^2 + \frac{11843}{36864}\varepsilon^4 + \mathcal{O}\left(\varepsilon^5\right). \tag{4.90}$$

These expansions are compared with numerical results in Figure 4.6.

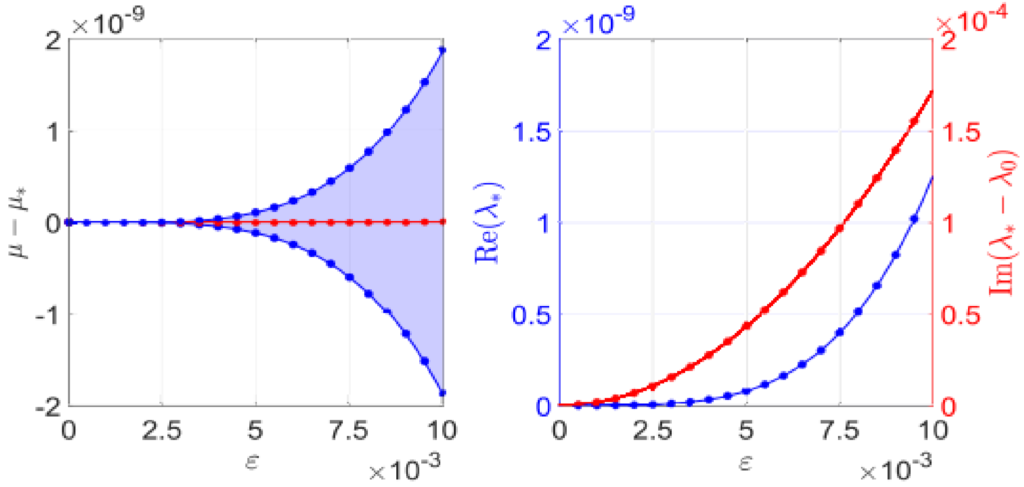

Figure 4.6: (Left) The interval of Floquet exponents parameterizing the $p = 2$ isola as a function of ε for $\alpha = \infty$. The most unstable Floquet exponent μ_* is removed from the Floquet axis for better visibility. The solid blue curves are the boundaries of this interval according to our asymptotic calculations. The blue dots are the boundaries computed numerically by the FFH method. The solid red curve gives the Floquet exponent of the most unstable eigenvalue on the isola according to our asymptotic calculations. The red dots are the Floquet exponent of the most unstable eigenvalue as computed by the FFH method. (Right) The real (blue) and imaginary (red) parts of the most unstable eigenvalue of the $p = 2$ isola with $\alpha = \infty$ as a function of ε. The zeroth-order correction of the eigenvalue is removed from the imaginary axis for better visibility. The solid curves are our asymptotic calculations. The colored dots are our numerical results using the FFH method.

4.7 Asymptotic Description of the $p = 3$ High-Frequency Instability

We extend the perturbation method developed in the previous section to obtain the leading-order behavior of the high-frequency isola that arises from $\lambda_{0,p}$ with $p = 3$. This isola is the second closest to the origin by Theorem 4.4.1, and its leading-order behavior is obtained at $\mathcal{O}(\varepsilon^3)$. As in the previous section, we expand the spectral data of (4.35) according to (4.51a)-(4.51c) and normalize the eigenfunctions according to (4.52) for convenience. The perturbation method proceeds as before, with two major changes:

(i) At $\mathcal{O}(\varepsilon^2)$, the solvability conditions are independent of γ_0 and linear in λ_2 and μ_2. As a consequence, λ_2 is purely imaginary, and the leading-order behavior of the isola is undetermined at this order.

(ii) At $\mathcal{O}(\varepsilon^3)$, the solvability conditions depend on γ_0, λ_3, and γ_1. Using solvability conditions from the previous order together with the collision condition (4.45), one shows that the dependence on γ_1 vanishes from these conditions.

Remark 4.7.1. *For explicit representations of the asymptotic expressions derived in this section, see the Mathematica file* wwp_isola_p3.nb*.*

4.7.1 The $\mathcal{O}(\varepsilon)$ Problem

At $\mathcal{O}(\varepsilon)$, the spectral problem takes the form (4.53). The solvability conditions simplify to

$$\lambda_1 = 0 = \mu_1, \tag{4.91}$$

and the normalized solution of the $\mathcal{O}(\varepsilon)$ problem is

$$\mathbf{w}_1 = \sum_{\substack{j=n-1 \\ j\neq n,n+p}}^{n+p+1} \hat{\mathcal{W}}_{1,j} e^{ijx} + \gamma_1 \begin{pmatrix} 1 \\ \frac{i}{\omega(n+p+\mu_0)} \end{pmatrix} e^{i(n+p)x}, \tag{4.92}$$

where the coefficients $\hat{\mathcal{W}}_{1,j}$ depend on α (possibly through intermediate dependencies on known zeroth-order results) and at most linearly on γ_0. At this order, $\gamma_1 \in \mathbb{C}$ is a free parameter.

4.7.2 The $\mathcal{O}(\varepsilon^2)$ Problem

At $\mathcal{O}(\varepsilon^2)$, the spectral problem takes the form (4.61). The solvability conditions are

$$\lambda_2 + i\mathfrak{c}_{2,1,n} = 0, \tag{4.93a}$$

$$\gamma_0 \left(\lambda_2 + i\mathfrak{c}_{2,-1,n+p}\right) = 0, \tag{4.93b}$$

where $\mathfrak{c}_{2,\sigma,j} = \mu_2 c_{g,\sigma}\left(j+\mu_0\right) - \mathfrak{p}_{2,j}$, as in Section 5 (although the quantities $\mathfrak{p}_{2,j}$ evaluate differently than those for the $p=2$ isolas). Since $\gamma_0 \neq 0$, the solution of (4.93a)-(4.93b) is

$$\lambda_2 = -i\left(\frac{\mathfrak{p}_{2,n+p}c_{g,1}(n+\mu_0) - \mathfrak{p}_{2,n}c_{g,-1}(n+p+\mu_0)}{c_{g,-1}(n+p+\mu_0) - c_{g,1}(n+\mu_0)}\right), \tag{4.94a}$$

$$\mu_2 = \frac{\mathfrak{p}_{2,n+p} - \mathfrak{p}_{2,n}}{c_{g,-1}(n+p+\mu_0) - c_{g,1}(n+\mu_0)}. \tag{4.94b}$$

Since λ_2 is purely imaginary, no instabilities are found at this order. The normalized solution of the $\mathcal{O}\left(\varepsilon^2\right)$ problem is

$$\mathbf{w}_2 = \sum_{j=n-2}^{n+p+2} \hat{\mathcal{W}}_{2,j} e^{ijx} + \gamma_2 \begin{pmatrix} 1 \\ \frac{i}{\omega(n+p+\mu_0)} \end{pmatrix} e^{i(n+p)x}, \tag{4.95}$$

where the coefficients $\hat{\mathcal{W}}_{2,j}$ depend on α (possibly through intermediate dependencies on known zeroth- and first-order results) and at most linearly on γ_0 and γ_1. At this order, $\gamma_2 \in \mathbb{C}$ is a free parameter.

4.7.3 The $\mathcal{O}\left(\varepsilon^3\right)$ Problem

At $\mathcal{O}\left(\varepsilon^3\right)$, the spectral problem becomes

$$\left(L_0 - \lambda_0 R_0\right)\mathbf{w}_3 = \left(\lambda_2 R_1 + \lambda_3 R_0\right)\mathbf{w}_0 - \sum_{j=0}^{2}\left(L_{3-j} - \lambda_0 R_{3-j}\right)\mathbf{w}_j, \tag{4.96}$$

with the aid of (4.91). The solvability conditions are

$$2\left(\lambda_3 + i\mu_3 c_{g,1}(n+\mu_0)\right) + i\gamma_0 \mathfrak{s}_{3,n} = 0, \tag{4.97a}$$

$$2\gamma_0\left(\lambda_3 + i\mu_3 c_{g,-1}(n+p+\mu_0)\right) + i\mathfrak{s}_{3,n+p} + i\gamma_1 \mathfrak{t}_{3,n+p} = 0. \tag{4.97b}$$

Using the solvability conditions (4.93a)-(4.93b) and the collision condition (4.45), it can be shown

$$\mathfrak{t}_{3,n+p} \equiv 0. \tag{4.98}$$

As in the $p=2$ case, the product of $\mathfrak{s}_{3,n}$ and $\mathfrak{s}_{3,n+p}$ is related to a perfect square:

$$\mathfrak{s}_{3,n}\mathfrak{s}_{3,n+p} = -\frac{\mathcal{S}_3^2}{\omega(n+\mu_0)\omega(n+p+\mu)}, \tag{4.99}$$

where

$$\mathcal{S}_3 = \mathcal{T}_{3,1} + \mathcal{T}_{3,2}\hat{N}_{2,2} + \mathcal{T}_{3,3}\hat{Q}_{2,2} + \mathcal{T}_{3,4}\hat{N}_{3,3} + \mathcal{T}_{3,5}\hat{Q}_{3,3}. \tag{4.100}$$

The expressions $\mathcal{T}_{3,j}$ are functions only of α, as are the Stokes wave corrections $\hat{N}_{2,2}$, $\hat{Q}_{2,2}$, $\hat{N}_{3,3}$, and $\hat{Q}_{3,3}$. When fully expanded, $\mathcal{S}_3$ involves several hundred terms, but each term depends only on α. The full expression of $\mathcal{S}_3$ can be found in the appropriate Mathematica notebook.

Solving for λ_3 in the solvability conditions, we find

$$\begin{aligned}\lambda_3 = -i\mu_3&\left(\frac{c_{g,-1}(n+p+\mu_0) + c_{g,1}(n+\mu_0)}{2}\right)\\ &\pm \sqrt{-\mu_3^2\left(\frac{c_{g,-1}(n+p+\mu_0) - c_{g,1}(n+\mu_0)}{2}\right)^2 + \frac{\mathcal{S}_3^2}{4\omega(n+\mu_0)\omega(n+p+\mu_0)}}.\end{aligned} \tag{4.101}$$

A plot of $\mathcal{S}_3$ *vs.* α reveals $\mathcal{S}_3 \neq 0$, except at $\alpha_2 = 0.8206431673...$ (Figure 4.7). Thus, we conjecture that Stokes waves of all wavenumbers and in all depths are unstable to the second closest high-frequency instability from the origin, with possible exceptions if $\alpha = \alpha_2$. Since $\alpha_2 \neq \alpha_1$, Stokes waves of all wavenumbers and in all depths appear to be unstable with respect to high-frequency instabilities.

Remark 4.7.2. *As $\alpha \to \infty$, $\mathcal{S}_3 \to 0$. Therefore, the leading-order behavior of the $p = 3$ isola in infinite depth is resolved at higher order. For ε on the order of 0.01 and smaller, this isola is already within the numerical error of the FFH method. For larger ε, the expansions deviate too quickly from the numerics to make comparisons.*

Provided $\alpha \neq \alpha_2$, (4.101) has nonzero real part for $\mu_3 \in (-M_3, M_3)$, where

$$M_3 = \frac{|\mathcal{S}_3|}{|c_{g,-1}(n+p+\mu_0) - c_{g,1}(n+\mu_0)|\sqrt{\omega(n+\mu_0)\omega(n+p+\mu_0)}}. \tag{4.102}$$

Unlike the $p = 2$ isola, this interval is symmetric about the origin. For μ_3 in this interval, the real and imaginary parts of (4.101), together with the lower-order corrections of λ, trace

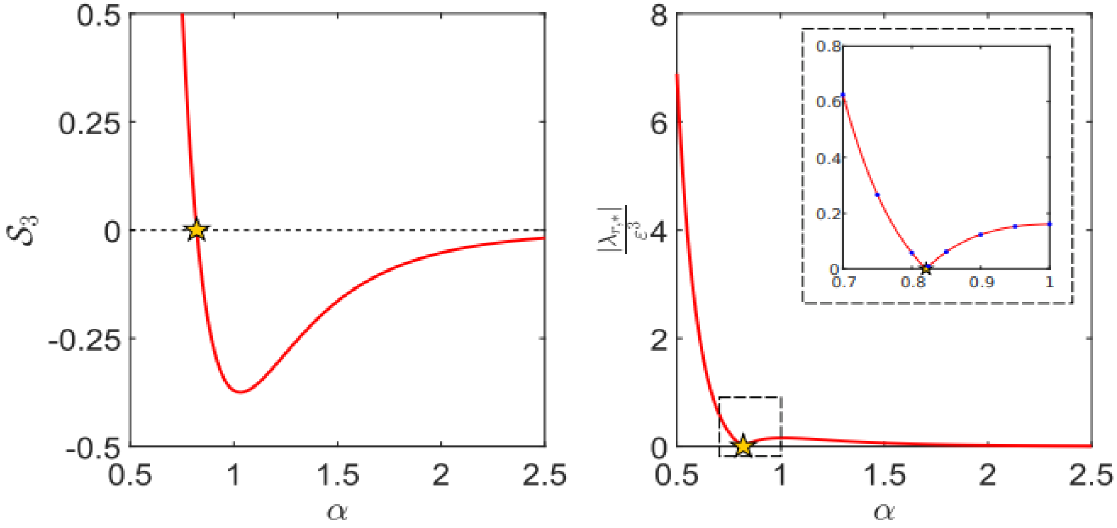

Figure 4.7: (Left) A plot of $\mathcal{S}_3$ *vs.* α (solid red). The zero of $\mathcal{S}_3$ for $\alpha > 0$ is $\alpha_2 = 0.8206431673...$ (gold star). (Right) The real part $\lambda_{r,*}$ of the most unstable eigenvalue on the $p = 3$ isola as a function of α according to our asymptotic calculations (solid red). The real part of the eigenvalue is normalized by ε^3 for better visibility. We zoom-in around $\alpha = \alpha_2$ (gold star) in the inlay. The real part of the most unstable eigenvalue on the isola vanishes as $\alpha \to \alpha_2$ according to our asymptotic calculations, which agrees with our numerical results using the FFH method with $\varepsilon = 0.01$ (blue dots).

an ellipse asymptotic to the $p = 3$ isola. This ellipse has semi-major and -minor axes that scale as $\mathcal{O}\left(\varepsilon^3\right)$ and a center that drifts form λ_0 like $\mathcal{O}\left(\varepsilon^2\right)$. The Floquet parameterization of this ellipse has width $\mathcal{O}\left(\varepsilon^3\right)$ and drifts from μ_0 like $\mathcal{O}\left(\varepsilon^2\right)$. As a result, this isola is more challenging to capture than the $p = 2$ isola in finite depth.

Comparing our asymptotic and numerical $p = 3$ isolas with $\varepsilon = 0.01$ (Figure 4.8), we observe that, while the real part of the numerical isola matches our $\mathcal{O}\left(\varepsilon^3\right)$ calculations, the imaginary part and Floquet parameterization of the isola require fourth-order corrections. This is in contrast with the $p = 2$ isola (Figure 4.2), for which we obtain the drifts in the imaginary part and Floquet parameterization at the same order as the real part. We obtain these drifts for the $p = 3$ isola in the following subsection.

Equating $\mu_3 = 0$ maximizes the real part of (4.101). Hence, the real and imaginary part of the most unstable eigenvalue on the $p = 3$ isola have asymptotic expansions

$$\lambda_{r,*} = \left(\frac{|\mathcal{S}_3|}{2\sqrt{\omega(n+\mu_0)\omega(n+p+\mu_0)}} \right) \varepsilon^3 + \mathcal{O}\left(\varepsilon^4\right), \tag{4.103a}$$

$$\lambda_{i,*} = -i\Omega_1(n+\mu_0) - \left(\frac{\mathfrak{p}_{2,n+p}c_{g,1}(n+\mu_0) - \mathfrak{p}_{2,n}c_{g,-1}(n+p+\mu_0)}{c_{g,-1}(n+p+\mu_0) - c_{g,1}(n+\mu_0)} \right) \varepsilon^2 + \mathcal{O}\left(\varepsilon^4\right), \tag{4.103b}$$

respectively, and the corresponding Floquet exponent has asymptotic expansion

$$\mu_* = \mu_0 + \left(\frac{\mathfrak{p}_{2,n+p} - \mathfrak{p}_{2,n}}{c_{g,-1}(n+p+\mu_0) - c_{g,1}(n+\mu_0)} \right) \varepsilon^2 + \mathcal{O}\left(\varepsilon^4\right). \tag{4.104}$$

Figure 4.9 compares the asymptotic expansions (4.103a)-(4.103b) and (4.104) with their numerical counterparts. Excellent agreement is found for the real and imaginary parts of the most unstable eigenvalue. The interval of Floquet exponents that parameterizes the isola requires a fourth-order correction to match the numerical predictions.

Before proceeding to the next order, we solve the $\mathcal{O}(\varepsilon^3)$ problem for $\mathbf{w}_3$:

$$\mathbf{w}_3 = \sum_{j=n-3}^{n+p+3} \hat{\mathcal{W}}_{3,j} e^{ijx} + \gamma_3 \begin{pmatrix} 1 \\ \frac{i}{\omega(n+p+\mu_0)} \end{pmatrix} e^{i(n+p)x}, \tag{4.105}$$

where the coefficients $\hat{\mathcal{W}}_{3,j}$ depend on α (possibly through intermediate dependencies on known zeroth-, first-, and second-order results) and at most linearly on γ_0, γ_1, and γ_2. At this order, $\gamma_3 \in \mathbb{C}$ is a free parameter.

4.7.4 The $\mathcal{O}(\varepsilon^4)$ Problem

At $\mathcal{O}(\varepsilon^4)$, the spectral problem (4.35) becomes

$$\left(L_0 - \lambda_0 R_0\right)\mathbf{w}_4 = \left(\sum_{j=0}^{2} \lambda_{4-j} R_j \right) \mathbf{w}_0 + \left(\sum_{j=0}^{1} \lambda_{3-j} R_j \right) \mathbf{w}_1 + \lambda_2 R_0 \mathbf{w}_2 - \sum_{j=0}^{3} \left(L_{4-j} - \lambda_0 R_{4-j}\right)\mathbf{w}_j. \tag{4.106}$$

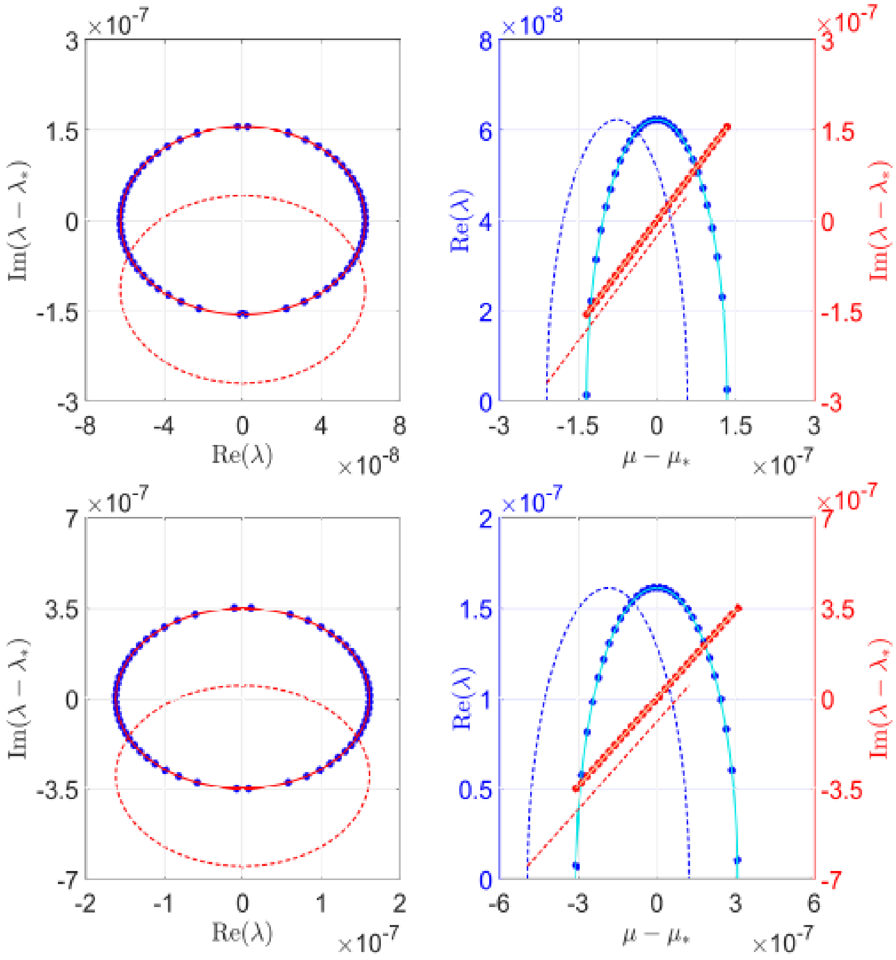

Figure 4.8: (Top, Left) The $p = 3$ isola with $\alpha = 1.5$ and $\varepsilon = 0.01$. The most unstable eigenvalue λ_* is removed from the imaginary axis for better visibility. The solid and dashed red curves are the ellipses obtained by our $\mathcal{O}\left(\varepsilon^4\right)$ and $\mathcal{O}\left(\varepsilon^3\right)$ asymptotic calculations, respectively. The blue dots are a subset of eigenvalues from the numerically computed isola using the FFH method. (Top, Right) The Floquet parameterization of the real (blue) and imaginary (red) parts of the isola on the left. The most unstable eigenvalue λ_* and its corresponding Floquet exponent μ_* are removed from the imaginary and Floquet axes, respectively, for better visibility. The solid teal and orange curves are our asymptotic results for the real and imaginary parts of the Floquet parameterization, respectively, to $\mathcal{O}\left(\varepsilon^4\right)$. The dashed blue and red curves are the same results to $\mathcal{O}\left(\varepsilon^3\right)$. The blue and red dots are the numerically computed real and imaginary parts of the Floquet parameterization, respectively, using the FFH method. (Bottom, Left & Right) Same with $\alpha = 1$.

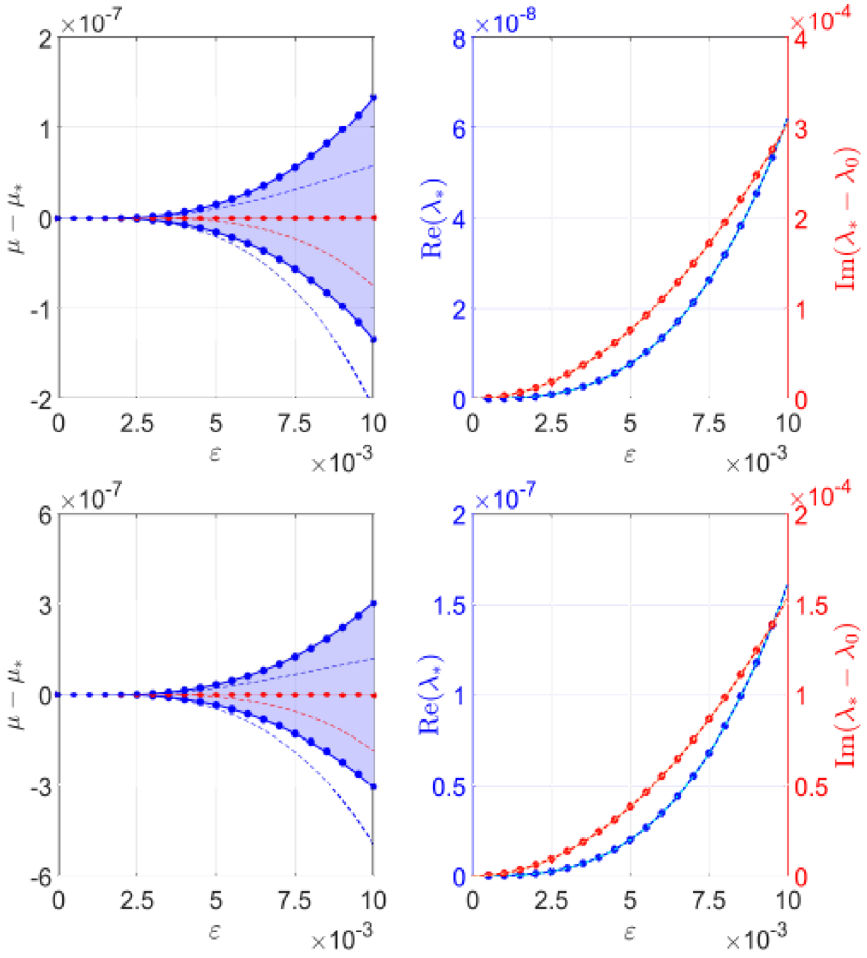

Figure 4.9: (Top, Left) The interval of Floquet exponents parameterizing the $p = 3$ isola as a function of ε for $\alpha = 1.5$. The most unstable Floquet exponent μ_* is removed from the Floquet axis for better visibility. The solid and dashed blue curves are the boundaries of this interval according to our $\mathcal{O}\left(\varepsilon^4\right)$ and $\mathcal{O}\left(\varepsilon^3\right)$ asymptotic calculations, respectively. The blue dots are the boundaries computed numerically by the FFH method. The solid and dashed red curves give the Floquet exponent of the most unstable eigenvalue on the isola according to our $\mathcal{O}\left(\varepsilon^4\right)$ and $\mathcal{O}\left(\varepsilon^3\right)$ asymptotic calculations, respectively. The red dots are the Floquet exponent of the most unstable eigenvalue as computed by the FFH method. (Top, Right) The real (blue) and imaginary (red) parts of the most unstable eigenvalue of the $p = 3$ isola with $\alpha = 1.5$ as a function of ε. The zeroth-order correction of the eigenvalue is removed from the imaginary axis for better visibility. The solid teal and orange curves are our asymptotic calculations for the real and imaginary parts of the most unstable eigenvalue to $\mathcal{O}\left(\varepsilon^4\right)$, respectively. The dashed blue and red curves are the same results to $\mathcal{O}\left(\varepsilon^3\right)$. The blue and red dots are the numerically computed real and imaginary parts of the most unstable eigenvalue using the FFH method. (Bottom, Left & Right) Same with $\alpha = 1$.

After some manipulation, the solvability conditions of (4.106) can be written as

$$\begin{pmatrix} 2 & i\mathfrak{s}_{3,n} \\ 2\gamma_0 & 2\left(\lambda_3 + i\mu_3 c_{g,-1}(n+p+\mu_0)\right) \end{pmatrix} \begin{pmatrix} \lambda_4 \\ \gamma_1 \end{pmatrix} + i\gamma_2 \begin{pmatrix} 0 \\ \mathfrak{t}_{4,n+p} \end{pmatrix} = \\ - 2i \begin{pmatrix} \mu_4 c_{g,1}(n+\mu_0) - \mathfrak{p}_{4,n} \\ \gamma_0 \left(\mu_4 c_{g,-1}(n+p+\mu_0) - \mathfrak{p}_{4,n+p}\right) \end{pmatrix}. \tag{4.107}$$

Using the solvability conditions at the previous order and the collision condition (4.45), one can show $\mathfrak{t}_{4,n+p} \equiv 0$. Then, (4.107) reduces to a linear system for λ_4 and γ_1.

For $\mu_3 \in (-M_3, M_3)$ with M_3 given by (4.102), the determinant of (4.107) simplifies to

$$\det \begin{pmatrix} 2 & i\mathfrak{s}_{3,n} \\ 2\gamma_0 & 2\left(\lambda_3 + i\mu_3 c_{g,-1}(n+p+\mu_0)\right) \end{pmatrix} = 8\lambda_{3,r}, \tag{4.108}$$

where $\lambda_{3,r} = \operatorname{Re}(\lambda_3)$. Provided $\alpha \neq \alpha_2$, (4.107) is invertible for all $\mu_3 \in (-M_3, M_3)$.

Solving (4.107) for λ_4,

$$\lambda_4 = i\Bigg[\frac{\left(\lambda_3 + i\mu_3 c_{g,-1}(n+p+\mu_0)\right)\left(c_{g,1}(n+\mu_0) - \mathfrak{p}_{4,n}\right)}{2\lambda_{3,r}} \\ + \frac{\left(\lambda_3 + i\mu_3 c_{g,1}(n+\mu_0)\right)\left(c_{g,-1}(n+p+\mu_0) - \mathfrak{p}_{4,n+p}\right)}{2\lambda_{3,r}}\Bigg]. \tag{4.109}$$

Since $\mathfrak{p}_{4,j}, \mu_4 \in \mathbb{R}$, the real and imaginary parts of $\lambda_4 = \lambda_{4,r} + i\lambda_{4,i}$ are

$$\lambda_{4,r} = \frac{\mu_3\left(c_{g,-1}(n+p+\mu_0) - c_{g,1}(n+\mu_0)\right)}{4\lambda_{3,r}}\Big[-\mu_4\left(c_{g,-1}(n+p+\mu_0) - c_{g,1}(n+\mu_0)\right) \\ + \mathfrak{p}_{2,n+p} - \mathfrak{p}_{2,n}\Big], \tag{4.110a}$$

$$\lambda_{4,i} = -\frac{1}{2}\Big[\mu_4\left(c_{g,-1}(n+\mu_0) + c_{g,1}(n+\mu_0)\right) - \left(\mathfrak{p}_{4,n+p} + \mathfrak{p}_{4,n}\right)\Big]. \tag{4.110b}$$

Given (4.110a)-(4.110b), we invoke the regular curve condition as in the previous chapters. According to this condition, all eigenvalue corrections must be bounded over the closure of $\mu_3 \in (-M_3, M_3)$. Notice $\lambda_{3,r} \to 0$ as $|\mu_3| \to M_3$. Thus, $\lambda_{4,r}$ is bounded only if

$$\mu_4 = \frac{\mathfrak{p}_{4,n+p} - \mathfrak{p}_{4,n}}{c_{g,-1}(n+p+\mu_0) - c_{g,1}(n+\mu_0)}. \tag{4.111}$$

Hence,

$$\lambda_4 = -i\left(\frac{\mathfrak{p}_{4,n+p}c_{g,1}(n+\mu_0) - \mathfrak{p}_{4,n}c_{g,-1}(n+p+\mu_0)}{c_{g,-1}(n+p+\mu_0) - c_{g,1}(n+\mu_0)}\right). \tag{4.112}$$

Remark 4.7.3. *If* $\alpha = \alpha_2$*, then* $\mathfrak{s}_{3,n} = 0$ *and* $\lambda_3 = 0 = \mu_3$*. Applying the Fredholm alternative to* (4.107)*, one arrives at* (4.111) *and* (4.112)*, but* γ_0 *and* γ_1 *remain arbitrary at this order.*

Equations (4.111) and (4.112) give the fourth-order drifts in the Floquet parameterization and imaginary part of the $p = 3$ isola, respectively. The corresponding isola is given by the real and imaginary parts of

$$\lambda(\mu_3; \varepsilon) = \lambda_0 + \lambda_2\varepsilon^2 + \lambda_3(\mu_3)\varepsilon^3 + \lambda_4\varepsilon^4, \tag{4.113}$$

which is in better agreement with numerics than the previous order, see Figures 4.8 and 4.9.

4.8 Conclusions

Building on work in the previous chapters, we have developed a formal perturbation method to compute high-frequency instabilities of small-amplitude Stokes waves for Euler's equations in arbitrary depth. This method allows us to approximate an entire high-frequency isola with uniform accuracy and estimate

(i) the Floquet exponents that parameterize the isola,

(ii) the real and imaginary parts of the most unstable eigenvalue on the isola, and

(iii) the curve asymptotic to the isola.

These expressions are compared directly with numerical computations of the isolas using the FFH method. Excellent agreement is found for the $p = 2$ isola. The $p = 3$ isola achieves similar agreement if higher-order corrections of the imaginary part and Floquet parameterization are computed using the regular curve condition.

According to our asymptotic results, Stokes waves of all aspect ratios, except $\kappa h = \alpha_1$ and $\kappa h = \alpha_2$, are unstable to the $p = 2$ and $p = 3$ high-frequency instabilities, respectively. Stokes waves are also unstable to high-frequency instabilities in infinite depth ($h = \infty$), although this requires a higher-order calculation than in finite depth. Based on these findings, we conjecture that Stokes waves of all depths and all wavenumbers are spectrally unstable to high-frequency instabilities, extending recent work by Hur and Yang [53], where the existence of the $p = 2$ high-frequency instability is proven only if $\kappa h \in (0.86430..., 1.00804...)$. The effect of the high-frequency instabilities on the Stokes waves has been illustrated in [35].

The perturbation method developed in this work is readily extended to higher-order isolas ($p \geq 4$). Just as in the previous chapters, it appears this method yields the first real-part correction of the isola at $\mathcal{O}\left(\varepsilon^p\right)$. In contrast, corrections to the imaginary part and Floquet parameterization of the isola appear at $\mathcal{O}\left(\varepsilon^2\right)$. Thus, we expect isolas further from the origin to decrease in size, while their centers drift along the imaginary axis like $\mathcal{O}\left(\varepsilon^2\right)$.

If correct, this conjecture highlights one of the primary challenges for analytical and numerical investigations of high-frequency instabilities: each isola is smaller than the previous, and each isola drifts from its known zeroth-order behavior quickly relative to its size. Our hope is that the perturbation method developed in this work can be used as a starting point for future proofs of high-frequency instabilities as well as improvements to the numerical resolution of high-frequency isolas far away from the origin in the complex spectral plane.

Chapter 5

AN ASYMPTOTIC DESCRIPTION OF THE BENJAMIN-FEIR INSTABILITY

5.1 Introductory Remarks

In this final chapter, we return our focus to the origin of the complex spectral plane, where eigenvalues collide in sufficiently deep water to create the Benjamin-Feir (or modulational) instability. There has been renewed interest in the spectrum of this instability over the past two years. In 2020, Nguyen and Strauss [73] proved the existence of unstable eigenvalues near the origin of the complex spectral plane for sufficiently small-amplitude Stokes waves in infinite depth using conformal mapping and Lyapunov-Schmidt reduction. This problem had been open since the seminal work of Bridges and Mielke [15] in 1995, which proved the existence of these eigenvalues in finite depth provided $\kappa h > \alpha_{BW} = 1.3627827567...$, where $\kappa > 0$ is the wavenumber of the Stokes wave and h is the mean depth of the water[1]. More recently, Hur and Yang [53] proved similar results for the instability spectrum in infinite depth using periodic Evans functions.

In recent months, extensive work by Berti, Maspero, and Ventura [10, 11] has confirmed the existence of the Benjamin-Feir figure-eight curve for sufficiently small-amplitude Stokes waves in finite and infinite depth, provided $\kappa h > \alpha_{BW}$. The proof of both cases relies on the Hamiltonian and reversibility properties of Euler's equations together with Kato's theory of similarity transformations [57] and KAM theory. Reported in the works of Berti, Maspero, and Ventura are explicit expressions for the figure-eight curves, up to real analytic functions of the Floquet exponent μ and the amplitude of the Stokes waves ε. A low-order

---

[1] The original arguments of Bridges and Mielke fail in the limit as the depth approaches infinity. We see why this occurs later in this chapter.

approximation of the curves is also given. We demonstrate later in this chapter that this approximation is not truly asymptotic to the figure-eight in the case of infinite depth.

In this chapter, we obtain high-order asymptotic expansions of the Benjamin-Feir figure-eight curve in finite and infinite depth. In particular, we seek high-order asymptotic estimates for the interval of Floquet exponents parameterizing the figure-eight and for the most unstable eigenvalue. Using the results in Chapter 4, we can compare the Benjamin-Feir and high-frequency growth rates analytically for the first time. This comparison suggests three regimes for Stokes waves:

(i) shallow water ($\kappa h < \alpha_{BW}$), in which only high-frequency instabilities exist,

(ii) intermediate water ($\alpha_{BW} < \kappa h < \alpha_{DO}(\varepsilon) = 1.4308061674... + \mathcal{O}\left(\varepsilon^2\right)$)

(iii) deep water ($\kappa h > \alpha_{DO}(\varepsilon)$), in which both instabilities are present, but the Benjamin-Feir instability dominates.

Our method to obtain these high-order asymptotic approximations is a modification of that developed for high-frequency instabilities in the previous chapters. Although the method is formal, it offers a more direct approach to the Benjamin-Feir figure-eight curve and produces results consistent with numerical computations (for sufficiently small ε) as well as with rigorous results appearing in [10, 11]. The method loses validity for sufficiently large ε, when the Benjamin-Feir instability spectrum separates from the origin and changes its topology, see Figure 5.1. Some of the lower-order details of our method are also presented by Akers [3] for the Benjamin-Feir instability in infinite depth, although this work uses different conventions for Euler's equations and the underlying Stokes waves. In contrast, our expressions in this chapter are in one-to-one correspondence with those appearing in [10, 11], giving confidence in the rigorous results as well as in our asymptotic calculations.

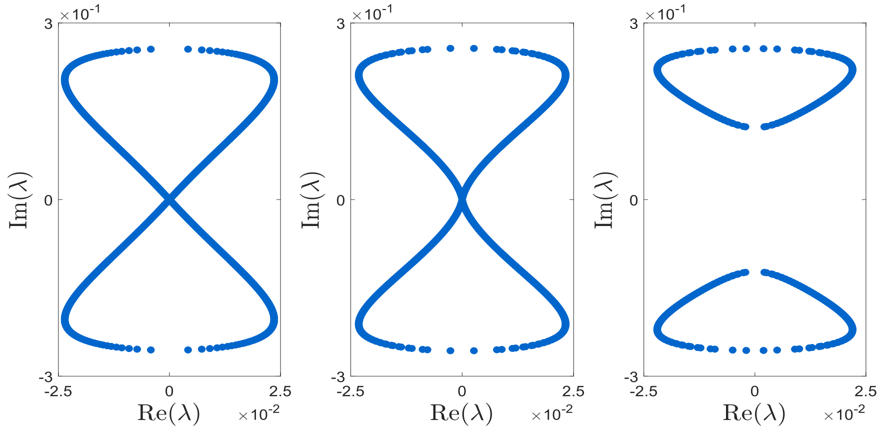

Figure 5.1: Numerically computed Benjamin-Feir instability spectra in infinitely deep water for Stokes waves of amplitude $\varepsilon = 0.31$ (left), $\varepsilon = 0.32$ (middle), and $\varepsilon = 0.33$ (right) using the Floquet-Fourier-Hill (FFH) method. The asymptotic methods presented in this work apply only for sufficiently small ε and, thus, do not capture the separation of the figure-eight from the origin.

5.2 *A Spectral Perturbation Method for the Benjamin-Feir Instability*

For ease of later comparisons, we adopt the same formulation of Euler's equations as in Chapter 4, *i.e.*, the AFM formulation. As a result, expressions for the Stokes waves and the stability spectrum are unchanged. In this chapter, we focus on the Benjamin-Feir instability, which arises from the eigenvalue $\lambda_0 = 0$ in the $\varepsilon = 0$ spectrum. A quick computation using (4.44b) shows that the corresponding Floquet exponent is $\mu_0 = 0$. In this section, we retain the variables λ_0 and μ_0 to reveal the structure of our perturbation method. However, since both variables are zero, one can omit them in what follows.

The eigenvalue λ_0 is has algebraic multiplicity 4 and geometric multiplicity 3 [10, 11, 15, 53, 73]. The corresponding eigenspace is spanned by

$$\mathbf{w}_{\mathbf{0},-\mathbf{1}}(x) = \begin{pmatrix} 1 \\ i/c_0 \end{pmatrix} e^{-ix}, \qquad \mathbf{w}_{\mathbf{0},\mathbf{0}}(x) = \begin{pmatrix} 0 \\ 1 \end{pmatrix}, \qquad \mathbf{w}_{\mathbf{0},\mathbf{1}}(x) = \begin{pmatrix} 1 \\ -i/c_0 \end{pmatrix} e^{ix}, \tag{5.1}$$

so that the most general eigenfunction corresponding to λ_0 is

$$\mathbf{w_0}(x) = \beta_{0,-1}\mathbf{w_{0,-1}}(x) + \beta_{0,0}\mathbf{w_{0,0}}(x) + \beta_{0,1}\mathbf{w_{0,1}}(x), \tag{5.2}$$

where $\beta_{0,\nu}$ for $\nu \in \{0, \pm 1\}$ are (for now) arbitrary constants.

Remark 5.2.1. *The generalized eigenspace is spanned by* (5.2) *together with the generalized eigenvector* $\mathbf{v_{0,0}} = (1, 0)^T$. *We mention this for completeness, but in practice, we only need* (5.1) *to approximate the unstable eigenvalues corresponding to the Benjamin-Feir instability.*

Remark 5.2.2. *Without loss of generality, one of the constants* $\beta_{0,\nu}$ *can be set to 1 since* $\mathbf{w}_0$ *is unique only up to a nonzero scalar. We retain all three constants in our calculations for reasons that become more clear when we consider infinite depth.*

We now turn on the small-amplitude parameter ε and track the unstable eigenvalues near the origin for $0 < \varepsilon \ll 1$. These eigenvalues trace out a figure-eight curve centered at the origin, as mentioned in the introduction of this thesis and again in the introduction of this chapter. To track these eigenvalues and their corresponding eigenfunctions, we formally expand our spectral data in powers of ε:

$$\lambda(\varepsilon) = \lambda_0 + \sum_{j=1}^{\infty} \lambda_j \varepsilon^j, \tag{5.3a}$$

$$\mathbf{w}(x;\varepsilon) = \mathbf{w_0}(x) + \sum_{j=1}^{\infty} \mathbf{w_j}(x)\varepsilon^j. \tag{5.3b}$$

As this curve deforms with ε, so too does its parameterization in terms of the Floquet exponent. Thus, as in previous chapters, we expand this parameter according to

$$\mu(\varepsilon) = \mu_0 + \varepsilon\mu_1\big(1 + r(\varepsilon)\big), \qquad \text{with} \qquad r(\varepsilon) = \sum_{j=1}^{\infty} r_j \varepsilon^j, \tag{5.4}$$

where μ_1 assumes an interval of values symmetric about zero and $r(\varepsilon)$ captures the higher-order deformations of this interval, see Figure 5.2.

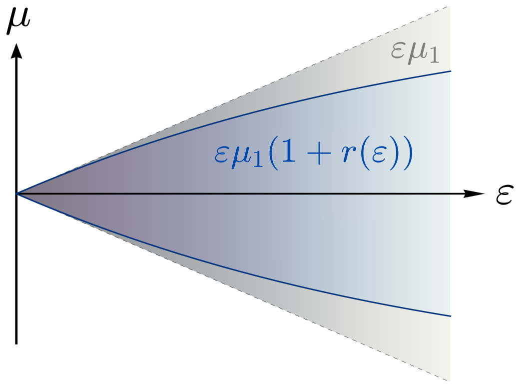

Figure 5.2: A schematic of the parameterizing interval of Floquet exponents for the Benjamin-Feir figure-eight curve as a function of ε. The gray-shaded region indicates the leading-order approximation of this interval $\varepsilon\mu_1$, where μ_1 is an interval of values symmetric about zero. The blue-shaded region indicates the true interval as a function of ε and is a uniform rescaling of the leading-order behavior by a factor of $1+r(\varepsilon)$, where r is an analytic function of ε such that $r(\varepsilon) = o(1)$ as $\varepsilon \to 0^+$. The boundaries of the true interval may be subtended by curves that are concave up or down, depending on α.

Remark 5.2.3. *Expansion* (5.4) *appears in a slightly different form than in previous chapters. This is because the parameterizing interval of Floquet exponents for the Benjamin-Feir instability remains symmetric about the origin for sufficiently small ε [10, 11]. For sufficiently large ε, the figure-eight curve separates from the origin (Figure 5.1), and thus, the parameterizing interval of Floquet exponents separates into two disjoint intervals. Ansatz* (5.4) *cannot account for this effect, which limits our analysis of the Benjamin-Feir instability spectrum to sufficiently small ε.*

We proceed as follows. Expansions (5.3a), (5.3b), and (5.4) are substituted into the full spectral problem (4.35). Powers of ε are equated, generating a hierarchy of linear inhomogeneous equations for the eigenfunction corrections $\mathbf{w_j}$. Each of these equations is solvable only if the Fredholm alternative removes secular inhomogeneous terms. This leads to a set of solvability conditions that impose constraints on the eigenvalue corrections λ_j as well as corrections to the constants appearing in $\mathbf{w_0}$. Corrections to the Floquet exponent require the regular curve condition, as in the previous chapters, which ensures the eigenvalue corrections remain bounded as one approaches the intersection of the figure-eight curve with the imaginary axis.

We present this method in more detail in the sections that follow, first in finite depth and then in infinite depth, where more care is needed. Results of the method are compared directly with numerical computations of the Benjamin-Feir instability using the FFH method. This is the first time that analytical and numerical descriptions of the Benjamin-Feir figure-eight curve have been quantitatively compared.

5.3 The Benjamin-Feir Spectrum in Finite Depth

5.3.1 The $\mathcal{O}(\varepsilon)$ Problem

Substituting (5.3a), (5.3b), and (5.4) into the full spectral problem (4.35), terms of $\mathcal{O}(\varepsilon^0)$ necessarily cancel by our choice of λ_0, $\mathbf{w_0}$, and μ_0 above. At $\mathcal{O}(\varepsilon)$, we find

$$\Big(\mathcal{L}_0 - \lambda_0\mathcal{R}_0\Big)\mathbf{w_1} = -\mathcal{L}_1\mathbf{w_0} + \mathcal{R}_0\Big(\lambda_1\mathbf{w_0}\Big) + \mathcal{R}_1\Big(\lambda_0\mathbf{w_0}\Big), \tag{5.5}$$

with

$$\mathcal{L}_j = \frac{1}{j!}\frac{\partial^j}{\partial\varepsilon^j}\mathcal{L}_{\mu(\varepsilon),\varepsilon}, \qquad \mathcal{R}_j = \frac{1}{j!}\frac{\partial^j}{\partial\varepsilon^j}\mathcal{R}_{\mu(\varepsilon),\varepsilon}. \tag{5.6}$$

The operator $\mathcal{L}_0 - \lambda_0\mathcal{R}_0$ is not invertible for $(\lambda_0,\mu_0) = (0,0)$. A solution $\mathbf{w_1}$ of (5.5) exists only if the inhomogeneous terms are orthogonal to the nullspace of the adjoint of $\mathcal{L}_0 - \lambda_0\mathcal{R}_0$ by the Fredholm alternative. A direct calculation shows

$$\text{Null}\Big((\mathcal{L}_0 - \lambda_0\mathcal{R}_0)^\dagger\Big) = \text{Span}\left\{\begin{pmatrix}1\\ ic_0\end{pmatrix}e^{-ix}, \begin{pmatrix}1\\ 0\end{pmatrix}, \begin{pmatrix}1\\ -ic_0\end{pmatrix}e^{ix}\right\}, \tag{5.7}$$

where $(\mathcal{L}_0 - \lambda_0\mathcal{R}_0)^\dagger$ denotes the adjoint operator with respect to the standard complex inner-product $\langle\cdot,\cdot\rangle$ on $\mathrm{L}^2_{\text{per}}(-\pi,\pi) \times \mathrm{L}^2_{\text{per}}(-\pi,\pi)$. From (5.7), we arrive at three solvability conditions for (5.5):

$$\left\langle -\mathcal{L}_1\mathbf{w_0} + \mathcal{R}_0\Big(\lambda_1\mathbf{w_0}\Big) + \mathcal{R}_1\Big(\lambda_0\mathbf{w_0}\Big), \begin{pmatrix} 1 \\ ic_0 \end{pmatrix} e^{-ix} \right\rangle = 0, \tag{5.8a}$$

$$\left\langle -\mathcal{L}_1\mathbf{w_0} + \mathcal{R}_0\Big(\lambda_1\mathbf{w_0}\Big) + \mathcal{R}_1\Big(\lambda_0\mathbf{w_0}\Big), \begin{pmatrix} 1 \\ 0 \end{pmatrix} \right\rangle = 0, \tag{5.8b}$$

$$\left\langle -\mathcal{L}_1\mathbf{w_0} + \mathcal{R}_0\Big(\lambda_1\mathbf{w_0}\Big) + \mathcal{R}_1\Big(\lambda_0\mathbf{w_0}\Big), \begin{pmatrix} 1 \\ -ic_0 \end{pmatrix} e^{ix} \right\rangle = 0. \tag{5.8c}$$

Simplifying (5.8a) and (5.8c) leads to

$$2\beta_{0,-1}\left(\lambda_1 + i\mu_1 c_g\right) = 0, \tag{5.9a}$$

$$2\beta_{0,1}\left(\lambda_1 + i\mu_1 c_g\right) = 0, \tag{5.9b}$$

respectively, where c_g denotes the group velocity of Ω_1 (4.44b) evaluated at $k = 1$. Explicitly,

$$c_g = \frac{\alpha(1 - c_0^4) - c_0^2}{2c_0}. \tag{5.10}$$

In contrast to (5.8a) and (5.8c), (5.8b) reduces to a trivial equality and does not contribute an additional solvability condition.

Remark 5.3.1. *If $c_0 > 0$, a direct calculation shows that $c_g < 0$ for $\alpha > 0$.*

If we require $\beta_{0,\nu} \neq 0$ so that the eigenspace of λ_0 remains three-dimensional, equations (5.9a) and (5.9b) imply

$$\lambda_1 = -i\mu_1 c_g. \tag{5.11}$$

Since $\mu_1 \in \mathbb{R}$, the unstable eigenvalues of the Benjamin-Feir instability are imaginary to $\mathcal{O}(\varepsilon)$.

Remark 5.3.2. *If $\beta_{0,\nu} = 0$ for some ν, one recovers the imaginary spectrum near the origin, as opposed to the figure-eight curve.*

Before proceeding to $\mathcal{O}\left(\varepsilon^2\right)$, we solve (5.5) subject to (5.11). The solution $\mathbf{w_1}$ decomposes into a direct sum of a particular solution $\mathbf{w_{1,p}}$ and a homogeneous solution $\mathbf{w_{1,h}}$:

$$\mathbf{w_1}(x) = \mathbf{w_{1,p}}(x) + \mathbf{w_{1,h}}(x). \tag{5.12}$$

The particular solution can be written as

$$\mathbf{w_{1,p}}(x) = \sum_{j=-2}^{2} \mathbf{w_{1,j}} e^{ijx}, \tag{5.13}$$

where $\mathbf{w_{1,j}} = \mathbf{w_{1,j}}(\alpha, \beta_{0,\nu}, \mu_1) \in \mathbb{C}^2$. The homogeneous solution is

$$\mathbf{w_{1,h}}(x) = \beta_{1,-1}\mathbf{w_{0,-1}}(x) + \beta_{1,0}\mathbf{w_{0,0}}(x) + \beta_{1,1}\mathbf{w_{0,1}}(x), \tag{5.14}$$

coinciding with the eigenspace of λ_0. The coefficients $\beta_{1,\nu}$ represent first-order corrections to the zeroth-order eigenfunction correction $\mathbf{w}_0$ and are undetermined constants at this order.

Remark 5.3.3. *The expressions for $\mathbf{w_{1,j}}$ as well as for all other algebraic expressions that are too cumbersome to include explicitly in this chapter are found in the companion Mathematica files* wwp_bf_fd.nb *(for finite depth expressions) and* wwp_bf_id.nb *(for infinite depth expressions).*

5.3.2 The $\mathcal{O}\left(\varepsilon^2\right)$ Problem

At $\mathcal{O}\left(\varepsilon^2\right)$, the spectral problem (4.35) takes the form

$$\Big(\mathcal{L}_0 - \lambda_0\mathcal{R}_0\Big)\mathbf{w_2} = -\sum_{j=1}^{2}\mathcal{L}_j\mathbf{w_{2-j}} + \mathcal{R}_0\Big(\sum_{k=1}^{2}\lambda_k\mathbf{w_{2-k}}\Big) + \sum_{j=1}^{2}\mathcal{R}_j\Big(\sum_{k=0}^{2-j}\lambda_k\mathbf{w_{2-j-k}}\Big). \tag{5.15}$$

Proceeding as above, we obtain three nontrivial solvability conditions for (5.15):

$$2\beta_{0,-1}\big(\lambda_2 + ic_g r_1\mu_1\big) + \beta_{0,0}S_{2,-1}\mu_1 + i\Big(U_{2,-1}\beta_{0,1} + \big(T_{2,-1}\mu_1^2 + V_{2,-1}\big)\beta_{0,-1}\Big) = 0, \tag{5.16a}$$

$$\beta_{0,0}T_{2,0}\mu_1^2 + iS_{2,0}\mu_1\big(\beta_{0,-1} + \beta_{0,1}\big) = 0, \tag{5.16b}$$

$$2\beta_{0,1}\big(\lambda_2 + ic_g r_1\mu_1\big) + \beta_{0,0}S_{2,1}\mu_1 + i\Big(U_{2,1}\beta_{0,-1} + \big(T_{2,1}\mu_1^2 + V_{2,1}\big)\beta_{0,1}\Big) = 0, \tag{5.16c}$$

where the subscripted coefficients S, T, U, and V are all real-valued functions of the aspect ratio α. More explicitly, we have:

$$S_{2,-1} = \frac{\alpha + 5c_0^2 - 2\alpha c_0^4 - c_0^6 + \alpha c_0^8}{4c_0^2}, \tag{5.17a}$$

$$T_{2,-1} = \frac{\alpha^2 - c_0^2\left(-1 + \alpha c_0^2\right)\left(-2\alpha + c_0^2 + 3\alpha c_0^4\right)}{4c_0^3}, \tag{5.17b}$$

$$U_{2,-1} = \frac{1 - 2\hat{N}_{2,2}c_0^2\left(1 - 3c_0^4\right) - 8\hat{Q}_{2,2}c_0^3 - 4c_0^4 + c_0^8}{4c_0^3}, \tag{5.17c}$$

$$T_{2,0} = \frac{\alpha^2 - 2\alpha c_0^2 + \left(1 - 2\alpha^2\right)c_0^4 - 2\alpha c_0^6 + \alpha^2 c_0^8}{4c_0^2}, \tag{5.17d}$$

where $\hat{N}_{2,2}$ and $\hat{Q}_{2,2}$ are the second-order corrections of the Stokes waves, see Section 4.3 in Chapter 4 for more details. The remaining coefficients follow from the identities

$$S_{2,-1} = -S_{2,1},\ T_{2,-1} = -T_{2,1},\ U_{2,-1} = -U_{2,1},\ V_{2,-1} = U_{2,-1},\ S_{2,-1} = c_0 S_{2,0}, \tag{5.18}$$

which hold for $\alpha > 0$. The proofs of these identities are shown in the companion Mathematica files. In addition to thesis identities, we have the following result:

Theorem 5.3.1. *For all* $\alpha > 0$*, we have* $S_{2,-1} > 0$*,* $T_{2,-1} > 0$*, and* $T_{2,0} < 0$*.*

Proof. Substituting $c_0 = \sqrt{\tanh(\alpha)}$ in (5.17a), we arrive at

$$T_{2,-1} = \frac{1}{8}\operatorname{csch}(\alpha)\operatorname{sech}^3(\alpha)\left(2\alpha + 3\sinh(2\alpha) + \sinh(4\alpha)\right), \tag{5.19}$$

from which $S_{2,-1} > 0$ follows immediately for $\alpha > 0$.

Doing the same for (5.17b), we arrive at

$$T_{2,-1} = \frac{-1 - 4\alpha^2 + 8\alpha^2\cosh(2\alpha) + \cosh^2(2\alpha) - 4\alpha\sinh(2\alpha)}{16\tanh^{3/2}(\alpha)\cosh^4(\alpha)}, \tag{5.20}$$

after some work. Rearranging terms in the numerator,

$$T_{2,-1} = \frac{\left(-1 - 4\alpha^2 + \cosh^2(2\alpha)\right) + 4\alpha\cosh(2\alpha)\left(2\alpha - \tanh(2\alpha)\right)}{16\tanh^{3/2}(\alpha)\cosh^4(\alpha)}. \tag{5.21}$$

Using the Taylor series of cosh, we have $-1 - 4\alpha^2 + \cosh^2(2\alpha) > 0$ immediately. Using the well-known bound $\tanh(|k|) < |k|$ for $k \in \mathbb{R}$, we have $2\alpha - \tanh(2\alpha) > 0$. It follows that $T_{2,-1} > 0$ for $\alpha > 0$.

Lastly, for (5.17d),

$$T_{2,0} = -\frac{1}{64}\operatorname{csch}(\alpha)\operatorname{sech}^3(\alpha)\left(e^{4\alpha} - (1+4\alpha)\right)\left(e^{-4\alpha} - (1-4\alpha)\right), \tag{5.22}$$

after some work. Using $\exp(k) > 1 + k$ for $k > 0$, we immediately conclude $T_{2,0} < 0$ for $\alpha > 0$, as desired. □

Equations (5.16a)-(5.16c) constitute a nonlinear system for the unknown variables λ_2 and $\beta_{0,\pm 1}$. The first-order Floquet correction μ_1 and first-order rescaling of the Floquet interval r_1 appear as parameters in this system. Because of the symmetry of the Floquet interval corresponding to the Benjamin-Feir figure-eight curve, we consider $\mu_1 > 0$ without loss of generality, as mentioned before. Also appearing as a parameter in our system is $\beta_{0,0}$, the coefficient of the zeroth mode of $\mathbf{w_0}$. Without loss of generality, we normalize the eigenfunction $\mathbf{w}$ so that $\beta_{0,0} > 0$. Under these assumptions, we solve (5.16a)-(5.16c) for λ_2. Using the identities listed in (5.18) as well as the inequalities in the claim above, we find

$$\lambda_2 = \lambda_{2,R} + i\lambda_{2,I}, \tag{5.23}$$

where

$$\lambda_{2,R} = \pm\frac{\mu_1}{2}\sqrt{T_{2,-1}\left(\frac{2\left(S_{2,-1}S_{2,0} - U_{2,-1}T_{2,0}\right)}{T_{2,0}} - T_{2,-1}\mu_1^2\right)}, \tag{5.24a}$$

$$\lambda_{2,I} = -r_1\mu_1 c_g. \tag{5.24b}$$

Defining

$$e_2 = 4T_{2,-1}, \quad e_{BW} = \frac{S_{2,-1}S_{2,0} - U_{2,-1}T_{2,0}}{T_{2,0}}, \quad \text{and} \tag{5.25a}$$

$$\Delta_{BW} = \sqrt{e_2\left(8e_{BW} - e_2\mu_1^2\right)}, \tag{5.25b}$$

(5.24a) simplifies to

$$\lambda_{2,R} = \pm\frac{\mu_1}{8}\Delta_{BW}. \tag{5.26}$$

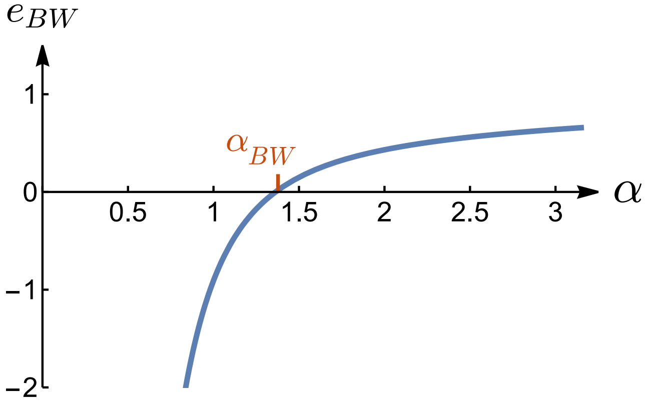

Figure 5.3: A plot of e_{BW} *vs.* α. The only root of e_{BW} for $\alpha > 0$ is $\alpha_{BW} = 1.3627827567...$.

For (5.26) to be nonzero, we must have $e_{BW} > 0$. It is well-known (see, for instance, [11]) that $e_{BW} > 0$ only if $\alpha > \alpha_{BW} = 1.3627827567...$, the critical threshold for modulational instability originally found by [8, 92]. A plot of e_{BW} as a function of α confirms this fact, see Figure 5.3.

Remark 5.3.4. *The variables e_2 and e_{BW} correspond directly to the variables e_{22} and e_{WB} in [11], respectively. Using the expressions for $S_{2,-1}$, $U_{2,-1}$, $S_{2,0}$, and $T_{2,0}$ above, we obtain an explicit representation of e_{BW}:*

$$e_{BW} = \frac{1}{(-1+8\alpha^2+\cosh(4\alpha)-4\alpha\sinh(4\alpha))\tanh^{3/2}(\alpha)}\Bigg(-4+8\alpha^2+8\cosh(2\alpha) \\ +5\cosh(4\alpha)+2\alpha\Big(-9\coth(\alpha)+18\alpha\,\mathrm{csch}^2(2\alpha)-2\sinh(4\alpha)+3\tanh(\alpha)\Big)\Bigg). \tag{5.27}$$

The root of this expression for $\alpha > 0$ is the critical threshold α_{BW}.

Provided $\alpha > \alpha_{BW}$, (5.26) has nonzero real part for

$$0 < \mu_1 < M, \quad M = \sqrt{\frac{8e_{BW}}{e_2}}. \tag{5.28}$$

Inequality (5.28) together with the first-order eigenvalue correction (5.11) and second-order eigenvalue corrections (5.24b) and (5.26) yield the leading-order parameterization for one loop of the figure-eight curve. Because $c_g < 0$ for all $\alpha > 0$, this loop is in the upper-half complex plane. The remaining loop is obtained if one repeats the analysis above for $\mu_1 < 0$. Then one finds $-M < \mu_1 < 0$ necessarily, so that the parameterizing interval of Floquet exponents for the entire figure-eight curve has the asymptotic expansion

$$\mu \in \varepsilon \left(-M, M\right) \Big(1 + r_1 \varepsilon\Big) + \mathcal{O}\left(\varepsilon^3\right). \tag{5.29}$$

Remark 5.3.5. *For the remainder of this work, we restrict to the positive branch of* (5.26) *and, therefore, obtain a parameterization only for the half-loop of the figure-eight curve in the first quadrant of the complex plane. By quadrafold symmetry of the stability spectrum* (4.35)*, we can recover a parameterization for the entire figure-eight curve from this half-loop.*

Both (5.24b) and (5.29) depend on the first-order rescaling parameter r_1. This results in ambiguity at $\mathcal{O}\left(\varepsilon^2\right)$ in both the Floquet parameterization and imaginary part of the figure-eight. We show at the next order that $r_1 = 0$ using the regular curve condition. Using this, we can assemble our expansions for the real and imaginary parts of the figure-eight curve

$$\lambda_R = \frac{\mu_1}{8} \Delta_{BW} \varepsilon^2 + \mathcal{O}\left(\varepsilon^3\right), \tag{5.30a}$$

$$\lambda_I = -\mu_1 c_g \varepsilon + \mathcal{O}\left(\varepsilon^3\right), \tag{5.30b}$$

respectively. Dropping terms of $\mathcal{O}\left(\varepsilon^3\right)$ and smaller and eliminating the μ_1 dependence, we obtain the algebraic curve

$$64 c_g^4 \lambda_R^2 = e_2 \lambda_I^2 \Bigg(8 e_{BW} c_g^2 \varepsilon^2 - e_2 \lambda_I^2\Bigg), \tag{5.31}$$

which is a lemniscate of Huygens (or Gerono) [54]. This lemniscate represents a uniformly accurate asymptotic approximation of the Benjamin-Feir figure-eight curve to $\mathcal{O}\left(\varepsilon^2\right)$ and is consistent with the low-order heuristic approximation presented in [11]. For sufficiently small ε, this lemniscate agrees well with numerical results, see Figure 5.4.

Given the asymptotic expansion of λ_R in (5.30a) above, a direct calculation shows that λ_R attains the maximum value

$$\lambda_{R,*} = \frac{e_{BW}}{2} \varepsilon^2 + \mathcal{O}\left(\varepsilon^3\right), \tag{5.32}$$

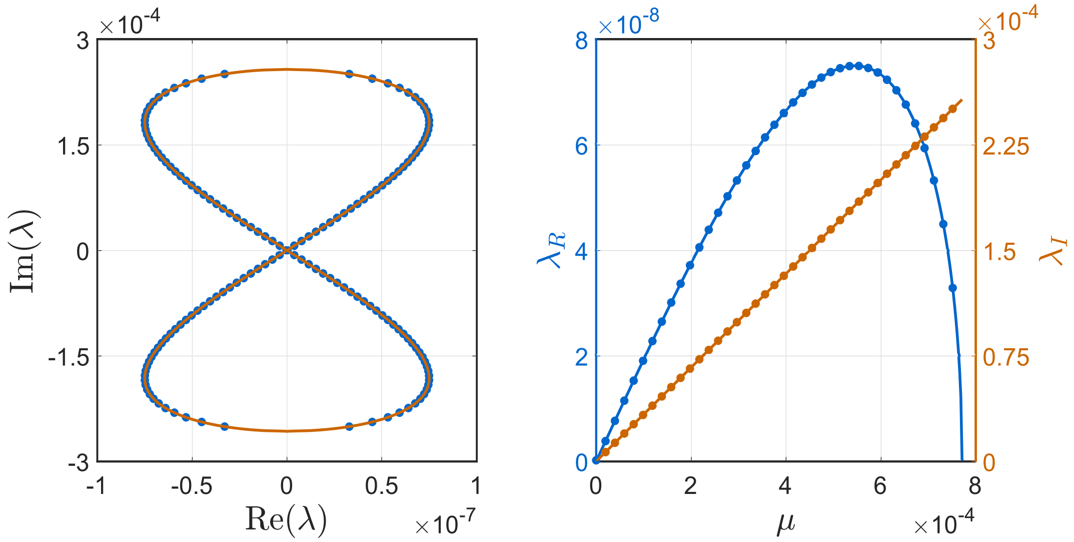

Figure 5.4: (Left) A plot of the Benjamin-Feir figure-eight curve for a Stokes wave with amplitude $\varepsilon = 10^{-3}$ and aspect ratio $\alpha = 1.5$. Numerical results are given by the blue dots, and the asymptotic results to $\mathcal{O}\left(\varepsilon^2\right)$ are given by the solid orange curve. (Right) The Floquet parameterization of the real (blue axis) and imaginary (orange axis) part of the figure-eight curve on the left. The respective numerical results are given by the correspondingly colored dots, and the respective asymptotic results to $\mathcal{O}\left(\varepsilon^2\right)$ are given by the correspondingly colored curves.

when μ_1 is equal to

$$\mu_{1,*} = 2\sqrt{\frac{e_{BW}}{e_2}}. \tag{5.33}$$

This gives an asymptotic expansion for the real part of the most unstable eigenvalue on the half-loop. Its corresponding imaginary part and Floquet exponent are

$$\lambda_{I,*} = -c_g\left(2\sqrt{\frac{e_{BW}}{e_2}}\right)\varepsilon + \mathcal{O}\left(\varepsilon^2\right), \tag{5.34a}$$

$$\mu_{*} = \left(2\sqrt{\frac{e_{BW}}{e_2}}\right)\varepsilon + \mathcal{O}\left(\varepsilon^2\right), \tag{5.34b}$$

respectively. These expansions agree with numerical computations up to $\varepsilon = 10^{-2}$, see Figure 5.5.

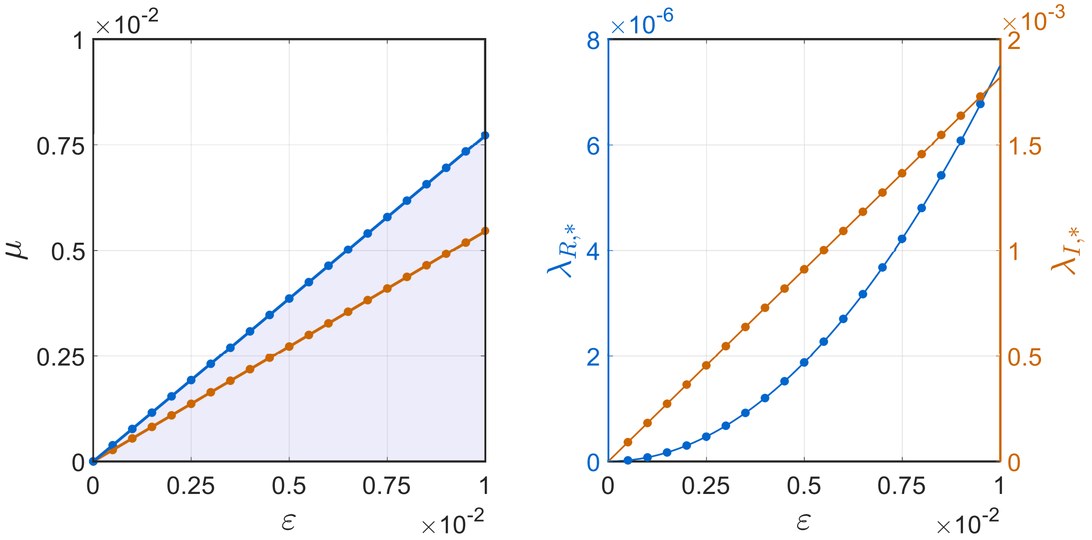

Figure 5.5: (Left) The interval of Floquet exponents parameterizing the half-loop of the Benjamin-Feir figure-eight curve for a Stokes wave with aspect ratio $\alpha = 1.5$ and variable amplitude ε. The numerically computed boundary of this interval is given by the blue dots, while the solid blue curve gives the asymptotic results to $\mathcal{O}\left(\varepsilon^2\right)$. The orange dots give the numerically computed Floquet exponents of the most unstable eigenvalue, while the solid orange curves give the corresponding asymptotic results to $\mathcal{O}\left(\varepsilon\right)$. (Right) The real (blue axis) and imaginary (orange axis) part of the most unstable eigenvalue with $\alpha = 1.5$ and variable ε. Numerical results are given by the correspondingly colored dots, and the asymptotic results for the real and imaginary part to $\mathcal{O}\left(\varepsilon^2\right)$ and $\mathcal{O}\left(\varepsilon\right)$, respectively, are given by the correspondingly colored solid curves.

Remark 5.3.6. *As we will see in Subsection 5.3.2, the first-order Floquet correction* $\mu_{1,*}$ *corresponding to the most unstable eigenvalue is given by a power series in* ε*. Equation* (5.33) *gives the leading-order term in this series. At this point, we do not know the higher-order corrections of this series and, as a result, are unable to predict the second-order terms of* (5.34a) *and* (5.34b)*. This is a common feature in our analysis of the most unstable eigenvalue:* $\lambda_{R,*}$ *is determined to one order higher in* ε *than* $\lambda_{I,*}$ *and* $\mu_{1,*}$*.*

To conclude our discussion of the $\mathcal{O}\left(\varepsilon^2\right)$ problem, we solve for the remaining unknowns in (5.16a)-(5.16c) and obtain

$$\beta_{0,-1} = \frac{(ie_2\mu_1 \mp \Delta_{BW})\, T_{2,0}\beta_{0,0}}{2e_2 S_{2,0}}, \tag{5.35a}$$

$$\beta_{0,1} = \frac{(ie_2\mu_1 \pm \Delta_{BW})\, T_{2,0}\beta_{0,0}}{2e_2 S_{2,0}}. \tag{5.35b}$$

Since we have chosen the positive branch of (5.24b), the negative branch is chosen for (5.35a), and the positive branch is chosen for (5.35b). Both (5.35a) and (5.35b) are determined up to the free parameter $\beta_{0,0}$, which is determined upon choosing a normalization for the eigenfunction $\mathbf{w}$.

Finally, given the solutions λ_2 and $\beta_{0,\pm 1}$ of (5.16a)-(5.16c), we solve the second-order problem (5.15) and obtain

$$\mathbf{w_2}(x) = \sum_{j=-3}^{3} \mathbf{w_{2,j}} e^{ijx} + \beta_{2,-1}\mathbf{w_{0,-1}}(x) + \beta_{2,0}\mathbf{w_{0,0}}(x) + \beta_{2,1}\mathbf{w_{0,1}}(x), \tag{5.36}$$

for $\mathbf{w_{2,j}} = \mathbf{w_{2,j}}(\alpha, \beta_{0,0}, \beta_{1,\nu}, \mu_1, r_1) \in \mathbb{C}^2$, see the companion Mathematica files for details. The constants $\beta_{2,\nu} \in \mathbb{C}$ are undetermined at this order.

5.3.3 The $\mathcal{O}(\varepsilon^3)$ Problem

At $\mathcal{O}(\varepsilon^3)$, the spectral problem (4.35) is

$$\Big(\mathcal{L}_0 - \lambda_0\mathcal{R}_0\Big)\mathbf{w_3} = -\sum_{j=1}^{3}\mathcal{L}_j\mathbf{w_{3-j}} + \mathcal{R}_0\Big(\sum_{k=1}^{3}\lambda_k\mathbf{w_{3-k}}\Big) + \sum_{j=1}^{3}\mathcal{R}_j\Big(\sum_{k=0}^{3-j}\lambda_k\mathbf{w_{3-j-k}}\Big). \tag{5.37}$$

Using the solvability conditions from previous orders, the solvability conditions of (5.37) simplify to a 3×3 linear system

$$\mathcal{M}\begin{pmatrix}\beta_{1,-1}\\ \lambda_3\\ \beta_{1,1}\end{pmatrix} = \begin{pmatrix} f_{3,1}\\ f_{3,2}\\ f_{3,3}\end{pmatrix}, \tag{5.38}$$

with

$$\mathcal{M} = \begin{pmatrix} 2(\lambda_2 + ic_g r_1\mu_1) + iT_{2,-1}\mu_1^2 + iV_{2,-1} & 2\beta_{0,-1} & iU_{2,-1} \\ iS_{2,0}\mu_1 & 0 & iS_{2,0}\mu_1 \\ iU_{2,1} & 2\beta_{0,1} & 2(\lambda_2 + ic_g r_1\mu_1) + iT_{2,1}\mu_1^2 + iV_{2,1} \end{pmatrix}, \tag{5.39}$$

and

$$\begin{aligned} f_{3,1} &= -\Big(\beta_{1,0}S_{2,-1}\mu_1 + \beta_{0,-1}\big(2ir_2\mu_1 c_g + \mu_1(A_{3,-1}\lambda_2 + iB_{3,-1}r_1\mu_1 + iC_{3,-1} + iD_{3,-1}\mu_1^2)\big) \\ &\qquad + \beta_{0,0}\big(iE_{3,-1}\lambda_2 + F_{3,-1}r_1\mu_1 + G_{3,-1}\mu_1^2\big)\Big), && (5.40a) \\ f_{3,2} &= -\Big(\beta_{1,0}T_{2,0}\mu_1^2 + \beta_{0,-1}\big(A_{3,0}\lambda_2 + ir_1\mu_1 B_{3,0} + iC_{3,0}\mu_1^2\big) + \mu_1\beta_{0,0}\big(iD_{3,0}\lambda_2 + E_{3,0}r_1\mu_1\big) \\ &\qquad + \beta_{0,1}\big(A_{3,0}\lambda_2 + ir_1\mu_1 B_{3,0} - iC_{3,0}\mu_1^2\big)\Big), && (5.40b) \\ f_{3,3} &= -\Big(\beta_{1,0}S_{2,1}\mu_1 + \beta_{0,1}\big(2ir_2\mu_1 c_g + \mu_1(A_{3,1}\lambda_2 + iB_{3,1}r_1\mu_1 + iC_{3,1} + iD_{3,1}\mu_1^2)\big) \\ &\qquad + \beta_{0,0}\big(iE_{3,1}\lambda_2 + F_{3,1}r_1\mu_1 + G_{3,1}\mu_1^2\big)\Big). && (5.40c) \end{aligned}$$

The capitalized coefficients in the expressions above are all real-valued functions of the aspect ratio α. Explicitly,

$$\begin{aligned} A_{3,-1} &= 1 + \frac{\alpha}{c_0^2} - \alpha c_0^2, && (5.41a) \\ B_{3,-1} &= \frac{\alpha(\alpha - c_0^2 + c_0^6 - \alpha c_0^8}{c_0^3}, && (5.41b) \\ C_{3,-1} &= \frac{1}{2c_0^5\left(-4c_0^2 + \omega_2^2\right)^2}\Big(8\alpha c_0^{16} + \alpha\omega_2^4 + c_0^2\omega_2^2\left(\alpha - \omega_2^2\right) - c_0^{14}\left(8 + 13\alpha\omega_2^2\right) \\ &\qquad + c_0^6\left(56 + 17\alpha\omega_2^2 + 10\omega_2^4\right) + c_0^{12}\left(28\alpha + 22\omega_2^2 - 4\alpha\omega_2^4\right) - 10c_0^4\big(2\alpha \\ &\qquad + \omega_2^2 + \alpha\omega_2^4\big) + c_0^8\left(-16\alpha - 44\omega_2^2 + 13\alpha\omega_2^4\right) + c_0^{10}\big(16 \\ &\qquad - 5\omega_2^2\left(\alpha + \omega_2^2\right)\big) - 2c_0^3\left(-\alpha + c_0^2 + \alpha c_0^4\right)\left(4c_0^2 - \omega_2^2\right)^2\left(c_2 - Q_{2,0}\right)\Big), && (5.41c) \\ D_{3,-1} &= \frac{1}{12c_0^5}\Big(3\alpha^2\left(\alpha - c_0^2\right) + \alpha c_0^4(3 + \alpha^2)\left(c_0^4 - 1\right) + c_0^6\left(3 + 6\alpha^2\right) - 3\alpha^2 c_0^{10}\left(-1 + \alpha c_0^2\right)\Big), && (5.41d) \\ E_{3,-1} &= \frac{1 - c_0^4}{2c_0}, && (5.41e) \end{aligned}$$

$$F_{3,-1} = \frac{1}{2}\left(3 - c_0^4\right), \tag{5.41f}$$

$$G_{3,-1} = \frac{\alpha^2 + 2\alpha c_0^2 - c_0^4(3+\alpha^2) - c_0^8(\alpha^2 - 1) - 2\alpha c_0^{10} + \alpha^2 c_0^{12}}{8c_0^4}, \tag{5.41g}$$

$$E_{3,0} = -\alpha + c_0^2 - \alpha c_0^4, \tag{5.41h}$$

where $Q_{2,0}$ is a second-order correction of the Stokes wave due to the traveling frame (see Subsection 2.2) and $\omega_2 = \omega(2)$ for ω in (4.44b). Analogous to (5.18), the remaining coefficients are determined by the following identities for $\alpha > 0$:

$$\begin{gathered} A_{3,-1} = -A_{3,1},\ B_{3,-1} = -B_{3,1}, C_{3,-1} = C_{3,1},\ D_{3,-1} = D_{3,1},\ E_{3,-1} = -E_{3,1},\ F_{3,-1} = -F_{3,1}, \\ G_{3,-1} = G_{3,1},\ A_{3,0} = -E_{3,-1}/c_0,\ B_{3,0} = F_{3,-1}/c_0,\ C_{3,0} = G_{3,-1}/c_0,\ D_{3,0} = c_0 A_{3,-1}. \end{gathered} \tag{5.42}$$

In addition, we have a new identity

$$T_{2,0}\Big(S_{2,0}\Big(c_g E_{3,-1} + F_{3,-1}\Big) + S_{2,-1}\Big(- c_g A_{3,0} + B_{3,0}\Big)\Big) - S_{2,-1}S_{2,0}\Big(c_g D_{3,0} + E_{3,0}\Big) = 0, \tag{5.43}$$

to be used momentarily. The proofs of (5.42) and (5.43) are found in the companion Mathematica files.

Taking the positive branch of λ_2 and corresponding branches of $\beta_{0,\pm1}$, a direct calculation shows

$$\det(\mathcal{M}) = \beta_{0,0} T_{2,0} \Delta_{BW} \mu_1^3, \tag{5.44}$$

which is nonzero for μ_1 satisfying (5.28). A similar result holds if the negative branch of λ_2 is chosen. Thus, (5.38) is an invertible linear system for all eigenvalues along the figure-eight curve. Solving this system for λ_3 on the half-loop, we find

$$\lambda_3 = \lambda_{3,R} + i\lambda_{3,I}, \tag{5.45}$$

where

$$\lambda_{3,R} = \frac{1}{4} r_1 \mu_1 \left(\frac{e_2 \Lambda_{3,R}}{\Delta_{BW}} - \frac{\Delta_{BW}\left(c_g A_{3,-1} - B_{3,-1}\right)}{e_2} \right), \tag{5.46a}$$

$$\lambda_{3,I} = \mu_1 \left(- r_2 c_g + \frac{\Lambda_{3,I}}{32 e_2 T_{2,0}^2} \right), \tag{5.46b}$$

and, after using (5.43) to simplify,

$$\Lambda_{3,R} = \mu_1^2 \left(c_g A_{3,-1} - B_{3,-1}\right), \tag{5.47a}$$

$$\begin{aligned}\Lambda_{3,I} = {} & -A_{3,-1}\Delta_{BW}^2 T_{2,0}^2 - 16e_2 T_{2,0}\left(-C_{3,0}S_{2,-1} - G_{3,-1}S_{2,0} + T_{2,0}\left(C_{3,-1} + D_{3,-1}\right)\right) \\ & + e_2^2\left(-2D_{3,0}S_{2,-1}S_{2,0} + T_{2,0}\left(-2A_{3,0}S_{2,-1} + 2E_{3,-1}S_{2,0} + A_{3,-1}T_{2,0}\mu_1^2\right)\right).\end{aligned} \tag{5.47b}$$

Solutions of (5.37) for $\beta_{1,\pm 1}$ are found in the companion Mathematica files.

It appears (5.46a) is singular as $\mu_1 \to M$ since $\Delta_{BW} \to 0$. If $r_1 \neq 0$, this singularity is not removable, as the following result shows.

Theorem 5.3.2. *Let* $\Lambda_{3,R}^{(M)} = \lim_{\mu_1 \to M} \Lambda_{3,R}$. *For* $\alpha > \alpha_{BW}$, $\Lambda_{3,R}^{(M)} \neq 0$.

Proof. Taking the appropriate limit of $\Lambda_{3,R}$ yields

$$\Lambda_{3,R}^{(M)} = \frac{8e_{BW}}{e_2}\Big(c_g A_{3,-1} - B_{3,-1}\Big). \tag{5.48}$$

Using explicit expressions for $A_{3,-1}$, $B_{3,-1}$, and c_g, a direct calculation shows

$$c_g A_{3,-1} - B_{3,-1} = -2T_{2,-1}. \tag{5.49}$$

Given $e_2 = 4T_{2,-1}$ by definition, we conclude

$$\Lambda_{3,R}^{(M)} = -4e_{BW} < 0, \tag{5.50}$$

for $\alpha > \alpha_{BW}$. This proves the claim. □

Because $\Lambda_{3,R}^{(M)}$ is nonzero for all $\alpha > \alpha_{BW}$, (5.46a) is singular as $\mu_1 \to M$, unless $r_1 = 0$. Since the Benjamin-Feir figure-eight curve consists of bounded eigenvalues that have non-singular dependence on the Floquet exponent [11], the regular curve condition [28, 29, 30] enforces the choice $r_1 = 0$ to remove the singularity, justifying our claim at the previous order.

With $r_1 = 0$, λ_3 is purely imaginary and depends on the second-order rescaling parameter r_2. To determine r_2 and the next real correction to the figure-eight curve, we must proceed to $\mathcal{O}\left(\varepsilon^4\right)$. This requires the solution of (5.37) subject to the solvability conditions above. We obtain

$$\mathbf{w_3}(x) = \sum_{j=-4}^{4} \mathbf{w_{3,j}} e^{ijx} + \beta_{3,-1}\mathbf{w_{0,-1}}(x) + \beta_{3,0}\mathbf{w_{0,0}}(x) + \beta_{3,1}\mathbf{w_{0,1}}(x), \tag{5.51}$$

where $\mathbf{w_{3,j}} = \mathbf{w_{3,j}}(\alpha, \beta_{0,0}, \beta_{1,0}, \beta_{2,\nu}, \mu_1, r_2) \in \mathbb{C}^2$ while $\beta_{3,\nu} \in \mathbb{C}$ are undetermined constants at this order, see the companion Mathematica files for details.

5.3.4 The $\mathcal{O}\left(\varepsilon^4\right)$ Problem

At $\mathcal{O}\left(\varepsilon^4\right)$, the spectral problem (4.35) is

$$\Big(\mathcal{L}_0 - \lambda_0\mathcal{R}_0\Big)\mathbf{w_4} = -\sum_{j=1}^{4} \mathcal{L}_j \mathbf{w_{4-j}} + \mathcal{R}_0\Big(\sum_{k=1}^{4} \lambda_k \mathbf{w_{4-k}}\Big) + \sum_{j=1}^{4} \mathcal{R}_j\Big(\sum_{k=0}^{4-j} \lambda_k \mathbf{w_{4-j-k}}\Big). \tag{5.52}$$

The solvability conditions of (5.52) simplify to a 3×3 linear system

$$\mathcal{M}\begin{pmatrix} \beta_{2,-1} \\ \lambda_4 \\ \beta_{2,1} \end{pmatrix} = \begin{pmatrix} f_{4,1} \\ f_{4,2} \\ f_{4,3} \end{pmatrix}, \tag{5.53}$$

where $\mathcal{M}$ is as before and

$$\begin{aligned} f_{4,1} = -\Big(&\beta_{2,0}S_{2,-1}\mu_1 + \beta_{1,-1}\big(2\left(\lambda_3 + ir_2\mu_1 c_g\right) + \mu_1(A_{3,-1}\lambda_2 + iC_{3,-1} + iD_{3,-1}\mu_1^2)\big) \\ &+ \beta_{1,0}\big(iE_{3,-1}\lambda_2 + G_{3,-1}\mu_1^2\big) + \beta_{0,-1}\big(2ir_3\mu_1 c_g + \mu_1(A_{3,-1}\lambda_3 + iB_{3,-1}r_2\mu_1 \\ &+ i\mu_1^3 I_{4,-1} + \mu_1(H_{4,-1}\lambda_2 + iG_{4,-1}^{0,-1}))\big) + \lambda_2 E_{4,-1} + iJ_{4,-1}^{0,-1} - i\lambda_2^2/c_0\big) \\ &+ \beta_{0,0}\big(iE_{3,-1}\lambda_3 + F_{3,-1}r_2\mu_1 + D_{4,-1}\mu_1^3 + \mu_1\left(iA_{4,-1}\lambda_2 + C_{4,-1}\right)\big) \\ &+ i\beta_{0,1}\big(\mu_1^2 G_{4,-1}^{0,1} + J_{4,-1}^{0,1}\big)\Big), \end{aligned} \tag{5.54a}$$

$$\begin{aligned} f_{4,2} = -\Big(&\beta_{2,0}T_{2,0}\mu_1^2 + \beta_{1,-1}\big(A_{3,0}\lambda_2 + iC_{3,0}\mu_1^2\big) + i\beta_{1,0}D_{3,0}\mu_1\lambda_2 \\ &+ \beta_{1,1}\big(A_{3,0}\lambda_2 - iC_{3,0}\mu_1^2\big) + \beta_{0,-1}\big(A_{3,0}\lambda_3 + iB_{3,0}r_2\mu_1 + \mu_1(D_{4,0}\lambda_2 + iF_{4,0} \\ &+ iG_{4,0}\mu_1^2)\big) + \beta_{0,0}\big(\mu_1(iD_{3,0}\lambda_3 + E_{3,0}r_2\mu_1 + H_{4,0}\mu_1^3 + C_{4,0}\mu_1) - \lambda_2^2\big) \\ &+ \beta_{0,1}\big(A_{3,0}\lambda_3 + iB_{3,0}r_2\mu_1 + \mu_1(-D_{4,0}\lambda_2 + iF_{4,0} + iG_{4,0}\mu_1^2)\big)\Big), \end{aligned} \tag{5.54b}$$

$$\begin{aligned} f_{4,3} = -\Big(&\beta_{2,0}S_{2,1}\mu_1 + \beta_{1,1}\big(2\left(\lambda_3 + ir_2\mu_1 c_g\right) + \mu_1(A_{3,1}\lambda_2 + iC_{3,1} + iD_{3,1}\mu_1^2)\big) \\ &+ \beta_{1,0}\big(iE_{3,1}\lambda_2 + G_{3,1}\mu_1^2\big) + \beta_{0,1}\big(2ir_3\mu_1 c_g + \mu_1(A_{3,1}\lambda_3 + iB_{3,1}r_2\mu_1 \\ &+ i\mu_1^3 I_{4,1} + \mu_1(H_{4,1}\lambda_2 + iG^{0,1}_{4,1}))\big) + \lambda_2 E_{4,1} + iJ^{0,1}_{4,1} + i\lambda_2^2/c_0\big) \\ &+ \beta_{0,0}\big(iE_{3,1}\lambda_3 + F_{3,1}r_2\mu_1 + D_{4,1}\mu_1^3 + \mu_1\left(iA_{4,1}\lambda_2 + C_{4,1}\right)\big) \\ &+ i\beta_{0,-1}\big(\mu_1^2 G^{0,-1}_{4,1} + J^{0,-1}_{4,1}\big)\Big). \end{aligned} \tag{5.54c}$$

As before, the capitalized coefficients above are all real-valued functions of α. The interested reader can consult the companion Mathematica files for the explicit representations of these functions. One can show that

$$\begin{gathered} A_{4,-1} = A_{4,1},\ C_{4,-1} = -C_{4,1},\ D_{4,-1} = -D_{4,1}, E_{4,-1} = E_{4,1},\ G^{0,1}_{4,-1} = -G^{0,-1}_{4,1}, \\ G^{0,-1}_{4,-1} = -G^{0,1}_{4,1},\ H_{4,-1} = H_{4,1},\ I_{4,-1} = -I_{4,1},\ J^{0,1}_{4,-1} = -J^{0,-1}_{4,1},\ J^{0,-1}_{4,-1} = -J^{0,1}_{4,1}, \\ J^{0,-1}_{4,-1} = J^{0,1}_{4,-1},\ D_{4,0} = -A_{4,-1}/c_0,\ F_{4,0} = C_{4,-1}/c_0, \end{gathered} \tag{5.55}$$

for $\alpha > 0$, analogous to (5.18) and (5.42) from the previous orders.

Solving (5.53) for λ_4 on the half-loop yields

$$\lambda_4 = \lambda_{4,R} + i\lambda_{4,I}, \tag{5.56}$$

with

$$\lambda_{4,R} = \frac{\mu_1}{256 T_{2,0}^3}\left(\frac{\Lambda^{(1)}_{4,R}}{T_{2,0}\Delta_{BW}} - \frac{\Delta_{BW}\Lambda^{(2)}_{4,R}}{c_0 e_2^2}\right), \tag{5.57a}$$

$$\lambda_{4,I} = -r_3\mu_1 c_g. \tag{5.57b}$$

The coefficients $\Lambda^{(j)}_{4,R}$ in (5.57a) decompose as

$$\Lambda^{(j)}_{4,R} = \Lambda^{(j,1)}_{4,R} r_2 + \Lambda^{(j,2)}_{4,R}, \quad j \in \{1, 2\}. \tag{5.58}$$

An application of (5.43) shows

$$\Lambda^{(1,1)}_{4,R} = 64 e_2 T_{2,0}^4 \mu_1^2 \left(c_g A_{3,-1} - B_{3,-1}\right), \tag{5.59}$$

$$\Lambda^{(2,1)}_{4,R} = 64 c_0 e_2 T_{2,0}^2 \left(c_g A_{3,-1} - B_{3,-1}\right). \tag{5.60}$$

The remaining coefficients $\Lambda_{4,R}^{(j,2)}$ are explicit functions of α and μ_1^2. These coefficients as well as the solutions $\beta_{2,\pm 1}$ of (5.53) are found in the companion Mathematica files.

Similar to the previous order, the real part of λ_4 is singular as $\mu_1 \to M$. To remove this singular behavior, we require

$$r_2 = -\frac{\Lambda_{4,R}^{(1,2,M)}}{\Lambda_{4,R}^{(1,1,M)}}, \tag{5.61}$$

using the regular curve condition, where

$$\Lambda_{4,R}^{(1,j,M)} = \lim_{\mu_1 \to M} \Lambda_{4,R}^{(1,j)}, \quad j \in \{1,2\}. \tag{5.62}$$

The rescaling parameter r_2 is well-defined for any fixed $\alpha > \alpha_{BW}$, since $\Lambda_{4,R}^{(1,1,M)} \neq 0$ over this interval by arguments similar to those in Theorem 5.3.1. However, r_2 is unbounded as $\alpha \to \alpha_{BW}^+$ or $\alpha \to \infty$, see Figure 5.6. Both limits suggest potentially unbounded growth in the imaginary part of the figure-eight curve at $\mathcal{O}\left(\varepsilon^3\right)$ (5.46b) and the real part of the curve at $\mathcal{O}\left(\varepsilon^4\right)$ (5.57a). Because μ_1 appears as a factor in both of these expressions, the apparent singular behavior as $\alpha \to \alpha_{BW}^+$ is arrested since $\mu_1 \to 0$ in this limit.

The same cannot be said as $\alpha \to \infty$. The culprit for this growth turns out to be the expressions for $\beta_{0,\pm 1}$ obtained at $\mathcal{O}\left(\varepsilon^2\right)$, see (5.35a) and (5.35b). In particular, $\beta_{0,\pm 1}$ both share a factor of $T_{2,0}$ in their respective numerators that becomes unbounded as $\alpha \to \infty$. This singular behavior is inherited by r_2 and ultimately affects the real and imaginary parts of the figure-eight curve at $\mathcal{O}\left(\varepsilon^4\right)$ and $\mathcal{O}\left(\varepsilon^3\right)$, respectively. This provides a first glimpse into the breakdown of compactness that distinguishes the Benjamin-Feir instability spectrum in finite and infinite depth, as discussed in more detail by [11, 73]. This difference will become even more clear when we consider the infinite depth case in Section 5.4.

Remark 5.3.7. *The singular behavior of* r_2 *as* $\alpha \to \alpha_{BW}^+$ *and* $\alpha \to \infty$ *also affects the parameterizing interval of Floquet exponents* (5.4) *at* $\mathcal{O}\left(\varepsilon^3\right)$. *For similar reasons as above, this singular behavior is avoided as* $\alpha \to \alpha_{BW}^+$, *but remains as* $\alpha \to \infty$.

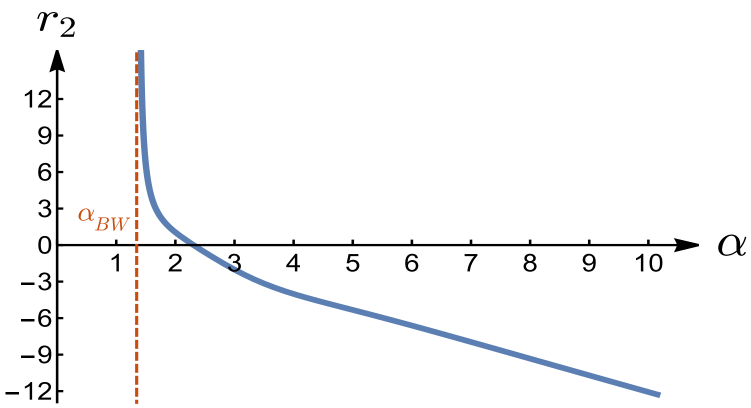

Figure 5.6: A plot of r_2 *vs.* α. For all $\alpha > \alpha_{BW}$, r_2 is well-defined. As $\alpha \to \alpha_{BW}^+$ or $\alpha \to \infty$, r_2 becomes singular. The singular behavior as $\alpha \to \alpha_{BW}^+$ is arrested by the factor of μ_1 in front of (5.46b) and (5.57a). The singular behavior as $\alpha \to \infty$ remains, showcasing the breakdown of compactness in finite versus infinite depth, see [11, 73] for further discussion.

In general, (5.56) has nonzero real part, and we have found a higher-order approximation to the figure-eight curve. This curve is parameterized by Floquet exponents

$$\mu \in \varepsilon\left(-M, M\right)\left(1 - \frac{\Lambda_{4,R}^{(1,2,M)}}{\Lambda_{4,R}^{(1,1,M)}}\varepsilon^2 + r_3\varepsilon^3\right) + \mathcal{O}\left(\varepsilon^5\right). \tag{5.63}$$

The real part along a half-loop of this curve has asymptotic expansion

$$\begin{aligned}\lambda_R = \frac{\mu_1}{8}\Delta_{BW}\varepsilon^2 + \frac{\mu_1}{256c_0\Delta_{BW}\Lambda_{4,R}^{(1,1,M)}e_2^2T_{2,0}^4}\Bigg(c_0e_2^2\left(\Lambda_{4,R}^{(1,1,M)}\Lambda_{4,R}^{(1,2)} - \Lambda_{4,R}^{(1,2,M)}\Lambda_{4,R}^{(1,1)}\right)\\ - T_{2,0}\Delta_{BW}^2\left(\Lambda_{4,R}^{(1,1,M)}\Lambda_{4,R}^{(2,2)} - \Lambda_{4,R}^{(1,2,M)}\Lambda_{4,R}^{(2,1)}\right)\Bigg)\varepsilon^4 + \mathcal{O}\left(\varepsilon^5\right),\end{aligned} \tag{5.64}$$

for $0 < \mu_1 < M$, and its corresponding imaginary part is

$$\lambda_I = -\mu_1c_g\varepsilon + \mu_1\left(\frac{c_g\Lambda_{4,R}^{(1,2,M)}}{\Lambda_{4,R}^{(1,1,M)}} + \frac{\Lambda_{3,I}}{32e_2T_{2,0}^2}\right)\varepsilon^3 - r_3\mu_1c_g\varepsilon^4 + \mathcal{O}\left(\varepsilon^5\right). \tag{5.65}$$

Quadrafold symmetry of the stability spectrum (4.35) extends (5.64) and (5.65) to a full parameterization of the higher-order approximation of the figure-eight curve.

At this order, r_3 is undetermined, leading to ambiguities in the Floquet parameterizing interval (5.63) and the imaginary part (5.65). Proceeding to $\mathcal{O}\left(\varepsilon^5\right)$, one can show via the

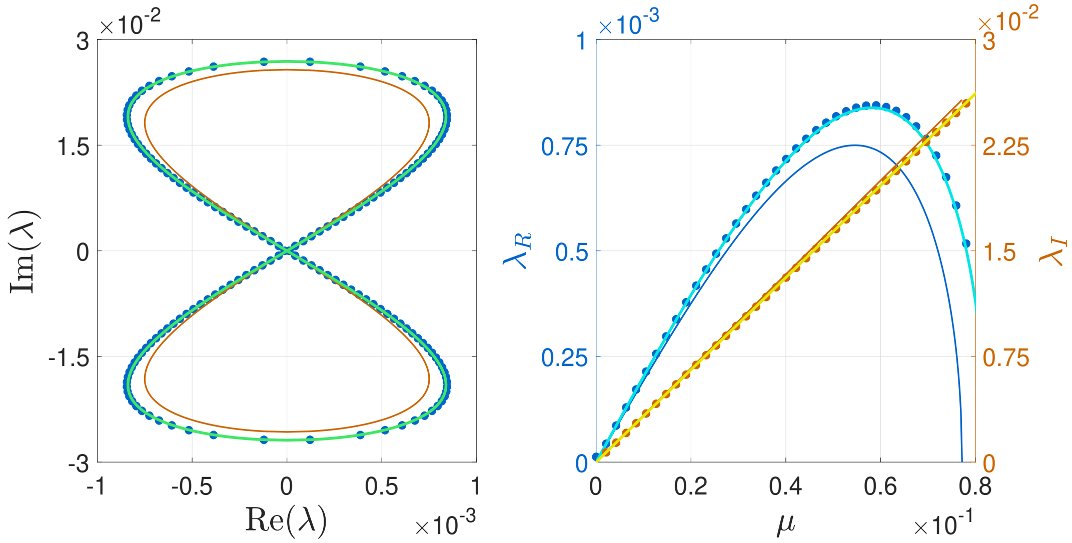

Figure 5.7: (Left) A plot of the Benjamin-Feir figure-eight curve for a Stokes wave with amplitude $\varepsilon = 0.1$ and aspect ratio $\alpha = 1.5$. Numerical results are given by the blue dots, while asymptotic results to $\mathcal{O}\left(\varepsilon^2\right)$ and $\mathcal{O}\left(\varepsilon^4\right)$ are given by the solid orange and green curves, respectively. (Right) The Floquet parameterization of the real (blue axis) and imaginary (orange axis) part of the figure-eight curve on the left. Numerical results are given by the correspondingly colored dots. The asymptotic parameterizations of the real part to $\mathcal{O}\left(\varepsilon^2\right)$ and $\mathcal{O}\left(\varepsilon^4\right)$ are given by the solid blue and light blue curves, respectively, while those for the imaginary part are given by the solid orange and yellow curves, respectively.

regular curve condition that $r_3 = 0$. Dropping terms of at least $\mathcal{O}\left(\varepsilon^5\right)$ in (5.64) and (5.65) and eliminating μ_1 leads, in theory, to a new algebraic curve that uniformly approximates the Benjamin-Feir figure-eight to $\mathcal{O}\left(\varepsilon^4\right)$. In practice, eliminating μ_1 from (5.64) and (5.65) is too cumbersome, and we leave this curve in its parameterized form on the half-loop. Figure 5.7 compares our higher-order approximation of the figure-eight with numerical results and the lower-order approximation of the figure-eight, obtained above. Both figure-eight approximations match numerical computations well for $\varepsilon \ll 0.1$. Around $\varepsilon = 0.1$, the lower-order approximation deviates from numerical results, while the higher-order approximation maintains excellent agreement, giving confidence in our higher-order asymptotic expansions. In addition to a higher-order description of the figure-eight curve, we can estimate its most unstable eigenvalue by examining the critical points of (5.64) with respect to μ_1. For ease of notation, let $\lambda_{2,R}$ and $\lambda_{4,R}$ denote the second- and fourth-order corrections of (5.64), respectively, and let $\mu_{1,*}$ denote the critical points. Then

$$\frac{\partial}{\partial \mu_1}\left(\lambda_{2,R}(\alpha,\mu_1)\varepsilon^2 + \lambda_{4,R}(\alpha,\mu_1)\varepsilon^4 + \mathcal{O}\left(\varepsilon^5\right)\right)\bigg|_{\mu_{1,*}} = 0. \tag{5.66}$$

Dropping terms of $\mathcal{O}\left(\varepsilon^5\right)$ and smaller, we arrive at an algebraic equation for the critical points:

$$\lambda'_{2,R}(\alpha,\mu_{1,*}) + \lambda'_{4,R}(\alpha,\mu_{1,*})\varepsilon^2 = 0, \tag{5.67}$$

where primes denote differentiation with respect to μ_1. When $\varepsilon = 0$, (5.67) has positive solution

$$\mu_{1,*_0} = 2\sqrt{\frac{e_{BW}}{e_2}}, \tag{5.68}$$

coinciding with the first-order correction of the most unstable Floquet exponent (5.33). When $0 < \varepsilon \ll 1$, we expect $\mu_{1,*}$ to bifurcate smoothly from $\mu_{1,*_0}$. Since the small parameter in (5.67) appears as ε^2, we expand $\mu_{1,*}$ in ε^2, yielding

$$\mu_{1,*} = \mu_{1,*_0} + \varepsilon^2\mu_{1,*_2} + \mathcal{O}\left(\varepsilon^4\right). \tag{5.69}$$

Substituting (5.69) into (5.67),

$$\mu_{1,*_2} = -\frac{\lambda'_{4,R}(\alpha,\mu_{1,*_0})}{\lambda''_{2,R}(\alpha,\mu_{1,*_0})}. \tag{5.70}$$

at $\mathcal{O}\left(\varepsilon^2\right)$. To simplify notation further, we drop the functional dependencies above, denoting $\lambda'_{4,R}(\alpha,\mu_{1,*_0})$ and $\lambda''_{2,R}(\alpha,\mu_{1,*_0})$ instead by $\lambda'_{4,R,*}$ and $\lambda''_{2,R,*}$, respectively. Substituting (5.70) into (5.4), we arrive at an asymptotic expansion for the Floquet exponent of the most unstable eigenvalue on the higher-order half-loop:

$$\mu_* = \left(2\sqrt{\frac{e_{BW}}{e_2}}\right)\varepsilon - \left(2\frac{\Lambda_{4,R}^{(1,2,M)}}{\Lambda_{4,R}^{(1,1,M)}}\sqrt{\frac{e_{BW}}{e_2}} + \frac{\lambda'_{4,R,*}}{\lambda''_{2,R,*}}\right)\varepsilon^3 + \mathcal{O}\left(\varepsilon^4\right). \tag{5.71}$$

If instead we substitute (5.69) into (5.64), we obtain an asymptotic expansion for the real part of the most unstable eigenvalue. Using our simplified notation above,

$$\lambda_{R,*} = \lambda_{2,R,*}\varepsilon^2 + \left(\lambda'_{2,R,*}\mu_{1,*_2} + \lambda_{4,R,*}\right)\varepsilon^4 + \mathcal{O}\left(\varepsilon^5\right). \tag{5.72}$$

Unpacking this notation, we obtain the more explicit expansion

$$\begin{aligned}\lambda_{R,*} = \frac{e_{BW}}{2}\varepsilon^2 + \frac{e_{BW}}{256c_0\Lambda^{(1,1,M)}_{4,R}e_2^2T_{2,0}^4}\Bigg(&c_0e_2\left(\Lambda^{(1,1,M)}_{4,R}\Lambda^{(1,2)}_{4,R,*} - \Lambda^{(1,2,M)}_{4,R}\Lambda^{(1,1)}_{4,R,*}\right)\\ &- 4\frac{T_{2,0}}{e_{BW}}\left(\Lambda^{(1,1,M)}_{4,R}\Lambda^{(2,2)}_{4,R,*} - \Lambda^{(1,2,M)}_{4,R}\Lambda^{(2,1)}_{4,R,*}\right)\Bigg)\varepsilon^4 + \mathcal{O}\left(\varepsilon^5\right),\end{aligned} \tag{5.73}$$

where $\Lambda^{(j,\ell)}_{4,R,*}$ denotes $\Lambda^{(j,\ell)}_{4,R}$ evaluated at $\mu_1 = \mu_{1,*_0}$. A similar calculation determines the asymptotic expansion for the imaginary part of this eigenvalue. After some work,

$$\lambda_{I,*} = -2c_g\varepsilon\sqrt{\frac{e_{BW}}{e_2}} + \left(-c_g\left(\frac{\lambda'_{4,R,*}}{\lambda''_{2,R,*}}\right) + 2\sqrt{\frac{e_{BW}}{e_2}}\left(\frac{c_g\Lambda^{(1,2,M)}_{4,R}}{\Lambda^{(1,1,M)}_{4,R}} + \frac{\Lambda_{3,I,*}}{32e_2T_{2,0}^2}\right)\right)\varepsilon^3 + \mathcal{O}\left(\varepsilon^4\right), \tag{5.74}$$

where $\Lambda_{3,I,*}$ denotes $\Lambda_{3,I}$ evaluated at $\mu_1 = \mu_{1,*_0}$. Expansions (5.71),(5.73), and (5.74) for the most unstable eigenvalue on the figure-eight match numerical computations to excellent agreement, even for sizeable values of ε on the order of 0.2. These expansions also improve upon results obtained at $\mathcal{O}\left(\varepsilon^2\right)$, see Figure 5.8.

5.3.5 Comparison of the Benjamin-Feir and High-Frequency Instabilities

As seen in Chapter 4, the largest high-frequency instability for sufficiently small ε is closest to the origin. Its most unstable eigenvalue has asymptotic expansion

$$\lambda^{(\mathrm{HF})}_{R,*} = \frac{|\mathcal{S}_2|}{2\sqrt{\omega(k_0)\omega(k_0+2)}}\varepsilon^2 + \mathcal{O}\left(\varepsilon^4\right), \tag{5.75}$$

where $\mathcal{S}_2$ is a complicated, but explicit, function of the aspect ratio α, ω is given by (4.44b), and k_0 is an implicit function of α defined as the unique solution of

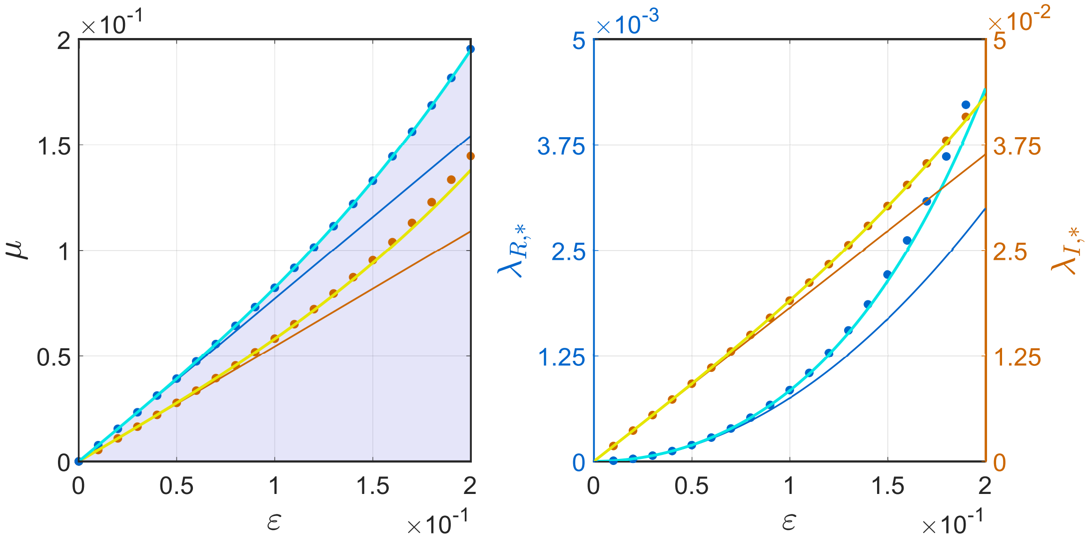

Figure 5.8: (Left) The interval of Floquet exponents parameterizing the half-loop of the Benjamin-Feir figure-eight curve for a Stokes wave with aspect ratio $\alpha = 1.5$ and variable amplitude ε. The numerically computed boundary of this interval is given by the blue dots, while the solid blue and light blue curves give the asymptotic results to $\mathcal{O}(\varepsilon)$ and $\mathcal{O}\left(\varepsilon^3\right)$, respectively. The orange dots give the numerically computed Floquet exponents of the most unstable eigenvalue, while the solid orange and yellow curves give the corresponding asymptotic estimates to $\mathcal{O}(\varepsilon)$ and $\mathcal{O}\left(\varepsilon^3\right)$, respectively. (Right) The real (blue axis) and imaginary (orange axis) part of the most unstable eigenvalue on the half-loop with $\alpha = 1.5$ and variable ε. Numerical results are given by the correspondingly colored dots. The asymptotic approximations of the real part to $\mathcal{O}\left(\varepsilon^2\right)$ and $\mathcal{O}\left(\varepsilon^4\right)$ are given by the solid blue and light blue curves, respectively. The asymptotic approximations of the imaginary part to $\mathcal{O}(\varepsilon)$ and $\mathcal{O}\left(\varepsilon^3\right)$ are given by the solid orange and yellow curves, respectively.

$$\Omega_1(k_0) = \Omega_{-1}(k_0+2), \tag{5.76}$$

for Ω_σ in (4.44b). The leading-order behavior of this instability is $\mathcal{O}\left(\varepsilon^2\right)$, similar to the Benjamin-Feir case:

$$\lambda_{R,*}^{(\mathrm{BFI})} = \frac{e_{BW}}{2}\varepsilon^2 + \mathcal{O}\left(\varepsilon^4\right). \tag{5.77}$$

By comparing coefficients of the leading-order terms in (5.75) and (5.77), we can directly compare the largest growth rates of the high-frequency and Benjamin-Feir instabilities for all $\alpha > 0$, see Figure 5.9. This is the first time the growth rates of these two instabilities have been compared using analytical methods.

For shallow water, $\alpha < \alpha_{BW}$, only high-frequency instabilities are present. For deep water, $\alpha > \alpha_{BW}$, we have two distinct behaviors. When $\alpha_{BW} < \alpha < \alpha_{DO}$, the high-frequency instabilities dominate the modulational Benjamin-Feir instabilities. When $\alpha > \alpha_{DO}$, the Benjamin-Feir instability dominates. The critical threshold α_{DO} that distinguishes these behaviors in deep water is well-approximated by the implicit solution of

$$\frac{|\mathcal{S}_2|}{\sqrt{\omega(k_0)\omega(k_0+2)}} = e_{BW}, \tag{5.78}$$

for k_0 defined in (5.76). If we solve (5.78) numerically, we find $\alpha_{DO} = 1.4308061674...$, matching the numerical result presented in [35] to four significant digits.

Remark 5.3.8. *If the* $\mathcal{O}(\varepsilon^4)$ *corrections are included in expansions* (5.75) *and* (5.77)*, then* $\alpha_{DO} = \alpha_{DO}(\varepsilon)$*, where* $\alpha_{DO}(0) = 1.4308061674....$ *By dominant balance, we argue that the next order correction of* α_{DO} *is* $\mathcal{O}(\varepsilon^2)$*, but obtaining this correction explicitly is a computational challenge.*

5.4 The Benjamin-Feir Spectrum in Infinite Depth

5.4.1 A Few Remarks about Infinite Depth

Our analysis so far pertains only to the Benjamin-Feir instability spectrum in finite depth. In this section, we consider the special case of infinite depth, when $\alpha \to \infty$. Unfortunately, this case is not as simple as taking the appropriate limit of the expressions obtained in Section 5.3. In fact, we have already seen that this limit is singular in the eigenfunction coefficients $\beta_{0,\pm1}$, which ultimately affects the description of the figure-eight curve at $\mathcal{O}(\varepsilon^3)$ and subsequent orders. The nature of this limit explains in part why the existence proof by Bridges *&* Mielke [15] fails in infinitely deep water as well as motivates the alternative proof covering this case by Nguyen *&* Strauss [73]. It also accounts for the qualitative differences

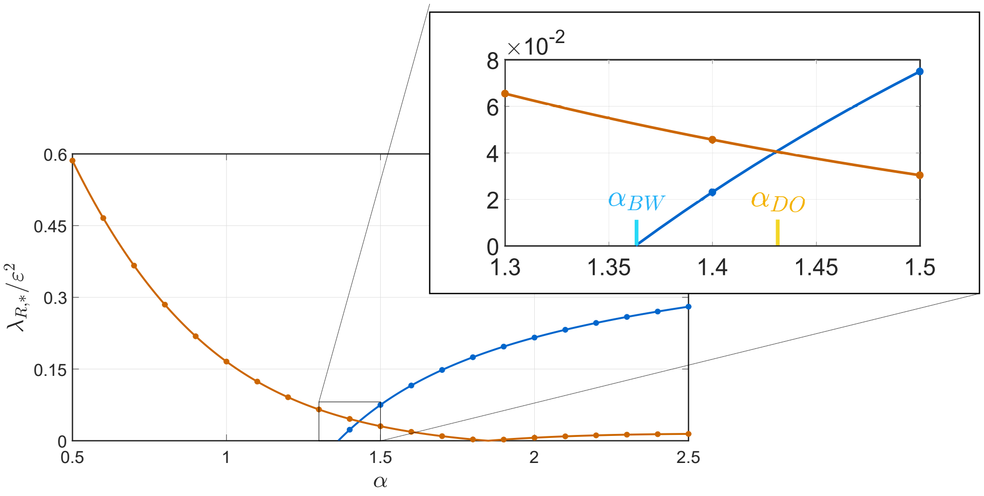

Figure 5.9: The real part of the most unstable eigenvalue (modulo ε^2) on the largest high-frequency instability (orange) and the Benjamin-Feir instability (blue) as a function of α. Numerical results using $\varepsilon = 10^{-3}$ are given by the correspondingly colored dots. The asymptotic results (5.75) and (5.77) are given by the correspondingly colored solid curves. We observe three regimes for the periodic water wave problem: (i) $\alpha < \alpha_{BW}$, (ii) $\alpha_{BW} < \alpha < \alpha_{DO}$, and (iii) $\alpha > \alpha_{DO}$, where α_{BW} is the root of (5.27) and α_{DO} is the root of (5.78). This agrees with the numerical results in Figure 11 of [35].

in the exact representations of the figure-eight curve in finite and infinite depth, as can be seen in the works of Berti *et al.* [10, 11].

In this section, we outline the steps of our spectral perturbation method applied to the Benjamin-Feir instability in infinite depth, starting with the unperturbed problem. Replacing the finite depth operators in the spectral problem (4.35) with their infinite depth equivalents (Section 4.4 in Chapter 4), we find the following spectral data at $\mathcal{O}\left(\varepsilon^0\right)$:

$$\lambda_0 = 0, \qquad \mu_0 = 0, \qquad \text{and} \tag{5.79a}$$

$$\mathbf{w_0}(x) = \beta_{0,-1}\mathbf{w_{0,-1}}(x) + \beta_{0,0}\mathbf{w_{0,0}}(x) + \beta_{0,1}\mathbf{w_{0,1}}(x), \tag{5.79b}$$

where $\beta_{0,j} \in \mathbb{C}$ are undetermined at this order and

$$\mathbf{w_{0,-1}}(x) = \begin{pmatrix} 1 \\ i \end{pmatrix} e^{-ix}, \quad \mathbf{w_{0,0}}(x) = \begin{pmatrix} 0 \\ 1 \end{pmatrix}, \quad \text{and} \quad \mathbf{w_{0,1}}(x) = \begin{pmatrix} 1 \\ -i \end{pmatrix} e^{ix}. \tag{5.80}$$

A direct calculation shows that $\mathbf{w_0}$ above is in fact the limit of $\mathbf{w_0}$ in finite depth (5.2) as $\alpha \to \infty$.

To proceed to the higher-order problems, we must expand the infinite depth operators as power series in ε. Some of these operators involve expressions of the form $|n+\mu|$, where $n \in \mathbb{Z}$. When we expand μ according to (5.4), it will become necessary to expand $|n+\mu|$ as well, despite the lack of analyticity of the absolute value function. To obtain these expansions, we exploit the following identity:

$$|a+b| = |a| + \operatorname{sgn}(a)b, \tag{5.81}$$

provided $a \in \mathbb{R} \setminus \{0\}$ and $b \in \mathbb{R}$ such that $|b| < |a|$. Substituting the Floquet expansion (5.4) into $|n+\mu|$, equating $\mu_0 = 0$, and applying (5.81) for ε sufficiently small yields the desired expansions

$$|n+\mu| = \begin{cases} |n| + \operatorname{sgn}(n)\varepsilon\mu_1(1+r(\varepsilon)) & n \neq 0 \\ |\varepsilon\mu_1|(1+r(\varepsilon)) & n = 0 \end{cases}. \tag{5.82}$$

Consequently, all infinite depth operators involving $|n+\mu|$ require two expansions: one when $n \neq 0$ and one when $n = 0$.

5.4.2 The $\mathcal{O}(\varepsilon)$ Problem

The $\mathcal{O}(\varepsilon)$ problem in infinite depth takes the same form as (5.5) with the finite depth operators replaced by their infinite depth equivalents and the expansions of these operators carried out appropriately. Three solvability conditions are obtained from this problem. One results in a trivial equality, similar to finite depth, and the remaining two are the following:

$$\beta_{0,-1}\left(\lambda_1 - i\frac{\mu_1}{2}\right) = 0, \tag{5.83a}$$

$$\beta_{0,1}\left(\lambda_1 - i\frac{\mu_1}{2}\right) = 0. \tag{5.83b}$$

Imposing $\beta_{0,\pm} \neq 1$ as in finite depth, we get

$$\lambda_1 = i\frac{\mu_1}{2}, \tag{5.84}$$

which is consistent with (5.11), since $c_g \to -1/2$ as $\alpha \to \infty$.

Having satisfied the solvability conditions, we solve the $\mathcal{O}(\varepsilon)$ problem for the first-order eigenfunction correction in infinite depth

$$\mathbf{w_1}(x) = \mathbf{w_{1,p}}(x) + \beta_{1,-1}\mathbf{w_{0,-1}}(x) + \beta_{1,0}\mathbf{w_{0,0}}(x) + \beta_{1,1}\mathbf{w_{0,1}}(x), \tag{5.85}$$

where $\beta_{1,j} \in \mathbb{C}$ are undetermined at this order and

$$\begin{aligned}\mathbf{w_{1,p}}(x) = \beta_{0,-1}\begin{pmatrix}1\\ i\end{pmatrix}e^{-2ix} + \frac{1}{2}i\mu_1\beta_{0,-1}\begin{pmatrix}0\\ 1\end{pmatrix}e^{-ix} + \frac{1}{2}i\mu_1\beta_{0,0}\begin{pmatrix}1\\ 0\end{pmatrix} + \frac{1}{2}i\mu_1\beta_{0,1}\begin{pmatrix}0\\ 1\end{pmatrix}e^{ix}\\ + \beta_{0,1}\begin{pmatrix}1\\ -i\end{pmatrix}e^{2ix}.\end{aligned} \tag{5.86}$$

A direct calculation shows that (5.86) coincides with the limit of the corresponding particular solution in finite depth as $\alpha \to \infty$.

5.4.3 The $\mathcal{O}(\varepsilon^2)$ Problem

Similar to (5.15) in finite depth, this problem has three nontrivial solvability conditions

$$2\beta_{0,-1}\left(\lambda_2 - i\frac{1}{2}r_1\mu_1\right) + i\left(-\beta_{0,1} + \left(\frac{1}{4}\mu_1^2 - 1\right)\beta_{0,-1}\right) = 0, \tag{5.87a}$$

$$\beta_{0,0}\mu_1^2 = 0, \tag{5.87b}$$

$$2\beta_{0,1}\left(\lambda_2 - i\frac{1}{2}r_1\mu_1\right) + i\left(\beta_{0,-1} + \left(-\frac{1}{4}\mu_1^2 + 1\right)\beta_{0,1}\right) = 0. \tag{5.87c}$$

Equations (5.87a) and (5.87c) are the limits of their respective equations (5.16a) and (5.16c) in the finite depth case, since

$$S_{2,-1} \to 0,\ T_{2,-1} \to \frac{1}{4},\ U_{2,-1} \to -1,\ V_{2,-1} \to -1, \tag{5.88}$$

as $\alpha \to \infty$. The same is true for the second equation (5.87b) if one divides the finite depth equation (5.16b) by $T_{2,0}$ first. Then, because

$$S_{2,0} \to 1,\ T_{2,0} \to -\infty, \tag{5.89}$$

as $\alpha \to \infty$, the rescaled (5.16b) tends to (5.87b) in the limit. The unbounded growth of $T_{2,0}$ as $\alpha \to \infty$ is ultimately responsible for the differences between the finite depth and infinite depth calculations, as mentioned in Subsection 3.3.

Equation (5.87b) implies either $\mu_1 = 0$ or $\beta_{0,0} = 0$. Both numerical experiments [35] and rigorous results [10, 73] suggest $\mu_1 \neq 0$, so we are forced to choose $\beta_{0,0} = 0$.

Remark 5.4.1. *That $\beta_{0,0} = 0$ in infinite depth is why we avoided normalizing $\mathbf{w}$ at the outset of our analysis. Indeed, had we chosen a normalization such that $\beta_{0,0}$ was nonzero, we would need to renormalize our asymptotic expansions in infinite depth to avoid inconsistencies at higher order.*

The remaining solvability conditions (5.87a) and (5.87c) form a nonlinear system of two equations in three unknowns, namely λ_2 and $\beta_{0,\pm 1}$. Without loss of generality, we choose $\beta_{0,-1}$ as a free parameter and solve for λ_2 and $\beta_{0,1}$. As in finite depth, we restrict our analysis to $\mu_1 > 0$. Solving for λ_2, we find

$$\lambda_2 = \lambda_{2,R} + i\lambda_{2,I}, \tag{5.90}$$

where

$$\lambda_{2,R} = \pm\frac{\mu_1}{8}\sqrt{8 - \mu_1^2}, \tag{5.91a}$$

$$\lambda_{2,I} = \frac{1}{2}r_1\mu_1. \tag{5.91b}$$

Equations (5.91a) and (5.91b) are the limits of (5.24a) and (5.24b), respectively, since

$$e_2 \to 1, \; e_{BW} \to 1, \tag{5.92}$$

and $c_g \to -1/2$ as $\alpha \to \infty$. For λ_2 to have a nonzero real part, we must have

$$0 < \mu_1 < 2\sqrt{2}, \tag{5.93}$$

which is consistent with (5.28) as $\alpha \to \infty$. Inequality (5.93) parameterizes a single loop of the Benjamin-Feir figure-eight curve in the upper-half complex plane. If we repeat our analysis with $\mu_1 < 0$, we find $-2\sqrt{2} < \mu_1 < 0$, which parameterizes the remaining loop of the figure-eight. All together, the full parameterizing interval of the figure-eight curve in infinite depth is

$$\mu \in \varepsilon \left(-2\sqrt{2}, 2\sqrt{2}\right)(1 + r_1\varepsilon) + \mathcal{O}\left(\varepsilon^3\right). \tag{5.94}$$

To simplify the remaining analysis, we restrict to a half-loop of the figure-eight curve by choosing the positive branch of (5.91a), as in the finite depth case.

The imaginary correction (5.91b) and Floquet parameterization (5.94) depend on the first-order rescaling parameter r_1, similar to finite depth. Using the regular curve condition at the next order, we determine $r_1 = -\sqrt{2}$. Thus, we may assemble our expansions for the real and imaginary parts of the half-loop in infinite depth:

$$\lambda_R = \frac{\mu_1}{8}\varepsilon^2\sqrt{8 - \mu_1^2} + \mathcal{O}\left(\varepsilon^3\right), \tag{5.95a}$$

$$\lambda_I = \frac{1}{2}\mu_1\varepsilon - \frac{1}{\sqrt{2}}\mu_1\varepsilon^2 + \mathcal{O}\left(\varepsilon^3\right), \tag{5.95b}$$

These expansions agree well with numerical computations for sufficiently small ε, see Figure 5.10. Dropping terms in these expansions beyond $\mathcal{O}\left(\varepsilon^2\right)$ and eliminating the μ_1 dependence yields the algebraic curve

$$4\left(-1 + 4\sqrt{2}\varepsilon - 12\varepsilon^2 + 8\sqrt{2}\varepsilon^3 - 4\varepsilon^4\right)\lambda_R^2 = 2\varepsilon^2\left(-1 + 4\sqrt{2}\varepsilon - 4\varepsilon^2\right)\lambda_I^2 + \lambda_I^4, \tag{5.96}$$

which is a lemniscate of Huygens, similar to finite depth. The coefficients of this lemniscate capture higher-order behavior in ε since $r_1 \neq 0$, which is distinct from the finite depth case when $r_1 = 0$. The low-order approximation of this curve obtained by [10] assumes $r_1 = 0$. This approximation works well enough for sufficiently small ε but is not asymptotic to the true figure-eight curve at $\mathcal{O}\left(\varepsilon^2\right)$, see Figure 5.11.

Remark 5.4.2. *The Floquet parameterization of the Benjamin-Feir instability in finite depth is*

$$\mu \in \varepsilon\mu_1\left(1 + r_2\varepsilon^2\right) + \mathcal{O}\left(\varepsilon^4\right), \tag{5.97}$$

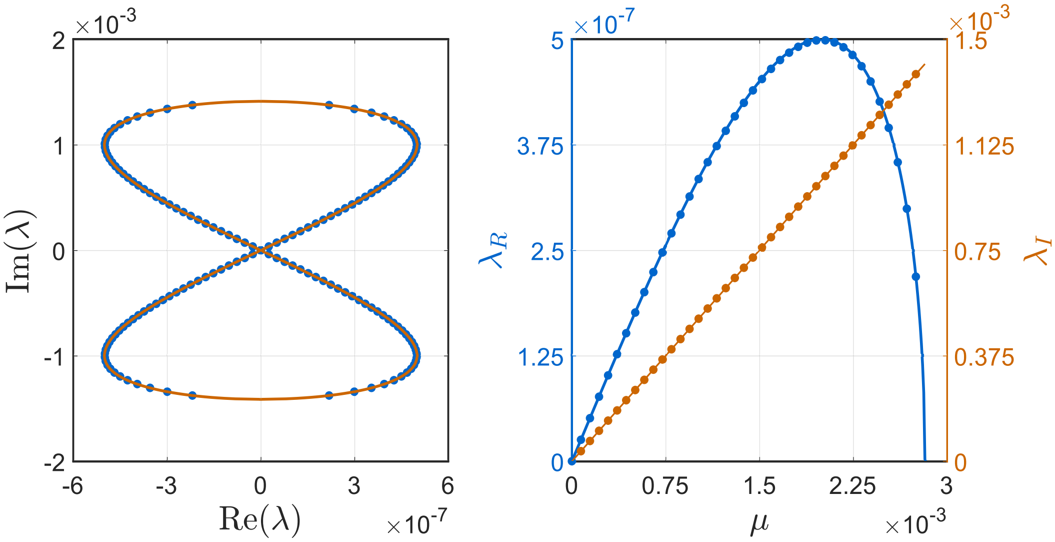

Figure 5.10: (Left) A plot of the Benjamin-Feir figure-eight curve for a Stokes wave with amplitude $\varepsilon = 10^{-3}$ in infinite depth. Numerical results are given by the blue dots, and the asymptotic results to $\mathcal{O}\left(\varepsilon^2\right)$ are given by the solid orange curve. (Right) The Floquet parameterization of the real (blue axis) and imaginary (orange axis) part of the figure-eight curve on the left. The respective numerical results are given by the correspondingly colored dots, and the asymptotic results for the real and imaginary part to $\mathcal{O}\left(\varepsilon^2\right)$ and $\mathcal{O}\left(\varepsilon\right)$, respectively, are given by the correspondingly colored curves.

where $r_2 = r_2(\alpha)$*. In infinite depth, it is*

$$\mu \in \varepsilon\mu_1\left(1 - \varepsilon\sqrt{2}\right) + \mathcal{O}\left(\varepsilon^3\right). \tag{5.98}$$

In order for the parameterization in finite depth to match that in infinite depth, the corrective term $r_2\varepsilon^2$ *must be promoted an order of magnitude in* ε*. Since* ε *can be made arbitrarily small, the only way this is possible is if* $|r_2| \to \infty$ *as* $\alpha \to \infty$*, which is precisely what we observed in Subsection 5.3.4.*

A direct calculation shows that (5.95a) attains a maximum value of

$$\lambda_{R,*} = \frac{1}{2}\varepsilon^2 + \mathcal{O}\left(\varepsilon^3\right), \tag{5.99}$$

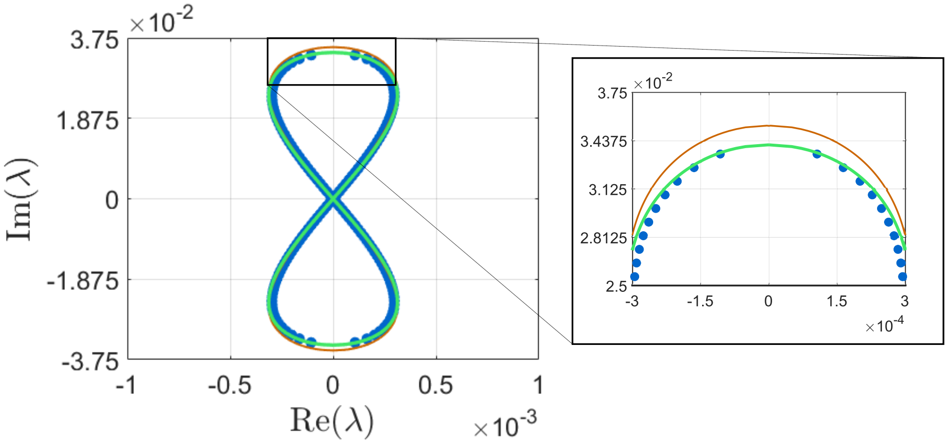

Figure 5.11: A plot of the Benjamin-Feir figure-eight curve for a Stokes wave with amplitude $\varepsilon = 2.5 \times 10^{-2}$ in infinite depth. Numerical results are given by the blue dots, and the asymptotic results to $\mathcal{O}\left(\varepsilon^2\right)$ are given by the solid green curve. The solid orange curve gives the heuristic approximation of Berti *et al.* [10]. This approximation is not asymptotic to $\mathcal{O}\left(\varepsilon^2\right)$ in the imaginary part of the figure-eight curve.

when μ_1 is equated to

$$\mu_{1,*} = 2. \tag{5.100}$$

Hence, (5.99) gives an asymptotic expansion for the real part of the most unstable eigenvalue on the infinite depth half-loop. Its corresponding imaginary part and Floquet exponent are

$$\lambda_{I,*} = \varepsilon + \mathcal{O}\left(\varepsilon^2\right), \tag{5.101a}$$

$$\mu_* = 2\varepsilon + \mathcal{O}\left(\varepsilon^2\right), \tag{5.101b}$$

respectively. These expansions are consistent with those in finite depth (Subsection 5.3.2) as well as numerical results (Figure 5.12).

Continuing our analysis of the $\mathcal{O}\left(\varepsilon^2\right)$ problem, we solve (5.87a) and (5.87b) for $\beta_{0,1}$ (assuming $\mu_1 > 0$). After some work, we find

$$\beta_{0,1} = \frac{1}{4}\Big(\mu_1^2 - 4 \mp 4i\mu_1\sqrt{8 - \mu_1^2}\Big)\beta_{0,-1}. \tag{5.102}$$

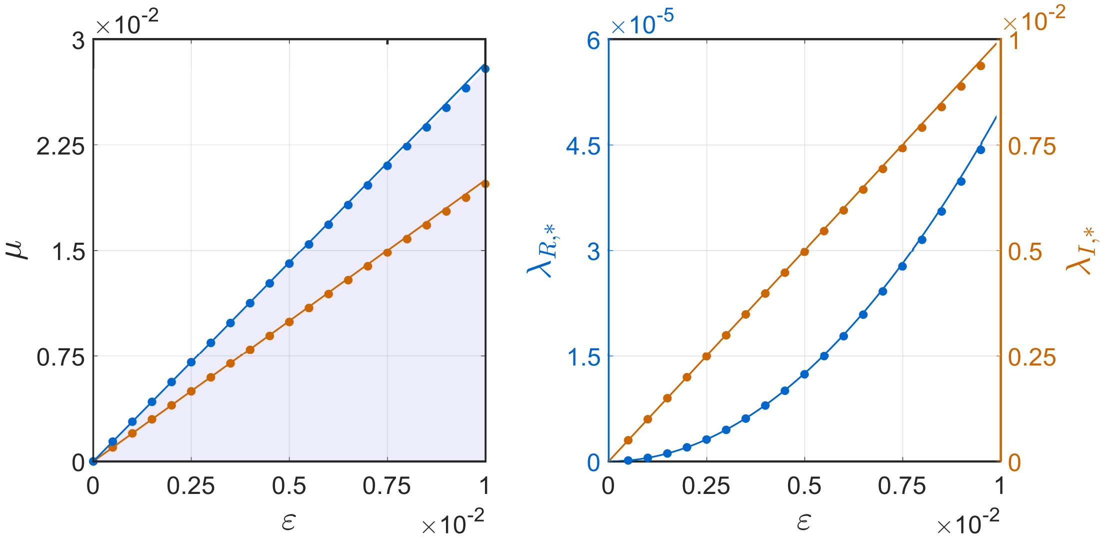

Figure 5.12: (Left) The interval of Floquet exponents parameterizing the half-loop of the Benjamin-Feir figure-eight curve for a Stokes wave with in infinite depth and variable amplitude ε. The numerically computed boundary of this interval is given by the blue dots, while the solid blue curve gives the asymptotic results to $\mathcal{O}\left(\varepsilon^2\right)$. The orange dots give the numerically computed Floquet exponents of the most unstable eigenvalue, while the solid orange curves give the corresponding asymptotic results to $\mathcal{O}\left(\varepsilon\right)$. (Right) The real (blue axis) and imaginary (orange axis) part of the most unstable eigenvalue in infinite depth with variable ε. Numerical results are given by the correspondingly colored dots, and the asymptotic results for the real and imaginary part to $\mathcal{O}\left(\varepsilon^2\right)$ and $\mathcal{O}\left(\varepsilon\right)$, respectively, are given by the correspondingly colored solid curves.

Since we chose the positive branch of $\lambda_{2,R}$ (5.91a) without loss of generality, we choose the negative branch of (5.102). In finite depth, $|\beta_{0,\pm 1}| \to \infty$ as $\alpha \to \infty$, which is inconsistent with (5.102). However, a direct calculation shows that the ratio $\beta_{0,1}/\beta_{0,-1}$ in finite depth tends to (5.102) as $\alpha \to \infty$, re-establishing consistency between the two results.

Before we proceed to the next order, we solve the $\mathcal{O}\left(\varepsilon^2\right)$ problem subject to the solvability conditions (5.87a)-(5.87b). We find

$$\mathbf{w_2}(x) = \mathbf{w_{2,p}}(x) + \beta_{2,-1}\mathbf{w_{0,-1}}(x) + \beta_{2,0}\mathbf{w_{0,0}}(x) + \beta_{2,1}\mathbf{w_{0,1}}(x), \tag{5.103}$$

where $\beta_{2,j} \in \mathbb{C}$ are undetermined at this order and

$$\mathbf{w_{2,p}}(x) = \sum_{j=-3}^{3} \mathbf{w_{2,j}} e^{ijx}, \tag{5.104}$$

where $\mathbf{w_{2,j}} = \mathbf{w_{2,j}}(\beta_{0,-1}, \beta_{1,\nu}, r_1) \in \mathbb{C}^2$, see the companion Mathematica files for details.

5.4.4 The $\mathcal{O}(\varepsilon^3)$ Problem

The solvability conditions of the $\mathcal{O}(\varepsilon^3)$ problem form a 3×3 linear system

$$\mathcal{M} \begin{pmatrix} \beta_{1,0} \\ \lambda_3 \\ \beta_{1,1} \end{pmatrix} = \begin{pmatrix} f_{3,1} \\ f_{3,2} \\ f_{3,3} \end{pmatrix}, \tag{5.105}$$

where $\mathcal{M}$ is given by

$$\mathcal{M} = \begin{pmatrix} \mu_1 & 2\beta_{0,-1} & -i \\ -\mu_1^2 & 0 & 0 \\ -\mu_1 & 2\beta_{0,1} & -\frac{i}{4}\left(-4 + 8i\lambda_2 + 4r_1\mu_1 + \mu_1^2\right) \end{pmatrix}, \tag{5.106}$$

and

$$f_{3,1} = \frac{i}{4}\beta_{1,-1}\left(4 + 8i\lambda_2 + 4r_1\mu_1 - \mu_1^2\right), \tag{5.107a}$$

$$f_{3,2} = -i\mu_1^2\left(\beta_{0,-1} + \beta_{0,1}\right), \tag{5.107b}$$

$$f_{3,3} = -i\left(\beta_{1,-1} + \frac{1}{4}\beta_{0,1}\mu_1\left(6 - 4r_2 + 4i\lambda_2 + \mu_1^2\right)\right). \tag{5.107c}$$

If we substitute expressions for λ_2 and $\beta_{0,1}$ on the half-loop into (5.106), we find

$$\det\left(\mathcal{M}\right) = \mu_1^3 \beta_{0,-1}\sqrt{8 - \mu_1^2}, \tag{5.108}$$

implying (5.105) has a unique set of solutions for $0 < \mu_1 < 2\sqrt{2}$, as desired. The solution for λ_3 is

$$\lambda_3 = \lambda_{3,R} + i\lambda_{3,I}, \tag{5.109}$$

where

$$\lambda_{3,R} = -\frac{\mu_1\left(2\mu_1 + r_1\left(-4+\mu_1^2\right)\right)}{4\sqrt{8-\mu_1^2}}, \tag{5.110a}$$

$$\lambda_{3,I} = -\frac{1}{16}\mu_1\left(16 - 8r_2 + \mu_1^2\right). \tag{5.110b}$$

To avoid singular behavior in $\lambda_{3,R}$ as $\mu_1 \to 2\sqrt{2}$, we choose r_1 such that

$$\lim_{\mu_1 \to 2\sqrt{2}} \left(2\mu_1 + r_1(-4+\mu_1^2)\right) = 0, \tag{5.111}$$

according to the regular curve condition. We find $r_1 = -\sqrt{2}$, justifying our prior claim.

Given $r_1 = -\sqrt{2}$, we see that (5.110a) and (5.110b) are nonzero for generic choices of $0 < \mu_1 < 2\sqrt{2}$. Hence, we have obtained a higher-order correction to both the real and imaginary parts of the figure-eight curve in infinite depth. This is in contrast with the finite depth case, in which only a purely imaginary correction was found at $\mathcal{O}\left(\varepsilon^3\right)$.

To characterize this higher-order correction, it is necessary to determine the value of the second-order rescaling parameter r_2, which appears in (5.110b). We show at the next order that $r_2 = 13/8$ by the regular curve condition. Assuming this is true for now, we assemble our expansions for the real and imaginary parts along a half-loop of this higher-order curve

$$\lambda_R = \frac{1}{8}\mu_1\varepsilon^2\sqrt{8-\mu_1^2}\left(1 + \left(\frac{2(-2\mu_1 + \sqrt{2}(-4+\mu_1^2))}{8-\mu_1^2}\right)\varepsilon\right) + \mathcal{O}\left(\varepsilon^4\right), \tag{5.112a}$$

$$\lambda_I = \frac{1}{2}\mu_1\varepsilon\left(1 - \sqrt{2}\varepsilon - \frac{1}{8}(3+\mu_1^2)\varepsilon^2\right) + \mathcal{O}\left(\varepsilon^4\right), \tag{5.112b}$$

respectively. The interval of Floquet exponents for the entire curve has asymptotic expansion

$$\mu \in \varepsilon\left(-2\sqrt{2}, 2\sqrt{2}\right)\left(1 - \sqrt{2}\varepsilon + \frac{13}{8}\varepsilon^2\right) + \mathcal{O}\left(\varepsilon^4\right). \tag{5.113}$$

These expansions agree well with numerical computations for sufficiently small ε, see Figure 5.13. In theory, one could eliminate the dependence of μ_1 from (5.112a) and (5.112b) to obtain an algebraic curve that approximates the true figure-eight to $\mathcal{O}\left(\varepsilon^3\right)$, but this process is cumbersome and provides little insight into the behavior of the true figure-eight curve.

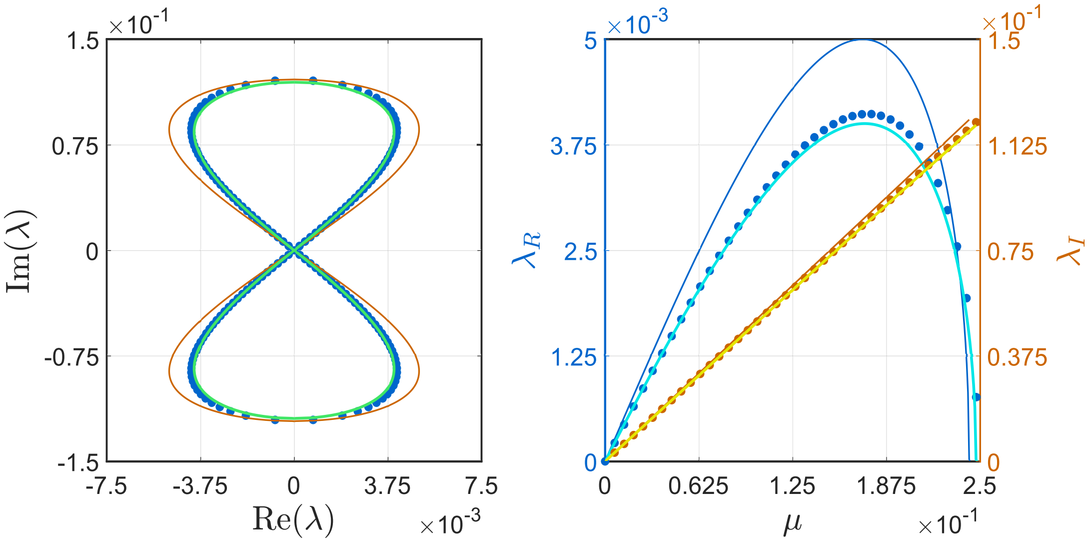

Figure 5.13: (Left) A plot of the Benjamin-Feir figure-eight curve for a Stokes wave with amplitude $\varepsilon = 0.1$ in infinite depth. Numerical results are given by the blue dots, while asymptotic results to $\mathcal{O}\left(\varepsilon^2\right)$ and $\mathcal{O}\left(\varepsilon^3\right)$ are given by the solid orange and green curves, respectively. (Right) The Floquet parameterization of the real (blue axis) and imaginary (orange axis) part of the figure-eight curve on the left. Numerical results are given by the correspondingly colored dots. The asymptotic parameterizations of the real part to $\mathcal{O}\left(\varepsilon^2\right)$ and $\mathcal{O}\left(\varepsilon^3\right)$ are given by the solid blue and light blue curves, respectively, while those for the imaginary part are given by the solid orange and yellow curves, respectively.

Following techniques in Subsection 5.3.4, we can derive an asymptotic expansion for the most unstable eigenvalue on this higher-order figure-eight as well as for its corresponding Floquet exponent. In particular, if we let $\mu_{1,*}$ denote a critical point of (5.112a), then

$$\frac{\partial}{\partial \mu_1}\left(\frac{1}{8}\mu_1\varepsilon^2\sqrt{8-\mu_1^2}\left(1+\left(\frac{2(-2\mu_1+\sqrt{2}(-4+\mu_1^2))}{8-\mu_1^2}\right)\varepsilon\right)+\mathcal{O}\left(\varepsilon^4\right)\right)\Bigg|_{\mu_1=\mu_{1,*}} = 0. \quad (5.114)$$

Dropping terms of $\mathcal{O}\left(\varepsilon^4\right)$ and smaller, we arrive at the following equation for $\mu_{1,*}$:

$$32 - 12\mu_{1,*}^2 + \mu_{1,*}^4 - \varepsilon\big(32\sqrt{2} + 32\mu_{1,*} - 24\mu_{1,*}^2\sqrt{2} - 2\mu_{1,*}^3 + 2\mu_{1,*}^4\sqrt{2}\big) = 0. \qquad (5.115)$$

When $\varepsilon = 0$, the only positive solution of (5.115) is $\mu_{1,*_0} = 2$, which coincides with (5.101b) from the previous order. When $0 < \varepsilon \ll 1$, we posit the following expansion for $\mu_{1,*}$:

$$\mu_{1,*} = \mu_{1,*_0} + \varepsilon\mu_{1,*_1} + \mathcal{O}\left(\varepsilon^2\right), \tag{5.116}$$

since ε appears as the small parameter in (5.115). Substituting (5.116) into (5.115), we find at $\mathcal{O}(\varepsilon)$ that $\mu_{1,*_1} = -3 + 2\sqrt{2}$. Thus, the Floquet exponent of the most unstable eigenvalue on the figure-eight has asymptotic expansion

$$\mu_* = \left(2 + (-3 + 2\sqrt{2})\varepsilon + \mathcal{O}\left(\varepsilon^2\right)\right)\varepsilon\left(1 - \varepsilon\sqrt{2} + \frac{13}{8}\varepsilon^2 + \mathcal{O}\left(\varepsilon^3\right)\right), \tag{5.117}$$

which simplifies to

$$\mu_* = 2\varepsilon - 3\varepsilon^2 + \mathcal{O}\left(\varepsilon^3\right).$$

Substituting (5.116) into (5.112a) and (5.112b), we obtain asymptotic expansions

$$\lambda_{R,*} = \frac{1}{2}\varepsilon^2 - \varepsilon^3 + \mathcal{O}\left(\varepsilon^4\right), \tag{5.118a}$$

$$\lambda_{I,*} = \varepsilon - \frac{3}{2}\varepsilon^2 + \mathcal{O}\left(\varepsilon^3\right), \tag{5.118b}$$

for the real and imaginary part of this most unstable eigenvalue on the half-loop, respectively. These expansions agree well with numerical computations (Figure 5.14), although not to the same degree as the corresponding expansions in finite depth. This is a result of resolving the higher-order figure-eight curve in infinite depth at $\mathcal{O}(\varepsilon^3)$ as opposed to $\mathcal{O}(\varepsilon^4)$.

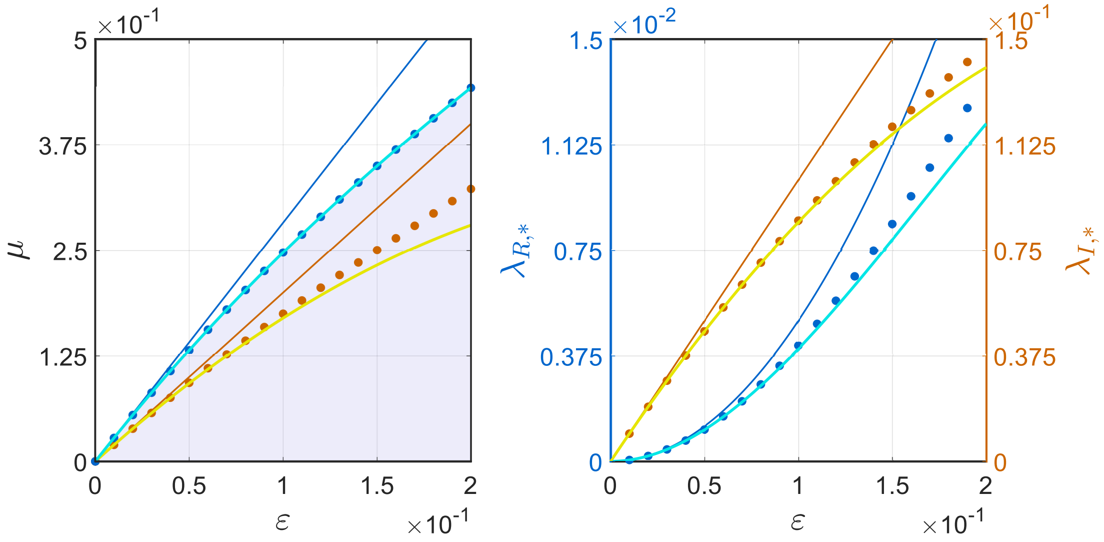

Figure 5.14: (Left) The interval of Floquet exponents parameterizing the half-loop of the Benjamin-Feir figure-eight curve for a Stokes wave in infinite depth with variable amplitude ε. The numerically computed boundary of this interval is given by the blue dots, while the solid blue and light blue curves give the asymptotic results to $\mathcal{O}\left(\varepsilon\right)$ and $\mathcal{O}\left(\varepsilon^3\right)$, respectively. The orange dots give the numerically computed Floquet exponents of the most unstable eigenvalue, while the solid orange and yellow curves give the corresponding asymptotic estimates to $\mathcal{O}\left(\varepsilon\right)$ and $\mathcal{O}\left(\varepsilon^2\right)$, respectively. (Right) The real (blue axis) and imaginary (orange axis) part of the most unstable eigenvalue on the half-loop in infinite depth with variable ε. Numerical results are given by the correspondingly colored dots. The asymptotic approximations of the real part to $\mathcal{O}\left(\varepsilon^2\right)$ and $\mathcal{O}\left(\varepsilon^3\right)$ are given by the solid blue and light blue curves, respectively. The asymptotic approximations of the imaginary part to $\mathcal{O}\left(\varepsilon\right)$ and $\mathcal{O}\left(\varepsilon^2\right)$ are given by the solid orange and yellow curves, respectively.

To complete our analysis of the solvability conditions (5.105), we report solutions for $\beta_{1,0}$ and $\beta_{1,1}$ on the half-loop with $r_1 = -\sqrt{2}$. We find

$$\beta_{1,0} = \mu_1 \beta_{0,-1}\left(\sqrt{8-\mu_1^2} + \frac{i}{4}\mu_1\right), \tag{5.119a}$$

$$\begin{aligned}\beta_{1,1} = \frac{1}{8}&\left(\mu_1\left(-4-4\mu_1\sqrt{2}+3\mu_1^2\right)\beta_{0,-1} + 2\left(-4+\mu_1^2\right)\beta_{1,-1}\right)\\ &+\frac{i\mu_1}{8\sqrt{8-\mu_1^2}}\left(\left(16\sqrt{2}+\mu_1\left(-16-4\mu_1\sqrt{2}+3\mu_1^2\right)\right)\beta_{0,-1} + 2\left(-8+\mu_1^2\right)\beta_{1,-1}\right),\end{aligned} \tag{5.119b}$$

where $\beta_{0,-1}$ and $\beta_{1,-1}$ depend on the normalization of $\mathbf{w}$.

Finally, we solve the $\mathcal{O}\left(\varepsilon^3\right)$ problem subject to the solvability conditions (5.105), arriving at an expression for the third-order eigenfunction correction

$$\mathbf{w_3}(x) = \sum_{j=-4}^{4} \mathbf{w_{3,j}} e^{ijx} + \beta_{3,-1}\mathbf{w_{0,-1}}(x) + \beta_{3,0}\mathbf{w_{0,0}}(x) + \beta_{3,1}\mathbf{w_{0,1}}(x) \tag{5.120}$$

where $\mathbf{w_{3,j}} = \mathbf{w_{3,j}}(\beta_{0,-1}, \beta_{1,-1}, \beta_{2,\nu}, r_2) \in \mathbb{C}^2$ while $\beta_{3,j} \in \mathbb{C}$ are undetermined constants at this order, see the companion Mathematica files for more details.

5.4.5 The $\mathcal{O}\left(\varepsilon^4\right)$ Problem

The solvability conditions at $\mathcal{O}\left(\varepsilon^4\right)$ also form a 3×3 linear system

$$\mathcal{M} \begin{pmatrix} \beta_{2,0} \\ \lambda_4 \\ \beta_{2,1} \end{pmatrix} = \begin{pmatrix} f_{4,1} \\ f_{4,2} \\ f_{4,3} \end{pmatrix}, \tag{5.121}$$

where $\mathcal{M}$ is the same as the previous order and

$$\begin{aligned} f_{4,1} = -\Bigg(& \beta_{2,-1}\left(2\lambda_2 + \frac{i}{4}\left(-4 + \mu_1 4\sqrt{2} + \mu_1^2\right)\right) + \beta_{1,-1}\Bigg(2\lambda_3 + \frac{\mu_1}{4}\big(-4ir_2 + 4\lambda_2 \\ & + i\big(6 + \mu_1^2\big)\big)\Bigg) - \frac{1}{4}\mu_1\beta_{1,0}\left(4\sqrt{2} + \mu_1\right) + \beta_{0,-1}\Bigg(-2i - i\lambda_2^2 + \lambda_3\mu_1 + \lambda_2\mu_1^2 \\ & - \frac{i}{8}\mu_1\left(12\sqrt{2} + 8r_3 + \mu_1\left(3 + 2\mu_1\left(\sqrt{2} - \mu_1\right)\right)\right)\Bigg) + i\beta_{0,1}\left(-2 + \frac{3}{16}\mu_1^2\right)\Bigg), \end{aligned} \tag{5.122a}$$

$$f_{4,2} = -i\mu_1^2\left(\beta_{1,-1} - \frac{i}{4}\beta_{1,0}\big(8\sqrt{2} + \mu_1\big) + \beta_{1,1} - \frac{1}{2}\beta_{0,-1}\big(4\sqrt{2} + \mu_1\big) - 2\beta_{0,1}\sqrt{2}\right), \tag{5.122b}$$

$$\begin{aligned} f_{4,3} = -\Bigg(& i\beta_{2,-1} + \mu_1\beta_{1,0}\big(\sqrt{2} - \frac{1}{4}\mu_1\big) + \beta_{1,1}\left(2\lambda_3 + \frac{i}{4}\mu_1\left(6 - 4r_2 + 4i\lambda_2 + \mu_1^2\right)\right) \\ & + i\beta_{0,-1}\big(2 - \frac{3}{16}\mu_1^2\big) + \beta_{0,1}\Bigg(2i + i\lambda_2^2 + \lambda_2\mu_1^2 - \frac{i}{8}\mu_1\big(12\sqrt{2} + 8r_3 - 8i\lambda_3 \\ & + \mu_1\big(-3 \;\; + 2\mu_1\big(\sqrt{2} + \mu_1\big)\big)\big)\Bigg)\Bigg). \end{aligned} \tag{5.122c}$$

Solving for λ_4 on the half-loop, we find

$$\lambda_4 = \lambda_{4,R} + i\lambda_{4,I}, \tag{5.123}$$

where

$$\begin{aligned}\lambda_{4,R} = \frac{\mu_1}{128\left(8-\mu_1^2\right)^{3/2}}\Big(&- 2176 + 32r_2\Big(32 - 12\mu_1^2 + \mu_1^4\Big) + \mu_1\Big(1024\sqrt{2} + \mu_1\Big(432 \\ &- 64\mu_1\sqrt{2} - 92\mu_1^2 + 5\mu_1^4\Big)\Big)\Big), \end{aligned} \tag{5.124a}$$

$$\lambda_{4,I} = \frac{1}{16}\mu_1\left(16\sqrt{2} + 8r_3 + \mu_1\left(8 + 3\mu_1\sqrt{2}\right)\right). \tag{5.124b}$$

For ease of notation, let $\Lambda_{4,R}$ denote the numerator of (5.124a). A direct calculation shows that $\Lambda_{4,R}$ factors as follows:

$$\begin{aligned}\Lambda_{4,R} = \mu_1\left(2\sqrt{2} - \mu_1\right)\Big(&- 544\sqrt{2} + 240\mu_1 + 168\mu_1^2\sqrt{2} + 52\mu_1^3 - 10\mu_1^4\sqrt{2} - 5\mu_1^5 \\ &- 32r_2\left(2\sqrt{2} + \mu_1\right)\left(-4 + \mu_1^2\right)\Big). \end{aligned} \tag{5.125}$$

In light of (5.125), it appears that (5.124a) already satisfies the regular curve condition, since $\Lambda_{4,R} \to 0$ as $\mu_1 \to 2\sqrt{2}$. However, the factor of $8 - \mu_1^2$ in the denominator of (5.124a) is one power larger than at the previous order (5.110a). Thus, we cannot guarantee regular behavior of $\lambda_{4,R}$ if only the first factor of (5.125) tends to zero as $\mu_1 \to 2\sqrt{2}$. We must also impose similar behavior on the second factor:

$$\begin{aligned}\lim_{\mu_1 \to 2\sqrt{2}}\Big(&- 544\sqrt{2} + 240\mu_1 + 168\mu_1^2\sqrt{2} + 52\mu_1^3 - 10\mu_1^4\sqrt{2} - 5\mu_1^5 \\ &- 32r_2\left(2\sqrt{2} + \mu_1\right)\left(-4 + \mu_1^2\right)\Big) = 0. \end{aligned} \tag{5.126}$$

Solving (5.126) for r_2 yields the desired result $r_2 = 13/8$. As a consequence, the final expression for the fourth-order real part correction (5.124a) becomes

$$\lambda_{4,R} = \mu_1\left(\frac{-512 + \mu_1\left(1024\sqrt{2} + \mu_1\left(-192 + \mu_1\left(-64\sqrt{2} + 5\mu_1\left(-8 + \mu_1^2\right)\right)\right)\right)}{128\left(8 - \mu_1^2\right)^{3/2}}\right). \tag{5.127}$$

Since (5.124b) and (5.127) are generically nonzero for $0 < \mu_1 < 2\sqrt{2}$, we have found another higher-order approximation to a half-loop of the figure-eight curve in infinite depth, up to the unknown third-order rescaling parameter r_3. Presumably, one can determine this value at $\mathcal{O}(\varepsilon^5)$ using the techniques presented in this section. We stop here, however, since we have already obtained a high-order approximation to the figure-eight at the previous order.

Remark 5.4.3. *For completeness, the final expressions of* $\beta_{2,0}$ *and* $\beta_{2,1}$ *solving* (5.121) *are found in the companion Mathematica files.*

5.5 Conclusions

Taking inspiration from our work with high-frequency instabilities in Chapters 2-4, we have developed a formal perturbation method to compute high-order asymptotic approximations of the Benjamin-Feir figure-eight curve. Unlike traditional methods in spectral perturbation theory [57], this method allows us to approximate the entire curve at once. Critical to this method is the use of the regular curve condition, which uniquely determines the expansion of the Floquet parameterization at high orders. Fromt his method, we determine

(i) the Floquet exponents that parameterize the figure-eight curve,

(ii) the real and imaginary parts of the most unstable eigenvalue on the figure-eight, and

(iii) algebraic curves asymptotic to the figure-eight curve.

We compare these expressions directly with numerical computations of the figure-eight curve using methods presented in [35]. This is the first time a numerical and analytical description of the Benjamin-Feir instability have appeared side by side. Excellent agreement between these descriptions is found in finite and infinite depth, even for modest values of the Stokes wave amplitude ε. Our expressions are also consistent with the rigorous results of Berti *et al.* [10, 11] and improve upon their heuristic approximations of the figure-eight curve.

In addition, our asymptotic results elucidate key differences between the behavior of the Benjamin-Feir instability spectrum in finite and infinite depth. In particular, the first-order rescaling parameter $r_1 = 0$ for the Floquet parameterization of the figure-eight curve in finite depth, while in infinite depth $r_1 = -\sqrt{2}$. Consequently, the second-order rescaling correction r_2 is singular in finite depth as one approaches infinitely deep water, *i.e.*, as $\alpha \to \infty$. This singularity propagates to the imaginary part of the figure-eight curve at third order and to the real part of the figure-eight curve at fourth order. Thus, the limit as $\alpha \to \infty$ is singular for the Benjamin-Feir instability, illustrating the breakdown of compactness mentioned in [11, 15, 73].

Using asymptotic results in this work and in [30], we are able to compare the Benjamin-Feir instability and the most unstable high-frequency instability for the first time analytically. Our analysis suggests three natural regimes for the water wave problem:

(i) Shallow water, which occurs when $\kappa h < \alpha_{BW} = 1.3627827567...$ and only high-frequency instabilities are present,

(ii) Intermediate water, which occurs when $\alpha_{BW} < \kappa h < \alpha_{DO}(\varepsilon) = 1.4308061674... + \mathcal{O}\left(\varepsilon^2\right)$ and both instabilities are present, but high-frequency instabilities dominate,

(iii) Deep water, which occurs when $\kappa h > \alpha_{DO}(\varepsilon)$ and both instabilities are present, but the Benjamin-Feir instability dominates.

Here, κ is the wavenumber of the Stokes wave and h is the depth of the water. These regimes are supported by numerical computations in [35]. We conclude that Stokes waves of all depths and all wavenumbers are unstable to the Benjamin-Feir instability, high-frequency instabilities, or both.

Chapter 6

CONCLUSIONS AND FUTURE WORK

Water waves display a vast array of phenomena due to hydrodynamic instability. Among these phenomena are tsunamis, rip tides, and rouge waves; all of which have direct impacts on human life and property. These examples (and many others unmentioned) motivate the need for a mathematical theory of water waves that addresses stability.

As we have seen, the governing equations of water waves, called Euler's equations, are traditionally expressed as a free boundary value problem in a domain evolving nonlinearly in time. A canonical class of solutions to these equations are the Stokes waves, which are small-amplitude, $2\pi/\kappa$-periodic disturbances of permanent shape in water of constant depth h traveling at a uniform velocity [64, 71, 86, 87]. In addition to their mathematical importance, the Stokes waves are readily generated in lab experiments [25] and observed, at least approximately, in nature [70].

Since the 1960s, it has been known that a Stokes wave of sufficiently small amplitude ε in sufficiently deep water ($\kappa h > \alpha_{BW} == 1.3627827567...$) is modulationally unstable to perturbations longitudinal to the wave's velocity [8, 9, 92], although a proof of this fact in finite depth was given thirty years later by Bridges and Mielke [15] and the proof in infinite depth was only resolved in 2020 by Nguyen & Strauss [73]. For many years, it was believed that Stokes waves in shallow water were unstable only to perturbations transverse to the wave's propagation, but recent numerical work by Deconinck and Oliveras [35] suggested that Stokes waves are also unstable in shallow water to longitudinal, quasi-periodic perturbations parameterized by a Floquet exponent μ. These instabilities are not modulational in the sense that their associated unstable spectral elements, obtained by linearizing Euler's equations about the Stokes waves, are not connected to the origin. These relatively new instabilities are called the high-frequency instabilities.

In this dissertation, we have constructed a spectral perturbation method to calculate the asymptotic behavior of the Benjamin-Feir and high-frequency instabilities in the complex spectral plane for sufficiently small-amplitude Stokes waves. From this method, we obtain asymptotic estimates of the Floquet exponents of the perturbations that cause instability, asymptotic estimates of the growth rates of these instabilities, and asymptotic representations of the instabilities in the complex spectral plane. These asymptotic approximations match numerical results using the Floquet-Fourier-Hill (FFH) method to excellent agreement. Not only can these asymptotic approximations be used to improve the overall numerical resolution of the Benjamin-Feir and high-frequency instabilities, but also allow us to establish the following fundamental results:

(i) Sufficiently small-amplitude, $2\pi/\kappa$-periodic Stokes waves are unstable to a high-frequency instability that grows with the square of the wave amplitude in all finite depths h, except when $\kappa h = \alpha_1 = 1.8494040837....$ For $\kappa h > \alpha_{BW}$, Stokes waves are also unstable to the Benjamin-Feir instability, which grows with the square of the wave amplitude.

(ii) Stokes waves with $\kappa h = 1.8494040837...$ are unstable to a high-frequency instability that grows with the cube of the wave amplitude. (They are also unstable to the Benjamin-Feir instability per (i).)

(iii) A Stokes wave in infinite depth is unstable to the Benjamin-Feir instability. Similar to finite depth, this instability grows with the square of the wave amplitude. We also find that these waves are unstable to high-frequency instabilities that grow with the fourth power of the wave amplitude.

(iv) For Stokes waves with $\alpha_{BW} < \kappa h < \alpha_{DO}(\varepsilon) = 1.4308061674... + \mathcal{O}\left(\varepsilon^2\right)$, the high-frequency instabilities grow faster than the Benjamin-Feir instability.

These results provide growing evidence that Stokes waves are spectrally unstable to longitudinal perturbations in all depths, contrary to prevailing beliefs dating to the 1960s.

The perturbation method developed in this thesis is readily implemented as a hybrid analytical-numerical method, allowing one to study higher-order isolas and their properties. The convergence of the resulting perturbation expansions may be improved using popular resummation techniques, *e.g.*, Padé approximants, as in [3]. Using these techniques, one could also explore higher-order deformations of the largest high-frequency isolas or even the separation of the Benjamin-Feir figure-eight curve from the origin in the complex spectral plane (Figure 5.1). Presumably the spectra of these two instabilities interact with each other when ε is sufficiently large. Although the perturbation method alone may not be powerful enough to describe this interaction completely, the resulting perturbation expansions may be used to inform numerical methods where approximately in parameter space to investigate.

We suspect that this perturbation method can accommodate additional physical effects in Euler's equations, such as surface tension or vorticity. The inclusion of surface tension, in particular, allows Stokes waves to develop so-called Wilton ripples [93], similar to the Kawahara equation. These ripples disrupt the classical construction of the Stokes waves and ultimately affect the behavior of the Benjamin-Feir and high-frequency instabilities. Recent work by [90] numerically computes the stability spectrum for Stokes waves exhibiting Wilton ripples. These computations showed that both the Benjamin-Feir and high-frequency instabilities not only persist in the presence of surface tension, but may be amplified for particular parameter regimes. Using a variation of the perturbation method outline in this thesis may lead to explicit asymptotic representations of these parameter regimes and the growth rates of both instabilities for sufficiently small ε.

We also suspect the method can be extended to transverse instabilities of Stokes waves. Akers [3] considers the leading-order effect of transverse perturbations on the modulational instability in infinite depth. The perturbation method developed in this thesis may be adapted to explore higher-order effects of transverse perturbations not only on the Benjamin-Feir figure-eight curve, but also the high-frequency isolas in both finite and infinite depth.

BIBLIOGRAPHY

[1] M. J. Ablowitz, A. S. Fokas, and Z. H. Musslimani. On a new non-local formulation of water waves. *Journal of Fluid Mechanics*, 562:313–343, 2006.

[2] M. J. Ablowitz and T. S. Haut. Spectral formulation of the two fluid euler equations with a free interface and long wave reduction. *Analysis and Applications*, 6(4):323–348, 2008.

[3] B. Akers. Modulational instabilities of periodic traveling waves in deep water. *Physica D*, 300:26–33, 2015.

[4] B. Akers and W. Gao. Wilton ripples in weakly nonlinear model equations. *Communications in Mathematical Sciences*, 10(3):1015–2024, 2012.

[5] B. Akers and D. P. Nicholls. Spectral stability of deep two-dimensional gravity water waves: repeated eigenvalues. *SIAM Journal on Applied Mathematics*, 130(2):81–107, 2012.

[6] B. Akers and D. P. Nicholls. The spectrum of finite depth water waves. *European Journal of Mechanics-B/Fluids*, 46:181–189, 2014.

[7] B. Akers and D. P. Nicholls. Wilton ripples in weakly nonlinear dispersive models of water waves: existence and analyticity of solution branches. *Water Waves*, 3(1):25–47, 2021.

[8] T. B. Benjamin. Instability of periodic wave trains in nonlinear dispersive systems. *Proceedings of the Royal Society A*, 299:59–79, 1967.

[9] T. B. Benjamin and J. Feir. The disintegration of wave trains on deep water. part i. theory. *Journal of Fluid Mechanics*, 27:417–430, 1967.

[10] M. Berti, A. Maspero, and P. Ventura. Full description of Benjamin-Feir instability of Stokes waves in deep water. *arXiv:2109.11852*, 2021.

[11] M. Berti, A. Maspero, and P. Ventura. Benjamin-Feir instability of Stokes waves in finite depth. *arXiv:2204.00809*, 2022.

[12] H. Bohr. *Almost Periodic Functions.* Chelsea Publishing Company, New York, 1947.

[13] J. Boussinesq. Théorie des ondes et des remous qui se propagent le long d'un canal rectangulaire canal des vitesses sensiblement pareilles de la surface au fond. *Journal de Mathématiques Pures et Appliquées*, 17:55–108, 1872.

[14] J. Boussinesq. On the change of form of long waves advancing in a rectangular canal, and on a new type of long stationary waves. *Philosophical Magazine*, 39(240):422–443, 1895.

[15] T. H. Bridges and A. Mielke. A proof of the Benjamin-Feir instability. *Archive for Rational Mechanics and Analysis*, 133:145–198, 1995.

[16] J. C. Bronski, V. M. Hur, and M. Johnson. Modulational instability in equation of KdV-type. In E. Tobisch, editor, *New Approaches to Nonlinear Waves. Lecture Notes in Physics*, pages 83–133. Springer, Cham, 2016.

[17] P. J. Bryant. Stability of periodic waves in shallow water. *Journal of Fluid Mechanics*, 66:81–96, 1974.

[18] P. J. Bryant. Oblique instability of periodic waves in shallow water. *Journal of Fluid Mechanics*, 86:783–792, 1978.

[19] J. D. Carter. Bidirectional whitham equations as models of waves on shallow water. *Wave Motion*, 82:51–61, 2018.

[20] A-L. Cauchy. Mémoire sur la théorie de la propagation des ondes à la surface d'un fluide pesant d'une profondeur indéfinie. *Présentés Divers Savans Acad. R. Sci. Inst. France*, 1:3–312, 1827.

[21] C. Chicone. *Ordinary Differential Equations with Applications, 2nd ed.* Springer, New York, 2006.

[22] K. Claassen and M. Johnson. Numerical bifurcation and spectral stability of wavetrains in bidirectional Whitham models. *Studies in Applied Mathematics*, 141:205–246, 2018.

[23] A. Constantin and W. A. Strauss. Pressure beneath a stokes wave. *Communications on Pure and Applied Mathematics: A Journal Issued by the Courant Institute of Mathematical Sciences*, 63(4):533–557, 2010.

[24] A. Constantin and E. Varvaruca. Steady periodic water waves with constant vorticity: regularity and local bifurcation. *Archive for Rational Mechanics and Analysis*, 199.1:33–67, 2011.

[25] W. Craig and M. D. Groves. Hamiltonian long-wave approximations to the water-wave problem. *Wave Motion*, 19(4):367–389, 1994.

[26] W. Craig and C. Sulem. Numerical simulation of gravity waves. *Journal of Computational Physics*, 108(1):73–83, 1993.

[27] A. D. D. Craik. The origins of water wave theory. *Annual Review of Fluid Mechanics*, 36:1–28, 2004.

[28] R. P. Creedon, B. Deconinck, and O. Trichtchenko. High-frequency instabilities of a Boussinesq-Whitham system: a perturbative approach. *Fluids*, 6(4), 2021.

[29] R. P. Creedon, B. Deconinck, and O. Trichtchenko. High-frequency instabilities of the Kawahara equation: a perturbative approach. *SIAM Journal on Applied Dynamical Systems*, 20(3):1571–1595, 2021.

[30] R. P. Creedon, B. Deconinck, and O. Trichtchenko. High-frequency instabilities of Stokes waves. *Journal of Fluid Mechanics*, 937:A24, 2022.

[31] C. Curtis and B. Deconinck. On the convergence of Hill's method. *Mathematics of Computation*, 79(296):169–187, 2010.

[32] A. Davey and K. Stewartson. On three-dimensional packets of surface waves. *Proceedings of the Royal Society of London A*, 338(1613):101–110, 1974.

[33] B. Deconinck and T. Kapitula. The orbital stability of the cnoidal waves of the Korteweg-deVries equation. *Physical Letters A*, 374:4018–4022, 2010.

[34] B. Deconinck and J. N. Kutz. Computing spectra of linear operators using the floquet-fourier-hill method. *Journal of Computational Physics*, 219(1):296–321, 2006.

[35] B. Deconinck and K. Oliveras. The instability of periodic surface gravity waves. *Journal of Fluid Mechanics*, 675:141–167, 2011.

[36] B. Deconinck and O. Trichtchenko. High-frequency instabilities of small-amplitude solutions of hamiltonian pdes. *Discrete and Continuous Dynamical Systems-A*, 37(3):1323–1358, 2017.

[37] F. Dias and C. Kharif. Nonlinear gravity and gravity-capillary waves. *Annual Review of Fluid Mechanics*, 31:331–341, 1999.

[38] E. Dinvay. On well-posedness of a dispersive system of the whitham-boussinesq type. *Applied Mathematics Letters*, 88:13–20, 2019.

[39] A. I. Dyachenko, V. E. Zakharov, and E. A. Kuznetsov. Nonlinear dynamics of the free surface of an ideal fluid. *Plasma Physics Reports*, 22.10:829–840, 1996.

[40] L. Euler. Continuation des recherches sur a la théorie du mouvement des fluides. *Mémoires de L'académie des Sciences de Berlin*, pages 316–361, 1757.

[41] L. Euler. Principes géneraux du mouvement des fluides. *Mémoires de L'académie des Sciences de Berlin*, pages 274–315, 1757.

[42] L. Euler. Principia motus fluidorum. *Novi Commentarii Academiae Scientiarum Petropolitanae*, pages 271–311, 1761.

[43] J. D. Fenton. A fifth-order Stokes theory for steady waves. *Journal of Waterway, Port, Coastal, and Ocean Engineering*, 111(2):216–234, 1985.

[44] M. Francius and C. Kharif. Three-dimensional instabilities of periodic gravity waves in shallow water. *Journal of Fluid Mechanics*, 561:417–437, 2006.

[45] R. Grimshaw. *Nonlinear Waves in Fluids: Recent Advances and Modern Applications.* Springer, Wein, 2005.

[46] J. Hammack and D. Henderson. Resonant interactions among surface water waves. *Annual Review of Fluid Mechanics*, 25:55–97, 1993.

[47] M. Haragus and T. Kapitula. On the spectra of periodic waves for infinite-dimensional hamiltonian systems. *Physica D*, 237:2649–2671, 2008.

[48] M. Haragus, E. Lombardi, and A. Scheel. Spectral stability of wave trains in the kawahara equation. *Journal of Mathematical Fluid Mechanics*, 8(4):482–509, 2006.

[49] S. E. Haupt and J. P. Boyd. Modeling nonlinear resonance: a modification to the stokes' perturbation expansion. *Wave Motion*, 10(1):83–98, 1988.

[50] J. C. R. Hunt. Nonlinear wave theory and the contributions of T. Brooke Benjamin (1929-1995). *Annual Review of Fluid Mechanics*, 38:1–25, 2006.

[51] V. M. Hur and A. K. Pandey. Modulational instability in a full-dispersion shallow water model. *Studies in Applied Mathematics*, 142:3–47, 2019.

[52] V. M. Hur and L. Tao. Wave breaking in a shallow water model. *SIAM Journal on Mathematical Analysis*, 50:354–380, 2019.

[53] V. M. Hur and Z. Yang. Unstable stokes waves. *arXiv:2010.10766*, 2022.

[54] C. Huygens. *Oeuvres complètes de Christiaan Huygens*, chapter Tome Dixième. Martinus Nijhoff Publishers, 1905.

[55] M. Johnson, K. Zumbrun, and J. C. Bronski. On the modulation equations and stability of periodic generalized Korteweg-deVries waves via bloch decompositions. *Physica D*, 239:2057–2065, 2010.

[56] T. Kapitula and K. Promislow. *Spectral and Dynamical Stability of Nonlinear Waves.* Springer, New York, 2013.

[57] T. Kato. *Perturbation Theory for Linear Operators.* Springer-Verlag, Berlin, 1966.

[58] T. Kawahara. Oscillatory solitary waves in dispersive media. *Journal of the Physical Society of Japan*, 33:1015–1024, 1972.

[59] C. Kharif and A. Ramamonjiarisoa. On the stability of gravity waves on deep water. *Journal of Fluid Mechanics*, 218:163–170, 1990.

[60] R. Kollár, B. Deconinck, and O. Trichtchenko. Direct characterization of spectral stability of small-amplitude periodic waves in scalar hamiltonian problems via dispersion relation. *SIAM Journal on Mathematical Analysis*, 51(4):3145–3169, 2019.

[61] A. O. Korotkevich, A. I. Dyachenko, and V. E. Zakharov. Numerical simulation of surface waves instability on a homogeneous grid. *Physica D*, 321-322:51–66, 2016.

[62] M. G. Krein. On the application of an algebraic proposition in the theory of matrices of monodromy. *Uspekhi Matematicheskikh Nauk*, 6(1):171–177, 1951.

[63] P. K. Kundu and I. M. Cohen. *Fluid Mechanics.* Academic Press, San Diego, 2002.

[64] T. Levi-Civita. Determination rigoureuse des ondes permanentes dampleur finie. *Mathematische Annalen*, 93(1):264–314, 1925.

[65] M. S. Longuet-Higgins. The instabilities of gravity waves of finite amplitude in deep water i. superharmonics. *Proceedings of the Royal Society A*, 360(1703):471–488, 1978.

[66] M. S. Longuet-Higgins. The instabilities of gravity waves of finite amplitude in deep water ii. subharmonics. *Proceedings of the Royal Society A*, 360(1703):489–505, 1978.

[67] R. S. MacKay and P. G. Saffman. Stability of water waves. *Proceedings of the Royal Society A*, 406(1830):115–125, 1986.

[68] T. R. Marchant and N. F. Smyth. The extended Korteweg-de Vries equation and the resonant flow of a fluid over topography. *Journal of Fluid Mechanics*, 221:263–287, 1990.

[69] J. W. McLean. Instabilities of finite-amplitude water waves. *Journal of Fluid Mechanics*, 114:315–330, 1982.

[70] C. C. Mei, M. Stiassnie, and D. K. P. Yue. *Theory and Applications of Ocean Surface Waves: Nonlinear Aspects*. World Scientific, New York, 2005.

[71] A. Nekrasov. On steady waves. *Izv. Ivanovo-Voznesensk. Politekhn. In-ta*, 3:52–65, 1921.

[72] I. Newton. *The Principia: Mathematical Principles of Natural Philosophy*. University of California Press, 1999 [1687].

[73] H. Nguyen and W. A. Strauss. Proof of modulational instability of Stokes waves in deep water. *arXiv:2007.05018*, 2020.

[74] D. P. Nicholls. Spectral stability of traveling water waves: analytic dependence of the spectrum. *Journal of Nonlinear Science*, 17(4):369–397, 2007.

[75] M. Nivala and B. Deconinck. Periodic finite-genus solutions of the KdV equation are orbitally stable. *Physica D*, 239(13):1147–1158, 2010.

[76] K. Oliveras. *Stability of Periodic Surface Gravity Water Waves*. PhD thesis, University of Washington, 2009.

[77] J. Pava and F. Natali. (Non)linear instability of periodic traveling waves: Klein-Gordon and KdV type equations. *Advanced Nonlinear Analysis*, 3(2):95–123, 2014.

[78] D. H. Peregrine. Water waves, nonlinear Schdrödinger equations and their solutions. *The ANZIAM Journal*, 25(1):16–43, 1983.

[79] H. Poincaré. *Les Méthodes Nouvelles de la Mécanique Célèste, II.* Dover Publications, New York, 1957 [1893].

[80] S. D. Poisson. Mémoire sur la théorie des ondes. *Présentés Divers Savans Acad. R. Sci. Inst. France*, 1:70–186, 1818.

[81] S. D. Poisson. *Traité de Mécanique, 2nd ed.* Bachelier, Paris, 1833.

[82] M. Reed and B. Simon. *Methods of Modern Mathematical Physics, IV. Analysis of Operators, 2nd ed.* Academic Press–Harcourt Brace Jovanovich Publishers, New York, 1978.

[83] R. P. Shaw. Boundary integral equation methods applied to wave problems. Technical report, State University of New York at Buffalo, Department of Engineering Science, Aerospace Engineering, and Nuclear Engineering, 1979.

[84] S.S. Shen. *A Course on Nonlinear Waves.* Springer, Dordrecht, 1993.

[85] J. J. Stoker. *Water Waves: The Mathematical Theory with Applications.* Wiley-Interscience, New York, 1992.

[86] G. G. Stokes. On the theory of oscillatory waves. *Transactions of the Cambridge Philosophical Society*, 8:441–455, 1847.

[87] D. Struik. Determination rigoureuse des ondes irrotationnelles periodiques dans un canal à profondeur finie. *Mathematische Annalen*, 95:595–634, 1926.

[88] L. N. Trefethen and D. Bau III. *Numerical Linear Algebra.* SIAM, 1997.

[89] O. Trichtchenko, B. Deconinck, and R. Kollár. Stability of periodic traveling wave solutions to the kawahara equation. *SIAM Journal on Applied Dynamical Systems*, 17(4):2761–2783, 2018.

[90] O. Trichtchenko, B. Deconinck, and J. Wilkening. The instability of wilton ripples. *Wave Motion*, 66:147–155, 2016.

[91] G. B. Whitham. Non-linear dispersion of water waves. *Journal of Fluid Mechanics*, 27:399–412, 1967.

[92] G. B. Whitham. Variational methods and applications to water waves. *Proceedings of the Royal Society A*, 299:6–25, 1967.

[93] J. R. Wilton. On ripples. *The London, Edinburgh, and Dublin Philosophical Magazine and Journal of Science*, 29(173):688–700, 1915.

[94] H. C. Yuen and B. M. Lake. Instabilities of waves in deep water. *Annual Review of Fluid Mechanics*, 12(1):303–334, 1980.

[95] V. E. Zakharov. Stability of periodic waves of finite amplitude on the surface of a deep fluid. *Journal of Applied Mechanics and Technical Physics*, 9(2):190–194, 1968.

[96] V. E. Zakharov and L. Ostrovsky. Modulation instability: the beginning. *Physica D*, 238(5):540–548, 2009.

Appendix A

STOKES WAVES BY NUMERICAL CONTINUATION

A.1 The Scalar Case

Suppose we have a nonlinear evolution equation of the form

$$u_t = \mathcal{L}u + \mathcal{N}(u), \tag{A.1}$$

where $u = u(x,t)$ is a real-valued function and $\mathcal{L}$ and $\mathcal{N}$ represent a linear and nonlinear differential operator[1] in x, respectively. Suppose also that $\mathcal{L}$ and $\mathcal{N}$ respect the continuous symmetry $x \to x + \phi$ for any $\phi \in \mathbb{R}$ (*i.e.*, $\mathcal{L}$ and $\mathcal{N}$ are autonomous) as well as the discrete symmetry $x \to -x$. Such an equation generalizes the first water wave model discussed in this thesis, the Kawahara equation. In this appendix, we show how to construct numerically the Stokes wave solutions of the general equation (A.1), *i.e.*, the small-amplitude, 2π-periodic[2] traveling wave solutions of (A.1), assuming they exist.

In a traveling frame $x \to x - ct$, (A.1) becomes

$$u_t = \mathcal{L}_c u + \mathcal{N}(u, u_x, u_{xx}, ...), \tag{A.2}$$

where $\mathcal{L}_c = \mathcal{L} + c\partial_x$. The velocity c of this frame is chosen so that the Stokes waves satisfying (A.2) are time-independent, giving us

$$0 = \mathcal{L}_c u_S + \mathcal{N}(u_S). \tag{A.3}$$

Here, $u_S = u_S(x;\varepsilon)$ represents a Stokes wave of small amplitude ε, where ε will be defined momentarily. Since the velocity of the correct traveling frame depends on the choice of Stokes wave, we must have $c = c(\varepsilon)$.

---

[1] Or, more generally, integro-differential operators.

[2] We can assume these solutions are 2π-periodic without loss of generality by appropriately rescaling (A.1).

Given (A.3) is autonomous and respects the symmetry $x \to -x$, we can use translation symmetry to arrange for u_S to be even in x without loss of generality. Consequently, Stokes waves satisfying (A.2) have a Fourier cosine series of the form

$$u_S(x;\varepsilon) = \sum_{j=0}^{\infty} a_j(\varepsilon)\cos(jx). \tag{A.4}$$

Our goal is to determine the values of $a_j(\varepsilon)$ and $c(\varepsilon)$ for a given ε by numerical methods.

We first truncate the Fourier cosine series (A.4) to $N+1$ terms,

$$u_S(x;\varepsilon) \approx \sum_{j=0}^{N} a_j(\varepsilon)\cos(jx), \tag{A.5}$$

and substitute expansion (A.5) into (A.3), giving

$$0 = \mathcal{L}_{c(\varepsilon)}\left(\sum_{j=0}^{N} a_j(\varepsilon)\cos(jx)\right) + \mathcal{N}\left(\sum_{j=0}^{N} a_j(\varepsilon)\cos(jx)\right). \tag{A.6}$$

We then introduce the Fourier cosine transform

$$\mathcal{F}_{C,k}[f(x)] = \begin{cases} \frac{1}{2\pi}\int_{-\pi}^{\pi} f(x)dx, & k = 0, \\ \frac{1}{\pi}\int_{-\pi}^{\pi} f(x)\cos(kx)dx, & k \in \mathbb{N}, \end{cases} \tag{A.7}$$

and apply this transform to both sides of (A.6) for $0 \le k \le N$. This leads to a system of $N+1$ equations for $N+2$ unknowns of the form:

$$\vec{0} = \widehat{\mathcal{L}_{c(\varepsilon)}} \begin{pmatrix} a_0(\varepsilon) \\ \vdots \\ a_N(\varepsilon) \end{pmatrix} + \widehat{\mathcal{N}}\Big(a_0(\varepsilon), ..., a_N(\varepsilon)\Big), \tag{A.8}$$

where $\vec{0} \in \mathbb{R}^{N+1}$, $\widehat{\mathcal{L}_{c(\varepsilon)}} \in \mathbb{R}^{(N+1)\times(N+1)}$ is a matrix with entries

$$\left[\widehat{\mathcal{L}_{c(\varepsilon)}}\right]_{mn} = \mathcal{F}_{C,m-1}\left[\mathcal{L}_{c(\varepsilon)}(\cos((n-1)x))\right], \qquad 1 \le m,n \le N+1, \tag{A.9}$$

and $\widehat{\mathcal{N}} : \mathbb{R}^{N+1} \to \mathbb{R}^{N+1}$ is a nonlinear function of $a_j(\varepsilon)$ given by

$$\widehat{\mathcal{N}}\Big(a_0(\varepsilon), ..., a_N(\varepsilon)\Big) = \begin{pmatrix} \mathcal{F}_{C,0}\left[\mathcal{N}\left(\sum_{j=0}^{N} a_j(\varepsilon)\cos(jx)\right)\right] \\ \vdots \\ \mathcal{F}_{C,N}\left[\mathcal{N}\left(\sum_{j=0}^{N} a_j(\varepsilon)\cos(jx)\right)\right] \end{pmatrix}. \tag{A.10}$$

Our system at present is underdetermined, but we have not yet specified the small-amplitude parameter ε. There are several candidates for the definition of ε. Some authors use the L^2-norm of u_S, while others use the distance between the crest and trough of u_S. For convenience, we define ε to be $a_1(\varepsilon)$ for all sufficiently small ε so that $u_S \sim \varepsilon\cos(x)$ as $\varepsilon \to 0$. Using this definition, we can augment system (A.8) with the equation

$$0 = \varepsilon - a_1(\varepsilon), \tag{A.11}$$

bringing us to $N+2$ equations for $N+2$ unknowns.

Upon choosing ε sufficiently small and N sufficiently large, we can solve our $(N+2) \times (N+2)$ nonlinear system by Newton's method, giving us a numerical approximation to the Stokes wave as well as its velocity. Since $u_S \sim \varepsilon\cos(x)$ as $\varepsilon \to 0$ by construction, we can initialize Newton's method with the guess $a_1(\varepsilon) = \varepsilon$ and $a_j(\varepsilon) = 0$ for $2 \le j \le N$. A guess for $c(\varepsilon)$ can be obtained by substituting $u_S \sim \varepsilon\cos(x)$ into equation (A.3), dropping terms of $\mathcal{O}\left(\varepsilon^2\right)$ and smaller, and solving for c. Doing so, one finds that this guess for c is exactly the dispersion relation of the operator $\mathcal{L}$ evaluated at unity[3].

For a sequence of increasingly larger values of ε, we can instead initialize Newton's method using the values of $a_j(\varepsilon)$ and $c(\varepsilon)$ for the preceding value of ε in the sequence. This gives us a numerical continuation method whereby the Stokes wave solutions are constructed by "marching up" the $c(\varepsilon)$ *vs.* ε and $a_j(\varepsilon)$ *vs.* ε bifurcation diagrams. There are several other numerical continuation methods ranging in sophistication that can be used to approximate Stokes waves in this way, see [22], for example. What we have described in this appendix is among the simplest such methods, and one that only works well for sufficiently small ε. Since our focus in this thesis concerns the stability of Stokes waves in the limit $\varepsilon \to 0$, this method is sufficient to approximate the Stokes waves numerically, but future investigations that wish to study Stokes waves of larger amplitude should consider alternative numerical continuation schemes.

---

[3] Even better guesses to initialize Newton's method are the asymptotic expansions for $a_j(\varepsilon)$ and $c(\varepsilon)$, which can be inferred directly from the Stokes wave expansions carried out in the main text of this thesis.

A.2 The Vector Case

Suppose instead we have

$$\mathbf{u}_t = \mathcal{L}\mathbf{u} + \mathcal{N}(\mathbf{u}), \tag{A.12}$$

where $\mathbf{u} = (\eta(x,t), u(x,t))^T$ is a real, vector-valued function and the operators $\mathcal{L}$ and $\mathcal{N}$ are analogous to their scalar counterparts in the previous section[4]. Then, equation (A.12) encompasses the HPBW system, as discussed in Chapter 3, and even Euler's equations if they are appropriately reformulated and the second component of $\mathbf{u}$ is interpreted as q_x, the x-derivative of the velocity potential at the surface. Following the same calculations as in the previous section (but replacing the appropriate scalar quantities with vector quantities), one arrives at a numerical approximation for the Stokes waves $\mathbf{u}_S = (\eta_S(x;\varepsilon), u_S(x;\varepsilon))^T$ in terms of a truncated Fourier cosine series as well as a numerical approximation for the velocity $c(\varepsilon)$ of these waves.

---

[4] In the context of Euler's equations, the discrete symmetry $x \to -x$ is no longer valid. However, in the traveling frame, we get the symmetry $x \to -x$ provided $c \to -c$, which is enough to transfer the major ideas of the numerical method illustrated in the previous section to the Stokes waves of Euler's equations.

Appendix B

THE FLOQUET-FOURIER-HILL METHOD

B.1 The Scalar Case

Suppose we are given the following generalized spectral problem:

$$\mathcal{L}(u_S, \mu, c)w = \lambda \mathcal{R}(u_S, \mu, c)w, \tag{B.1}$$

where $w = w(x)$ is a 2π-periodic, complex-valued function and $u_S = u_S(x; \varepsilon)$ is a 2π-periodic, real-valued function with auxiliary dependence on a small parameter ε. The differential operators[1] $\mathcal{L}(\mu_S, \mu, c)$ and $\mathcal{R}(\mu_S, \mu, c)$ are linear with nonautonomous coefficients that depend on u_S and its spatial derivatives, a Floquet exponent $\mu \in [-1/2, 1/2)$ that is free to be chosen, and a scalar parameter $c \in \mathbb{R}$ that is dictated by u_S. In the context of this thesis, (B.1) defines the stability spectrum λ of the Stokes wave $u_S = u_S(x; \varepsilon)$ for a scalar model of water waves, such as the Kawahara equation in Chapter 2. The operators $\mathcal{L}(u_S, \mu, c)$ and $\mathcal{R}(u_S, \mu, c)$ are obtained by linearizing the given model about its Stokes wave solutions in a frame moving at velocity c and then applying separation of variables and Floquet theory.

In general, solving (B.1) is impossible to do exactly by analytical methods. In this thesis, we have shown how to exploit the small amplitude ε of the Stokes wave solutions u_S to determine the asymptotic behavior of the stability spectrum in the limit as $\varepsilon \to 0$. When not working in this limiting case, we resort to the Floquet-Fourier-Hill method to compute the stability spectrum numerically. This is a well-studied method, see [31] and [34], for example, but for the sake of completeness, we sketch the main ideas of the method in this appendix.

---

[1] Or, more generally, integro-differential operators.

We begin by choosing a small-amplitude[2] parameter ε and obtaining a numerical approximation for u_S using the method presented in Appendix A. From this method, we find

$$u_S(x;\varepsilon) \approx \sum_{j=0}^{N} a_j(\varepsilon)\cos(jx), \tag{B.2}$$

for sufficiently large N, where the Fourier cosine coefficients $a_j(\varepsilon)$ and the velocity of the Stokes wave $c(\varepsilon)$ are given numerically. We then substitute (B.2) as well as the value of $c(\varepsilon)$ into the coefficients of the linear operators $\mathcal{L}(u_S,\mu)$ and $\mathcal{R}(u_S,\mu)$ in (B.1), giving

$$\mathcal{L}\left(\sum_{j=0}^{N} a_j(\varepsilon)\cos(jx),\mu,c(\varepsilon)\right) w = \lambda\mathcal{R}\left(\sum_{j=0}^{N} a_j(\varepsilon)\cos(jx),\mu,c(\varepsilon)\right) w. \tag{B.3}$$

We then expand w as a Fourier series, since w is periodic:

$$w(x) = \sum_{j=-\infty}^{\infty} \widehat{W}_j e^{ijx}. \tag{B.4}$$

Unlike the Fourier expansion of u_S, the expansion of w cannot be expressed in terms of cosines alone, as (B.1) is nonautonomous and does not respect the discrete symmetry $x \to -x$.

To proceed, we truncate the Fourier expansion of w to $2M+1$ terms for M sufficiently large and arrive at the approximation

$$w(x) \approx \sum_{j=-M}^{M} \widehat{W}_j e^{ijx}. \tag{B.5}$$

We then substitute this approximation into (B.3), yielding

$$\mathcal{L}\left(\sum_{j=0}^{N} a_j(\varepsilon)\cos(jx),\mu,c(\varepsilon)\right)\left(\sum_{j=-M}^{M}\widehat{W}_j e^{ijx}\right) = \\ \lambda\mathcal{R}\left(\sum_{j=0}^{N} a_j(\varepsilon)\cos(jx),\mu,c(\varepsilon)\right)\left(\sum_{j=-M}^{M}\widehat{W}_j e^{ijx}\right). \tag{B.6}$$

---

[2] Note that the Floquet-Fourier-Hill method does not require ε to be small. In fact, the method can be used to obtain the stability spectrum of large-amplitude solutions as well. In the context of this work, however, ε is chosen to be sufficiently small so that we may compare with our asymptotic methods.

Introducing the Fourier transform

$$\mathcal{F}_k[f(x)] = \frac{1}{2\pi}\int_{-\pi}^{\pi} f(x)e^{-ikx}dx, \tag{B.7}$$

and applying it to both sides of (B.6) for $-M \leq k \leq M$ yields a matrix generalized eigenvalue problem of the form

$$\widehat{\mathcal{L}}(a_j(\varepsilon), \mu, c(\varepsilon)) \begin{pmatrix} \widehat{W}_{-M} \\ \vdots \\ \widehat{W}_M \end{pmatrix} = \lambda \widehat{\mathcal{R}}(a_j(\varepsilon), \mu, c(\varepsilon)) \begin{pmatrix} \widehat{W}_{-M} \\ \vdots \\ \widehat{W}_M \end{pmatrix}, \tag{B.8}$$

where $\widehat{\mathcal{L}}(a_j(\varepsilon), \mu, c(\varepsilon)) \in \mathbb{C}^{(2M+1)\times(2M+1)}$ and $\widehat{\mathcal{R}}(a_j(\varepsilon), \mu, c(\varepsilon)) \in \mathbb{C}^{(2M+1)\times(2M+1)}$ are matrices with entries

$$\left[\widehat{\mathcal{L}}(a_j(\varepsilon), \mu, c(\varepsilon))\right]_{mn} = \mathcal{F}_{m-(M+1)}\left[\mathcal{L}\left(\sum_{j=0}^{N} a_j(\varepsilon)\cos(jx), \mu, c(\varepsilon)\right) e^{i(n-(M+1))x}\right], \tag{B.9a}$$

$$\left[\widehat{\mathcal{R}}(a_j(\varepsilon), \mu, c(\varepsilon))\right]_{mn} = \mathcal{F}_{m-(M+1)}\left[\mathcal{R}\left(\sum_{j=0}^{N} a_j(\varepsilon)\cos(jx), \mu, c(\varepsilon)\right) e^{i(n-(M+1))x}\right], \tag{B.9b}$$

for $1 \leq m, n \leq 2M+1$. We then solve (B.8) over a chosen mesh of values for the Floquet exponent $\mu \in [-1/2, 1/2)$ using a standard eigenvalue solver, *e.g.*, the shifted QR algorithm [88]. The union of eigenvalues obtained over the full range of Floquet exponents gives a spectrally accurate approximation of the stability spectrum of the Stokes wave u_S, see [31] for a proof.

B.2 The Vector Case

Suppose instead we have the generalized spectral problem

$$\mathcal{L}(\mathbf{u}_S, \mu, c)\mathbf{w} = \lambda \mathcal{R}(\mathbf{u}_S, \mu, c)\mathbf{w}, \tag{B.10}$$

where $\mathbf{w} = (U(x), V(x))^T$ is a 2π-periodic, complex-valued function of two components, $\mathbf{u}_S = (\eta_S(x;\varepsilon), u_S(x;\varepsilon))^T$ represents our Stokes wave solutions from Appendix A, and the operators $\mathcal{L}(\mathbf{u}_S, \mu, c)$ and $\mathcal{R}(\mathbf{u}_S, \mu, c)$ are analogous to those in the scalar case (but are now represented by 2 × 2 matrix differential operators). The spectral problem for the Stokes waves of the HPBW system and Euler's equations are of the form (B.10), although Euler's equations must be reformulated and the second component of $\mathbf{u}_S$ and $\mathbf{w}$ must be interpreted as q_x (the x-derivative of the velocity potential at the free surface) and the perturbation applied to q_x, respectively.

By following the same calculations as in the previous section (but replacing the appropriate scalar quantities with vector quantities), one arrives at a $2(2M+1) \times 2(2M+1)$ block matrix eigenvalue problem of the form

$$\left(\begin{array}{c|c} \widehat{\mathcal{L}}^{(1,1)} & \widehat{\mathcal{L}}^{(1,2)} \\ \hline \widehat{\mathcal{L}}^{(2,1)} & \widehat{\mathcal{L}}^{(2,2)} \end{array}\right) \left(\begin{array}{c} \widehat{U}_{-M} \\ \vdots \\ \widehat{U}_{M} \\ \hline \widehat{V}_{-M} \\ \vdots \\ \widehat{V}_{M} \end{array}\right) = \lambda \left(\begin{array}{c|c} \widehat{\mathcal{R}}^{(1,1)} & \widehat{\mathcal{R}}^{(1,2)} \\ \hline \widehat{\mathcal{R}}^{(2,1)} & \widehat{\mathcal{R}}^{(2,2)} \end{array}\right) \left(\begin{array}{c} \widehat{U}_{-M} \\ \vdots \\ \widehat{U}_{M} \\ \hline \widehat{V}_{-M} \\ \vdots \\ \widehat{V}_{M} \end{array}\right), \tag{B.11}$$

where $\widehat{U}_k$ and $\widehat{V}_k$ represent the kth Fourier coefficient of the first and second components of $\mathbf{w}$, respectively, and the matrices $\widehat{\mathcal{L}}^{(i,j)} \in \mathbb{C}^{(2M+1)\times(2M+1)}$ and $\widehat{\mathcal{R}}^{(i,j)} \in \mathbb{C}^{(2M+1)\times(2M+1)}$ are the Fourier representations of the (i,j)th component of the 2 × 2 matrix differential operators $\mathcal{L}(\mathbf{u}_S, \mu, c)$ and $\mathcal{R}(\mathbf{u}_S, \mu, c)$, respectively. For more details on the explicit representation of these matrices in the context of Euler's equations, see [35] and [76].

Upon choosing a value for the small-amplitude parameter ε as well as a Floquet exponent $\mu \in [-1/2, 1/2)$, the eigenvalue problem (B.11) is solved numerically by a standard eigenvalue solver. The union of the numerically computed eigenvalues of (B.11) over a mesh of Floquet exponents yields a spectrally accurate approximation of the stability spectrum of the Stokes wave solution.